

Université du Québec
Institut national de la recherche scientifique
Énergie Matériaux Télécommunications

Nimble Radiation-Pattern Antennas Using Agile Frequency Selective Surfaces

by
Mahmoud Niroo-Jazi

A dissertation submitted in partial fulfillment of the requirements for the degree of
Doctor of Philosophy (Ph.D.) in Telecommunications

Evaluation Jury

External examiner	Prof. Chan-Wang Park Université du Québec à Rimouski (UQAR)
External examiner	Prof. Qingsheng Zeng Communications Research Centre Canada (CRC)
Internal examiner	Prof. Serioja Ovidiu Tatu INRS-Energie, Matériaux et Télécommunications
Research director	Prof. Tayeb A. Denidni INRS-Energie, Matériaux et Télécommunications

Abstract

The synergy gained between frequency selective surfaces as partially reflective/transparent screens and reflector antennas is exploited to present a new class of reconfigurable antennas for tactical communication systems in this thesis. The potentials of frequency selective surfaces in creating controllable electromagnetic shutters are theoretically and experimentally explored to fully take advantages of them in increasing the functionality of traditional reflector antennas. The related transmission line models of the corresponding sheets are also extracted to interpret their electromagnetic responses. To control the scattering responses of these shutters, high frequency switches are precisely incorporated into their constructing periodic elements. The possible DC-biasing feed schemes of active elements are investigated and the relevant reconfiguration mechanisms dictated by these schemes are identified. Furthermore, the effect of required biasing feed lines on the transmission/reflection responses of screens is evaluated. The adverse effects of non-ideal active elements are also examined to elaborate the screens according to the desired transmission/reflection responses.

In the proposed new class of multi-functional reconfigurable antennas, an appropriate radiation mechanism is utilized, and a simple design guideline based on the key principles of reflector antennas and frequency selective surfaces is presented. The designed planar frequency selective surfaces are applied in this radiation topology as a controllable electromagnetic window, and their performances are evaluated. The pros and cons of each antenna in providing different functionalities are investigated to emerge a new class of antenna called “Nimble-Antenna”. Indeed, a nimble-antenna refers to an

antenna with two functionalities, including sweeping its radiation over all azimuth angles and reconfiguring the antenna radiation-pattern between directional/omni-directional cases.

In the final designed reconfigurable electromagnetic window, a hybrid technique is also applied to enhance the nimble antenna performances and extend the functionality of the proposed radiation topology across two different frequency bands. In this structure, the number of active elements and overall antenna size are also reduced compared to the other presented prototypes.

Acknowledgement

First I would like to express my gratitude to my supervisor Prof. Tayeb A. Denidni for his support and continuous encouragement throughout my research. I really appreciate his guidance, insights and suggestions on this research, which will be a valuable experience for my future career.

I gratefully acknowledge my thesis committee members for their remarks and suggestions on my dissertation.

I also pass my sincere thanks to all my past and current technical colleagues at Institute National de la Recherche Scientifique— Énergie, Matériaux et Télécommunications (INRS-EMT) for their generous helps and constructive discussions.

The most and for most, my special appreciations go to my family for their extensive encouragements and continuous supports during this past five years, which gave me all the strength needed to successfully finish my PhD career. I deeply indebted to my mother and father for their understanding and all their unforgettable supports during whole of my career. I also express my sincere thanks to my brother for his encouragement and helps.

Last but not the least, I thank my beloved wife for her understanding, patience and supports through this period of time. Without her kind cares and patience, the difficulties of my PhD objectives and being far from of family would never be endured.

Table of Contents

Abstract	I
Acknowledgement	II
List of figures	VIII
List of tables	XV
Chapter 1 Introduction	1
1.1 Motivation	1
1.2 Problem identification	2
1.3 Problem remedies and project objectives	4
1.4 Thesis executive summary and accomplishments	5
1.4.1 Thesis summary	5
1.4.2 List of Publications	7
Chapter 2 Reconfigurable antennas	9
2.1 Introduction	9
2.2 Reconfigurable antennas	10
2.2.1 Frequency reconfiguration	11
2.2.2 Polarization reconfiguration	11
2.2.3 Radiation-pattern-gain reconfiguration	12
2.3 Reconfiguration methods	13
2.4 Reconfigurable antennas and their practical issues	15
2.5 Conclusion	16

Chapter 3	Periodic structures and their applications in antennas and microwave	17
3.1	Introduction	17
3.2	Frequency selective surfaces	19
3.2.1	Design parameters for frequency selective surfaces	20
3.2.2	Applications of frequency selective surfaces	25
3.3	Planar grid array of parallel strips	26
3.3.1	Scattering mechanism of a planar parallel array strips	27
3.3.2	Inductive and capacitive grids	29
3.3.3	Characterization of an inductive planar periodic array of strips	34
3.3.4	Applications of inductive and capacitive periodic strips for band stop filters 36	
3.4	Conclusion.....	38
Chapter 4	Active planar grid of metallic strips and its applications in reconfigurable antennas	40
4.1	Introduction	40
4.2	Active planar metallic strips.....	42
4.2.1	Inductive grid characterization	42
4.2.2	Capacitive grid characterization	45
4.2.3	Active element integration	51
4.2.4	Reconfiguration mechanisms and DC-biasing feed line.....	53
4.3	Applications of agile transparent/opaque screens in reconfigurable antennas...	55
4.4	Reconfigurable flat-reflector antenna design	56
4.4.1	Flat-reflector design	56
4.4.2	Reconfigurable flat-reflector using planar agile metallic grid	60
4.5	Conclusion.....	65
Chapter 5	Cylindrical FSS screens and nimble radiation-pattern antennas	66
5.1	Introduction	66
5.2	Design of cylindrical reconfigurable reflector antenna.....	68
5.2.1	Simulation results of a semi-cylinder reflector antenna	70
5.3	Reconfigurable cylindrical FSS reflector antenna design	72

5.4	Switched-beam reconfigurable antenna using cylindrical frequency selective surface.....	73
5.4.1	Reconfigurable mechanism of FSS screen used in switched-beam antenna 74	
5.4.2	Antenna configuration and simulation results	75
5.4.3	DC-Feeding lines effect	78
5.4.4	Measurement results and discussion.....	79
5.5	Nimble radiation-pattern antenna.....	83
5.5.1	Unit cell configuration and reconfiguration mechanism	83
5.5.2	Antenna radiation performances and the effect of modified unit cell	86
5.5.3	Measurement results and discussion.....	88
5.6	Conclusion.....	92
Chapter 6	Agile frequency nimble antenna.....	94
6.1	Agile frequency nimble radiation-pattern antenna.....	94
6.1.1	Hybrid reconfigurable FSS screen design.....	95
6.1.2	Antenna design.....	98
6.1.3	Simulation parametric study results.....	100
6.2	Experimental results of agile frequency nimble antenna and discussion.....	104
6.2.1	Transmission coefficient measurements	104
6.2.2	Antenna measurement results and discussion.....	106
6.3	Conclusions	112
Chapter 7	Conclusion and future research works	114
7.1	Conclusion.....	114
7.2	Future research works	116
Chapter 8	Résumé.....	118
8.1	Introduction	118
8.1.1	Motivation.....	118
8.1.2	Identification du problème	119
8.1.3	Solutions au problème et objectifs du projet.....	120
8.2	Grille SSF active métallique planaire.....	121

8. 2. 1	Caractérisation d'une grille inductive	122
8. 2. 2	Caractérisation de la grille capacitive	123
8. 2. 3	Intégration d'éléments actifs	125
8. 2. 4	Mécanisme de reconfiguration et ligne d'alimentation de polarisation DC 126	
8. 3	Applications de surfaces agiles transparentes/opagues dans les antennes reconfigurables.....	S
8. 3. 1	Résultats de simulations et de mesures	128
8. 4	SSF cylindrique et antennes agiles en diagramme de rayonnement	130
8. 4. 1	Antenne reconfigurable à faisceau commuté utilisant une SSF cylindrique 131	
8. 4. 2	Antenne agile en diagramme de rayonnement.....	135
8. 4. 3	Antenne agile en diagramme de rayonnement et en fréquence	138
8. 5	Conclusion.....	146
8. 6	Axes des futures recherches	146

List of Figures

Fig. 1-1 Cylindrical EBG-antenna configuration.....	3
Fig. 1-2 Transmission coefficient response of a typical EBG-structure.....	4
Fig. 3-1 The most typical elements used in FSSs [17].	22
Fig. 3-2 Four types of grids used in FSSs, possessing various degrees of symmetry. (a) Rectangular. (b) Skewed. (c) Square. (d) Equilateral triangular [61].	24
Fig. 3-3 Dual frequency reflector antenna with an FSS sub-reflector [67].	25
Fig. 3-4 Grating geometry of infinite parallel strips [80].	28
Fig. 3-5 Inductive grid geometry and its equivalent transmission line model.....	30
Fig. 3-6 Transmission power response of an inductive planar grid and its transmission line model.....	35
Fig. 3-7 Schematic representation of passive FSS filters. (a) Square-loop screen [60]. (b) Gridded square-loop screen [59].	38
Fig. 4-1 Passive capacitive grid incorporated with ideal active elements. (a) Geometry of the grid. (b) Typical transmission response of the passive inductive and capacitive grid for normal incident.....	41
Fig. 4-2 Geometry of inductive FSS screen and its transmission line model.	44
Fig. 4-3 Effect of inductive grid periodicity on transmission coefficient.....	44

Fig. 4-4 Effect of strip width on transmission coefficient in an inductive FSS screen.....	45
Fig. 4-5 Geometry of capacitive FSS screen and its transmission line model.....	47
Fig. 4-6 Transmission coefficient response of the screen shown in Fig. 4-5 for various P_x	47
Fig. 4-7 Transmission coefficient response of the screen shown in Fig. 4-5 for various P_y	48
Fig. 4-8 Transmission coefficient response of the screen shown in Fig. 4-5 for various w	48
Fig. 4-9 Transmission coefficient response of the screen shown in Fig. 4-5 for various g_0	49
Fig. 4-10 Effect of P_y/P_x ratio on capacitive grid response.	50
Fig. 4-11 Effect of supporting dielectric on the grid response.	52
Fig. 4-12 Effect of gap width on the grid response.....	53
Fig. 4-13 Effect of active element on the grid response. (a) PIN-diode model. (b) Simulated transmission coefficient for different parasitic capacitance values.	53
Fig. 4-14 Geometries of two serial-fed reconfiguration mechanisms and their transmission coefficient responses. (a) Vertical fed. (b) Horizontal fed.	54
Fig. 4-15 Flat reflector antenna geometry.....	56
Fig. 4-16 Reflection coefficient of the flat reflector antenna for different values of h_d . $L_d = 44, H = \lambda, L = 2\lambda$ (All dimensions are in mm).....	57
Fig. 4-17 Parametric studies of flat reflector antenna carried out for realized gain at different values of H, L, and hd . $L_d = 0.36\lambda, H = \lambda, L = 2\lambda, hd = 0.3\lambda$ (All dimensions are in mm).....	58
Fig. 4-18 Parametric studies of flat reflector antenna carried out for H-plane radiation-pattern at different values of hd (a), H (b), and L (c). $L_d = 0.36\lambda, H = \lambda, L = 2\lambda, hd = 0.3\lambda$ (All dimensions are in mm).....	59

Fig. 4-19 Parametric studies of flat reflector antenna carried out for E-plane radiation-pattern at different values of hd (a), H (b), and L (c). $Ld = 0.36\lambda$, $H = \lambda$, $L = 2\lambda$, $hd = 0.3\lambda$ (All dimensions are in mm).....	60
Fig. 4-20 Transmission coefficient measurement setup.	61
Fig. 4-21 Evaluating the performances of a FSS screen based on the first proposed unit cell. (a) Four different FSS screens constructed using 24×4 elements of these unit cells. (b) Measured transmission coefficient compared to the simulation.	62
Fig. 4-22 Photo of fabricated prototype (a), and reflection coefficient results (b).	63
Fig. 4-23 Antenna radiation-patterns. (a) E-plane pattern. (b) H-plane pattern.	64
Fig. 5-1 Geometry of the proposed active reconfigurable cylindrical frequency selective surface antenna (ARCFSSA).	67
Fig. 5-2 Geometry of the semi-cylindrical reflector antenna.....	68
Fig. 5-3 Geometry of a corner reflector superimposed into a semi-cylindrical reflector antenna.	69
Fig. 5-4 Reflection coefficient of semi- cylindrical reflector antenna for different values of R . (a) Results for different values of R . (b) Results for different values of L	71
Fig. 5-5 Realized gain of semi- cylindrical reflector antenna. (a) Results for different values of R . (b) Results for different values of L	71
Fig. 5-6 Radiation-patterns of semi- cylindrical reflector antenna for different values of R and L . (a) H-plane for different R values. (b) H-plane for different L values. (c) E-plane for different R values. (d) E-plane for different L values.	72
Fig. 5-7 Cylindrical FSS screen and number of active elements along its length and circumference.....	73
Fig. 5-8 Reconfigurable cylindrical reflector antenna. (a) Perspective view of the antenna (b) Schematic distributed geometry of FSS screen, $P_x = 28.8$, $P_y = 52$, $w = 1$. (c) Dipole antenna used in the proposed switched-beam cylindrical reflector antenna $Ld = 40$, $Rd = 3$, (All values are in mm).	74

Fig. 5-9 A unit cell of the proposed FSS screen and its coefficient response. (a) Geometry of the unit cell, $P_x = 30$, $P_y = 52$, $w = 1$ (all in mm). (b) Amplitude and phase of reflection coefficient. (c) Amplitude and phase of transmission coefficient. 75

Fig. 5-10 Parametric study of antenna shown in Fig. 4-7 performed for various R values. (a and b) Reflection coefficient for various R and P_y . (c and d) Gain for various R and P_y . (e and f) Normalized H-plane radiation-pattern for various R and P_y . (g and h) Normalized E-plane radiation-pattern for various R and P_y 77

Fig. 5-11 Comparison of antenna radiation characteristics for the cases with and without parallel DC-feeding lines. (a) Reflection coefficient. (b) Gain. (c) H-plane radiation-pattern. (d) E-plane radiation-pattern. 78

Fig. 5-12 Photo of fabricated switched-beam reconfigurable antenna. 79

Fig. 5-13 Measured and simulated results for switched-beam reconfigurable antenna (a) Reflection coefficient. (b) Realized gain. (c) H-plane radiation-pattern. (d) E-plane radiation-pattern. 82

Fig. 5-14 Nimble radiation-pattern antenna. (a) Antenna configuration. (b) Distributed configuration of applied cylindrical FSS screen. 84

Fig. 5-15 Simple and modified unit cell configurations FSS screen used in nimble radiation-pattern antenna. 84

Fig. 5-16 Scattering parameters of simple and modified unit cells. (a) Amplitude of transmission coefficient. (b) Phase of transmission coefficient. (c) Amplitude of reflection coefficient. (d) Phase of reflection coefficient. 85

Fig. 5-17 Antenna radiation characteristics performed for various R values. (a) Reflection coefficient. (b) Realized gain. (c) E-plane radiation-pattern. (d) H-plane radiation-pattern. 87

Fig. 5-18 Antenna radiation characteristics performed for various L_s values. (a) E-plane radiation-pattern. (b) H-plane radiation-pattern. 87

Fig. 5-19 Parametric study performed for different stub length showing its effect on the stop-band performance. 88

Fig. 5-20 Photo of fabricated nimble beam antenna. 90

Fig. 5-21 Simulated and measured reflection coefficient for nimble beam antenna.	90
Fig. 5-22 Measured radiation-pattern for nimble beam antenna (a) H-plane radiation-pattern. (b) E-plane radiation-pattern.....	91
Fig. 5-23 Measured and simulated realized gain of nimble antenna.	92
Fig. 6-1 Geometry of dual band reconfigurable FSS screen and transmission line model of its unit cell.	96
Fig. 6-2 Transmission coefficient response of two basic resonant elements. (a) Discontinuous strips. (b) Discontinuous elliptical rings.	97
Fig. 6-3 Transmission and reflection coefficient response of hybrid dual band reconfigurable FSS screen (a) Transmission coefficient. (b) Reflection coefficient.....	97
Fig. 6-4 Transmission coefficients of hybrid unit cell for different unit cell sizes. (a) For different values of P_y . (b) For different values of Le . (c) For different values of W . (All values are in mm).....	98
Fig. 6-5 Agile frequency nimble radiation-pattern antenna. (a) Antenna geometry. (b) Excitation source.....	99
Fig. 6-6 Parametric studies on reflection coefficients carried out for the most crucial dimensions. (a) For different values of R . (b) For different values of Le . (c) For different values of W	101
Fig. 6-7 Parametric studies on radiation-patterns carried out for the most crucial dimensions at 2.45GHz. (a) E-plane for different values of R . (b) E-plane for different values of Le . (c) E-plane for different values of W . (d) H-plane for different values of R . (e) H-plane for different values of Le . (f) H-plane for different values of W	102
Fig. 6-8 Parametric studies on antenna gain carried out for the most crucial dimensions. (a) For different values of R . (b) For different values of Le . (c) For different values of W	103
Fig. 6-9 Measured and simulated transmission coefficients. (a) FSS-A. (b) FSS-B.	105
Fig. 6-10 Fabricated prototype of agile nimble radiation-pattern antenna.	107
Fig. 6-11 Measured and simulated reflection coefficients of dipole and agile frequency nimble.	108

Fig. 6-12 Measured and simulated realized gain of agile frequency nimble antenna.....	109
Fig. 6-13 Measured and simulated radiation-pattern of agile frequency nimble antenna in directional case. (a) H-plane. (b) E-plane.	110
Fig. 6-14 Measured and simulated radiation-pattern of dipole and agile frequency nimble antenna in omni-directional case. (a) H-plane. (b) E-plane	111
Fig. 8-1 Configuration d'antenne BIE cylindrique.	119
Fig. 8-2 Grille capacitive passive intégrée à des éléments actifs.....	121
Fig. 8-3 Géométrie d'un écran SSF inductif et son model en ligne de transmission.....	122
Fig. 8-4 Effet de la périodicité de la grille sur le coefficient de transmission.	123
Fig. 8-5 Géométrie d'un écran capacitif SSF, son modèle en ligne de transmission, et sa réponse en coefficient de transmission.	124
Fig. 8-6 Effet d'un élément actif sur la réponse de la grille (a) Modèle de la diode PIN. (b) coefficient de transmission Simulé pour différentes valeurs de capacités parasites.	125
Fig. 8-7 Géométries de deux mécanismes de reconfiguration d'alimentations séries et leurs réponses en coefficient de transmission. (a) Alimentation verticale. (b) Alimentation horizontale.....	127
Fig. 8-8 Géométrie d'une antenne à réflecteur plan.	128
Fig. 8-9 Évaluation des performances d'une SSF basé sur la cellule de base proposée. (a) Quatre différents SSF construits en utilisant 24×4 éléments de ces cellules de base. (b) Coefficient de transmission mesuré comparé à la simulation.....	129
Fig. 8-10 Photo du prototype fabriqué (a), et des résultats du coefficient de réflexion (b).	129
Fig. 8-11 Diagramme de rayonnement de l'antenne. (a) Diagramme E plan (b) Diagramme H plan.....	130
Fig. 8-12 Géométrie de l'antenne SSF active, reconfigurable, cylindrique proposée (ASSFARC).	131
Fig. 8-13 Antenne reconfigurable à réflecteur cylindrique. (a) Vue en perspective de l'antenne (b) Schéma de la géométrie distribuée de la SSF $P_x = 28.8, P_y = 52, w = 1$.	

(c) Antenne dipôle utilisée dans l'antenne à réflecteur cylindrique à faisceau commuté $Ld = 40, Rd = 3$, (valeurs en mm).	132
Fig. 8-14 Photo de l'antenne reconfigurable à faisceau commuté fabriquée.....	133
Fig. 8-15 Résultats mesurés et simulés pour l'antenne à faisceau reconfigurable commuté (a) Coefficient de réflexion (b) Gain réalisé. (c) Diagramme de rayonnement dans le plan H (d) Diagramme de rayonnement dans le plan E.....	134
Fig. 8-16 Antenne agile en diagramme de rayonnement (a) Configuration de l'antenne (b) SSF cylindrique appliquée à une configuration distribuée.	135
Fig. 8-19 Diagramme de rayonnement mesuré pour antenne à faisceau agile (a) Diagramme de rayonnement dans le plan H. (b) Diagramme de rayonnement dans le plan E.....	136
Fig. 8-17 Photo de l'antenne agile fabriquée.....	136
Fig. 8-18 Coefficient de réflexion simulé et mesuré pour antenne à faisceau agile.	136
Fig. 8-20 Simulation et mesures du gain réalisé de l'antenne agile.....	137
Fig. 8-21 Géométrie d'une SSF double bande reconfigurable et modèle de ligne de transmission de sa cellule de base.....	139
Fig. 8-22 Réponse des coefficients de transmission et réflexion d'une SSF double bande hybride reconfigurable. (a) Coefficient de transmission. (b) Coefficient de réflexion...	140
Fig. 8-23 Antenne agile en diagramme de rayonnement et en fréquence. (a) Géométrie de l'antenne (b) Source d'excitation.....	141
Fig. 8-24 Coefficients de transmission simulés et mesurés. (a) SSF-A. (b) SSF-B.	142
Fig. 8-25 Prototype fabriqué de l'antenne agile en diagramme de rayonnement.	143
Fig. 8-26 Coefficients de réflexion simulé et mesuré et gain du dipôle et de l'antenne agile en fréquence. (a) Coefficient de réflexion. (b) Gain.	143
Fig. 8-27 Diagramme de rayonnement simulé et mesuré du cas d'une antenne agile en fréquence dans le cas directif. (a) Plan H. (b) Plan E.	145
Fig. 8-28 Diagramme de rayonnement simulé et mesuré du cas d'une antenne agile en fréquence dans le cas omnidirectionnel. (a) Plan H. (b) Plan E.	145

List of Tables

Tab. 2-1 Comparison of different reconfigurable approaches.	14
Tab. 3-1 FSS lattice type and grating-lobe criteria [61].	24
Tab. 5-1 Final dimensions of the switched-beam reconfigurable antenna.	74
Tab. 5-2 Radiation characteristics of switched-beam antenna.....	80
Tab. 5-3 Final dimensions of nimble radiation-pattern antenna.	88
Tab. 5-4 Radiation characteristics of Nimble antennas compared to semi-cylindrical reflector.	92
Tab. 6-1 Final dimensions of the agile nimble beam antenna.	101
Tab. 6-2 Final dimensions of the fabricated FSS sheets and agile frequency nimble antenna.	104
Tab. 6-3 Antennas characteristics.	112
Tab. 8-1 Caractéristiques de rayonnement de l’antenne à faisceau commuté.	134
Tab. 8-2 Caractéristiques de rayonnement d’antennes agiles comparés au réflecteur semi-cylindrique.	138
Tab. 8-3 Caractéristiques des antennes.	146

Chapter 1

Introduction

1.1 Motivation

Advanced communication systems have recently received a growing attention because of their abilities to provide various functionalities in an individual unit, introducing less cost, more versatility, robustness, and significant saving in volume and maintenance. For instances, increasing number of cell-phone users, aside of the main purpose of instant vocal accessibility, is interested to benefit other amenities, including multimedia, GPS, and internet [1, 2]. Each of these services operates over different frequency bands, or may need to use polarization/space diversity to improve the quality of the system. These trends show that more and more communications can be performed with a single platform.

Intelligent systems, as another example of modern systems, are on the rise in both industrial or military applications, which are looking for new generation of small, low cost and versatile components to increase the overall system performances as well [3]. Depending on the type of the communication functions, a modern system requires to provide desired actions in the reception modules as well as data processing units. Therefore, because of holding a paramount role in the antenna system embodiments, antenna design and development have attracted a great eminence in the antenna design arena to explore various types of multi-functional configurations. This leads to increase the overall performances of the communication systems by integrating a few functions in a single element and hence not littering the platform by multiple antennas to handle each function.

Accordingly, recently a particular research subject, called reconfigurable antenna (RA), has received a growing attention to explore new antennas with different operating characteristics, including frequency, polarization, and radiation-pattern (RAs) according to the desired system requirements [4]. On the other hand, RA alleviates detriments of the traditional antennas and mitigates demerits of adaptive or smart antennas leading to increase the overall communication system performances. This indeed is achieved by effectively exploiting the available frequency spectrum and all the antenna-system potentials, which may improve the system efficiency. The extensive applications of agile components in Antennas & Microwave areas and more important the outstanding merits of RAs for modern communication systems have motivated us to establish a comprehensive research in this area. Therefore, this project aims to design, analysis, and fabricate a number of new reconfigurable antennas based on periodic structures for modern tactical communication systems.

1.2 Problem identification

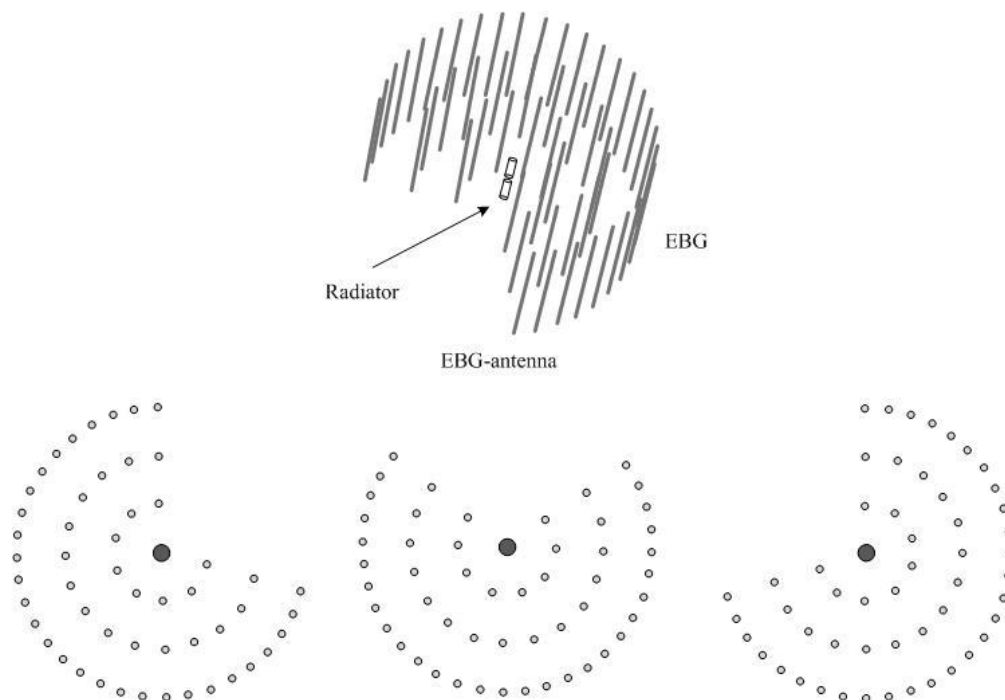
It is well known that because of their anomalous behavior, periodic structures have widely been applied in microwave and antennas by exploring their desired characteristics. They are designed in different configurations as summarized in [5] in which they are either served to create new materials with unusual electromagnetic properties or treat in a special way with the incident waves. The former is generally recognized as negative materials, while the later can be classified as electromagnetic band-gap materials (EBG) and frequency selective surfaces (FSS). EBG materials are used to create an electromagnetic band-gap response or direct the waves by inserting a defect in the periodic structure. These properties have found interesting applications in antennas to alleviate the surface waves in the planar array configuration [6], increase antenna gain [7-12], and provide efficient low profile antennas by creating high impedance surface (HIS) or artificial magnetic conductor (AMC) as a ground plane [6, 13].

By changing the periodic pattern shape using a certain reconfiguration mechanism, the electromagnetic properties of periodic structures can also be controlled. This concept has been used in antenna domain to control the antennas' radiation performances in terms of direction of the radiation-pattern or gain [14]. In particular, in [15] a periodic array of metallic rods arranged in a cylindrical shape, as shown in Fig. 1-1, has been utilized to create a directive radiation-pattern. The transmission coefficient response of the periodic structure, analyzed using CST Microwave Studio software in Fig. 1-2, demonstrates that a band-gap is realized by this periodic pattern at low frequencies, prohibiting the propagation of the incident waves through the periodic elements. On the other hand, the inserted angular defect into the periodic pattern directs the electromagnetic waves excited

by the sources at its center. Therefore, a directive radiation-pattern is created by this structure [16].

It is well known that by inserting some discontinuities along the rods, the band-gap response can be eliminated at the desired operating frequency. These discontinuities can be realized by integrating some high frequency PIN-diodes into the structure, offering a reconfigurable band-gap response for the periodic array of rods. Therefore, by using this reconfiguration mechanism, the angular direction of the defect in the periodic pattern is changed. Indeed, this reconfigurable defect provides the feasibility of sweeping entire azimuth angles in a few steps. However, this structure must be implemented in multi-layer configuration, making it complex and difficult in fabrication. Furthermore, a large number of active elements are needed, which increases the cost of the antenna system. The functionalities of the antenna are also limited to sweeping beam and reconfigurable between directional and omni-directional beams.

Therefore, this thesis aims to introduce new antenna configurations based on other periodic structures, i. e., frequency selective surfaces, to reduce the number of used active elements and hence lessen the antenna complexity. Moreover, it is expected to take advantages of the hybrid periodic structures and increases the functionality of the antenna.



Top cross section views of reconfigured EBG pattern for different defect pattern.

Fig. 1-1 Cylindrical EBG-antenna configuration.

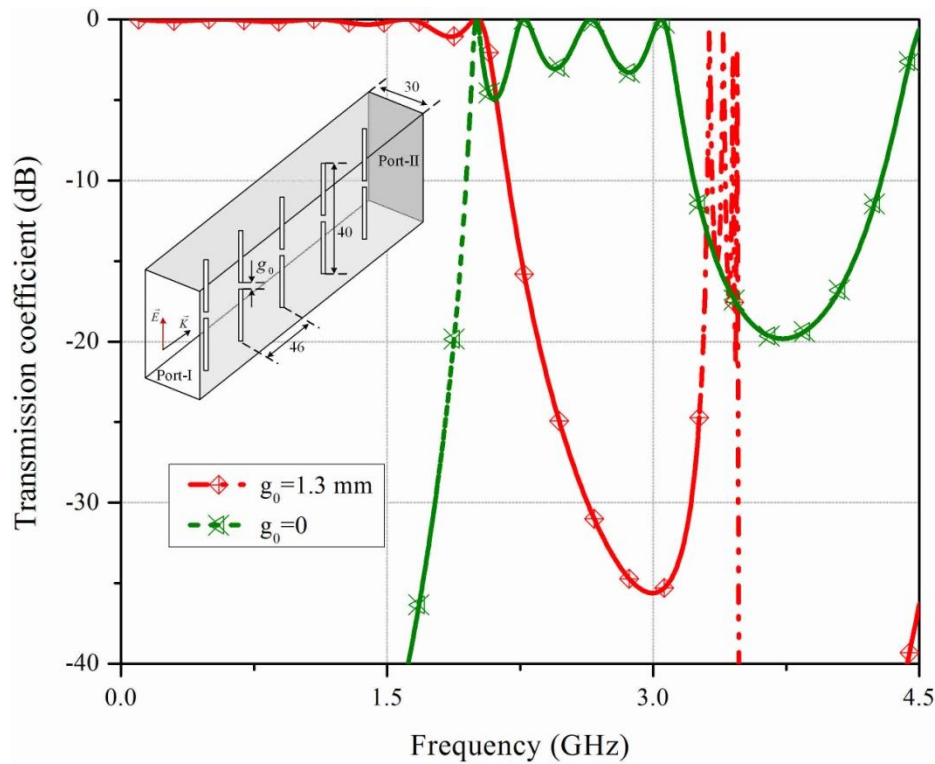


Fig. 1-2 Transmission coefficient response of a typical EBG-structure.

1.3 Problem remedies and project objectives

As a kind of periodic structures, frequency selective surfaces (FSS) have received a particular attention in the microwave and antenna domains. They are usually used to filter out the incident electromagnetic waves over a specific bandwidth or let them pass through the FSS screen. This finds appropriate applications in the reflectors, filters, absorbers, and radomes [17-19]. When the phase of the incident/transmission wave is controlled, the FSS structure can be used to manipulate the antenna beam direction [20], change the polarization of the scattered waves [17], or provide zero phase reflection surfaces [13]. In most of these applications, the FSSs are passive and they cannot electronically or mechanically change their electromagnetic responses.

The benign electromagnetic behavior of FSS screens in respect to the incident electromagnetic (EM) waves has grasped researchers' attention to benefit them in reconfigurable antennas, as well. In [21-23], a low profile reconfigurable antenna has been addressed in which an active meta-surface has been used as a partially reflecting surface to tune the resonant frequency and enhance the antenna gain. For some other contributions, tunable high impedance surfaces (HIS) or artificial magnetic conductors (AMC) based on the FSS concept have been proposed to steer the antenna radiation-

pattern [14, 24, 25]. Reconfigurable FSS textures have also been used to develop some phase shifters as the elements of reflect array antennas to steer the antenna radiation-pattern or as elements of a lens antenna [20, 26, 27].

In this work, a new class of reconfigurable FSS screens is proposed to create a number of reconfigurable antennas, and hence to tackle the disadvantages of the above mentioned EBG-based reconfigurable structure, shown in Fig. 1-1. Indeed, the transmission/reflection responses of each planar FSS are carefully delineated to elaborately reshape the screens to a cylindrical form. The cylindrical shape is deliberately chosen to achieve the desired sweeping beam performances over all azimuth angles. Then, by precisely controlling the active elements integrated into the cylindrical FSS, the radiated field of an RF-source at the center of the cylinder is controlled to achieve the desired functionality.

As specific objectives, the designed antennas must operate at 2.45GHz, to be able to sweep whole azimuth angles over minimum 15% of bandwidth using a directive pattern with more than 10dB realized gain. This feature is demanded in the adaptive or smart antenna systems for space diversity or having a directive radiation-pattern at different angles with a single antenna element. The radiation-pattern is also interested to be reconfigured to the omni-directional pattern case, covering instantaneously all azimuth angles. This feature also can be used in the intelligent systems demanding a gain diversity to enhance the performance of the system by increasing the signal-to-noise ratio. The back-lobe level of the radiation-pattern in the directive case would be expected to be better than 20dB. In the design process, the number of active elements needs to be kept as minimum as possible to decrease the antenna cost and also enhance its radiation performances.

1.4 Thesis executive summary and accomplishments

1.4.1 Thesis summary

In order to tackle the above mentioned objectives, firstly a literature review on the reconfigurable antennas is carried out in Chapter-2 to clearly identify this concept. The possible reconfigurable antenna characteristics are explained and their impacts in improving the overall system performances are explained. The most commonly used reconfiguration methods are also described and compared to each other, and finally the chapter is ended up with some remarks on practical considerations.

Following to the research survey presented in the first chapter, comprehensive studies on periodic structures and in particular frequency selective surfaces are presented in

Chapter-3. The FSS elements are classified in this section and the substantial design considerations of FSSs are described. As a kind of frequency selective surfaces, the scattering performances of planar inductive and capacitive grids are theoretically and analytically delineated and their responses to incident TE-waves are described according to their lattice dimensions.

Applications of inductive and capacitive partially reflective/transparent surfaces in reconfigurable antennas are the subject of investigations in Chapter-4. The effect of lattice dimensions on the transitivity/reflectivity performances of the grids are analytically explained by their proposed transmission line models. Moreover, the active element integration effects and impact of DC-biasing feed lines on determining the reconfiguration mechanism in designing planar reconfigurable electromagnetic windows are explained in this part. Then, the performances of these surfaces in reconfigurable flat reflector antennas are experimentally evaluated.

To increase the functionality of the flat reflector antenna, two types of reconfigurable antenna based on principles of cylindrical reflector antennas are presented in Chapter-5. Firstly, the principles of cylindrical reflector antennas are investigated to identify the overall design guidelines of the antenna. Then, two screens introduced in the previous chapter are reformed to a conformal cylindrical shape to construct two reconfigurable antennas. The constraints of DC-feeding line method on both the reconfiguration mechanism and the functionality of the antennas are experimentally explored in this part. Moreover, the limitations of each method because of the undesired effects of DC-feeding lines and non-ideal active elements are identified. Furthermore, in this chapter, a new antenna called “nimble-antenna” is introduced and its practical radiation performances are presented. This antenna is able to both sweep entire azimuth angles and reconfigure its pattern between directional and omni-directional cases.

To improve the nimble antenna performances and its functionality, a new FSS is proposed using a hybrid unit-cell configuration in Chapter-6. The design procedure of this hybrid unit cell is presented and its transmission/reflection response is evaluated for agile frequency nimble antenna applications. The most useful practical results of the fabricated prototypes are presented in this chapter, and the potentials of the applied hybrid FSS in creating single band or agile-frequency dual-band reconfigurable antenna are revealed.

At the end, a summary of this work accomplishment is presented in Chapter-7, and the thesis is closed with some research lights gleaming for new future investigation avenues. A French summary of thesis is also presented in Chapter-8.

1. 4. 2 List of Publications

- [1]. M. N. Jazi and T. A. Denidni, "Electronically Sweeping Beam Antenna Using a New Cylindrical Active Frequency Selective Surface," *IEEE Trans. on Ant. and Propag.*, to be appeared, May 2012.
- [2]. M. N. Jazi and T. A. Denidni, "Analytical and Experimental Results of a Novel Rejection-Band Ultra-Wideband Dielectric Resonator Antenna Using Hybrid Techniques," *IEEE on Ant. And Wireless Propag. Lett.*, Vol. 11, p.p. 492-495, May 2012.
- [3]. E. Erfani, J. Nourinia, C. Ghobadi, M. N. Jazi, T. A. Denidni, "Integrated UWB/Reconfigurable-Narrowband Antenna for Cognitive Radio System Applications," *IEEE on Ant. and Wireless Propag. Lett.*, Vol. 11, p.p. 77-80, March 2011.
- [4]. M. N. Jazi and T. A. Denidni, "Triple-Band Monopole-Like Radiation-pattern Circular Ring Patch Antenna Using Hybrid Technique," *IEEE Trans. on Ant. and Propag.*, Vol. 59, No. 10, p.p. 3512-3517, October 2011.
- [5]. M. N. Jazi and T. A. Denidni, "Frequency Selective Surfaces and Their Application for Nimble-Radiation-pattern Antennas," *IEEE Trans. on Ant. and Propag.*, Vol. 58, No. 7, p.p. 2227 - 2237, July 2010.
- [6]. T. A. Denidni, Z. Weng and M. N. Jazi, "Z-Shaped Dielectric Resonator Antenna for Ultra-Wideband Applications," *IEEE Trans. on Ant. and Propag.*, Vol. 58, No. 12, p.p. 4059-4062, September 2010.
- [7]. M. N. Jazi and T. A. Denidni, "Agile Radiation-Pattern Antenna Based on Active Cylindrical Frequency Selective Surfaces," *IEEE on Antenna and Wireless Propag. Lett.*, Vol. 9, p.p. 387-388, April 2010.
- [8]. M. N. Jazi, and T. A. Denidni, "Design and Implementation of an Ultra-Wide Band Dielectric Skirt Monopole Antenna," *IEEE on Antenna and Wireless Propag. Lett.*, Vol.7, p.p. 493 - 496, August 2008.
- [9]. M. N. Jazi and T. A. Denidni, "Reconfigurable Schemes of Parallel Metallic Strips for Nimble Antennas," in *IEEE Int. Conf. on Ant. and Propag.*, Chicago, USA, July 8-14, 2012.
- [10]. E. Erfani, M. N. Jazi and T. A. Denidni, "Switchable UWB/Multi-Narrowband Antenna for Cognitive Radio Applications," in *IEEE Int. Conf. on Ant. and Propag.*, Chicago, USA, July 8-14, 2012.
- [11]. M. N. Jazi and T. A. Denidni, "Reconfigurable Dual-Band Frequency Selective Surface Using a New Hybrid Element," in *IEEE Int. Conf. on Ant. and Propag.*, Washington State, USA, July 1-7, 2011.

-
- [12].M. N. Jazi and T. A. Denidni, "Ultra-Wideband Dielectric-Resonator Antenna with Band Rejection," in *IEEE Int. Conf. on Ant. and Propag.*, Toronto, Canada, July 11-17, 2010.
- [13].M. A. Habib, M. N. Jazi, A. Djaiz, M. Nedil, M. C. E. Yagoub and T. A. Denidni, "On IP3 Performance Investigation in Reconfigurable Active EBG Antenna," in *IEEE Int. Conf. on Ant. and Propag.*, Toronto, Canada, July 11-17, 2010.
- [14].M. N. Jazi, T. A. Denidni and Adel R. Sebak, "Ultra-Wideband Dielectric-Resonator Antenna Based on Hybrid Techniques," in *Int. Symp. on ANTEM/AMEREM*, Ottawa, Canada, July 5-9, 2010.
- [15].M. N. Jazi and T. A. Denidni, "Design and Implementation of an Ultra-Wide Band Dielectric Resonator Antenna for Communication Systems," in *the 18th Iranian Conf. on Elec. Eng.*, Isfahan, Iran, May 11-13, 2010.
- [16].M. N. Jazi, M. A. Habib and T. A. Denidni, "Electronically Switching Radiation-pattern Antenna Using an Active Cylindrical Frequency Selective Surface," in *IEEE Int. Conf. on Ant. and Propag.*, Charleston, USA, July 1-5, 2009.
- [17].M. N. Jazi, M. A. Habib and T. A. Denidni, "Reconfigurable Radiation-Pattern Antenna Based on Active Frequency Selective Surfaces," in *IEEE Int. Conf. on Ant. and Propag.*, Charleston, USA, July 1-5, 2009.
- [18].M. A. Habib, M. N. Jazi, A. Djaiz, M. Nedil and T. A. Denidni, "Switched-Beam Antenna Based on EBG Periodic Structures," in *Int. Microwave Symp. (IMS)*, Boston, USA, 2009.
- [19].M. N. Jazi and T. A. Denidni "A New Hybrid Skirt Monopole Dielectric Resonator Antenna," in *IEEE Int. Conf. on Ant. and Propag.*, San Diego, USA, July 5-12, 2008.
- [20].M. N. Jazi, and T. A. Denidni, "Design and Implementation of an Ultra-Wide Band Dielectric Resonator Antenna for Electronic Warfare (EW) Systems," in *the second Int. Conf. on Wireless Communications in Underground and Confined Areas (ICWCUCA)*, p.p. 107-109, Canada, August 25-27, 2008.

Chapter 2

Reconfigurable antennas

2.1 Introduction

Demands on low cost, high quality, robust and high data rate communication systems, capable of adapting to the unpredictable or/and harsh electromagnetic environments, have proliferated some attractive emerging research topics so called electronically controlled, smart-adaptive, and agile-reconfigurable antennas [1, 2, 4, 28, 29]. Certainly, all these research areas have been conducted, more or less in a common reason, to ameliorate the restrictions of commonly used antennas. Indeed, the conventional antenna in intelligence systems, for instance planar phased-array technology, restricts both scan angles and operation because of the limitations of individual array elements and antenna element spacing. On the other hand, smart-adaptive antennas refer to a bunch of antennas positioned in a special configuration to be weighted by a particular terminology for a precise scenario, improving the overall performances of the communication system. In this way, the antenna system is able to adapt their radiation characteristics to the new required operating requirements in a harsh EM environment. In particular, by applying the concept of beam-forming method, the radiation intensity of the antenna system can be focused in a desired direction, leading to eliminate undesired signals. This actually entails a higher S/N ratio at the receivers and saves the battery power at the transmitters. However, smart-adaptive antenna systems require a complex and complicated adaptive feed network and also a controlling system to weight each antenna element according to the desired beam-forming scenario [1, 2, 30]. Moreover, there is no any smartness in the antenna elements, limiting the overall performances of the communication system.

Alternatively, reconfigurable antennas have been extensively exploited to mitigate detriments of the conventional antennas as well as demerits of the smart or adaptive antenna systems [4]. By applying reconfiguration mechanism in a single antenna element, different tasks can be handled by only one antenna in a communication system, leading to reduce the antenna complexity, cost, and improve the overall system performances. Moreover, introducing some smartness in the antenna elements of adaptive phased-array can significantly increase the versatility of the smart antenna array.

Therefore, this chapter aims to address the reconfiguration concept and its feasible methods. In addition, the typical reconfiguration mechanisms used in some agile antennas are also introduced and compared together in terms of different technical standpoints. Finally, a few reconfigurable structures in antenna and microwave applications are briefly introduced to demonstrate their myriad applications.

2.2 Reconfigurable antennas

The term of reconfigurable antenna is referred to any radiation structure in which either one or some of its fundamental operating characteristics are controlled by means of electrical or mechanical approaches. Indeed, the key principle in designing these antennas are based on the theory of conventional antennas, and by tailoring the radiator structure, controlling the current distribution, or changing the electrical parameters of the antenna, their desired radiation characteristics are tuned.

Reconfigurable antennas are able to independently alter their operating frequency, bandwidth, polarization, and radiation-pattern to accommodate changing operating requirements. For instance, the ability to tune the frequency could be utilized to change the operating band, filter out the interfering signals, or tune the antenna to account for the new environments [31]. On the other hand, the polarization of the antenna can be reconfigured to separate or distinguish desired signals and hence forming a space filter for the unwanted signals [32-34]. In addition, radiation-pattern reconfiguration can also be used as a space filtering or effectively send the signals to a desired direction [35, 36]. This increases the sensitivity of the receiver or the maximum transmitting range of the system.

Changing more than one property of the antenna at the same time is another feature that is highly demanded in the modern communication systems [4, 30, 37]. However, the reconfiguration on one property, for instance frequency, has direct consequence on the radiation-pattern. Likewise, reconfiguration that results in radiation-pattern will also alter the frequency response of antennas. This linkage is one of the largest challenges faced by reconfigurable antenna developers who would usually prefer the characteristics to be separable. This research topic is called “compound reconfigurable antennas” which can

also be classified as multi-functional antennas. Although, some structures have been proposed to implement compound antennas, individually controlling each property without affecting the others is a holy grail. In the following sub-sections, three fundamental reconfigurable properties of antennas are described in more details.

2. 2. 1 Frequency reconfiguration

In the modern communication systems, different operating bands are required to perform the relevant tasks. Therefore, in except of using one antenna for each task, a dynamic frequency antenna can be applied to carry out all functions. This also reduces the system cost and may increase its overall performances. A reconfigurable frequency antenna is the only candidate that can be used to meet the system requirements. In these antennas, since the antenna size relative to the wavelength is kept constant, almost the same characteristics are obtained by changing the frequency.

The frequency reconfiguration can be performed continuously or by means of switch. Both methods are based on a unique key principle— that is changing the effective electrical length of the radiator or, on the other hands, the effective current distribution on the radiator. By using continuous variation, the frequency of the antenna can be reconfigured smoothly over a specific bandwidth; while, for discontinuous cases, reconfiguration is realized by switching between different bands. The main difference between these two methods is the means that are used to change the effective electrical length or current distribution of the antenna. Electrical or mechanical switch including optical switches, PIN-Diodes, FETs, and radio-frequency micro-machined (RF-MEMS) switches are some kind of methods classified as discontinuous frequency reconfigurable approaches. Mechanically changing the antenna structure and material properties are other approaches, which can continuously change the frequency of the antenna. However, each method has its own advantages and drawbacks that according to their potentials for the desired application are chosen.

2. 2. 2 Polarization reconfiguration

Polarization reconfiguration potentially is able to introduce immunity to the interfering signals in the unpredictable environments as well as creating an additional degree of freedom to enhance link quality by means of antenna diversity. Basically, the direction of the current distribution on the antenna dictates the polarization of the radiated electric fields in the far zone regions. Therefore, the polarization reconfiguration is realized by managing the direction of the current distribution usually by changing the antenna structure, material properties, and/or feed configuration. However, it is important to

maintain an efficient polarization reconfiguration while keeping the desired radiation-pattern and matching. This is because by changing the polarization, other antenna radiation characteristics may significantly change. This is the main consideration point in designing this type of reconfiguration property. Although, the key principle of polarization diversity is similar to the one of frequency diversity, the available reported research shows that the switching methods are the most popular approach for polarization reconfigurations.

2. 2. 3 Radiation-pattern-gain reconfiguration

Radiation-pattern/gain reconfiguration is another interesting topic in the reconfigurable antennas, which is usually used as space filtering for increasing the link quality by effectively focusing the radiated signals to the desired direction. This can be achieved even by changing the amplitude and phase of the electric or magnetic currents on the structure. However, because of changing in the current distribution, it is expected to have some variation in the frequency response of the antenna as well. This is the main technical point that should be considered in the design process to minimize the effect of pattern/gain reconfiguration on the frequency response and hence matching bandwidth.

Depending on the antenna structure, frequency of operation, and fabrication technology, different types of tunable approaches have been proposed for pattern/gain reconfiguration. For instance, structural changing by means of electrical or mechanical actuators is one of approaches in changing the radiation-pattern shape. As an electrical method, MEMS switches have been applied into the antenna structure to change the current distribution and therefore its radiation-pattern [38, 39]. Similar to the frequency reconfiguration, controlling material properties is another method that has been suggested to manage the radiation-pattern. However, applying this method, especially using ferromagnetic materials, introduces the main constraints of losses, higher cross polarization, being bulk and needing a particular biasing structure [40-42]. Using parasitic elements around the primary antenna is another approach, which has been proposed to change the direction of the radiation-pattern. This method possesses attractive qualities, including isolation from the driven element, potentially wide frequency bandwidth, and a range of available topologies and functionalities [43, 44]. In one other approach, the pattern reconfiguration can be achieved by an array of tunable elements in which phase of each element can be adjusted to focus the radiated energy in a particular direction [45]. As it can be deduced, in all radiation-pattern reconfiguration mechanism, by tailoring the antenna structure to different shapes or by changing the electrical parameters of the antenna structural embodiment, the radiation-pattern is reconfigured. In the next sub-section, some of the commonly used reconfiguration mechanisms have been described.

2.3 Reconfiguration methods

The study on the reconfiguration properties shows that the reconfiguration mechanisms are usually achieved by means of mechanical or electrical approaches [4]. In the mechanical method, the structure of the radiator is moved by electromechanical actuators in order to reshape the antenna structure. Piezo-electric actuators or micro-machined plastic deformation are some kinds of recently proposed methods to reconfigure the frequency and radiation-pattern. This method delivers a wide range of frequency of operation limited by the practical constraints and it can continuously sweep the desired property through a bandwidth or switch between different regimes. In addition, it provides low loss, linear behavior at high frequencies, which are remarkable merits to alleviate the inter-modulation (IMD) harmonic problem. However, needing to a specific complex actuation system and being low speed are the main drawbacks of this approach.

On the other hand, in the electrical methods there is no any movement in the configuration and the changes in the overall shape is electronically achieved. Indeed, this is realized by connecting/disconnecting different parts of the structure, changing the elements of the equivalent electrical circuit model of the antenna via variable capacitors or by changing the material properties. Optical switches, high frequency PIN-Diodes, FETs, and radio frequency micro-mechanical switches (MEMS) are some kinds of commonly used means applied to connect or disconnect different parts of the antenna. These components are applicable to reconfigure frequency, polarization, or radiation-pattern. Inter-modulation (IMD) harmonic level, losses, and speed are the main important issues for these approaches, which determine the component type for the desired operating requirements. Among these drawbacks, the undesired natural parasitic elements introduced by component packaging and soldering, for instance in PIN-Diodes and FETs, are the main reasons in limiting their applications. This leads to increase the elements nonlinearity and hence increase the IMD problem. MEMS technology is the potential approach to get rid of the losses and parasitic elements by packing the reconfiguration mechanism and antenna structure during the fabrication process. However, this method is not practical for all applications and is not extensively available in the market.

Alternatively, variable capacitors are other components that are usually used to continuously reconfigure the frequency response of the antenna over a specific bandwidth. This can be realized by chip variable capacitors integrated into the structure. These capacitors are usually based on the semiconductor or MEM technologies. However, because of packaging parasitic elements and losses, the application of these components is limited, especially for the components based on the semiconductor technologies.

Tab. 2-1 Comparison of different reconfigurable approaches.

	Technology	Tuning range	Power consumption	Bias	Speed	IMD
Semi-conductors	Schottky (GaAs)	High	<1 mW	<5 V	<1 ns	Poor
	HBV(GaAs)		<1 mW	<20 V	<5 ns	Poor
	Abrupt p-n junction (Si)		<5 mW	<30 V	<10 ns	Poor
	PIN-Diode		<0.1 mW	<10 V	<1 μ s	Poor
Magnetic	YIG (Variable permeability ferromagnetic resonance)	-	High	Current (Coil)	<5 ms	-
	Remnant magnetization	-	Low	Current (Coil)	<5 ms	-
	Magneto-static (spin) wave	-	Low	-	<5 ms	-
Ferroelectric	Thin film	Moderate to high	Negligible	<30 V	<1 ns	Low
	Thick film	Moderate to high	Negligible	<1000 V	<10 ns	Low
	Bulk	Moderate to high	Negligible	<15 KV	<1 μ s	Low
Liquid crystal	Cavity/Bulk	Moderate	Negligible	<40 V	<10 ms	-
Optical	Photoconductivity	-	<10 mW	Current (LD, LED)	10 fs-10 ms	-
Mechanical	MEM Varactor	Low	Negligible	<50 V	>10 μ s	Excellent
	Piezo-transducer	High	Negligible	>100 V	>100 μ s	Good

Changing the material properties is another interesting method, which mainly is applied to reconfigure the radiation-pattern and frequency response [46-48]. Liquid crystals (LC), ferroelectric and ferromagnetic materials are some kind of these materials, which have been utilized as means of reconfiguration. In these methods, by applying a DC voltage or magnetic field, the electrical properties of the dielectrics are changed, leading to alter the EM response of the structure. Ferromagnetic materials and LCs are bulkier than ferroelectric materials and they create more losses than ferroelectrics. Moreover, creating higher cross polarization level in ferromagnetic is other reason to not widely apply these materials directly as radiators in the antenna applications.

In summary, the above mentioned reconfiguration approaches have been compared in different technical standpoints in Tab. 2-1. Based on the data listed in this table, it can be conclude that implementing the reconfiguration structure by means of MEM technology proposes better performances in terms of loss, speed, power consumption, and more important IMD level. It can be observed form this table that ferroelectric materials may ranks as the second approaches to implement a high speed, low loss reconfigurable structure with low IMD level. However, the practical limitations, operating frequencies,

and technology constraints restrict the designer to choose a specific reconfiguration mechanism for the desired applications.

2.4 Reconfigurable antennas and their practical issues

The technical advantages offered by tunable/reconfigurable antennas have introduced them as potential candidates for multi-function or smart communication systems. Therefore, they have found a myriad of applications in different areas including satellite communications, base stations, wireless sensors, and medical areas. Moreover, by growing different technologies to develop agile materials, for instance, high frequency semi-conductor switches and capacitors, micro electromechanical systems (MEMS) [49], ferroelectric materials [40, 41], liquid crystals [50], and most recently plasma materials [51], they are getting more interest for the future modern communication systems.

However, there are still some practical issues that may limit or pose some constraint on the applications of these antennas. In many cases, the selected antenna topology and intended applications restrict the choice of reconfiguration mechanism and some trade-offs need to be considered. Those trade-offs may include, reconfiguration speed, power consumption, actuation requirements (voltage or current), fabrication complexity, durability, device lifetime, complexity of control and bias networks, weight, size, cost, dynamic range, sensitivity, and, of course, overall performance of antenna system.

Once the reconfiguration mechanism is selected, the integration of reconfiguration mechanism inside the radiator element is one of the most challenging issues in developing reconfigurable antennas. Indeed, the required controlling network for the selected relevant reconfiguration mechanism must be comprehensively considered in the design process. For instance, if RF-MEMS or PIN-diode switches are selected as reconfiguration method, the required biasing network and also any non-ideal effect must be included in the design. Moreover, sometimes by reconfiguring one characteristic, the antenna matching is deviated. This demands a matching circuit that is required to be integrated into the antenna structure.

The above mentioned difficulties are usually faced in the design steps. Reviewing reported research reveals that reconfigurable antennas have been under development in the past a few decades; however, not all of them put in to the operation in the today systems. Indeed, there are some other technical points that need to be considered for the future design to effectively take advantages of them in the practice.

The first issue is the benefits and costs of the reconfigurable antenna in the system point of views. Although, there are a handful of reported quantitative studies in which the system-level performance of these antennas has been considered [4], still more work

needs to be performed on the linkage between system-level and hardware so that, eventually, a particular reconfigurable antenna with clear features can address known limitations or predicted operating scenarios. Moreover, to fully take advantages of multi-functionality feature and select the best antenna configuration, collaborative efforts are demanded between the designers in the hardware and software levels.

In terms of the cost and complexity, sometimes introducing the reconfiguration into the system significantly increases the complexity and cost of the system. This is because some more controlling units which are required to collect and process the received data, and then select the new system requirements according to the new operating scenario. Therefore, budgetary constraints may simply preclude inclusion of a reconfigurable antenna in a system. To make reconfigurable antennas more affordable in the future systems, some advances can be introduced in the fabrication and system implementation. For instance, directly integrating the switch elements and associated control lines during the design and implementation process would result in more economical configuration. In summary, still more work both in hardware and software is demanded to effectively bring these antennas in the current practical smart systems.

2.5 Conclusion

The research survey on the topic of reconfigurable antenna demonstrates that still this topic is in the developing period and more multi-disciplinary research considering both hardware and software level of the antenna system is demanded. Integrating reconfiguration mechanism into the antenna structure is one of the challenging topics in this area to alleviate or eliminate the undesired effect of the applied reconfiguration mechanism. Serving new technologies to propose more versatile reconfigurable structures is another attractive research area in this topic. Furthermore, introducing a smart element as components of an adaptive array antenna can also be an ultimate challenging configuration for the future modern smart communication systems.

Chapter 3

Periodic structures and their applications in antennas and microwave

3.1 Introduction

In the past two decades, an interesting area, broadly named as Meta-materials, has increasingly attracted researcher attention to develop and improve performance of electrical components in RF, microwave, and high frequency bands [5]. Depending on the way that they treat with the incident electromagnetic waves, these materials can be realized as Double Negative (DNG) materials, Electromagnetic Bandgap structures (EBG) or Photonic Bandgap materials (PBG), and Frequency Selective Surfaces (FSS). They are constructed of an array of periodic elements arranged in one, two or three dimensional pattern. Each element of these arrays can be metallic, dielectric or a composite material of metal and dielectric. The element shape, array texture, electrical parameters of material, and the distance between elements in the array dictate their electromagnetic properties. All these materials might treat in distinct ways to the waves with different incident angles or polarizations. Therefore, their performances for vertical and horizontal polarization at various incident angles are the subject of investigation depending on the desired application.

For instance, DNG materials in response to the incident electromagnetic waves provide negative dielectric constant and dielectric permeability. The periodicity of the array elements in these types of periodic structures (PS) is much smaller than the operating wavelength. DNG materials have received considerable attention in developing scanning

beam antennas, lens antennas, and microwave filters. A broad range of DNG applications have been addressed in [52] that the readers are referred. Alternatively, PBG or EBG materials are another type of meta-materials that prohibit the propagation of incident waves across a range of frequency band. The periodicity of the array in these materials is in the range of a half wavelength. They have found intense applications in antennas to enhance the gain or suppress the surface waves as high impedance ground surface (HIS) or artificial magnetic conductors (AMC) [5, 6], in microwave filters to create band stop responses [53, 54], and in electromagnetic shielding applications [55]. Recent contributions on the application of these materials in antennas and microwave have been described in [56].

Finally, the subject of interest in this thesis, i. e. FSS surfaces, is a kind of planar periodic arrays of metallic patches or perforated conductors with a particular pattern. Depending on their impact on either one or both of amplitude and phase of the incident waves, they have found considerable applications in antennas, filters, polarizers, radomes, and electromagnetic shielding [17-19]. Moreover, by cascading some layers of these surfaces, FSS-based EBG configurations have also been developed for antenna applications [57]. In this perspective, comprehensive research studies have been carried out during past a few decades to theoretically and experimentally investigate the performances of these surfaces in one or cascaded multi-layer configurations. The element types, lattice geometry selection, supporting dielectrics' effect, incident angles and polarizations sensitivity, and reconfiguration feasibility have been individually examined to design robust FSS electromagnetic windows [17]. To perform these investigations, different theoretical approaches based on electromagnetic full wave solutions have been developed to calculate the FSS response. A comprehensive research survey on these methods has been summarized in [58].

On the other hand, as more easier method with less tedious computer calculations, an equivalent transmission line model is an alternative approach to predict the transmission/reflection performance of these surfaces [59, 60]. Although, this method has been developed for a certain regular element and lattice shapes for a limited range of incident angles, it easily provides the initial values of the FSS dimensions and describes the physical scattering mechanism of the surfaces.

Since the objectives of this thesis are proposing and developing a new class of sweeping-beam reconfigurable radiation-pattern antennas based on periodic structures (PS), the relevant reported contributions on this particular application are reviewed and discussed in this chapter. In this perspective, as a type of periodic structures, FSS screens are described and their electromagnetic characteristics are explained. Typical elements used in FSS textures are classified and the FSS design considerations are identified. Then, some of the most important applications of FSS surfaces are addressed. Finally, as basic principles used in this thesis to design a class of FSS-based reconfigurable

antennas, the fundamentals of capacitive and inductive FSS screens constructed by gridded array of strips are theoretically and analytically explored.

3.2 Frequency selective surfaces

Frequency selective surfaces (FSSs) are referred to a two-dimensional infinite array of metal patches or an array of aperture in a metal sheet [17]. Since FSS surfaces have originally been developed as spectral filters, sometimes those can be recognized as dichroic surfaces as well [19]. The first FSS prototype as a partially reflector surface has been reported in 1919 by Marconi and Franklin. However, because of the highly demanded interest in military, intense theoretical and experimental investigations have been embarked on this subject in the mid-1960s.

FSSs are fundamentally characterized by their responses to the incident electromagnetic (EM) waves. Indeed, these screens will transmit nearly all EM waves over a specific bandwidth while reflecting nearly all energy through another frequency bandwidth. A single layer FSS screen is generally constructing by aperture or patch elements. Free space standing aperture and patch elements provide a complementary response [17]. The electromagnetic fields are totally transmitted by a resonant aperture, while an FSS screen constructed by an array of resonant patches blocks the propagation of EM waves. The phase of transmitted or reflected waves can also be altered by the screen. This helps to eliminate a specific electric field component of the EM waves passing though the screen or change the polarization of the reflected or transmitted waves. Depending on the system requirements of a design, the frequency response may be tailored to be narrow or wide, to have multiple pass or stop-bands, or to be polarization dependent. Elements spacing, element shape and dielectric parameters are the key factors, dictating the frequency response of the screen. FSS lattice can also be considered as a design parameters to attain particular performances, for instance, packing the elements to mitigate the incident angle dependency of the EM response of FSS screens and therefore alleviate the grating lobe responses. Consequently, this is the desired application and system requirements that dictate the FSS design parameters. The range of these applications extends across the electromagnetic spectrum, from the microwave to infrared where screens are fabricated with micromachining capabilities [61]. In the following sections, the design parameters of FSSs are identified and some of the basic applications of these antennas are introduced.

3. 2. 1 Design parameters for frequency selective surfaces

With a set of application requirements on the frequency selective surfaces, the screen parameters are designed to meet the required spectral response. Given the type of surface needed to fulfill the desired feature, the key parameters associated in the design procedure are element shape and lattice pattern [17, 19, 62, 63]. They essentially dictate the center frequency and bandwidth of transmission or reflection responses, the dependency of the polarization response, cross polarization level, and onset of grating lobes. Some other parameters, including supporting dielectrics, the number of required FSS layers, and the spacing between these sheets can also be used to tailor the response of the screen for the intended application [64-67]. For instance, supporting dielectrics used for mechanical reason on one or both sides of the FSS screen significantly change its response, and they can be used to improve the stability of the center frequency and bandwidth of the sheet with incident angles. This section will focus on identifying some of these design parameters and explore the effect of each one in the spectral response of the FSS sheets.

3. 2. 1. 1 Element types

The element used in the infinite periodic array is a primary determinant of the resonant frequency, bandwidth, polarization response, and angular coverage of an FSS. Although, there are endless configurations of reference element that might be considered for FSS applications, this is the intended application that dictates the element type. In general, aperture type elements are used to realize transmission band response, while stop-band performance can be obtained by applying resonant patch elements in the FSS. When designing either a band-pass or a band-stop FSS, although the grid lattice strongly influences the sheet response, the element must primarily be chosen to meet the desired bandwidth and cross polarization. Some elements offer low cross polarization, broad bandwidth with less sensitivity to the polarization states, while others inherently are narrow band with a high cross polarization level. Therefore, a careful selection of element in an appropriate lattice texture is required to completely fulfill the application request [17, 19, 61].

Fig. 3-1 demonstrates some of reported elements used for different applications. These elements may be broadly classified into four categories— those are center-connected or N-pole elements, loop elements, solid interior elements and combination elements [17]. The first two groups, depending on the desired performances, are the most commonly used elements in designing FSSs. Some typical elements of the center connected group are straight element, three-legged element, anchor element, the Jerusalem cross, and spiral element. The length of these elements at the first dominant resonance is about a

half-wavelength. Because of the element shapes, they can be packed together to create super dense screens with a broad band response [17]. This also pushes the grating responses to higher frequencies and also enhances the screen bandwidth. Among the above mentioned elements of the first group, spiral is the only element that can interestingly provide both stop- and pass-band responses [17]. Moreover, it provides a broadband response approaching to the hexagon element of the second group. Since spirals are locked into each other, the onset frequency of trapped grating lobe shifts to higher frequencies.

Since in FSS designing, small elements with a stable resonant frequency in response to different angles of incident are utmost of interest, the second group, i. e. loop types are the only candidates fulfilling this feature. The loop types such as the three- and four-legged loaded elements, the circular loops, and the square and hexagonal loops are the most recommended elements for both band-stop and band-pass applications. By shaping elements of this group, a broad range of narrow to broad band responses can be realized. In this category, the hexagon element provides the broadest bandwidth with almost stable response with angel of incident and polarizations. Four- or three-legged loaded elements offer the minimum bandwidth. The size of these elements is about 0.3λ , which this leads to a compacted element design. This gives the designer enough space to choose an appropriate lattice pattern for the intended application. The length of loop elements is about a wavelength at the dominant resonant frequency.

The third group is usually used for a certain purpose applications. In this category, the element dimension is close to half a wavelength. This impose inter element spacing of larger than $\lambda/2$, leading to an FSS with high sensitivity to the incident angle and also early onset of grating lobes. Moreover, the center frequency and bandwidth change in opposite sense for parallel and vertical polarizations as a function of incident angles. This limits the application of third group. Therefore, these elements are solely used alone in FSS screens. They are usually applied in conjunction with a complementary FSS in close vicinity of them. Finally, the fourth group, i. e. hybrid elements are constructed by combination of the other three group members and an endless number of elements can be designed. It means that for the desired application, by tailoring or combining other elements, different types of transmission/reflection responses can be achieved to meet the demanded features.

In conclusion, for designing an FSS, although the lattice pattern is an important factor in determining the overall response, the element shape is the first concerning parameter to meet the intended application requirements. In this perspective, having an element with minimum size and stable response to the different incident angles is the most criteria in element selection. This is the element shape that sometimes dictates a certain lattice configuration to fulfill the expected performances.

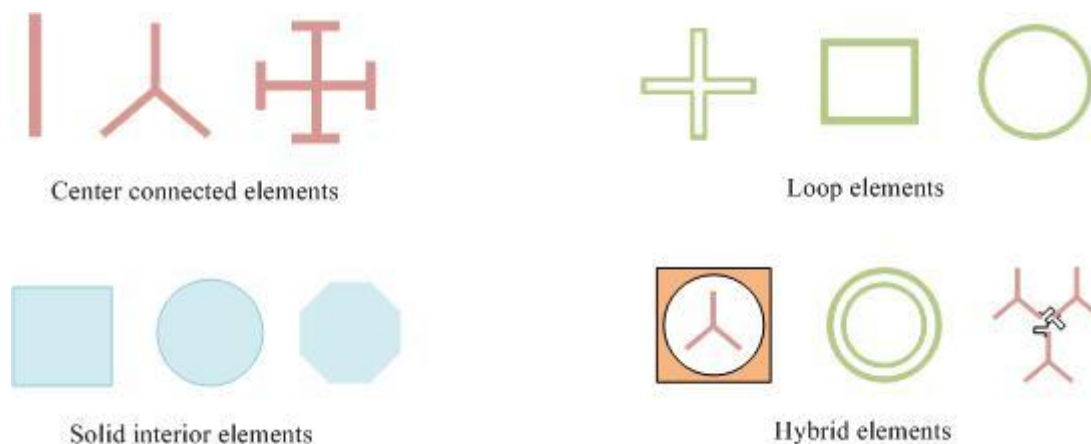


Fig. 3-1 The most typical elements used in FSSs [17].

3. 2. 1. 2 Dielectric loading

In practice, the FSS screen must be supported by dielectrics not only for mechanical reasons, but also to control the roll-off rate, flatness of the bandwidth, and controlling the drift of resonant frequency with incident angle variations [17, 62, 67-69]. Bonding the FSS in one side to dielectric or embedding it with dielectric on both sides significantly changes its transmission/reflection responses. The results show that by embedding the FSS in a dielectric, its resonant frequency decreases with $1/\sqrt{\epsilon_r}$ ratio. This holds even for a dielectric with a thickness of 0.05λ . When an FSS is bonded on one side by a dielectric, the frequency decreases with a ratio of $1/\sqrt{\epsilon_e}$, where $\epsilon_e = \frac{1+\epsilon_r}{2}$. However, for the slot types, it exhibits an oscillatory behavior around a response proportional to decreasing rate, i. e. $1/\sqrt{\epsilon_e}$ [67].

The dielectric thickness also has a considerable effect on the FSS response by changing the incident angles and polarizations. To achieve an angular stable resonant slot, the thickness of dielectrics on both sides of the FSS must be a multiple of a quarter wavelengths. When the FSS is bonded in one side by dielectric, its thickness has to be a multiple of a half-wavelength to eliminate the mismatch loss. For the resonant patch array, no matter what is the thickness, having dielectric on both sides of the FSS, the reflection at the two air/dielectric interfaces are tuned out [19].

In some applications, a broad band flat top with rapid roll-off response is required, which are stable with polarization and angle of incident. Therefore, multiple layers of FSSs are used in conjunction with supporting dielectric to achieve the desired response. The thickness of dielectric layer in the middle needs to be chosen appropriately to obtain

a flat top response, while the outer dielectrics are selected about a quarter-wavelength to reduce the transmission loss and also enhance the angular stability [64-67, 69].

3. 2. 1. 3 Periodic array lattice and grating lobe responses

As it was described earlier, the lattice pattern is also an important parameter in affecting the final transmission/reflection response of the FSS. Therefore, depending on the application features, both elements and lattice geometry must be deliberately chosen to meet all demands. The distance of elements and also the geometrical position of adjacent elements significantly affect the center frequency, bandwidth, angular sensitivity, and also cross polarization level [17, 19, 63]. The symmetry property not only in element determines the cross polarization level, but also in the lattice selection must be considered to qualify the desired level. Although element geometry may possess any degree of rotational symmetry, the grid cannot. In general, there are four grid types commonly used in planar FSS— as shown in Fig. 3-2, those are: rectangular, regular skewed, square, and equilaterally triangular.

From this figure, one can observe that rectangular and skewed grids have two-fold rotational symmetry, the square has four-fold rotational symmetry, and equilateral triangular has six-fold rotational symmetry. The transmission/reflection responses of FSS configurations with more than two-fold rotational symmetry are independent of polarization at normal angle of incident. Furthermore, there is no cross polarization in the plane of symmetry for any angle of incidence. Therefore, the overall degree of symmetry that the designed FSS will possess depends on the combination of element and grid geometry. It means that the choice of grid lattice for a given application substantially depends on the used reference element.

Grating or Bragg lobes are undesired secondary main responses in the transmission/reflection coefficients that need to be considered in FSS design. Since the periodic array elements in FSS behave similarly to an infinite conventional array, the largest lattice size to prevent grating lobe responses should obey the same rule that is achieved by a traditional array antenna theory [61]. In general, for normal angle of incident, the spacing must be kept below one-half of wavelength. Tab. 3-1 summarizes grating lobe criteria for two lattice geometries of square and triangular.

By following the criteria, the onset of grating lobe is delayed to higher frequencies. As it can be noticed from Tab. 3-1, the square type offers the most closely packed elements, while triangular shape has the largest spacing. Approximately, two-third or less of that given in this table is practically recommended to select as initial lattice size in the FSS designing process. This avoids wasting energy by not even letting shoulder regions of grating lobes to enter in the real space. In addition of delaying grating lobes, as a bonus, the operational bandwidth of FSS can also be increased by reducing the grid spacing [19].

This is because by decreasing the element distance, the real part of array self-impedance is increased, while its imaginary part remains almost the same. According to the equivalent transmission line theory of one-pole filters, the transmission coefficient is close to unity over a larger frequency band [17].

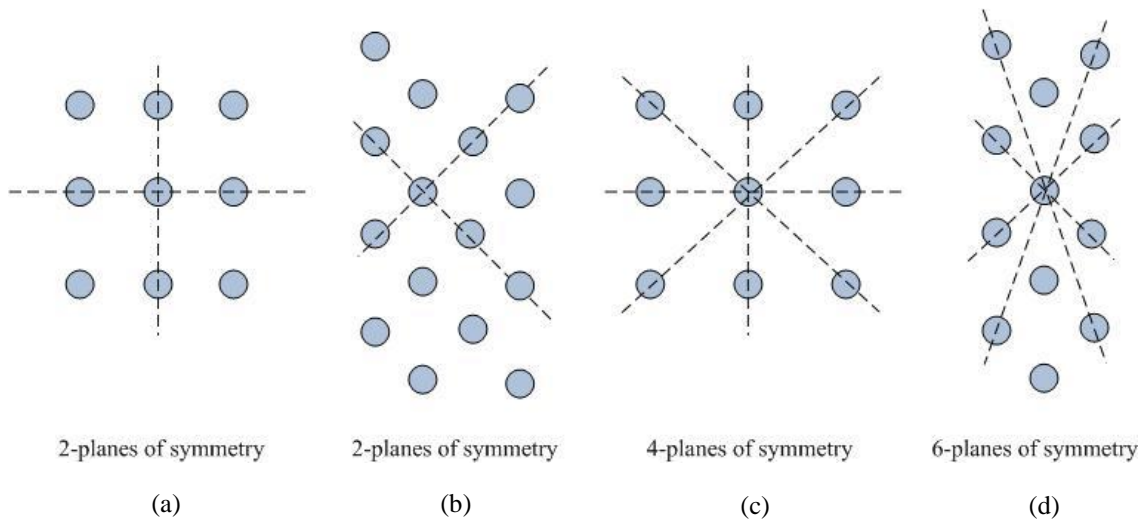
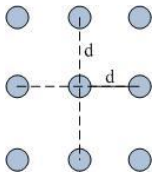
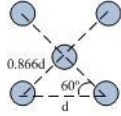


Fig. 3-2 Four types of grids used in FSSs, possessing various degrees of symmetry. (a) Rectangular. (b) Skewed. (c) Square. (d) Equilateral triangular [61].

Tab. 3-1 FSS lattice type and grating-lobe criteria [61].

Lattice type	Max. spacing	$\theta=0^\circ$	$\theta=45^\circ$
Square spacing 	$\frac{d}{\lambda_0} < \frac{1}{1 + \sin\theta}$	$\frac{d}{\lambda_0} < 1$	$\frac{d}{\lambda_0} < 0.59$
Equilateral-triangular spacing 	$\frac{d}{\lambda_0} < \frac{1.15}{1 + \sin\theta}$	$\frac{d}{\lambda_0} < 1.15$	$\frac{d}{\lambda_0} < 0.67$

3. 2. 2 Applications of frequency selective surfaces

Periodic structures, in particular frequency selective surfaces have a myriad of applications over a vast range of the electromagnetic spectrum, from below UHF to far infrared regions. Traditional applications of frequency selective surfaces have been well classified in [17], those are hybrid radomes, band-stop filters, dichroic reflectors, absorbers, and polarizers. Radomes are usually used to protect the antenna against the severe weather conditions. However, to reduce the antenna radar cross-section (RCS), frequency selective surfaces are used in the radome structure. Moreover, to electromagnetically protect the antenna by filtering out the undesired signals in some applications, the antennas are covered by band-stop filters. FSSs have also been designed as sub and main reflectors in quasi-optical antenna systems to create multi-frequency operation. For instance in [70], an FSS sub-reflector has been used in a high-gain reflector-antenna system to diplex two different frequency bands. In the first operating band, the sub-reflector is transparent for the feed horn located in its prime focus of the Cassegrain, while it operates as sub-reflector in the second higher frequency band for the other feed horn placed in the focal point of the main reflector. Therefore, by using only one main reflector at two different operating frequencies, tremendous reduction in mass, volume, and cost are achieved. Fig. 3-3 demonstrates this quasi-optical dichroic reflector antenna system.

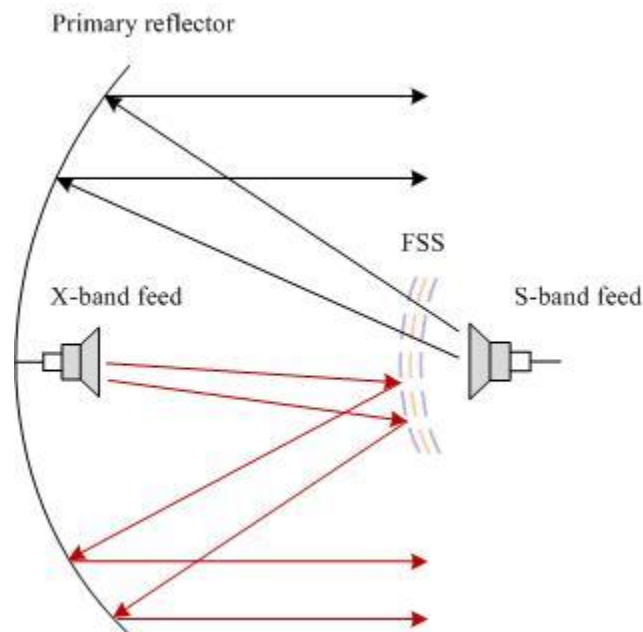


Fig. 3-3 Dual frequency reflector antenna with an FSS sub-reflector [67].

By applying one or a few layers of FSS in front of a perfect electric surface, either narrow or broad band absorbing materials will be realized. These types of sheets have found considerable interest in stealth or electromagnetic shielding applications [71-75]. Changing the polarization of the electromagnetic waves or filtering the undesired polarization are another applications of FSS [76]. Indeed, by cascading a few capacitive and inductive FSS screen, the electric field components of the incident electromagnetic waves are deliberately controlled to realize the required fundamental electric field characteristics.

Integrating FSS with active components has also introduced more attractive applications in recent decades [77]. Designing phased array antennas, transmit array antennas, and reflect array antennas are some typical reported passive/active FSS configurations that have offered more functionality into the antenna systems. Undoubtedly, as time proceeds, more and more advanced applications of frequency selective surfaces are appeared by applying different technologies. In recent years, a new emerging antenna technology so called “reconfigurable antennas” has been introduced which dynamically increases the functionalities of the antenna compared to the traditional configurations [4]. In this perspective, reconfiguration mechanism has successfully introduced in periodic structures to design different versatile antennas. In [37, 38], by deliberately biasing the incorporated high frequency switches inside an antenna aperture constructed of an array of periodic elements, the radiation parameters of the aperture antenna can be controlled. Moreover, active frequency selective surfaces have also been used as superstrates or active ground plane to control the direction of the antenna radiation-pattern beam [14, 23]. In conclusion, by growing the communication tasks in modern communication systems and also emerging new technologies, periodic structures are one of the most foreseen versatile tools in creating smart/tunable structures.

3.3 Planar grid array of parallel strips

Arrays of parallel metallic wires or strips have been used as partial reflectors in antennas since long time ago [17, 19, 78]. Therefore, their scattering properties have been the subject of theoretical and experimental assessment often time by time, discussing their surface impedance characteristics and incident angle sensitivities. The transmission or reflection coefficient response of these surfaces can be accurately evaluated by complex full wave numerical methods [58]. The angle of incident effect for both vertical and horizontal polarizations and the cross polarization scattering responses of the surface with complex pattern for a single or multiple layers can be examined using the full wave method at the computational time expense.

Equivalent transmission line model is an alternative easier solution, eliminating the required tedious mathematical calculations. This model also offers a quick physical

explanation of scattered waves from the screen, and gives the designer direct guidelines to calculate the initial dimension values for more complex designs. Marcuvitz has presented the basic equations of simple equivalent impedance model for an inductive grid illuminated by TE or TM electromagnetic waves [79]. However, this model is limited to the normal incident and cannot predict the impedance surface for some polarization states. A more generalized model has been proposed in [59], tackling in some sort the limitations of the Marcuvitz model. The achieved results show an accuracy of 2% for normal incident in this model. Oblique incident angle effects of up to 45° can be examined by this model with an acceptable result. In the following section, the design relations of planar and capacitive screens are described and some typical modeled geometries are presented.

3.3.1 Scattering mechanism of a planar parallel array strips

A planar grid composed of parallel thin metallic strips, as shown in Fig. 3-4, is imposed by TE-incident waves, where the electric field is polarized along the strips. The grid re-radiates the electric fields in a certain directions [80]. These scattered waves are classified into three direct, side, and evanescent waves. The first two types, i. e. direct and side waves, are the only ones that are re-radiated by the grid as simple plane waves. However, because of the periodic nature of the structure, an infinite number of evanescent waves are potentially excited. The nature of these waves can be changed into the side waves, for instance by incident angle variations, and hence contributing in undesired re-radiation. This can be easily shown, for the case of $1 < \lambda/d < 2$ by calculating the phase relation between the adjacent parallel strips $Kd \sin \theta$, where $K = 2\pi/\lambda$.

Consequently, for oblique incident angle of θ , the induced currents on adjacent strips are equal in magnitude, but differing in phase by

$$Kd \sin \theta \quad (3-1)$$

The waves re-radiated by the strips, therefore, arrive in the same phase in any plane whose normal makes an angle ψ_n with the normal to the grid, where

$$\psi_n = \sin \theta \pm n\lambda/d \quad n = 0,1,2,\dots \quad (3-2)$$

Equation (3-2) clearly define the angle of scatter when

$$|\sin \theta \pm n\lambda/d| < 1 \quad (3-3)$$

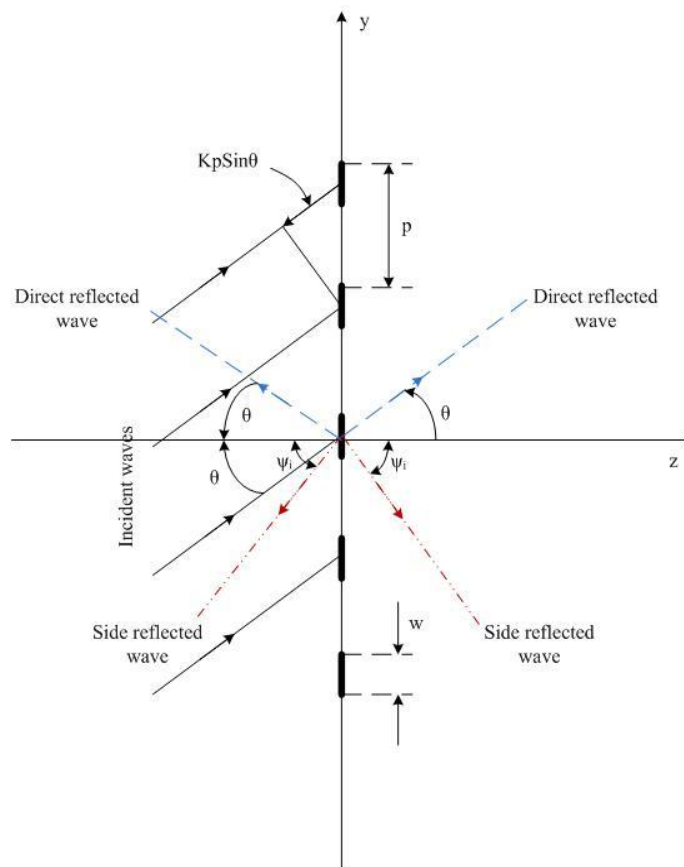


Fig. 3-4 Grating geometry of infinite parallel strips [80].

Therefore, equation (3-3) shows that depending on the angle of incident and the strips spacing, the grid re-radiates the incident waves in certain discrete directions. In this equation, the re-radiated direct waves at angles θ and $\pi - \theta$ are achieved for $n=0$, while the side waves are obtained for $n=1$, which are reflected in $\psi_1 = \arcsin(\sin \theta - \lambda/d)$ and $\pi - \psi_1$. The side waves always appear in pairs of symmetrical about the plane of the grid. These two categories are the only waves re-radiated as simple plane waves. Other waves, however, are produced as evanescent modes, which are contained in equation (3-3). They are defined by the complex values of ψ_n , which satisfy equation (3-3) and there is an infinite number of them. The complex scattering angle can be found from

$$\psi_n = \pi/2 \pm j \operatorname{arc} \cosh(n\lambda/d + \sin \theta) \quad (3-4)$$

$$\psi'_n = 3\pi/2 \pm j \operatorname{arc} \cosh(n\lambda/d - \sin \theta) \quad (3-5)$$

These expressions show that the evanescent waves are appeared in a pair travelling along the grid normal to the strips with amplitude falling off exponentially with distance

from the plane of the grid. Furthermore, for these waves, surfaces of constant phases are normal to the grid and parallel to the strips, and constant amplitude planes are parallel to the plane of the grid. These waves are, therefore, confined to immediate vicinity of the grid, and they constitute a storage field vibrating 90° out of phase with the incident fields. In [80], it has been demonstrated that for the case of $1 < \lambda/d < 2$, by increasing the angle of incident some sort of evanescent waves can be easily changed into the side waves, and therefore re-radiated as simple plane waves. The first pair of evanescent waves has become a symmetrical pair of side waves at the critical angle

$$\theta_1 = \arcsin(\lambda/d - 1) \quad (3-6)$$

Expression (3-6) shows that for a periodic array of elements with periodicity of d , a certain number of evanescent waves can be transformed into side waves by changing the incident angle. In this particular considered lattice pattern, by further increasing the incident angle, the critical values will not transform any other evanescent waves into side waves [80]. This equation also demonstrates that by increasing the grid periodicity of d , the evanescent waves tend to appear as side waves for small values of θ .

The earlier described scattering mechanism reveals that when a planar grid is used as a reflector, loss of power in side waves must be avoided, and the incident wave is only reflected at $\pi - \theta$ for all angle of incident provided $2d < \lambda$. For angles of incident in the range $0 < \theta < \arcsin(\lambda/d - 1)$, this property holds true when $\lambda < 2d < 2\lambda$. Therefore, in the design process, the grid dimensions should be designed such that the onset of grating response (side waves) is prevented at the desired operating region. In the next section, more detail about the required criteria is presented to calculate the grid dimensions with a compromise between grid distance and the incident angle.

3.3.2 Inductive and capacitive grids

A free space standing infinite parallel thin, continuous, perfectly conducting strips are considered in Fig. 3-5. The interaction of incident electromagnetic waves with this screen is represented as a wave travelling down a transmission line, with a shunt lumped circuit impedances modeling the periodic array. The shunt impedance is either inductive or capacitive depending on the polarization state of incident waves with respect to the orientation of strips. Referring to this figure, for an inductive grating, TE- polarization occurs when the incident waves are perpendicular to the plane of incident, i. e. $\varphi=0^\circ$; while the TM-polarization is defined for the incident wave parallel to the incidence plane, i. e. $\theta=0^\circ$. The incident plane is defined by the propagation vector and the vector normal to the infinite array screen.

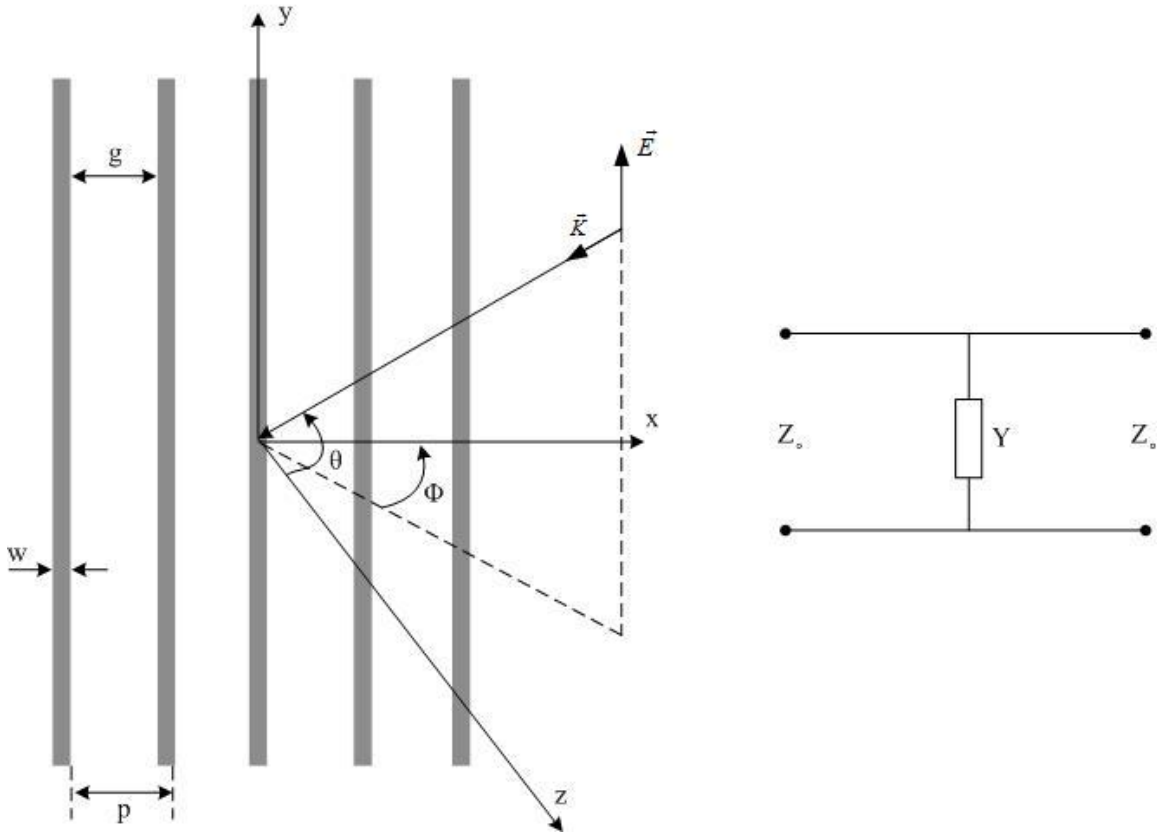


Fig. 3-5 Inductive grid geometry and its equivalent transmission line model.

When the incident wave is polarized parallel to the long strips, the grating gives rise to a storage inductive field in the immediate vicinity of the array. This can be modeled as a reactance in its equivalent transmission line model. On the other hand, for the incident waves polarized perpendicular to the strips, this can be represented by a capacitive susceptance. The related equations of the corresponding equivalent normalized admittance for different incident polarizations in two principal planes are summarized here [59]:

TE-polarized wave incident in xz - plane ($\varphi=0^\circ$):

$$X_{TE} = F(p, w, \lambda) = \frac{p \cos \theta}{\lambda} \left[\text{In cosec} \left(\frac{\pi w}{2p} \right) + G(p, w, \lambda, \theta) \right] \quad (3-7)$$

where λ is the wavelength, and the correction term G is derived as followed. The susceptance expression for TM-incidence can be extracted using Babinet's duality conditions as is given by (3-8) for y - z incidence plane

$$B_{TM} = 4F(p, g, \lambda) = \frac{4p \cos \phi}{\lambda} \left[\text{Incossec} \left(\frac{\pi g}{2p} \right) + G(p, g, \lambda, \phi) \right] \quad (3-8)$$

Equations (3-7) and (3-8) are valid for $w \ll p$, $g \ll p$ and $p \ll \lambda$. The immittance expressions for the two other cases take the following form [59].

The inductance for TM-polarized wave incident in y-z planes is:

$$X_{TM} = F(p, w, \lambda) = \frac{p \sec \phi}{\lambda} \left[\text{Incossec} \left(\frac{\pi w}{2p} \right) + G(p, w, \lambda, \phi) \right] \quad (3-9)$$

The inductance for TM-polarized wave incident in x-z planes is:

$$B_{TE} = 4F(p, g, \lambda) = \frac{4p \sec \theta}{\lambda} \left[\text{Incossec} \left(\frac{\pi g}{2p} \right) + G(p, g, \lambda, \theta) \right] \quad (3-10)$$

In expressions (3-7) and (3-11), the calculated immittances are normalized to Z_0 , representing the characteristic impedance of the medium surrounding the planar grid, that is free space for the current case. The first order correction terms for both TE- and TM-wave incidences is given by

$$G \left(p, w, \lambda, \theta, \phi \right) = \frac{0.5(1-\beta^2)^2 \left[\left(1-\beta^2/4\right)(C_{1+} + C_{1-}) + 4\beta^2 C_{1+} C_{1-} \right]}{\left(1-\beta^2/4\right) + \beta^2 \left(1+\beta^2/2 - \beta^4/8\right)(C_{1+} + C_{1-}) + 2\beta^6 C_{1+} C_{1-}} \quad (3-11)$$

where $\beta = \sin(\pi w / 2p)$. In (3-11), the first order coefficients $C_{1\pm}$ are calculated from

$$C_n = \frac{1}{t S_n} - \frac{1}{|n|}, n = \pm 1, \pm 2, \dots \quad (3-12)$$

For TE-incidence

$$t = j \frac{p \cos \theta}{\lambda} \quad (3-13)$$

$$S_n = \frac{\gamma_n}{\gamma_0} \quad (3-14)$$

where the propagation constant γ_n is given by

$$\gamma_n = -j \sqrt{\left(\sin \theta + \frac{n\lambda}{p}\right)^2 - 1} \quad (3-15)$$

and therefore $\gamma_0 = \cos \theta$.

From equations (3-12) and (3-15)

$$C_{n\pm}^{TE} = \frac{1}{\sqrt{\left(\frac{p \sin \theta}{\lambda} \pm n\right)^2 - \frac{p^2}{\lambda^2}}} - \frac{1}{|n|} \quad (3-16)$$

Therefore,

$$C_{1\pm}^{TE} = \frac{1}{\sqrt{\left(\frac{p \sin \theta}{\lambda} \pm 1\right)^2 - \frac{p^2}{\lambda^2}}} - 1 \quad (3-17)$$

Similarly, for TM-incidence

$$t = j \frac{p \sec \phi}{\lambda} \quad (3-18)$$

$$S_n = \gamma_n \gamma_0 \quad (3-19)$$

and

$$\gamma_n = -j \sqrt{\sin^2 \phi + \frac{n^2 \lambda^2}{p^2} - 1} \quad (3-20)$$

and therefore $\gamma_0 = \cos \phi$.

From equations (3-18) and (3-19)

$$S_n t = \sqrt{\left(\frac{p \sin \phi}{\lambda}\right)^2 + n^2 - \frac{p^2}{\lambda^2}} \quad (3-21)$$

and again substituting into equation (6) gives

$$C_{n\pm}^{TM} = \frac{1}{\sqrt{\left(\frac{p \sin \phi}{\lambda}\right)^2 + n - \frac{p^2}{\lambda^2}}} - \frac{1}{|n|} \quad (3-22)$$

and for the first order coefficient

$$C_{1\pm}^{TM} = \frac{1}{\sqrt{1 - \left(\frac{p \cos \phi}{\lambda}\right)^2}} - 1 \quad (3-23)$$

Using equations (3-7~11), inductive and capacitive components of FSS array elements are calculated in all plane of incidence. θ and ϕ must be interchanged in equations (3-17) and (3-23) for the capacitive cases.

Using the approximate values of immittances describing the stored magnetic and electric energy of the grid, the transmission line model of the grid can now be easily characterized. The equivalent circuit model is represented in Fig. 3-5, in which the admittance Y is normalized to the impedance (Y_0) of free space, and the admittance seen by a plane wave incident normally on the grid is Y_i . The grid transmission coefficient is now expressible in terms of the grid admittance Y [81]. The input admittance, Y_i , is

$$Y_i = 1 + Y \quad (3-24)$$

The corresponding voltage reflection, R , is

$$R = (1 - Y_i) / (1 + Y_i) \quad (3-25)$$

and the grid power transmission, $|\tau|^2$, is

$$|\tau|^2 = 1 - |R|^2 \quad (3-26)$$

Therefore, the grid transmission response is calculated in terms of its dimensions. In the next section, the transmission and reflection properties of an inductive grid for TE-incident are evaluated based on the equivalent transmission line model described in Fig. 3-5.

3.3.3 Characterization of an inductive planar periodic array of strips

It is supposed that a free standing parallel array of strips, as shown in Fig. 3-5, is illuminated by TE-incident waves, in which the electric field is polarized parallel to the strips and the incident angle (θ) varies in xz-plane. For a grid pattern with dimensions $w \ll p$ and $p \ll \lambda$, the transmission power pattern is similar to a single pole inductive high pass filter before onset of grating responses [59, 78, 81, 82]. Fig. 3-6 shows its equivalent circuit model and also the related power transmission curve. As it can be observed, the undesired null around frequency f_{GL} limits the higher edge of the high pass filter bandwidth. This null is related to the grating lobe response created by the periodic nature of the array strips and it strongly depends on the angle of the incident and grid pattern dimensions. Therefore, the equivalent transmission response is essentially valid for the frequencies before onset of gratings and cannot predict the grating responses.

The transmission power curve characteristics can now be calculated using the circuit model represented in Fig. 3-6. In this model, the normalized equivalent impedance for TE-incident is found from expression (3-7). Considering the grid pattern dimensions, the inductive impedance is approximated using

$$X_{TE} = F(p, w, \lambda) \approx \frac{p \cos \theta}{\lambda} \left[\ln \left(\frac{2p}{\pi w} \right) + G(p, w, \lambda, \theta) \right] \quad \text{for } w \ll p \quad (3-27)$$

The small value of the correction term G can be neglected for the case where both $w \ll p$ and $p \ll \lambda$ are satisfied. The impedances in the model are normalized with respect to the impedance (Z_0) of free space, and the impedance seen by a plane wave incident normally to the surface is

$$Z_i = (jX) / (1 + jX) \quad (3-28)$$

Therefore, the corresponding voltage reflection and transmission coefficients, R and τ , are

$$R = (Z_i - 1) / (Z_i + 1) = -1 / (1 + j2X) \quad (3-29)$$

$$|\tau|^2 = (1 - |R|^2) = 4X^2 / (1 + 4X^2) \quad (3-30)$$

The transmission coefficient can be expressed in the complex form [81]:

$$\tau = j2X / (1 + j2X) \quad (3-31)$$

For the transmission line model shown in Fig. 3-6, the pass-band of power transmission extends from f_l to f_{GL} and the reflection bandwidth from very low frequency to f_{rl} . From equations (3-27) and (3-31) the reflection frequency of the lower stop-band λ_{rl} and the lower edge of pass-band region λ_l are calculated using

$$\lambda_l = 0.7p \cos\theta \ln(2p/\pi w) \quad (3-32)$$

$$\lambda_{rl} = 6p \cos\theta \ln(2p/\pi w) \quad (3-33)$$

From equations (3-32) and (3-33), the typical ratio of $\lambda_l/\lambda_{rl} = 9$ is achieved for a single layer inductive planar strips, representing a slow transition from the lower stop-band to the inductive pass band region [65].

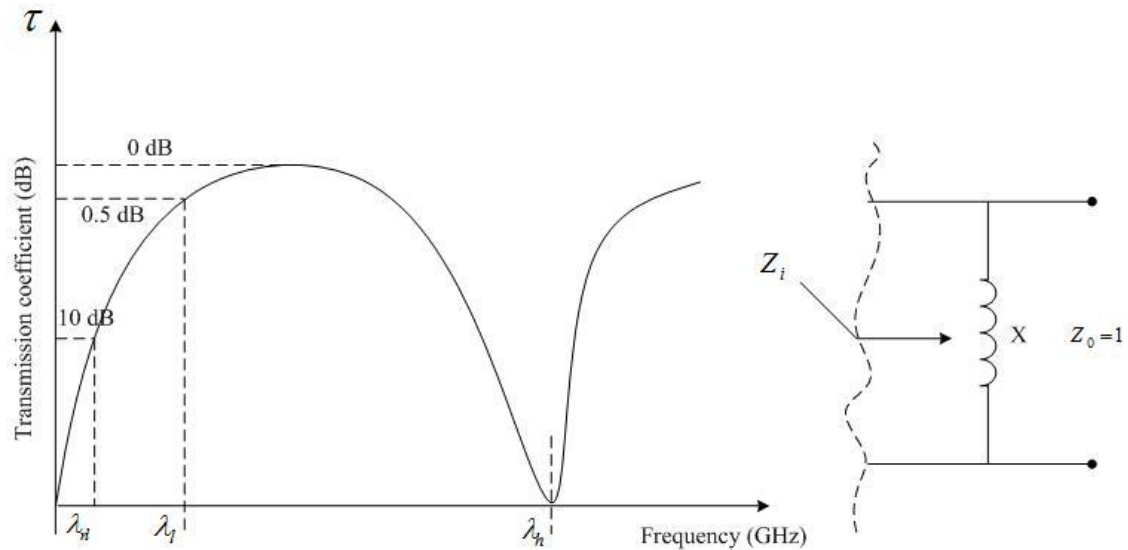


Fig. 3-6 Transmission power response of an inductive planar grid and its transmission line model.

Alternatively, the higher edge of the transmission region is limited by onset of first grating response at wavelength λ_h . The first grating lobe emerges at wavelength:

$$\lambda_h = \lambda_{GL} = \begin{cases} p(1 + \sin\theta) & \text{for } TE \\ p \cos\theta & \text{for } TM \end{cases} \quad (3-34)$$

where θ is the angle of incident wave. This equation predicts a narrower transmission bandwidth for the TE- than TM- incident waves. In addition, as it can be described by (3-34), the lower edge of transmission region λ_l depends on the angle of incidence, lattice periodicity, and the width of strips. To achieve larger pass-band, this frequency must be reduced by increasing the inductance in the equivalent circuit model. This can be realized using narrower strips or longer periodicity. However, width of strips is restricted by practical constraints, and increasing the periodicity reduces the onset of the first grating frequency as it can be predicted from equation (3-34). Convoluted technique is one approach to enhance the bandwidth of the inductive periodic array by increasing the effective inductance of the screen [59, 78, 81, 82]. The anomalous resonances created by the geometrical asymmetry in the convoluted technique, nonetheless, must be considered in the design process. This may pose some problems for wideband FSS designs using cascading inductive and capacitive grids [65].

3.3.4 Applications of inductive and capacitive periodic strips for band stop filters

Passive frequency filters have found intensive applications in the quasi-optical duplexers for reflector antennas and reflect array structures [77, 78, 81]. They are usually constructed of single or cascaded layers of capacitive or inductive resonant metallic periodic elements. Depending on the requested performances, the pattern of a unit cell in the periodic array can be a resonant short dipole strip, square-loop, double-square, gridded-square, or any other hybrid resonant element. Equivalent transmission line models have been proposed for some of these patterns in which the unit cell is described based on the simple inductive and capacitive impedance models presented in section (3.3.2). To completely describe the model, some of the values in the transmission line model are empirically extracted by fitting the measurement results to the simulation ones [60, 83]. Here, two types of band-stop surfaces are introduced and their equivalent transmission line model are presented and described.

Fig. 3-7 shows the square-loop and gridded square-loop screens with their equivalent circuit impedances [60, 84]. The capacitances and inductances in their transmission line models represent the effect of stored electric and magnetic fields in the close neighborhood of the strips parallel or perpendicular to the incident electric field, respectively. Fig. 3-6a shows a single LC circuit shunted across a transmission line of impedance Z_0 , where Z_0 is the characteristic impedance of free space. The values of inductance and capacitance are determined based on the TE-incident expressions represented in equations (3-7) and (3-8). However, the discontinuity effect g must be

compensated in these equations by a factor of d/p . Therefore, the inductance and susceptance are calculated by

$$X_L(w) = \frac{d}{p} F(p, 2w, \lambda) \quad (3-35)$$

$$B_c(g) = 4 \frac{d}{p} F(p, g, \lambda) \quad (3-36)$$

where, $X_L(w)$ and $B_c(g)$ are normalized to Z_0 . In (3-35), a conductor width of $2w$ is necessary to fit the experimental results with the equivalent circuit model [60, 84]. The measurement results in [60, 84] shows an accuracy of 2% in predicting resonant frequency at normal incident. However, the performance at normal incident is a reasonable estimation to the experimental behavior at oblique incident angles of up to 50° . The results show that the typical transmission/reflection band ratio is larger than 2.5:1 for square-loop screen.

To improve the transmission/reflection band, gridded square-loop screen has also been investigated, and a transmission line model has been proposed as shown in Fig. 4b. This grid proposes a transmission response with transmission/reflection band ratio in the range of 1.3 to 2:1, which is less than square-loop screen [59]. In the proposed model, the inner loop is represented by a series inductance and capacitance, while the inductive grid is modeled by a parallel inductance. The discontinuity effect has been taken into account by $\frac{d}{p}$ factor, and the coupling effect of side parts of the loop parallel to the inductive grid are considered by two parallel inductors calculated in (3-37). The equivalent normalized (to free space characteristic impedance) inductance and capacitance for gridded-square loop screen are calculated by

$$X_{L1}(w) = 2(X_{L2} \parallel X_{L3}) \quad (3-37)$$

$$X_{L2}(w) = F(p, w_1, \lambda) \quad (3-38)$$

$$X_{L3}(w) = F(p, 2w_2, \lambda) \cdot \frac{d}{p} \quad (3-39)$$

$$B_{c1}(g) = 2\varepsilon_{eff} F(p, g, \lambda) \cdot \frac{d}{p} \quad (3-40)$$

where ε_{eff} is the effective dielectric constant of supporting dielectric material.

For this model, the accuracy of the predicted resonant frequency at normal incident angle is about 5%. A close agreement between modeled and measured resonant frequencies is also achieved for both TE- and TM-polarizations [59].

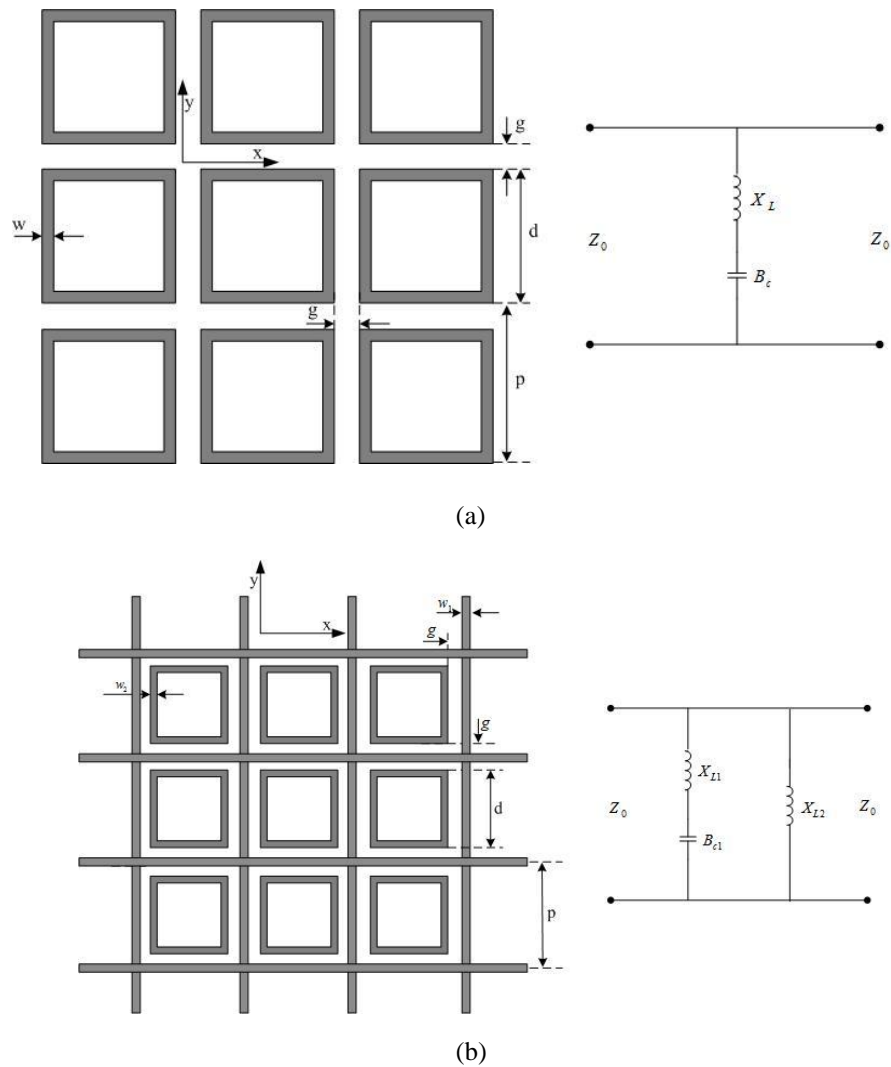


Fig. 3-7 Schematic representation of passive FSS filters. (a) Square-loop screen [60]. (b) Gridded square-loop screen [59].

3.4 Conclusion

The conducted research survey on the periodic structures reveals that periodic structures have attracted a lot of attention since long time back, and by growing the technology up, they are seeking new avenues in developing new materials and smart structures. To successfully design and implement these structures, original and comprehensive

theoretical and experimental investigations are required. In particular, by increasing demands on the agile/smart materials for multi-functional systems and also the synergy between these demands and the new technologies, more research in these areas are foreseen in the future from low frequency to infrared region of electromagnetic spectrum.

Chapter 4

Active planar grid of metal strips and its applications in reconfigurable antennas

4.1 Introduction

In Chapter-3, the basic principles of transmission line theory of inductive and capacitive grids were explored and described. These passive periodic arrays have been used to create tunable/reconfigurable planar or conformal surfaces, controlling the incident electromagnetic waves [85-87]. This is achieved by changing the equivalent impedance of the screen seen by the incident plane waves from an inductive state to a capacitive case. As summarized in Tab. 2-1, due to their availability in the markets, high frequency PIN-diode is one of typical means to control the states of the screen. Although, the parasitic elements of these components affect the desired transmission response of these surfaces and introduce some degree of nonlinearity in the scattered waves [88-91], they are still preferred compared to other methods because of the design and fabrication simplicity using these elements.

Fig. 4-1 demonstrates a typical reconfigurable grid constructed with array elements of short strip dipoles, incorporating active elements. In this screen, $w \ll p_x$, $p_x \ll \lambda$, and $g_0 \ll P_x$ are considered to extract the related transmission lines. Moreover, since the strips are very thin compared to the wavelength, the thickness effect is also neglected. When the diodes are activated, a high pass response is created for TE-incident waves (polarized parallel to the strips). On the other hand, a stop-band is achieved in the

transmission response by activating the diodes. Therefore, the transparency level of the screen can be controlled across a range of frequency bandwidth by changing the surface impedance. Based on this principle, reconfigurable EBG materials or partially reflector surfaces can be proposed for antenna applications [87, 88, 90-93].

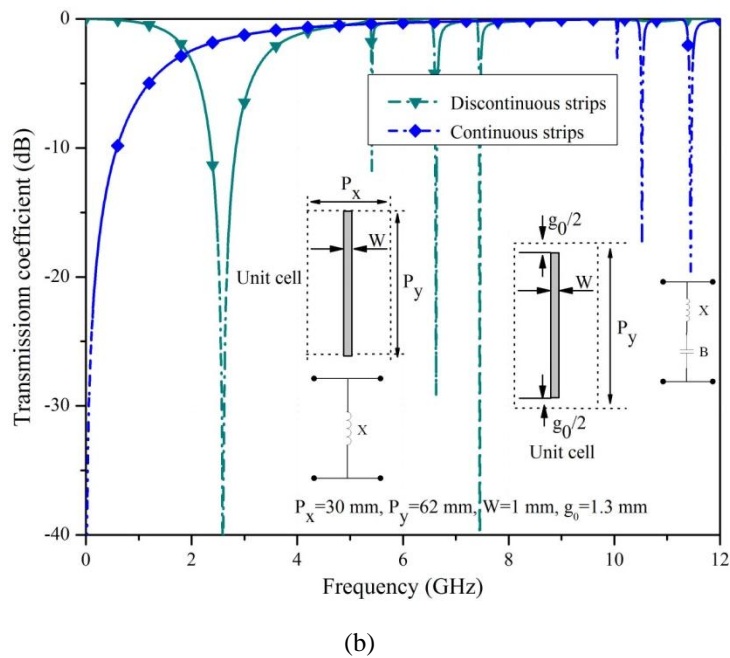
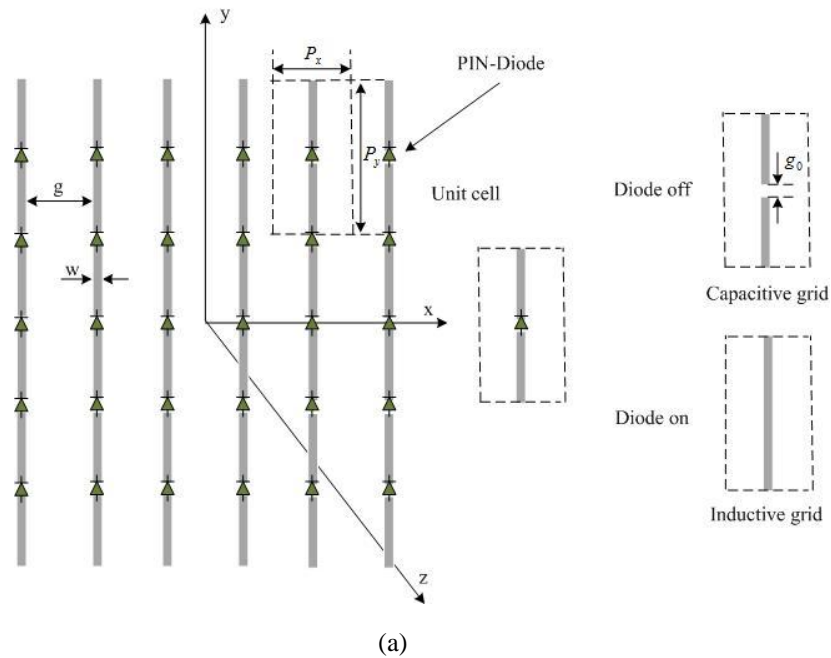


Fig. 4-1 Passive capacitive grid incorporated with ideal active elements. (a) Geometry of the grid. (b) Typical transmission response of the passive inductive and capacitive grid for normal incident.

The objectives of this thesis are based on applying this principle in frequency selective surfaces for reconfigurable radiation-pattern antennas. Therefore, our main goal is to achieve a reconfigurable transmission/reflection band(s) with a minimum insertion loss across the capacitive stop-band (opaque window) when the screen is turned to transparent state. The transparency can be either realized by a capacitive or inductive surface. This will be explained in the following sections.

In this chapter, to delineate the performance of the surface shown in Fig. 4-1, its transmission performances are analyzed using CST Microwave Studio for both inductive and capacitive states. The screen is characterized by calculating its transmission/reflection coefficient responses using Floquet analysis method. All dimensions of a unit cell of the grid are examined using a parametric study to determine design constraints of this surface in creating a reconfigurable transparent/opaque surface. In addition, the effects of integrating high frequency PIN-diodes into the screen and also the feeding network are carefully examined to achieve the desired electromagnetic performances. According to the characterization results, the key principle of this active inductive/capacitive grid is explored in detail to propose it as a tunable reflector for a class of reconfigurable radiation-pattern antennas. To physically and analytically describe the performance of the FSS screen, the equivalent transmission line models of the surface for two capacitive/inductive states are also proposed and their responses are compared to the achieved results by CST Microwave Studio.

4.2 Active planar metallic strips

4.2.1 Inductive grid characterization

Fig. 4-2 shows a typical free space standing inductive grid constructed using parallel array of strips with periodicity of P_x and width w . The screen is illuminated with a plane wave polarized parallel to the strips. The incident angle measured from the normal to the grid plane is considered as θ . According to the equivalent circuit modeling presented in section 3.2.2, the transmission response of this surface is similar to an inductive high pass filter, which its high frequency response is limited by onset of grating lobe. This can be clearly observed in the Fig. 4-3, the calculated transmission response by CST for normal incident, i. e. $\theta=0^\circ$. Grating lobe response tends to appear around 10GHz. On the other hand, the lower edge of pass-band frequency response is determined by the lattice periodicity, strip width and angle of incident. To delineate the performance of this inductive FSS screen, the equivalent surface impedance of the surface is calculated and then the results are analytically described by this model.

According to the equivalent reactance value of incident TE-waves to an inductive surface calculated by equation (3-7), this expression can be simplified for the normal incident to the following equation:

$$X_{TE} = F(p_x, w, \lambda) = \frac{p_x}{\lambda} \left[\text{Incosec} \left(\frac{\pi w}{2p_x} \right) + G(p_x, w, \lambda) \right], \quad w \ll p_x \quad (4-1)$$

when $p_x \ll \lambda$, the small correction term G can also be neglected and this equation can be rewritten as

$$X_{TE} = \frac{p_x}{\lambda} \ln \left(\frac{2p_x}{\pi w} \right), \quad w \ll p_x \ll \lambda \quad (4-2)$$

Using this expression, the transmission response performances of the inductive screen can be easily described in terms of grid lattice dimensions. This equation clearly shows that the total inductance of the grid is directly proportional to the periodicity in x-direction. In addition, by increasing the width of strips, the logarithmic term in this equation reduces, which leads to less inductance for a given set of periodicities. Therefore, to increase the total inductance of the screen, the periodicity of p_x needs to be increased and w must be decreased.

From equations (3-31) and (4-2), the related 0.5dB lower edge of pass band (λ_L) and -10dB point of the reflection band at low frequencies (λ_{RL}) are $f_L = 4.83\text{GHz}$ and $f_{RL} = 0.57\text{GHz}$, respectively. As it is expected, the ratio of transmission to reflection band edges is $f_L/f_{RL} = 8.6$. The obtained values for these points using CST simulator are very close to the ones calculated by the equivalent transmission line model— those are $f_L = 4.98\text{GHz}$ and $f_{RL} = 0.672\text{GHz}$, realizing a frequency ration of $f_L/f_{RL} = 7.4$. The calculated response for different values of grid periodicity P_x in Fig. 4-3 shows that to reduce the lower edge of transmission band f_L , the periodicity needs to be increased. Decreasing the strip width depicted in Fig. 4-4 is another method to reduce this frequency. Indeed, increasing the periodicity and decreasing the strip width both, as shown by expression (4-2), increase the equivalent inductance of the surface seen by the incident waves. However, there is a fabrication limitation for narrow strips; and the accommodation of PIN-diodes across the strips must be also considered. The upper edge of the transmission band according to the onset grating equation is determined to be around 10GHz. The simulation result predicts this frequency at $f_G = 10.51\text{GHz}$.

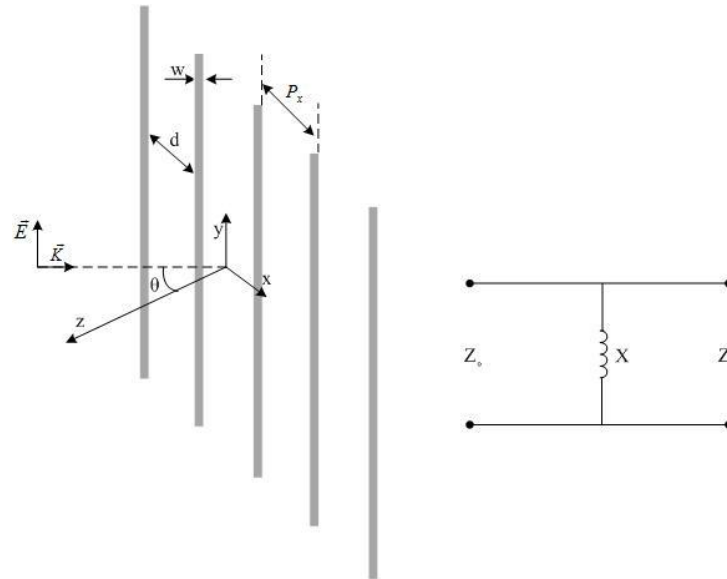


Fig. 4-2 Geometry of inductive FSS screen and its transmission line model.

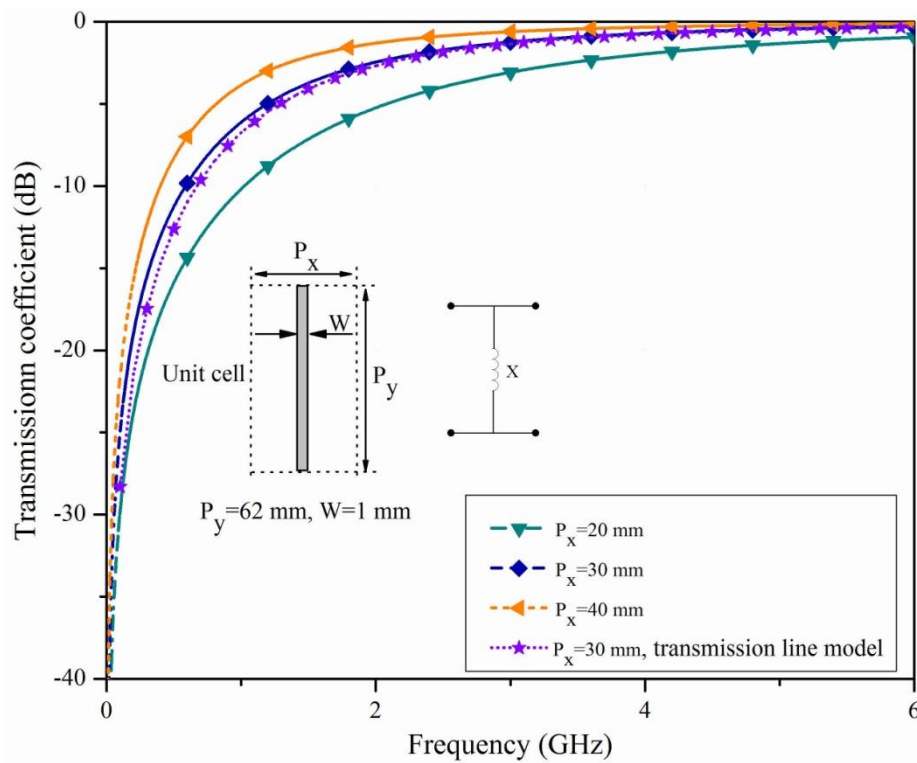


Fig. 4-3 Effect of inductive grid periodicity on transmission coefficient.

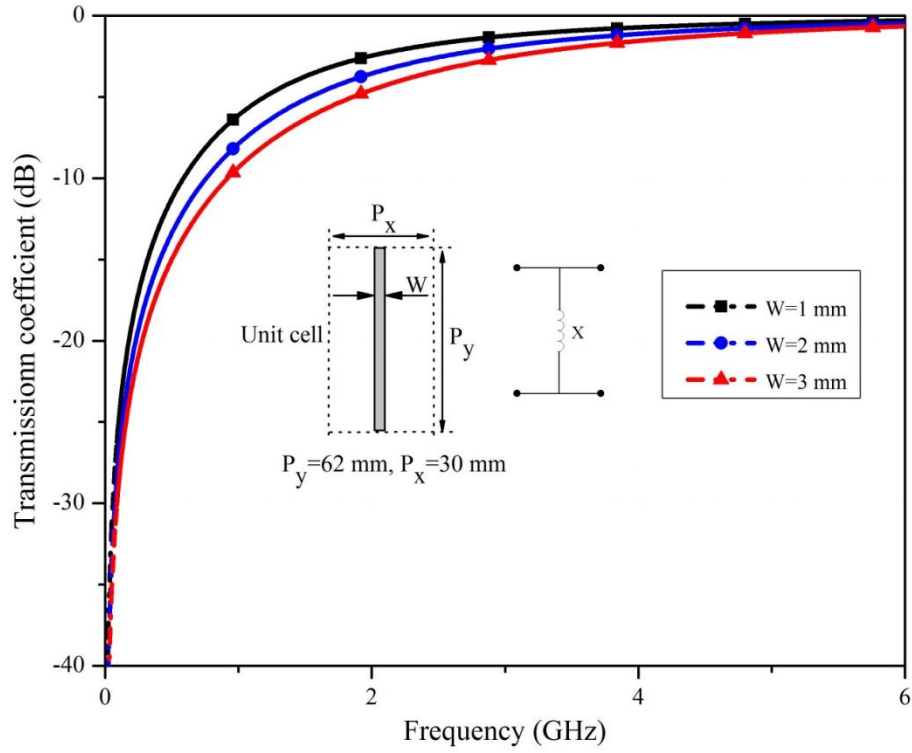


Fig. 4-4 Effect of strip width on transmission coefficient in an inductive FSS screen.

4. 2. 2 Capacitive grid characterization

Deactivating the PIN-diodes in Fig. 4-1 leads to a capacitive screen shown in Fig. 4-5. This resonant screen provides a band stop response where its frequency resonance is dictated by the resonant length of discontinuous strips included in one of its unit cell. The equivalent susceptance of the screen in this state is achieved from a serial LC circuit shunted across a transmission line with Z_0 characteristic impedance. The effective length of the resonant short strip dipole determines the inductance value, and the gap distance and P_y/P_x ratio are the main parameters affecting the capacitance of the circuit [82]. As far as the lattice dimensions fulfill $w \ll p_x$, $p_x \ll \lambda$, and $g_0 \ll P_x$, the magnetic field about the grid due to the current flowing along the strips is approximately the same as that about a corresponding uniform inductive grid expressed in (4-3).

$$X_{TE} = \frac{P_y - g_0}{P_y} \frac{P_x}{\lambda} \ln\left(\frac{2P_x}{\pi w}\right) \approx \frac{P_x}{\lambda} \ln\left(\frac{2P_x}{\pi w}\right), \quad w \ll p_x \ll \lambda \quad (4-3)$$

On the other hand, with regard to the distribution of electric field, it is noted from symmetry considerations that there is no component of electric field normal to strips in between each two gaps. In other words, in the quasi static case, for the current lattice dimension ($p_x \ll \lambda$ and $g_0 \ll P_x$), the electric flux about the grid elements is concentrated between the discontinuous gaps across the inductive strips. Therefore, the effective strip width is a crucial factor to reasonably predict resonant frequency. By incorporating the fringing field effect in the gap in the effective width of strips as $w_{eff} = Aw$, the related susceptance according to equation (3-8) is calculated by

$$B = 4F(p_y, g_0, \lambda) \frac{w_{eff}}{p_x} = \frac{4w_{eff} P_y}{p_x \lambda} \left[\text{Incos}ec \left(\frac{\pi g_0}{2p_y} \right) + G(p_y, g_0, \lambda) \right] \quad (4-4)$$

where, A is a correction factor incorporating the fringing field effect and is proportional to the periodicities ratio. With regard to the lattice dimensions of the grid, this relation can be simplified to

$$B = \frac{4w_{eff} P_y}{p_x \lambda} \ln \frac{2p_y}{\pi g_0} = 4 \left(a \frac{P_y}{P_x} \right) \left(\frac{w}{P_x} \right) \frac{p_y}{\lambda} \ln \frac{2p_y}{\pi g_0} \quad (4-5)$$

The ratio of P_y/P_x is a crucial parameter, affecting the capacitance value. Therefore, for a fixed gap distance and strip width, both the length of discontinuous strips (p_y) and periodicity along the x axis (p_x) dictate the related capacitance of the equivalent circuit model. Accordingly, the predicted wavelength for this LC circuit can be obtained by

$$\lambda_r \approx 2 \sqrt{p_y w_{eff} \ln \frac{2p_x}{\pi w} \ln \frac{2p_y}{\pi g_0}} = 2p_y \sqrt{\frac{aw}{p_x} \ln \frac{2p_x}{\pi w} \ln \frac{2p_y}{\pi g_0}} \quad (4-6)$$

This expression demonstrates that the grid periodicities in both directions strongly influence the center frequency of the stop-band. However, as it was expected [94], P_y and the effective area capturing the capacitive field across the gap discontinuities, i. e. w/p_x are the main parameters determining this resonant frequency for $P_y/P_x > 1$. The simulated transmission coefficient by CST Microwave Studio shows a stop-band centered around 2.6GHz for this grid dimensions. A correction factor of $a=2.5$ is, therefore, required to fit the calculated resonant frequency to the simulated one for the current lattice dimensions. Since for a capacitive screen constructed with short dipole strips, the resonant length of about $\lambda/2$ is expected [17], where λ is the wave length at the center frequency of the stop-band, the equivalent resonant length for the achieved stop-band is

$p_y = 58\text{mm}$. This value is close to the periodicity $p_y = 62\text{mm}$ of the screen shown in Fig. 4-5 with an accuracy of about 6%.

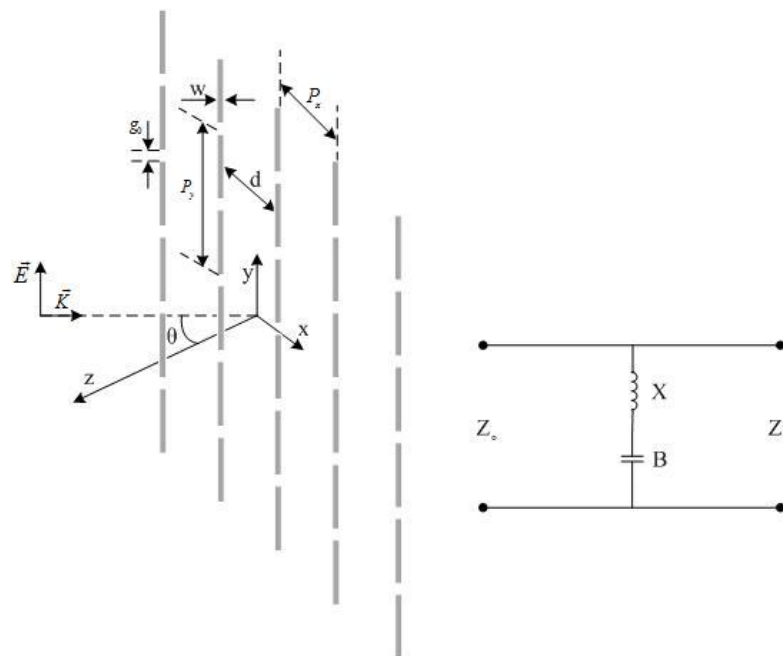


Fig. 4-5 Geometry of capacitive FSS screen and its transmission line model.

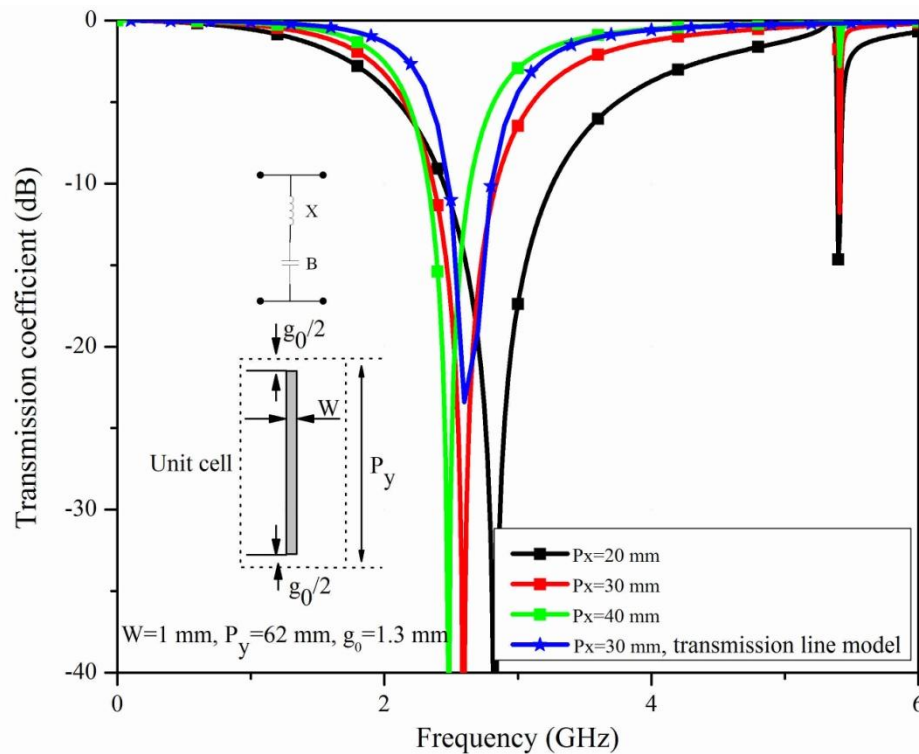


Fig. 4-6 Transmission coefficient response of the screen shown in Fig. 4-5 for various p_x .

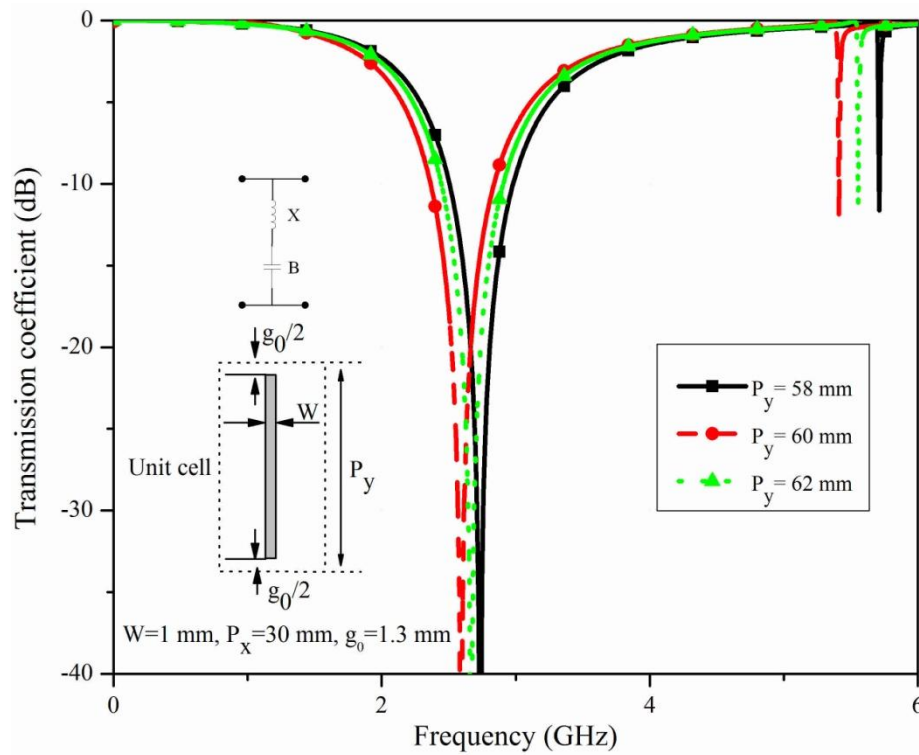


Fig. 4-7 Transmission coefficient response of the screen shown in Fig. 4-5 for various P_y .

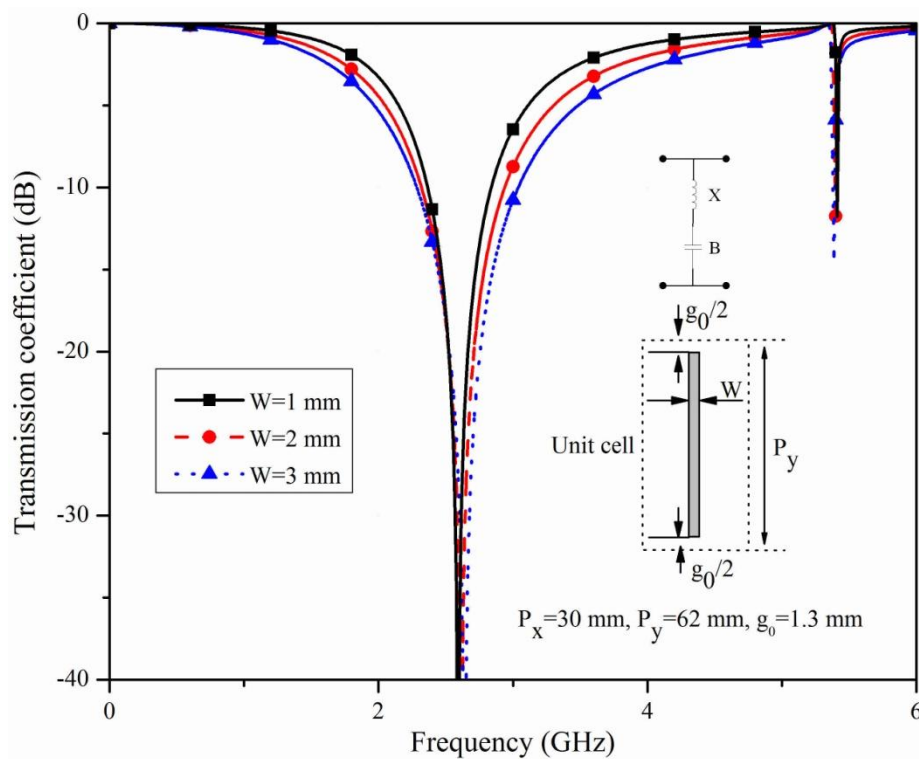


Fig. 4-8 Transmission coefficient response of the screen shown in Fig. 4-5 for various w .

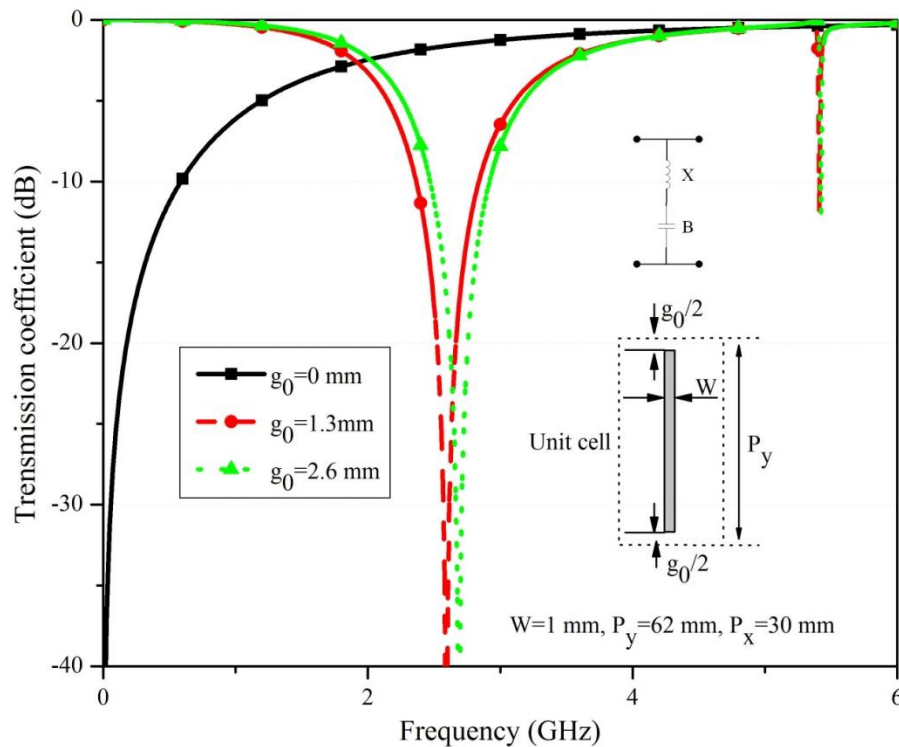


Fig. 4-9 Transmission coefficient response of the screen shown in Fig. 4-5 for various g_0 .

To investigate the effect of screen parameters, parametric studies carried out using the simulator have been demonstrated for all grid dimensions in Fig. 4-6 to Fig. 4-9. Increasing g_0 leads to decrease the capacitance value created by the electric field concentrated around the gap. Therefore, this reduces the resonant frequency of the unit cell. This can also be interpreted by the expression calculating the effective capacitance of the unit cell in (4-5). Increasing the lattice periodicities as expected from equation (4-3) results in more inductance value in the equivalent transmission line, and hence lower stop-band center frequency.

In other words, the periodicity ratio must be chosen deliberately according to the desired transmission coefficient response. Moreover, as it will be discussed, this ratio is also important in determining the onset of grating responses. In addition, as it is obvious from Fig. 4-6 and Fig. 4-8, the -10dB bandwidth of the stop frequency region is affected by the periodicity in x direction and also the width of the strips.

4. 2. 2. 1 Influence of lattice dimensions on the grid performance

The effect of lattice periodicity ratio on the transmission coefficient of the structure is examined in Fig. 4-10 for different values of P_y/P_x in larger scale. As it is obvious, by decreasing this value, the center frequency of the stop-band shifts toward higher frequencies and hence the bandwidth of stop-band is significantly increased. On the other hand, when this ratio is increased, the stop-band shifts down to the lower frequencies and the grating response start to appear. In this figure, the grating tends to appear around 4.5GHz for $P_y/P_x = 1.1$, which is in consistent with the predicted response by (4-6), i. e., $\lambda_{GL} = P_x$. The other two nulls, appeared around 5.4GHz, are related to the higher order modes created by modal interactions and the second harmonic of the fundamental mode [17]. Therefore, to suppress the undesired grating response and also higher order harmonics close to the desired operating band, the ratio of P_y/P_x should be chosen deliberately according to the given design requirement set of the required transmission coefficient performances. The most important issue that can be observed in these curves is the dependency of the stop-band center frequency to the length of the short strip dipoles. As it is clear, the center frequency of the stop-band is very close to the related equivalent resonant wavelength of the short strip dipoles, i. e., $\lambda_r \approx (P_y - g_0)/2$.

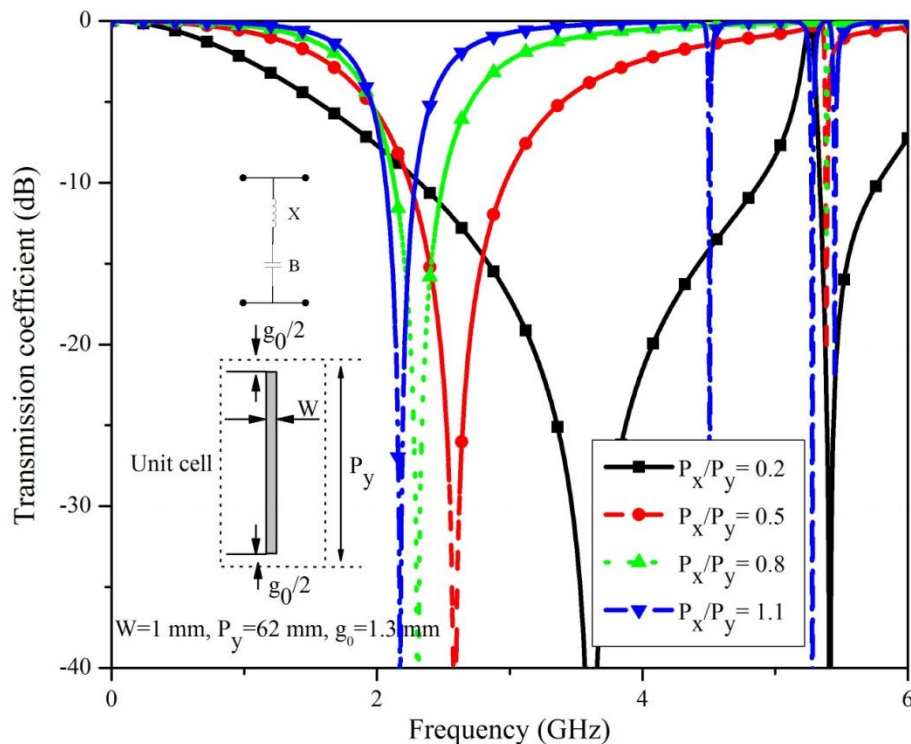


Fig. 4-10 Effect of P_y/P_x ratio on capacitive grid response.

4. 2. 2. 2 Influence of dielectric constant on the grid performance

In reality, a dielectric is usually used to support the free standing grid. This dielectric has a considerable effect on the transmission performance of the capacitive grid. This effect has been demonstrated in Fig. 4-11. As it is obvious from this figure, inserting a dielectric with $\epsilon_r = 3$ and thickness of 0.3mm, it shifts the center frequency of the stop-band down to 2.4GHz. However, the effect of this stand on the inductive grid is not significant across all depicted frequency range. On the other hand, inserting a dielectric next to the screen leads to more fringing electric-field concentration across the gaps. This increases the effective width of the capacitance created by the gaps, and therefore, larger susceptance is achieved. In this case, to fit the equivalent transmission line model to the achieved simulation results, the effect of dielectric should also be considered in determining the effective width of the capacitance. Therefore, the susceptance expression of (4-4) should be rewritten to the following equation to consider the effect of dielectric constant.

$$B = 4\epsilon_{\text{reff}} F(p_y, g_0, \lambda) \frac{w_{\text{eff}}}{p_x} = \frac{4\epsilon_{\text{reff}} w_{\text{eff}} p_y}{p_x \lambda} \left[\text{incosec} \left(\frac{\pi g_0}{2p_y} \right) + G(p_y, g_0, \lambda) \right] \quad (4-7)$$

Using this expression, in the current lattice configuration the effective dielectric constant is $\epsilon_{\text{eff}} = 1.2$ to fit the achieved simulation results with the calculated response by an equivalent transmission-line model. Considering this effective dielectric constant value, the length of short strip dipoles is related to the stop-band by $\lambda_r \approx (p_y - g_0) / 2\sqrt{\epsilon_{\text{eff}}}$. The calculated transmission coefficient using equivalent transmission-line model is compared with the one obtained by CST in Fig. 4-11.

From Fig. 4-12, it can also be deduced that by only increasing the width of the strips close to the gap discontinuity, the capacitance value of the equivalent susceptance of the grid surface impedance can be changed. Indeed, by increasing the effective surface of the capacitance created across the gaps, the center frequency of the stop-band can be considerably changed.

4. 2. 3 Active element integration

High frequency PIN-Diodes, in spite of their nonlinearity demerit [89], are one of the most commonly used active elements applied to reconfigure the EM response of an FSS texture. These elements are usually modeled by RLC components in their on and off states. In this thesis, the equivalent circuit model depicted in Fig. 4-13 is applied for the

GMP4201 PIN-diode in all the simulations [95]. In the forward biased case, the diode mainly represents a small resistance, which has a negligible effect on the desired response of the grid screen [96]. However, when the diode is deactivated, the LC parasitic elements substantially change the transmission response of the grid by shifting down the stop-band center frequency, as shown in Fig. 4-13, for different values of L_d and C_d . The simulation shows that the parasitic capacitance is more severe in reducing the stop-band position than the inductance. As a potential bonus in this part of examination, one can deduce an interesting point by applying this effect to change the center frequency of the band-stop. Indeed, by using variable capacitance, one can reconfigure the band-stop over a wide frequency range. This promises a more attractive application as a multi-functional antenna, which is able to reconfigure its operating frequency as well as its radiation-pattern.

In addition, the simulated transmission coefficient, shown in Fig. 4-13, has also been compared by the ones calculated using the equivalent transmission model in which the capacitive parasitic element is incorporated as an individual capacitance parallel with the discontinuity capacitance. The calculated stop-bands are in close agreement with the simulated ones. An interesting point is the effect of capacitance in suppressing the higher order harmonics. These results show that by increasing the capacitance, although the stop-band position shifts down, the grating responses and higher order modes move toward higher frequencies. However, the parasitic inductance causes to bring them to the lower frequency and hence making them closer to the desired stop-band region. Therefore, it can be concluded that to compensate the undesired effect of the parasitic elements, their values must be considered during the design process, which includes any active component.

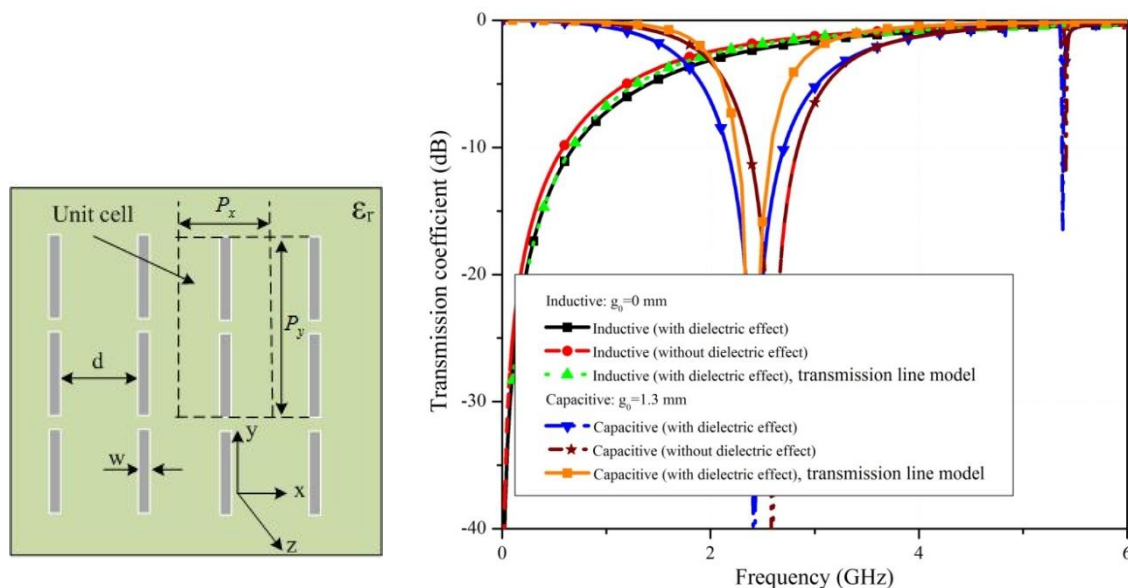


Fig. 4-11 Effect of supporting dielectric on the grid response.

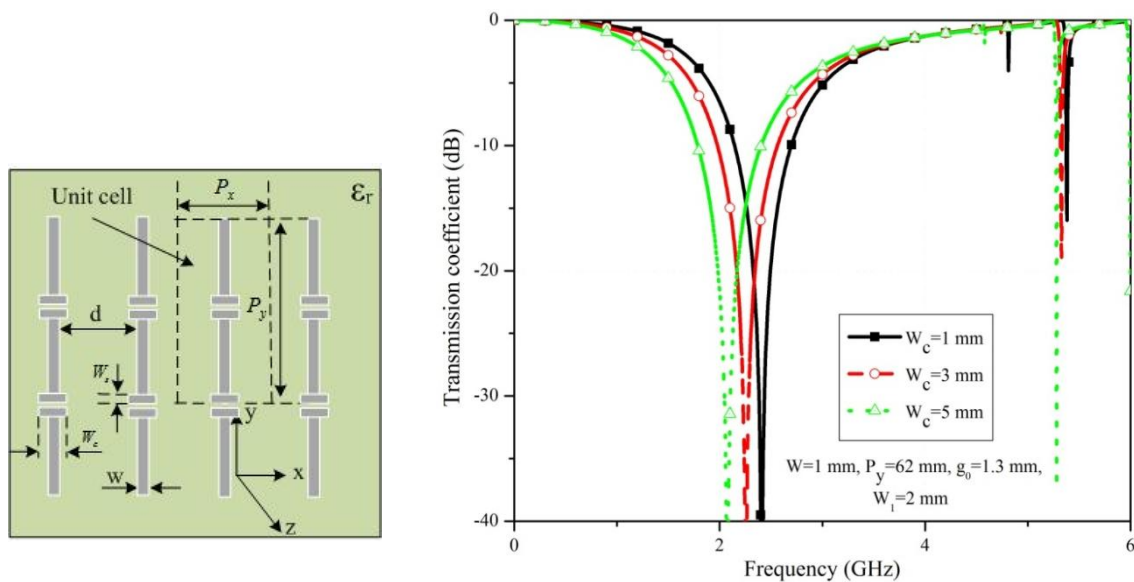


Fig. 4-12 Effect of gap width on the grid response.

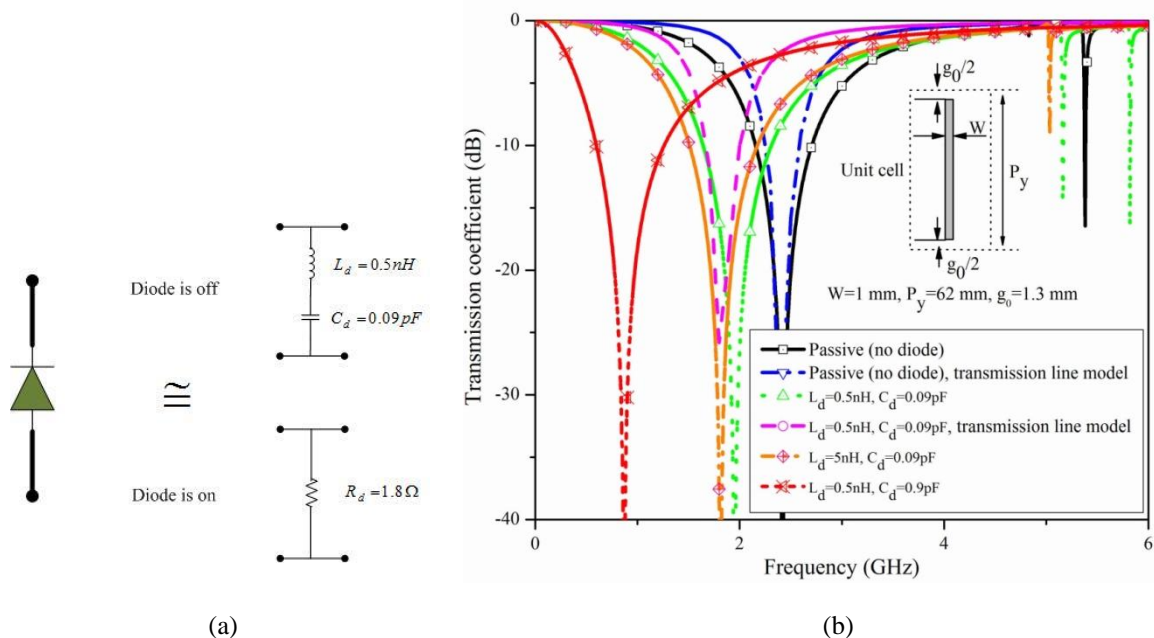


Fig. 4-13 Effect of active element on the grid response. (a) PIN-diode model. (b) Simulated transmission coefficient for different parasitic capacitance values.

4. 2. 4 Reconfiguration mechanisms and DC-biasing feed line

Fig. 4-14 shows two types of reconfiguration mechanisms and their transmission performances for this resonant element. In the first method, each column of strip dipoles

are vertically fed, and the reconfiguration mechanism is achieved by changing the surface from inductive state to a capacitive one. The desired transparency level in the on case must be close to unity across the desired stop-band of the opaque case. Therefore, the diode parasitic elements, especially the capacitance, are crucial parameters and their effects should be compensated in the design process.

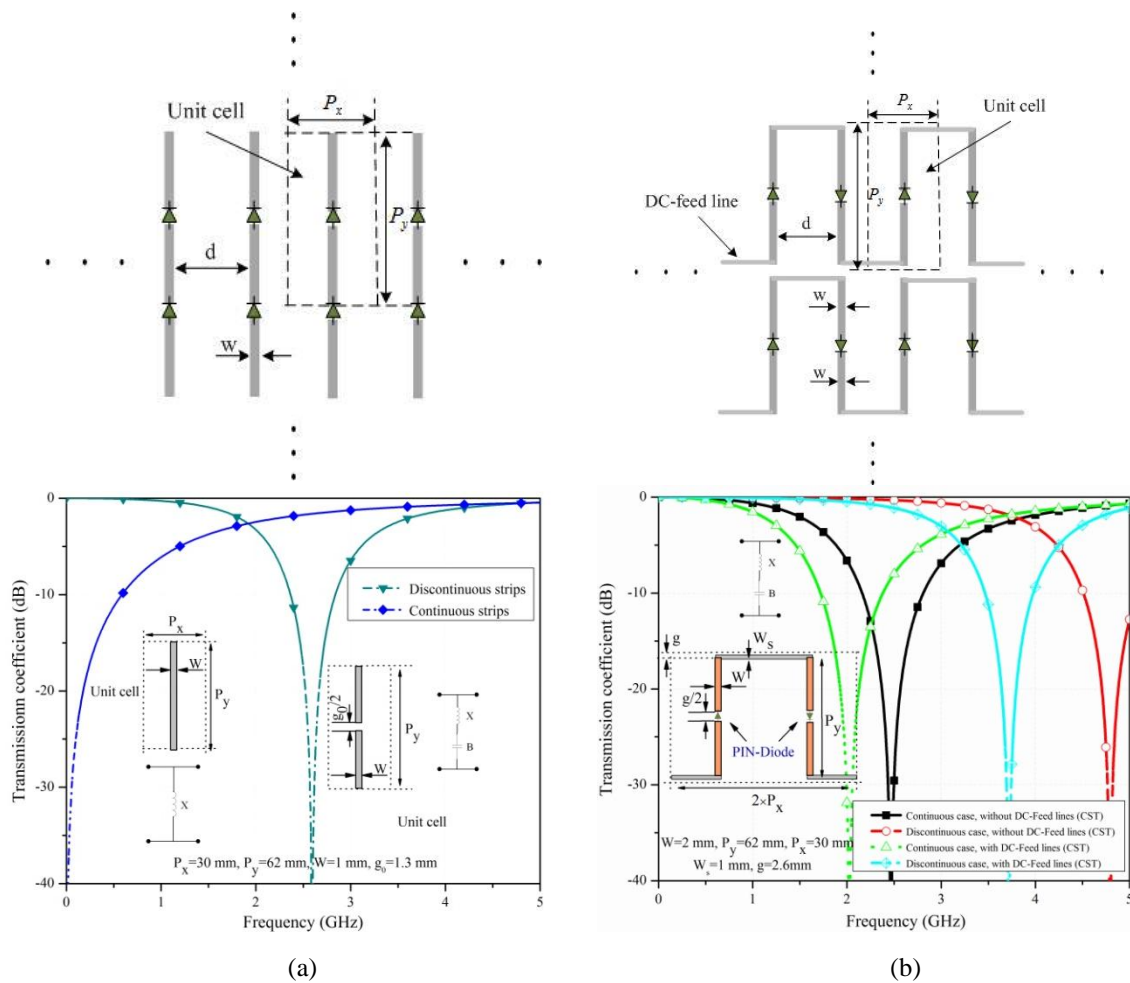


Fig. 4-14 Geometries of two serial-fed reconfiguration mechanisms and their transmission coefficient responses. (a) Vertical fed. (b) Horizontal fed.

By arranging active elements with a same polarity along each row and horizontally feeding them, a new reconfiguration mechanism has been achieved [91, 93]. In this mechanism, the reconfiguration is realized by shifting the position of the stop-band to higher frequencies. This provides capacitive dual responses for on and off states of the diodes. However, the loading effect of DC-feed lines changes the equivalent impedance of the surface compared to the one for vertical fed mechanism.

As it can be noticed from the simulated transmission coefficient curves, inserting the feed lines causes a considerable reduction in the stop-band position for both on and off states. Basically, because of changing the total L and C in the resonant circuit model of the proposed unit cell, the loading effect of these lines undesirably impacts the EM response of the unit cell, which causes some downward shift in the position of stop-band. In addition, the loading effect of the discontinuous case is more affecting the stop-band position compared to the continuous one. This is because, in this case, the capacitance C is considerably changed along with the inductance, resulting in a greater shift. Therefore, it can be concluded that even though the structure provides the desired transparency and opaque surface for the incident EM waves, the DC-feed lines severely impact the position of the stop-band. This causes to reduce the desired transparency level of this state. Furthermore, the DC-feed network limits the application of the surface to a particular reconfigurable configuration. In the next chapter, this effect will be explored in more details for cylindrical reconfigurable antenna applications.

4.3 Applications of agile transparent/opaque screens in reconfigurable antennas

In Chapter-2, a brief description about frequency selective surfaces and their applications in antennas was presented. The element type, lattice geometry, number of FSS layers, and the supporting dielectrics are the main parameters that should be considered in the designing process, respecting the expected electromagnetic performances. The element type and lattice configuration are chosen according to the expected transmission/reflection performances in terms of desired bandwidth, cross polarization level, and grating lobe response. The supporting dielectric and number of layers are in the second order of importance when a rapid roll off with a flat stop/pass band response is expected. Furthermore, the overall type of the FSS screen is also determined by the applications and the desired operating function from the FSS surface.

In this part, an application of planar array of dipole strips for reconfigurable radiation-pattern antenna is presented. Fig. 4-15 shows the antenna geometry in which the solid metallic reflector is replaced with a reconfigurable partially reflective surface. By changing the state of the partially reflector from opaque to transparent, the antenna radiation-pattern is reconfigured from uni-directional to omni-directional case. By this method, spatial filtering in transmitting or receiving signal is achieved. The operating frequency of this antenna is 2.45GHz with vertical polarization.

The radiation mechanism laid behind this antenna is based on the principles of reflector antennas. Therefore, to determine the overall dimensions of the proposed reconfigurable antenna, firstly a directional beam flat reflector antenna is designed for maximum

bandwidth and gain with side-lobe level of less than 20dB. Then the reflector is replaced by a reconfigurable frequency selective surface. In addition, to reduce the required number of active elements, the reflector size is designed for the minimum size that fulfills the above mentioned objectives. In summary, the most designing considerations of the active FSS screen include:

- Minimum number of active elements;
- Narrow strip width;
- Minimum acceptable screen size;
- Frequency of operation 2.45GHz;
- Maximum transparency level for the on state around the operating frequency;
- The DC biasing mechanism and its constraint according to the desired features.

According to these constraints, the design procedure of the flat reflector antenna and the flat FSS grid is described in the following sub sections.

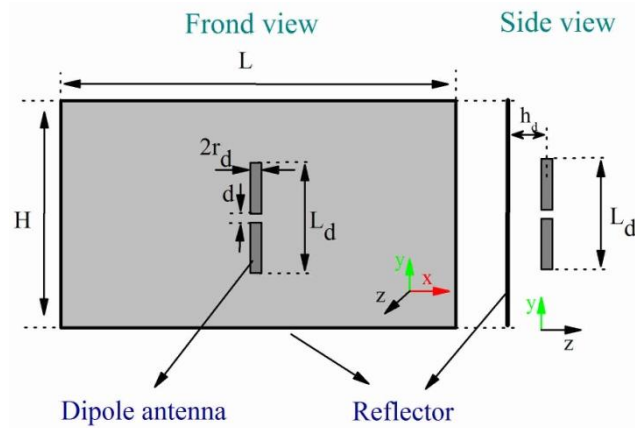


Fig. 4-15 Flat reflector antenna geometry.

4.4 Reconfigurable flat-reflector antenna design

4.4.1 Flat-reflector design

In Fig. 4-15, a simple $\lambda/2$ wavelength dipole resonator is placed in a distance h_d far from of a perfect electric conductor with dimensions of $H \times L$. A comprehensive parametric study was performed for different antenna dimensions, as shown in Fig. 4-16 to Fig. 4-19, to explore the effect of each one on the antenna radiation characteristics. The simulated reflection coefficient results in Fig. 4-16 show that the distance h_d is the main parameter affecting the antenna radiation resistance, and hence their matching and realized gain.

Moving the dipole radiator close to the reflector increases the directivity and lowers the side-lobe level of the radiated pattern at the expense of narrower bandwidth. Indeed, by closing the antenna to the reflector, more energy is stored in the vicinity of the dipole. This causes to reduce the bandwidth of the dipole radiator [97].

The maximum directivity in Fig. 4-17 is achieved when the dipole distance is in the range of $0.1\lambda < h_d < 0.3\lambda$. This is the first dipole position range to achieve the maximum directivity without any null in the main beam [97]. Because of the mutual coupling between the reflector and the dipole radiator, as depicted in Fig. 4-16, some shift in the resonant frequency of the flat reflector antenna can be expected by changing the dipole position. Therefore, the required length of the dipole for this range of distance is slightly less than $\lambda/2$ at the desired resonant frequency 2.45GHz, i. e., $0.4\lambda \leq L_d \leq 0.52\lambda$.

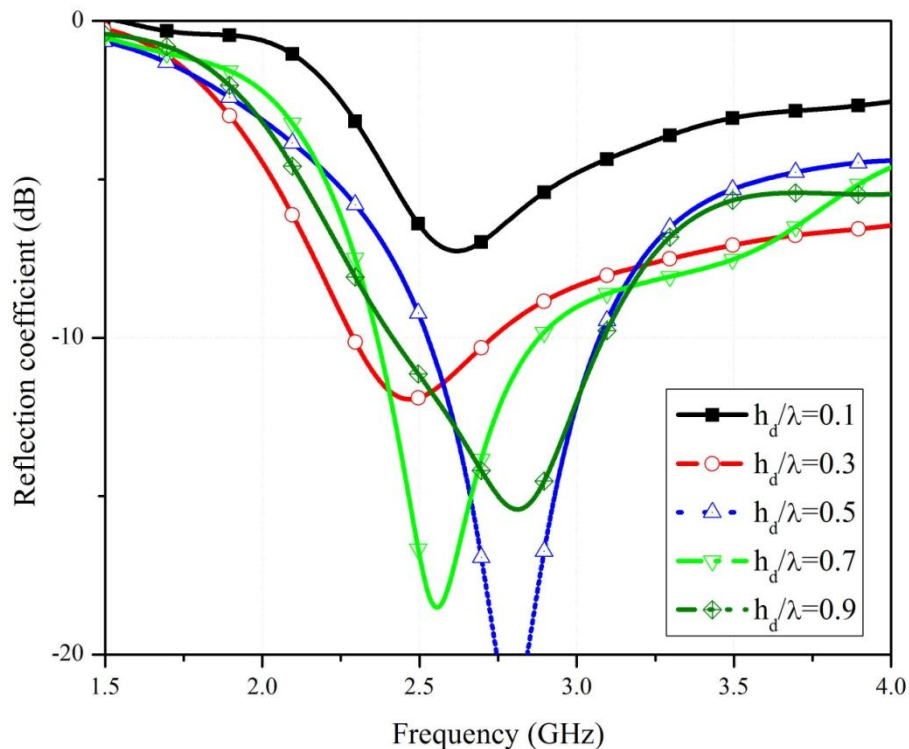


Fig. 4-16 Reflection coefficient of the flat reflector antenna for different values of h_d . $L_d = 44$, $H = \lambda$, $L = 2\lambda$ (All dimensions are in mm).

The curves shown in Fig. 4-18 and Fig. 4-19 reveal that the reflector dimensions are dictating the amount of radiated power in the rear region of the reflector [97]. The parameter H mainly affects the side-lobe level in the E-plane, while L determines the side-lobe variation in the H-plane radiation-pattern. The results in [97] show that a value of $\lambda < L < 3\lambda$ and $0.6\lambda < H < 2\lambda$ can be good enough to achieve the desired gain with acceptable side-lobe level in both principal planes. In general, this antenna provides a

gain of more than 6dB with side-lobe level of less than -15dB in both E- and H-planes at the designed operating frequency.

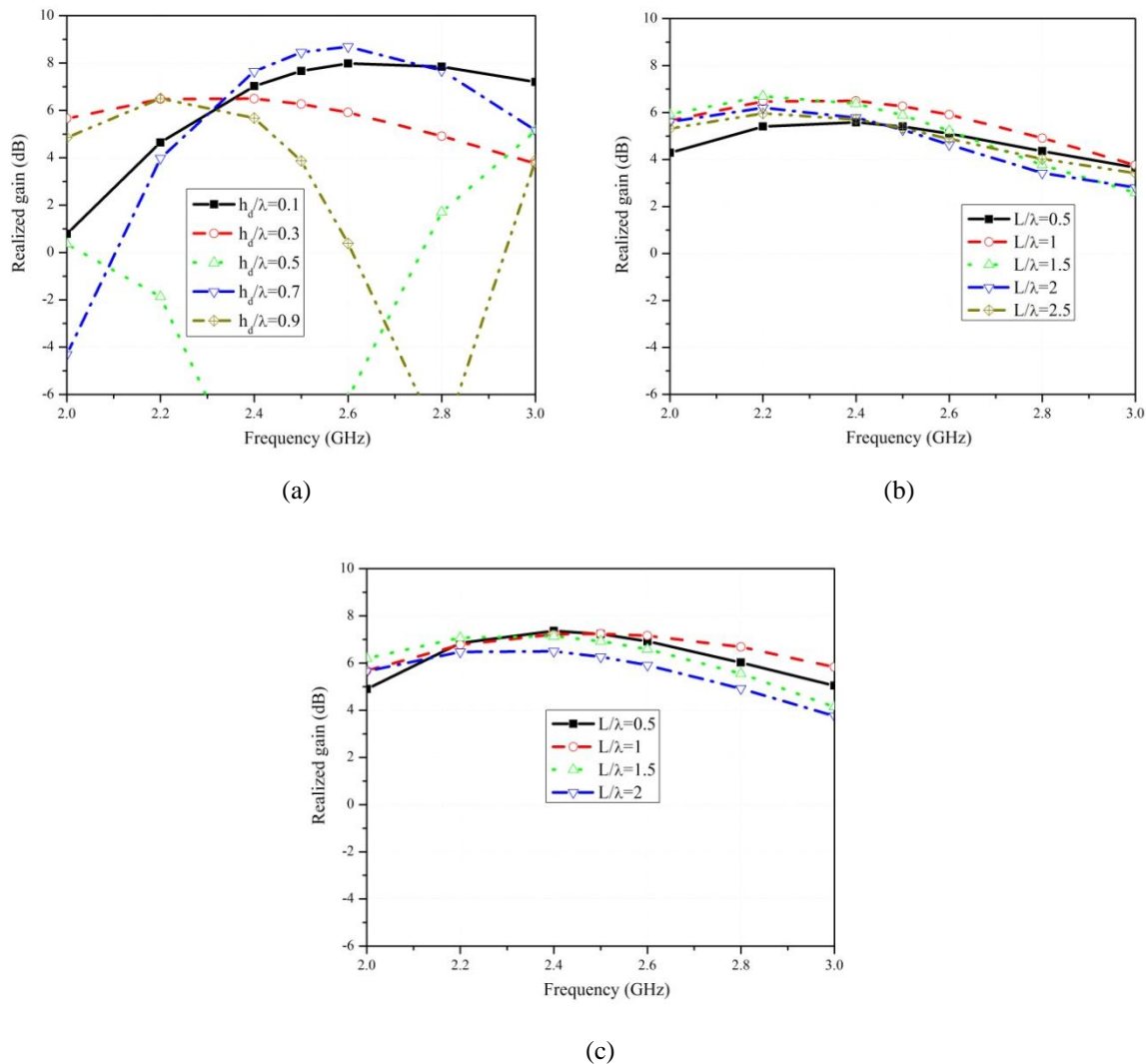


Fig. 4-17 Parametric studies of flat reflector antenna carried out for realized gain at different values of H, L, and h_d . $L_d = 0.36\lambda$, $H = \lambda$, $L = 2\lambda$, $h_d = 0.3\lambda$ (All dimensions are in mm).

For typical dimensions of $L_d = 0.36\lambda$, $H = \lambda$, $L = 2\lambda$, $h_d = 0.2\lambda$, the antenna bandwidth is about 20% around the frequency 2.45GHz. The half power beam-width of the antenna in the E- and H-planes are 59.6° and 90° , respectively. Moreover, the antenna realized gain is about 8.5dB for this value of dipole distance, and changing the reflector dimensions does not offer any considerable variation in the antenna gain. This is in an agreement with the results presented in [97] for a similar planar reflector antenna. In all simulations, the radius of the dipole antenna is equal to 3mm. This radius was chosen to achieve minimum 10% bandwidth for a simple dipole.

Therefore, according to the simulation results, the design guidelines for the antenna geometry shown in Fig. 4-15 are:

- 1- The dipole distance to the reflector is chosen in the range of $0.1\lambda < h_d < 0.3\lambda$.
- 2- The dipole length is considered in the range of $0.4\lambda \leq L_d \leq 0.52\lambda$ and its radius is 3mm to guarantee a 10% bandwidth for the dipole.
- 3- The reflector size are chosen by $0.6\lambda < H < 2\lambda$ and $\lambda < L < 3\lambda$.

The final design values are determined by a compromise between the acceptable size, gain, and bandwidth of the antenna.

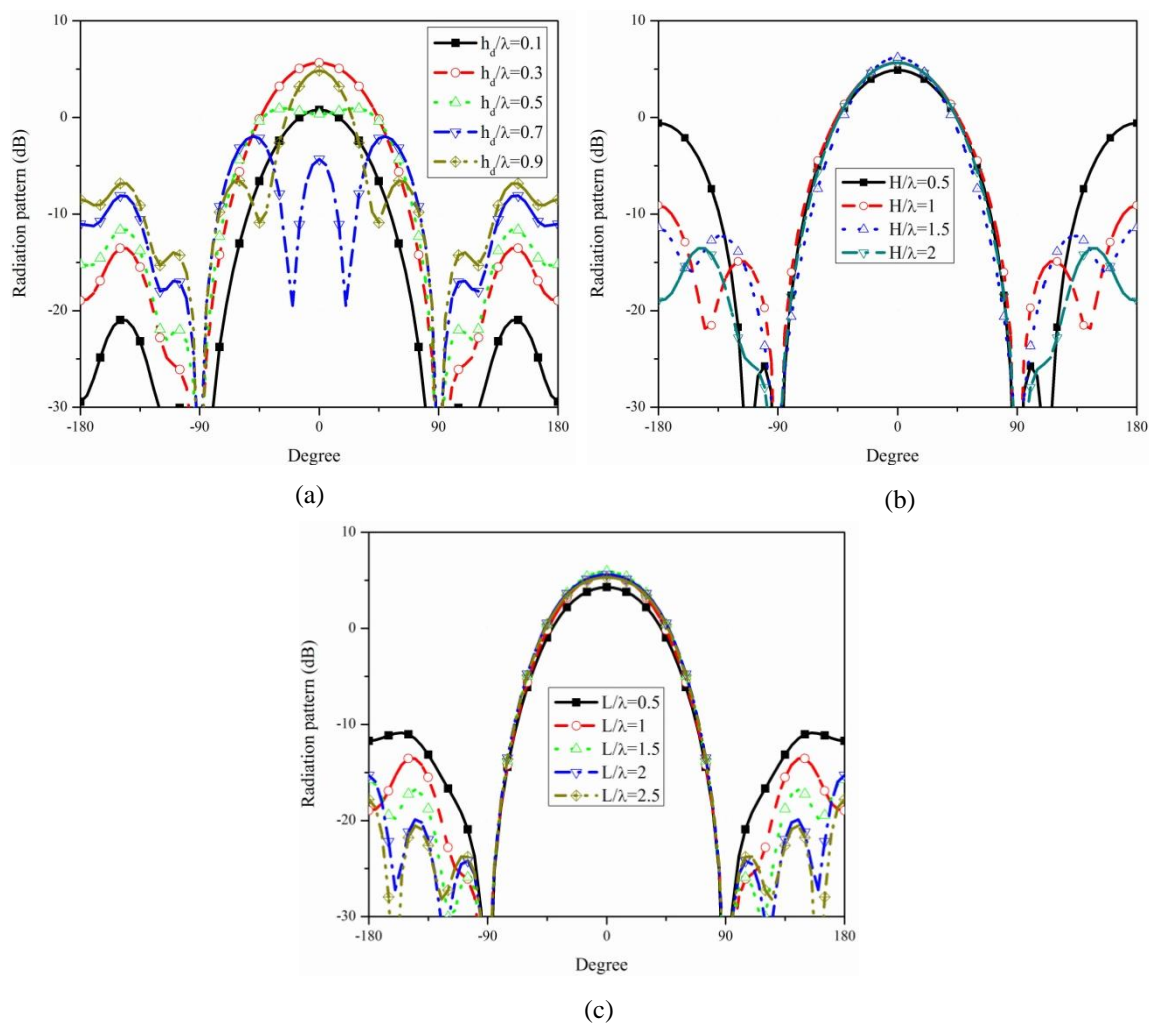


Fig. 4-18 Parametric studies of flat reflector antenna carried out for H-plane radiation-pattern at different values of h_d (a), H (b), and L (c). $L_d = 0.36\lambda$, $H = \lambda$, $L = 2\lambda$, $h_d = 0.3\lambda$ (All dimensions are in mm).

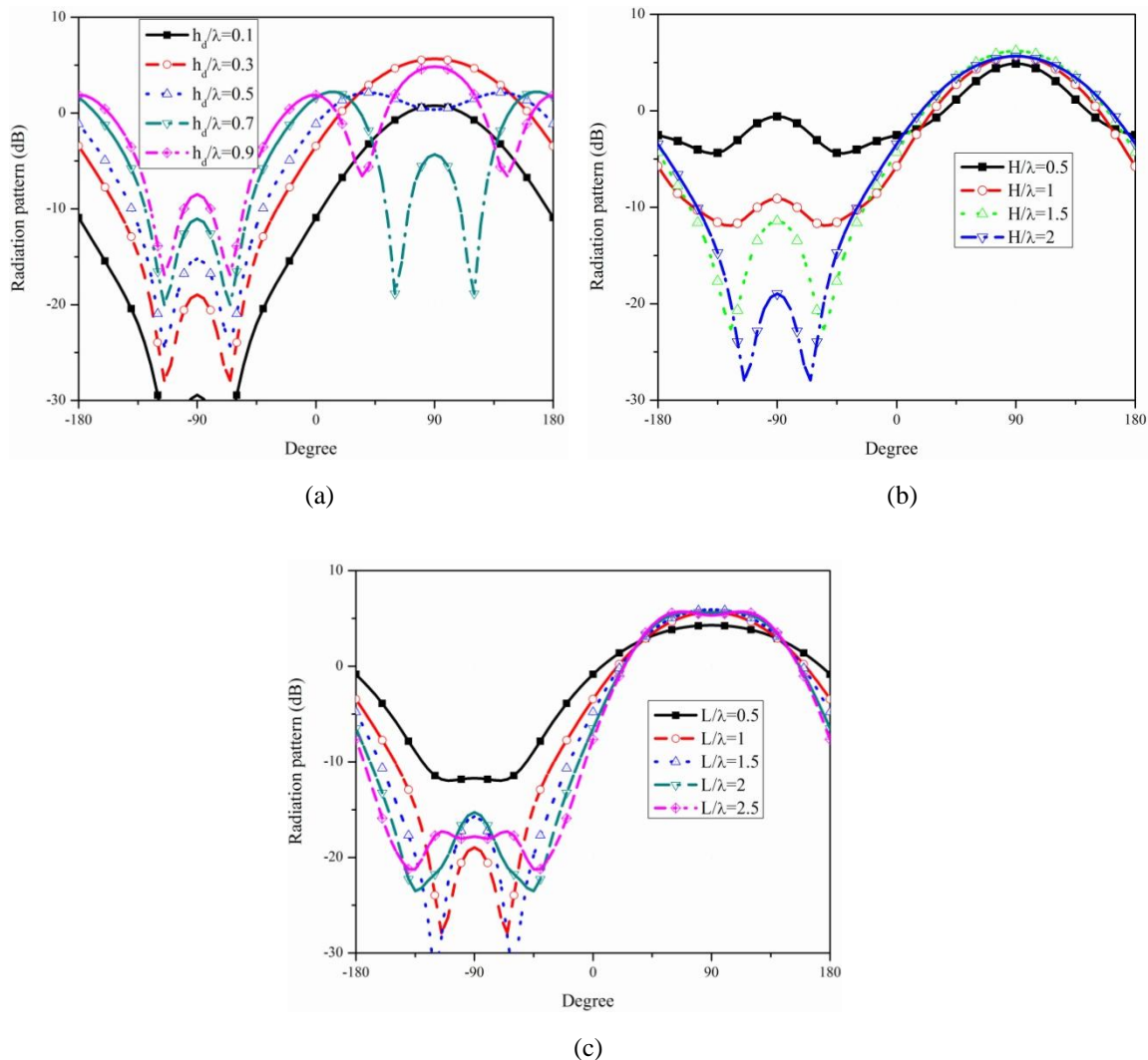


Fig. 4-19 Parametric studies of flat reflector antenna carried out for E-plane radiation-pattern at different values of h_d (a), H (b), and L (c). $L_d = 0.36\lambda$, $H = \lambda$, $L = 2\lambda$, $h_d = 0.3\lambda$ (All dimensions are in mm).

4.4.2 Reconfigurable flat-reflector using planar agile metallic grid

A reconfigurable flat reflector radiator can be achieved by changing the solid perfect electric conductor of Fig. 4-15 with a controllable partially reflective/transparent surface [93]. This tunable electromagnetic shutter must be able to mimic a perfect electric conductor in one state, while it passes the incident wave without any interaction in the other state. To validate this concept, the second reconfiguration mechanism, shown in Fig. 4-14b, was chosen as a reconfigurable partially flat reflector. In this design, to reduce the number of active elements, the minimum dimensions are selected for the reflector. The number of active elements in x and y directions are calculated according to the

required overall size of the perfect electric conductor calculated for a directive radiation-pattern antenna and the unit cell periodicities.

4.4.2.1 Simulation and measurement results

An antenna prototype based on the second reconfiguration mechanism was simulated and fabricated [93]. The reconfigurable screen is composed of 8×4 rows of the proposed ideal unit cell in Fig. 4-14b, which is etched on RO3003 with dielectric constant of $\epsilon_r = 3$ and thickness of 0.254mm. This grid is placed at 20mm from a dipole. The dipole is constructed by two rods with 3mm radius and 23mm length connected to an SMA connector. High frequency PIN-diode of GMP4201 [95] has been used as a switching element in the proposed grids. The inductance and capacitance parasitic elements of $L=0.5\text{nH}$ and $C=0.09\text{pF}$ are considered to model the diode in the simulation. This sheet is designed to operate at the desired frequency in which the DC-feed line and parasitic effect are compensated.

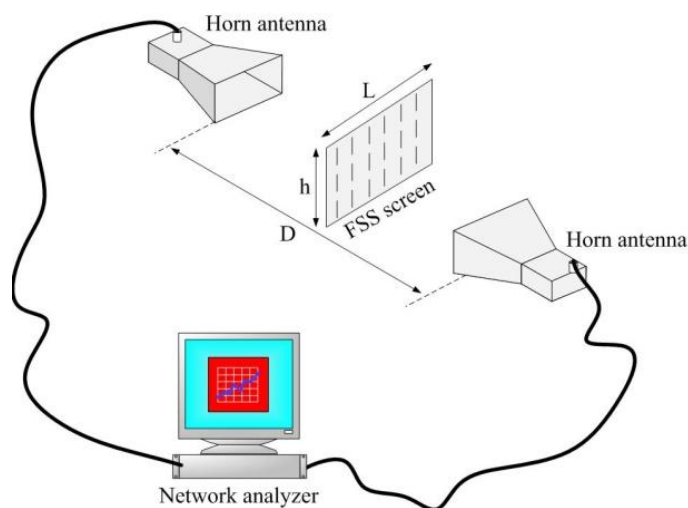


Fig. 4-20 Transmission coefficient measurement setup.

To precisely evaluate the performance of the proposed grid, its transmission coefficient is measured step-by-step. Two broadband horn antennas are used in a measurement setup. The setup is calibrated for the case without FSS sheet to eliminate the directional coupling between antennas as well as the multipath phenomenon. In order to achieve more accurate measurement results, the sheet dimensions should be large enough to capture all the power introduced by the horn antennas at the sheet surface. Therefore, a larger sheet composed of 13×4 unit cells was fabricated and used in this part of the measurement. Fig. 4-20 shows the setup used in the measurement.

The transmission coefficients were carried out for four different cases of Fig. 4-21. As it can be observed from the achieved transmission coefficient results, the first measurement performed for the passive structure well confirms the simulation prediction. The simulation in this figure was performed for a unit cell without considering the DC-feed line and parasitic effects to examine each case. Inclusion of PIN-diode into the unit cell significantly lowers the stop-band center frequency. Furthermore, as it is expected, loading effect of the DC-feed lines also shifts further down the stop-band. When the sheet is activated, the measurement results show a good stop-band around the desired frequency, confirming the integrity of the design process. Furthermore, these measurement results prove the potential of the proposed structure to create an agile FSS screen by considering the undesired parasitic elements and DC-feed loading effect.

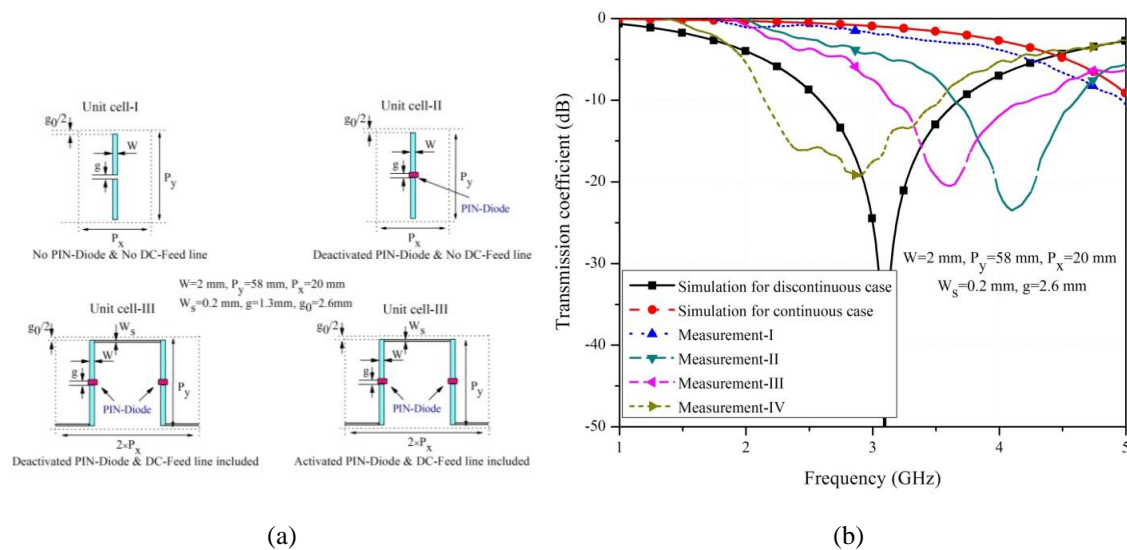
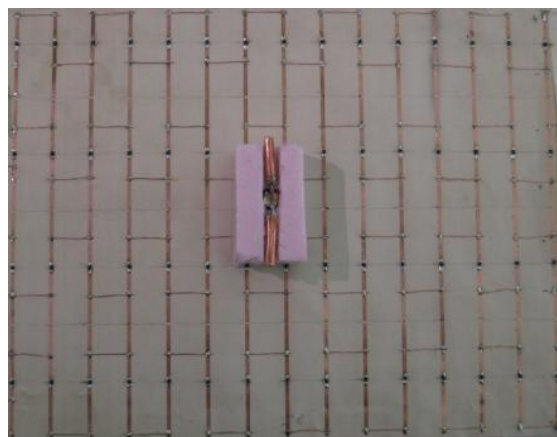


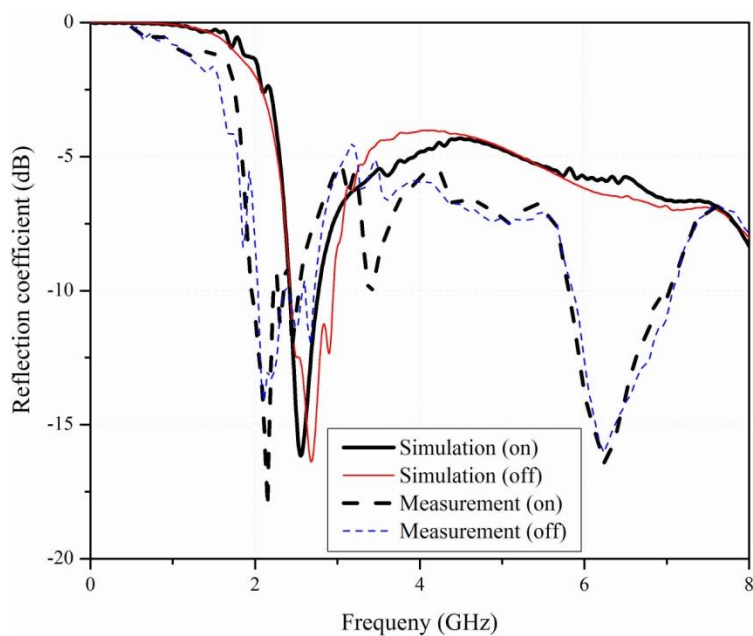
Fig. 4-21 Evaluating the performances of a FSS screen based on the first proposed unit cell. (a) Four different FSS screens constructed using 24×4 elements of these unit cells. (b) Measured transmission coefficient compared to the simulation.

This sheet was applied to implement the proposed reconfigurable flat reflector antenna shown in Fig. 4-15. The fabricated prototype and antenna parameters have been demonstrated in Fig. 4-22 and 4-23. As it can be noticed, the measured results confirm the simulation ones quite well. The results for the return loss indicate a bandwidth of 370MHz and 530MHz for on and off cases. The measured radiation-patterns for 2.4GHz, 2.5 GHz, 2.6 GHz, and 2.8GHz show that the best radiation-pattern with low back-lobe in directional case is achieved at 2.6GHz. Fig. 4-23 shows the E- and H-plane radiation-patterns of this antenna at 2.6GHz. In these curves, for comparison purpose, each curve has been normalized to its maximum value. It can be observed that the H-plane radiation-pattern is almost operating like a dipole antenna when the screen is transparent. However,

there is some deviation between the simulated and measured E-plane patterns in the off case, which is believed this is because of the screen performance in this plane by changing the angle of incident. The half power beam-widths of the antenna in H- and E-planes are 107° and 63° , respectively. In conclusion, the achieved measurement results confirm the potential of the proposed screen in creating a reconfigurable radiation-pattern antenna in which the spatial coverage area and also the gain of the radiator placed close to screen are controlled.

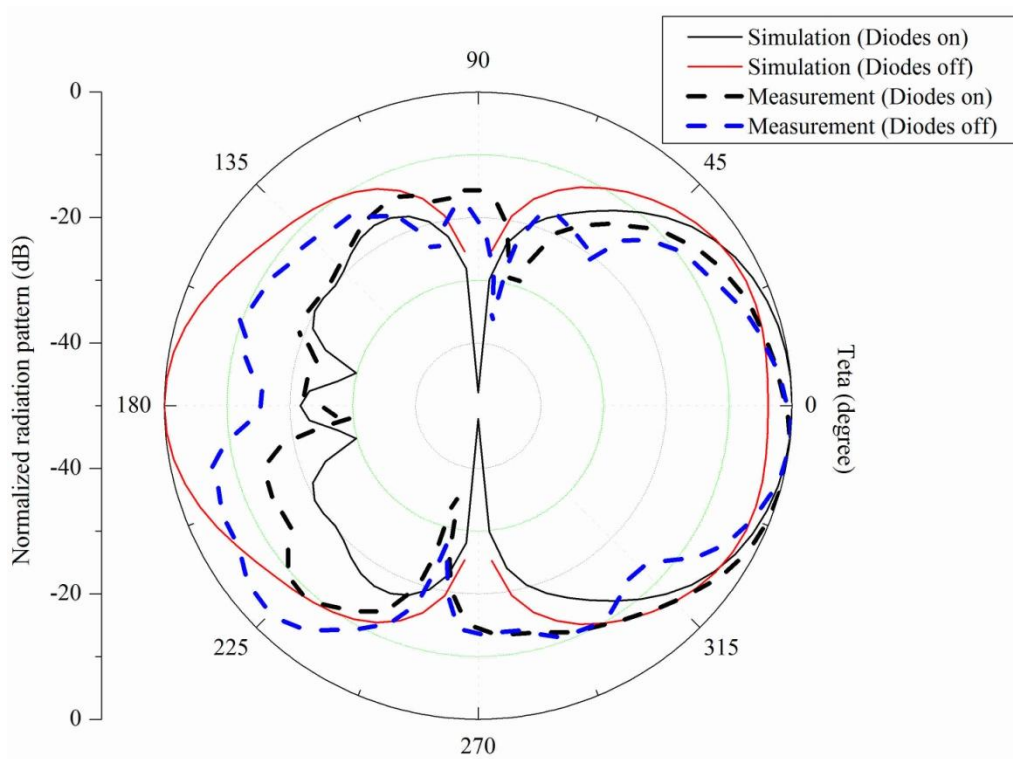


(a)

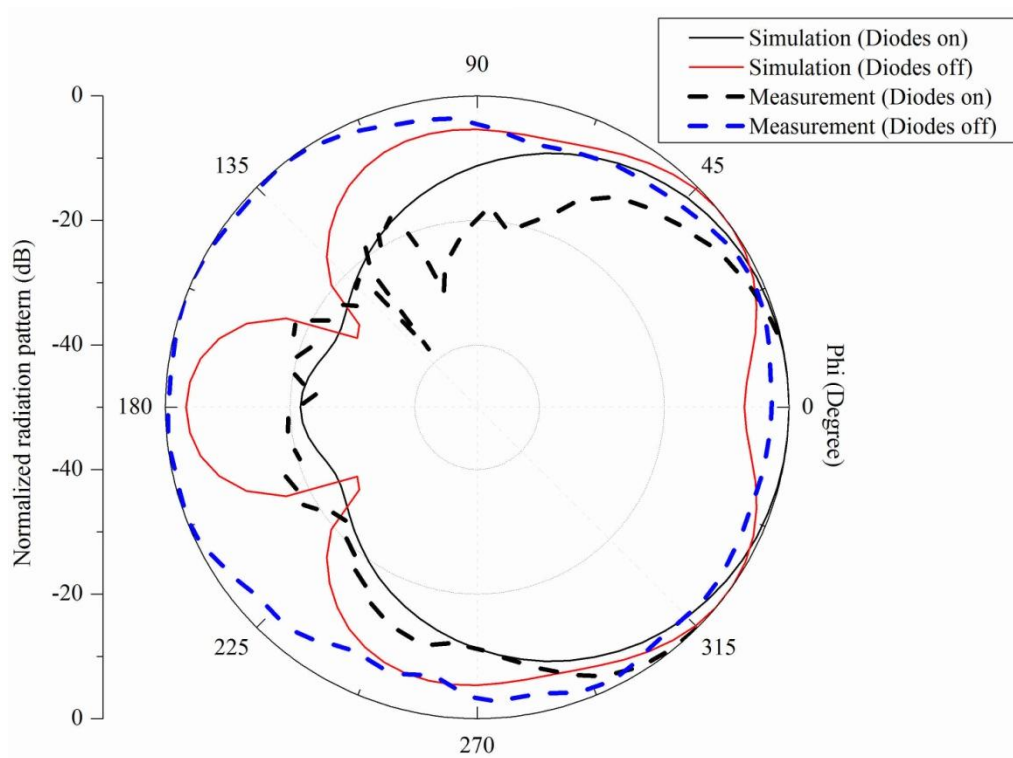


(b)

Fig. 4-22 Photo of fabricated prototype (a), and reflection coefficient results (b).



(a)



(b)

Fig. 4-23 Antenna radiation-patterns. (a) E-plane pattern. (b) H-plane pattern.

4.5 Conclusion

In this chapter, a planar grid of active frequency selective surface has been theoretically and analytically investigated and its application for reconfigurable radiation-pattern antenna has been assessed. As it was expected, the transmission/reflection coefficient of the grid can be predicted by equivalent transmission line theory with an acceptable accuracy for the frequency range of before onset of grating lobes. Using this model, since the width of strips is narrow compared to the periodicity orthogonal to the strips, the effect of fringing fields around the gap should be compensated to fit the measured results with the calculated one. The results show that by locally increasing the strip width at the edges of the gap, the fringing field effect can be neglected in predicting the resonant frequency. This also reduces the required unit cell size for the given stop-band center frequency.

The effect of high frequency PIN-diode parasitic elements has precisely been examined, and it has been demonstrated that those must be compensated to obtain the desired reconfiguration performance. In addition, it has been shown that depending on the DC-fed biasing network, different reconfiguration mechanism can be achieved. Moreover, the feeding network also affects the transmission performance of the active FSS screen by changing the effective inductance and capacitance in the transmission line model. Therefore, the feeding mechanism and parasitic elements' effect restrict the application of the proposed FSS sheet.

The measured results carried out for a fabricated prototype of a reconfigurable FSS screen also confirm its potential in creating a controllable electromagnetic window by considering the above mentioned constraints in the design process. These screens can be used as tunable reflectors or spatial filters in the microwave frequencies. In the next chapter, their applications in implementing a class of multi-function reconfigurable antennas are presented and discussed.

Chapter 5

Cylindrical FSS screens and nimble radiation-pattern antennas

5.1 Introduction

In Chapter-4, the potentials of planar FSS screens constructed by periodic array of discontinuous strips were evaluated for reconfigurable electromagnetic shutter applications. It was theoretically and experimentally shown that by incorporating active elements into these surfaces with deliberate biasing feed lines, the desired dual transmission response can be achieved to create a reconfigurable flat-reflector antenna. However, the functionality of flat reflectors was limited to directional or omni-directional radiation-patterns.

This chapter is aimed to introduce a class of reconfigurable antennas with more functionality by using FSS screens proposed in Fig. 4-14 [91]. The desired antenna radiation parameters are briefly summarized as follows:

- Directional radiation-pattern;
- Sweeping all angles in azimuth;
- Vertical polarization;
- Reconfigurable radiation-pattern from directional to omni-directional;
- Minimum 10% bandwidth for both impedance and gain;
- Medium gain around 8dB;
- Minimum antenna size and hence less active elements;

- Operating frequency 2.45GHz;
- Side/back lobe level less than -20 in both E- and H-planes.

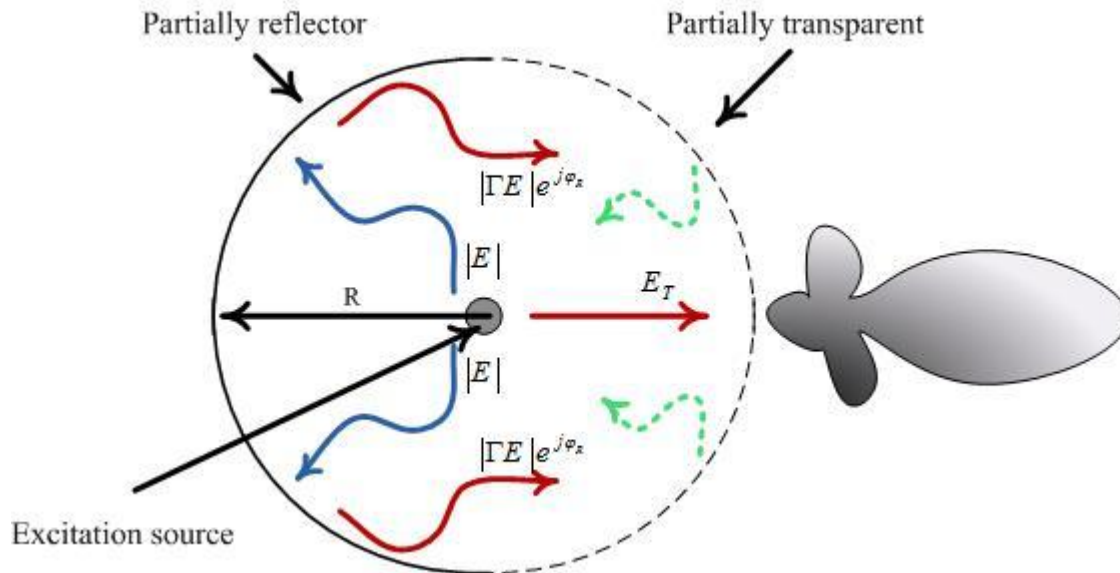


Fig. 5-1 Geometry of the proposed active reconfigurable cylindrical frequency selective surface antenna (ARCFSSA).

To realize these objectives, a cylindrical reflector antenna using reconfigurable frequency selective surfaces is proposed in Fig. 5-1. In this configuration, the controllable partially reflective/transparent surface is illuminated by a simple dipole radiator placed at the center of the cylinder. To realize a directional beam, semi part of this cylinder is mimicking a reflector, while the other part is transparent for the waves emanated from the dipole and the ones reflected from the other opaque part. By constructive interactions between these waves, a directive radiation-pattern is obtained in front of the reflector. Alternatively, when the entire cylinder surface is transparent for the dipole radiator, the overall antenna radiation is expected to be only the one of the dipole resonator. Therefore, the directive beam is turned into a low gain omni-directional pattern. For sweeping the direction of the radiation, the semi-cylinder opaque/transparent part of the reflector is moved around the cylinder by sequentially activating/deactivating the relevant unit cell elements on the FSS surface. By this technique, the pattern can be easily swept in the azimuth with a certain step dictated by the number of the active elements on the circumference of the cylinder.

According to the DC-biasing approach used for active elements, two types of vertical- and horizontal-fed FSS array of discontinuous strips are proposed as a cylindrical reconfigurable surface for the antenna shown in Fig. 5-1. Then, the pros and cons of each

antenna are presented and discussed. To do these tasks, the overall dimensions of the cylinder are firstly determined using principles of reflector antennas. Afterward, the proposed planar FSS screens are reformed to a cylindrical shape to construct a reconfigurable antenna based on the earlier mentioned radiation mechanism. The antenna dimensions are finally optimized by CST to achieve the desired radiation objectives for each antenna prototype.

5.2 Design of cylindrical reconfigurable reflector antenna

Since the radiation mechanism of the antenna is based on the reflector principles, the overall antenna dimensions are calculated using the semi-cylindrical reflector shown in Fig. 5-2. Then, the perfect electric conductor is replaced with reconfigurable partially reflective surfaces proposed in Chapter-4. In this radiation geometry, the reflector is illuminated by a dipole antenna at the center of the cylinder. The initial radius and length of the circular reflector are mathematically calculated based on the design guidelines of a corner-reflector antenna with an apex angle of 90° [97].

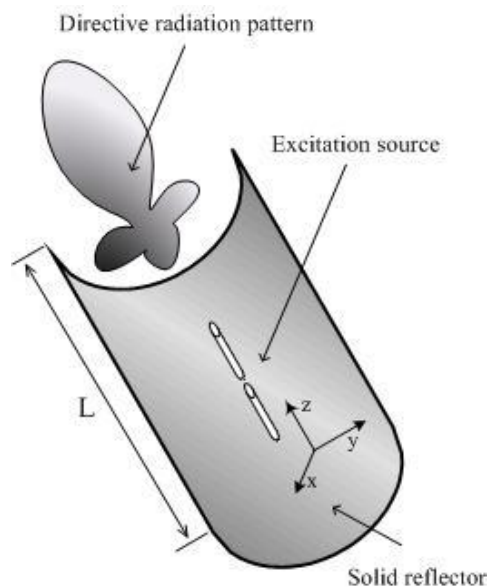


Fig. 5-2 Geometry of the semi-cylindrical reflector antenna.

Fig. 5-3 shows the cross section of a corner reflector fitted into a semi-cylinder with radius R . According to the optical ray tracing theory for 90° corner reflector antennas [97], when a dipole is placed at a distance of R from its apex, a low side/back-lobe level

directional beam can be achieved provided that the side sheet length is large enough to capture the most electromagnetic waves emanated from the dipole. In fact, depending on the distance of the dipole to the apex of the reflector, i.e., R , the reflected waves from the side sheets of the corner reflector can be in phase. Moreover, this distance substantially dictates the existence of the secondary lobes, the side/back-lobe level of the radiation-pattern and also the radiation resistance of the corner-reflector antenna. Therefore, depending on the illuminator position R , different design dimensions can be achieved with an efficient and directive radiation-pattern.

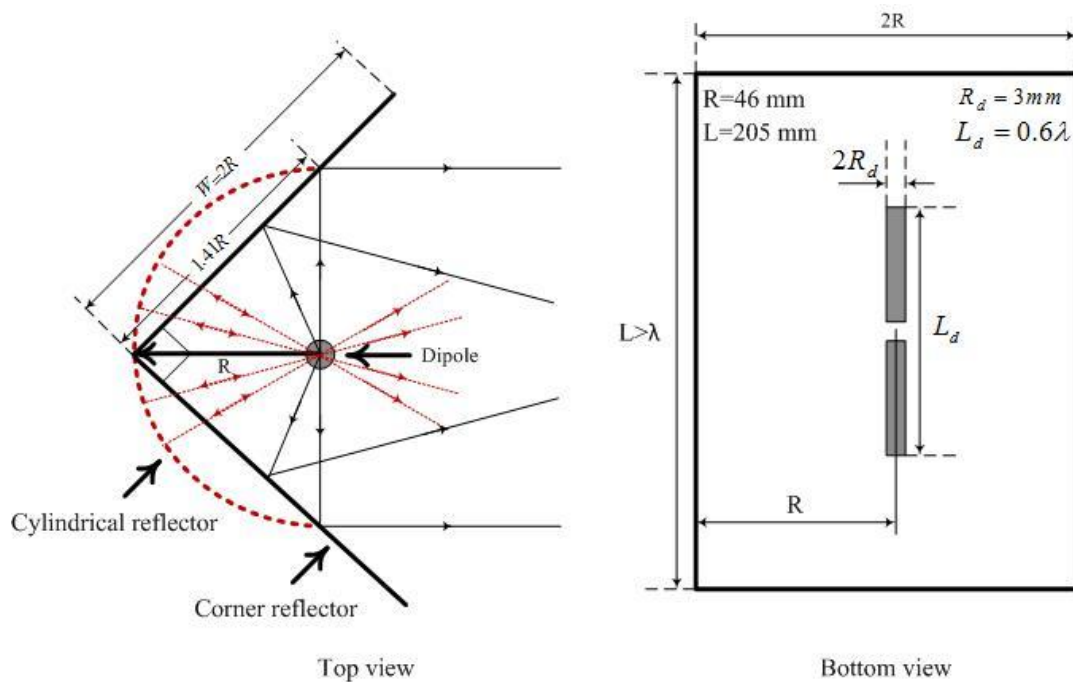


Fig. 5-3 Geometry of a corner reflector superimposed into a semi-cylindrical reflector antenna.

In this work, according to the corner reflector design guidelines in [97], a dipole with the first place position is considered to achieve the minimum dimensions for the cylindrical reflector. This reduces the required active elements and hence the cost of the reconfigurable reflector. For this corner reflector, the width of $W=2R$ is large enough to reflect the substantial part of the waves contributing in the main lobe of the radiation-pattern [97]. However, the crucial part of the reflector is that close to the point where a wave emanated from the dipole is reflected parallel to its axes, i.e., a reflector with side widths of $W=1.41R$. Therefore, a circle superimposed to this corner reflector with a radius R can ably capture the main part of the waves emanated from the dipole at its center. In fact, this semi-cylindrical reflector can provide a radiation performance close to a corner reflector with dimensions of $1.41R \times L$, where the length of reflector, i. e., L , is chosen larger than dipole length to reduce the back radiation in the E-plane.

An approximate value of R can be calculated by considering the required constructive phase relation of the interfered electric fields. It means that the interactions between the waves reflected from the cylinder and the ones emanated directly from the dipole must be in-phase to achieve a directive radiation-pattern in front of the reflector. To determine this relation, the scattering mechanism depicted in Fig. 5-1 is considered. It is supposed that an infinitely long cylinder is excited by an infinite thin dipole at its center. Because of geometrical symmetry around the axes of cylinder, almost entire inner surface of the cylinder is illuminated with co-phased electric fields. To achieve a directive radiation-pattern, the pass phase of reflected fields should be in-phase with the fields emanated from the dipole.

$$\Delta\phi = \phi_G - \phi_R = 2k\pi, \quad k = 0, 1, 2, \dots \quad (5-1)$$

where $\phi_R = 2R \times (2\pi/\lambda)$ and $\phi_G = -\pi$. This equation can be simplified to

$$R = k\lambda/2 + \phi_G\lambda/4\pi \quad (5-2)$$

The minimum value of $R = 0.25\lambda$ is achieved for this ideal case. In reality, since R is comparable with wavelength, the reflector is in the near field of the dipole antenna. In fact, the cylinder is illuminated while neither the amplitude of incident waves is uniform, nor they are in-phase. Therefore, the contribution of cylindrical reflector is not exactly -180° . Then, a distance of usually larger than $R=0.25\lambda$ is required to fulfill the in-phase condition of interfered electric fields. This relation is in agreement with the required antenna-to-apex distance of 0.25λ - 0.7λ for a corner reflector to achieve a directive radiation-pattern at its first dipole position [97].

5.2.1 Simulation results of a semi-cylinder reflector antenna

Using the initial values calculated in the previous sub-section, a semi-cylindrical reflector antenna was designed by CST Microwave Studio for the earlier mentioned design feature. A gain of more than 9dB and a back lobe level of less than -20dB across a bandwidth of at least 10% are the most important design objectives. Fig. 5-4 to Fig. 5-6 show the parametric simulations carried out for antenna dimensions. As it can be noticed, the radius R is the crucial parameter affecting both the reflection coefficient and antenna radiation-patterns. The results show that a radius in the range of 40-50mm can be a good choice for the desired performances. For this range of R , it provides a minimum 1.25GHz matching bandwidth, gain of about 10dB, and side/back lobe level of less than -25dB in both principal planes. As it can be observed from Fig. 5-5b, the length of the reflector is very important in determining the frequency of maximum realized gain. The antenna

beam-width for $R=46\text{mm}$ and $L=205\text{mm}$ in E- and H-planes are 46° and 70° , respectively. Simulation shows that the aperture efficiency offered by this antenna is about $A_{eff} = G \lambda^2 / 4\pi \approx 0.65$. The relevant total radiation efficiency of 97% is predicted for this antenna by the simulator.

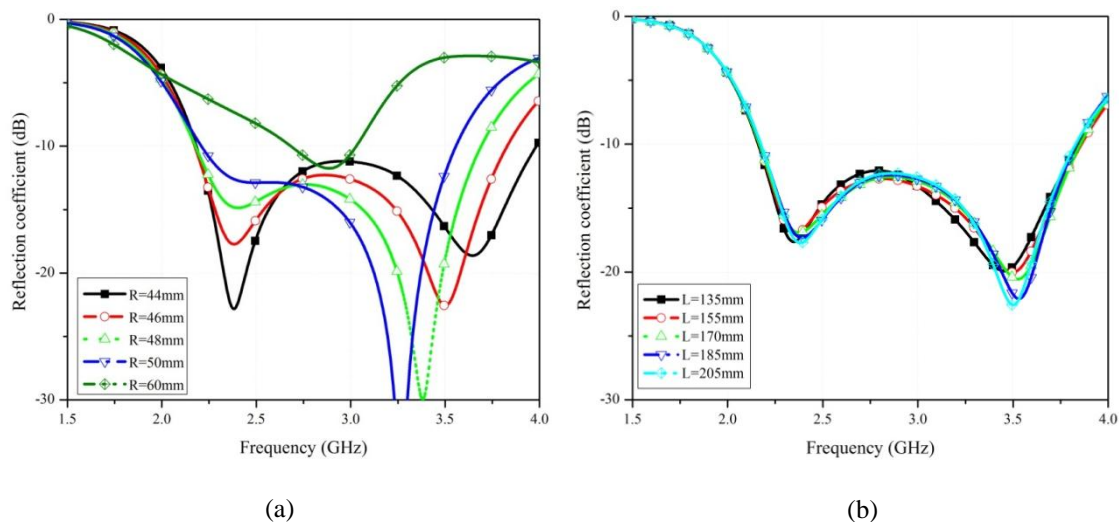


Fig. 5-4 Reflection coefficient of semi-cylindrical reflector antenna for different values of R and L . (a) Results for different values of R . (b) Results for different values of L .

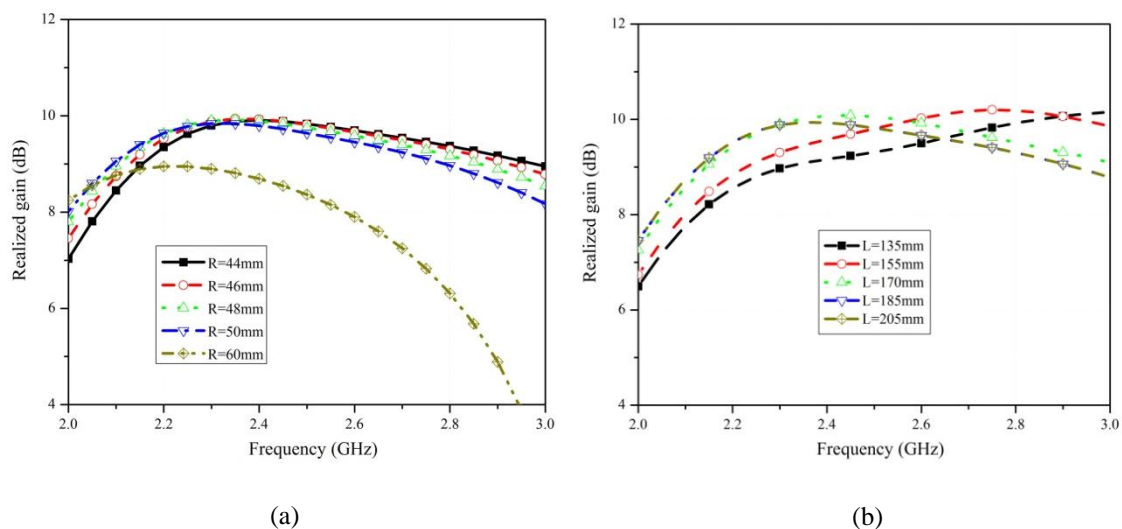


Fig. 5-5 Realized gain of semi-cylindrical reflector antenna. (a) Results for different values of R . (b) Results for different values of L .

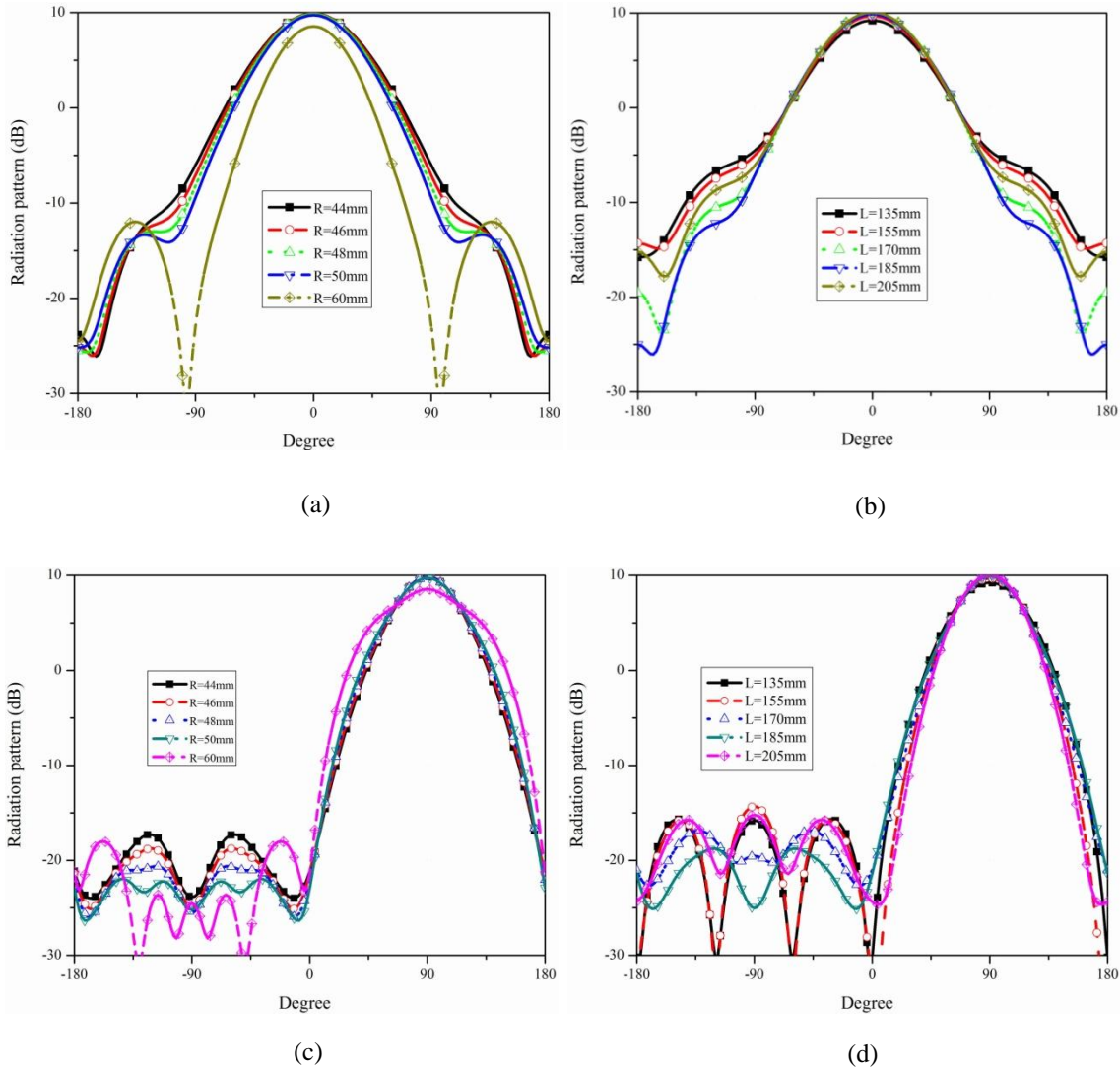


Fig. 5-6 Radiation-patterns of semi- cylindrical reflector antenna for different values of R and L. (a) H-plane for different R values. (b) H-plane for different L values. (c) E-plane for different R values. (d) E-plane for different L values.

5.3 Reconfigurable cylindrical FSS reflector antenna design

The initial values of the overall antenna dimensions shown in Fig. 5-2 were estimated in the previous section and the antenna performances were also verified by simulation. By having the length and radius of the solid reflector, an equivalent partially reflective surface can be designed as a reconfigurable reflector shown in Fig. 5-7.

Considering the antenna structure in this figure, number of the required unit cell along the circumference of the cylinder is determined according to the unit cell angular

periodicity of the designed FSS $P_t = r \times \alpha = P_x$ and radius of the cylinder. Therefore, $N_x = 2 \times \pi R / P_x = 10$ is selected to construct the CFSS sheet, dictating the number of sweeping steps for the radiation-pattern to entirely cover the azimuth angles. With regard to the reflector length, $N_y = 4$ elements of unit cells are also considered along the length of the cylinder. By determining the overall configuration of the cylindrical FSS reflector, the designed planar unit cell in Chapter-4 is reformed to a cylindrical shape. However, it is expected that by reforming a flat FSS screen to a curved structure, its EM response is altered according to the new lattice pattern, incident angle of EM waves and the radius of the curvature [98]. Here, because of no variation in the incidence angles of EM waves emanating from the dipole at the center of the cylinder, almost the same EM responses is expected in the cylindrical shape. Nonetheless, the finite dimension of the FSS screen can affect a little the EM response of the surface compared to the infinite case [91]. Therefore, the final dimensions of the antenna are optimized using the CST simulator for the desired radiation performances. The dimensions used for fabrication are summarized in Tab. 5-1.

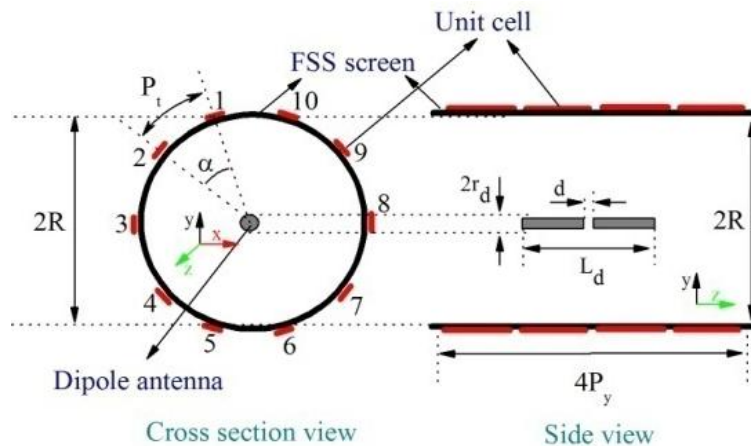


Fig. 5-7 Cylindrical FSS screen and number of active elements along its length and circumference.

5.4 Switched-beam reconfigurable antenna using cylindrical frequency selective surface

The geometry of switched-beam reconfigurable antenna and distributed configuration of its cylindrical FSS reflector are demonstrated in Fig. 5-8. The reconfiguration mechanism is achieved by changing the periodicity of the capacitive FSS screen. It is obvious from the distributed schematic of the FSS surface, because of feeding mechanism, this antenna is able to provide only two switchable directive beams oriented in two opposite directions. At each time, one part of the antenna is transparent while the other part

mimics a partially reflective surface. In this structure, the parallel DC-feeding lines along the cylinder axis are isolated from the screen by RF-chocks. It will be demonstrated that these biasing feed lines considerably affect the H-plane radiation and antenna gain.

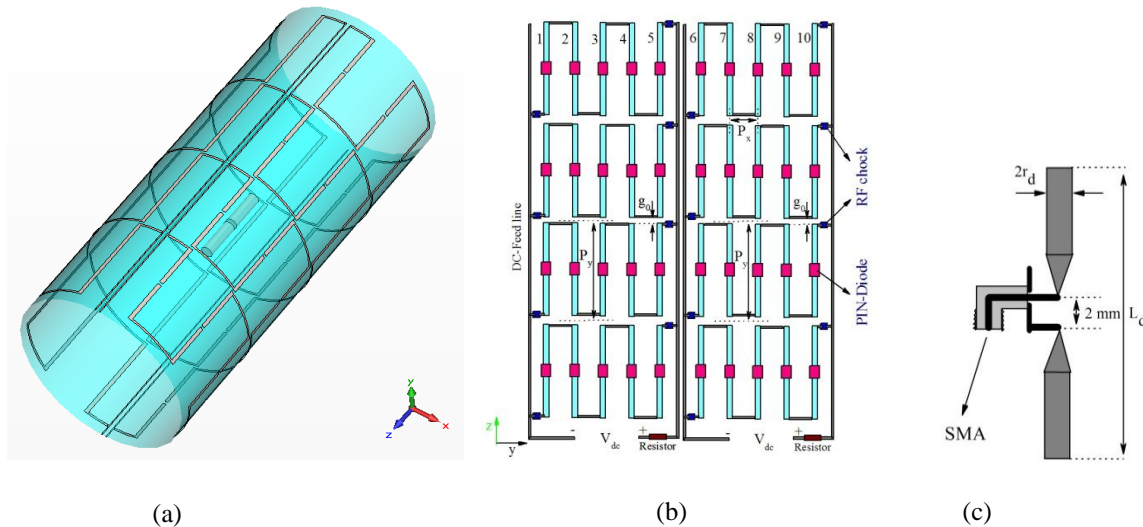


Fig. 5-8 Reconfigurable cylindrical reflector antenna. (a) Perspective view of the antenna (b) Schematic distributed geometry of FSS screen, $P_x = 28.8, P_y = 52, w = 1$. (c) Dipole antenna used in the proposed switched-beam cylindrical reflector antenna $L_d = 40, R_d = 3$, (All values are in mm).

Tab. 5-1 Final dimensions of the switched-beam reconfigurable antenna. All dimensions are in mm.

Parameters	R	P_y	g_0	g	L_d	r_d	W	W_s	L_s	h
Value	46	52	1.3	2.6	40	3	2	1	-	-

5.4.1 Reconfigurable mechanism of FSS screen used in switched-beam antenna

Fig. 5-9 shows a unit cell of the relevant planar FSS screen and their amplitude and phases of transmission/reflection coefficient responses. To mimic a perfect electric conductor, this surface must provide maximum reflection with phase of $\varphi_R = -1.1\pi$ at the center frequency of the stop-band in the on state. On the other hand, it should be completely transparent with almost zero phases at this frequency for the vertically polarized incident waves in the off state. However, the calculated phase shows a capacitive value of $\varphi_T = -0.15\pi$. These phase values dictate a radius in the range of about $R = 0.31\lambda$ to fulfill the expression (5-2) for a constructive radiation-pattern, where λ is the wave length at 2.45GHz. This value is in the range that was predicted for a semi-cylindrical solid reflector antenna in section 5. 2.

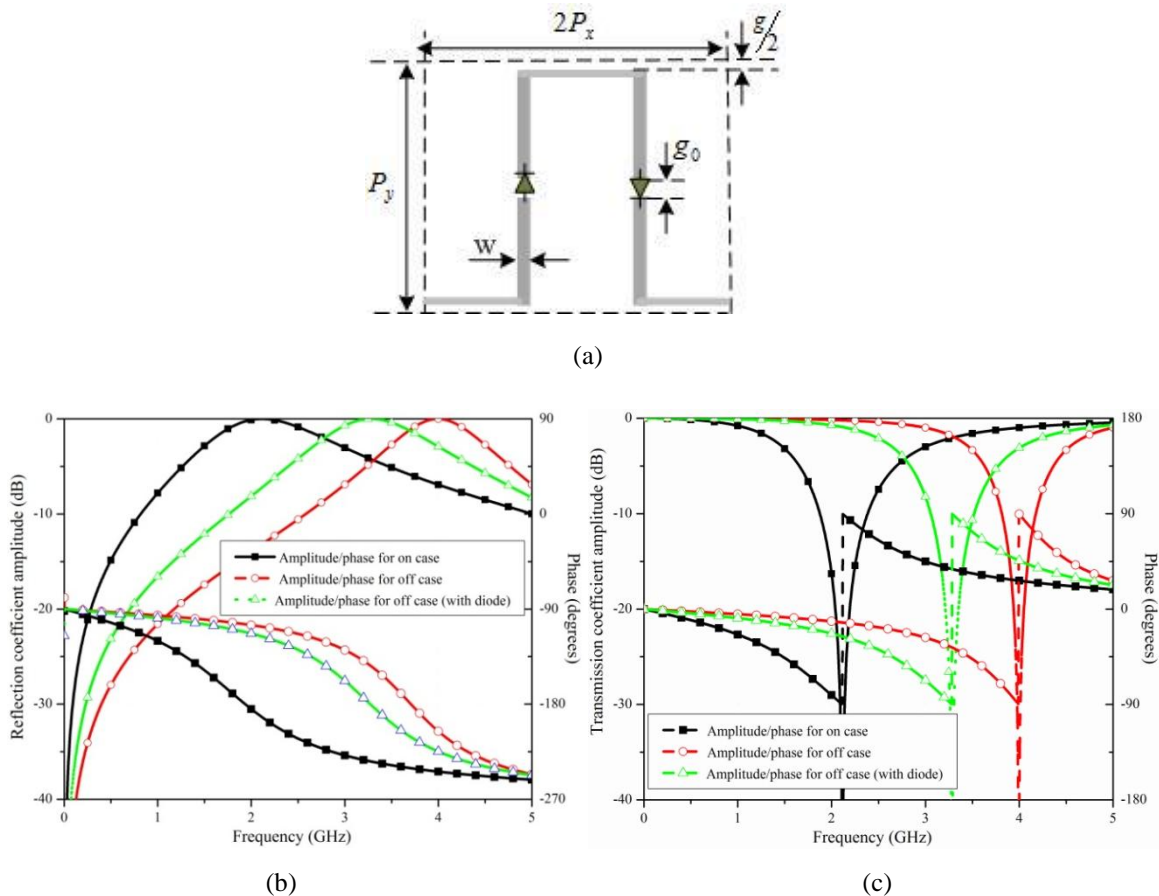


Fig. 5-9 A unit cell of the proposed FSS screen and its coefficient response. (a) Geometry of the unit cell, $P_x = 30$, $P_y = 52$, $w = 1$ (all in mm). (b) Amplitude and phase of reflection coefficient. (c) Amplitude and phase of transmission coefficient.

In Chapter-4, it was explained that the reconfiguration mechanism in this unit cell was realized by changing its periodicity using two high frequency PIN-diodes. The center of the stop-band for the off state is almost two times far of the one for on state. Nonetheless, because of the diode parasitic elements, the higher stop-band of FSS screen shifts toward lower frequency. This indeed deviates the total transparency level of the screen. It means that the parasitic elements effect of the diode must be considered in the FSS screen design process to achieve the desired reflectivity/transparency level across the operating band. This effect can be clearly observed in the calculated coefficient responses in Fig. 5-9b and c.

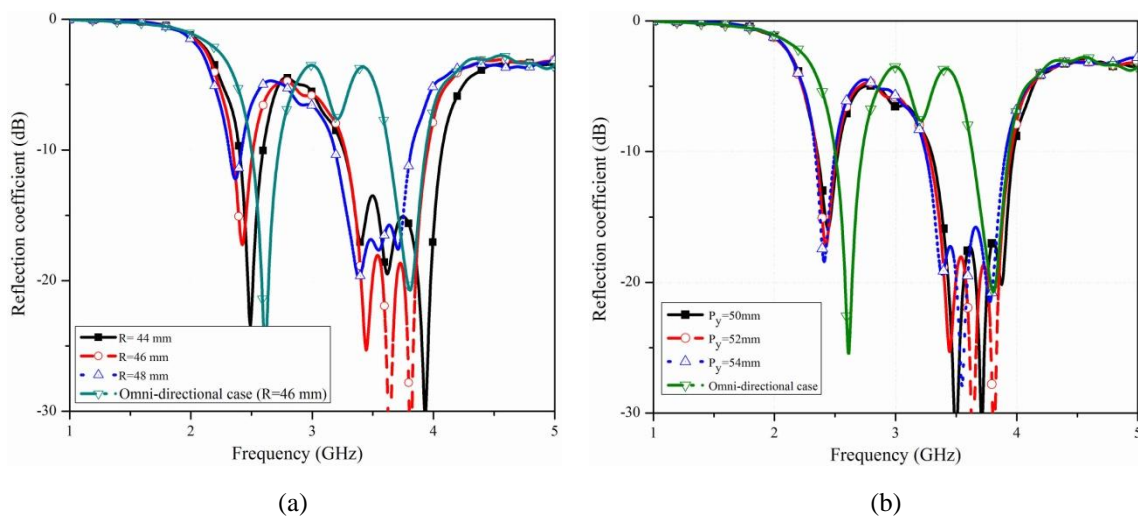
5.4.2 Antenna configuration and simulation results

A comprehensive parametric study depicted in Fig. 5-10 was performed by CST to calculate final dimensions of the antenna, producing the desired radiation performances.

It was predicted for the semi-cylindrical solid reflector that the radius of the cylinder R is the crucial parameter affecting the antenna radiation performances. The impacts of R and the unit cell periodicity along the cylinder axis are compared for different values in Fig. 5-10. To evaluate the antenna performance when the FSS reflector is completely transparent, the radiation-patterns of the antenna are also compared to the case where all active elements are deactivated.

The simulated reflection coefficient shows that the matching frequency of the antenna is strongly affected by the radius. The return loss bandwidth of the directional radiation-pattern is about 175MHz. The simulated realized gain of the proposed configuration, predicts more than 10dB gain over a bandwidth of 150MHz, which is significantly affected by the radius of the cylinder. This amount of gain was achieved just with one layer of FSS structure, which is very close to the results predicted for an equivalent semi-cylindrical solid reflector. Moreover, it seems that by changing the FSS configurations, it is possible to further reduce the number of active elements for the same performance. Some asymmetry noticed in the E-plane radiation-pattern is mainly due to the required parallel DC-feed lines on the sides of the cylinder that are required to bias the diodes. The antenna half power beam-width and side-lobe level in the E- and H-planes in directional case are $(41.6^\circ, -13.1\text{dB})$ and $(64.4^\circ, -13.2\text{dB})$, respectively. The total antenna radiation efficiency is estimated to be %97 by simulator for this antenna.

In addition, as it would be expected, when all the diodes are deactivated, these DC-feed lines degrade the H-plane radiation-pattern as well. Therefore, this leads to not be a completely omni-directional pattern. Furthermore, the return loss diagram is substantially affected for omni-directional case, which is mainly due to the coupling effect of the cylindrical FSS texture on the dipole antenna. Tab. 5-2 shows the summary of antenna radiation parameters, compared to the measurement results.



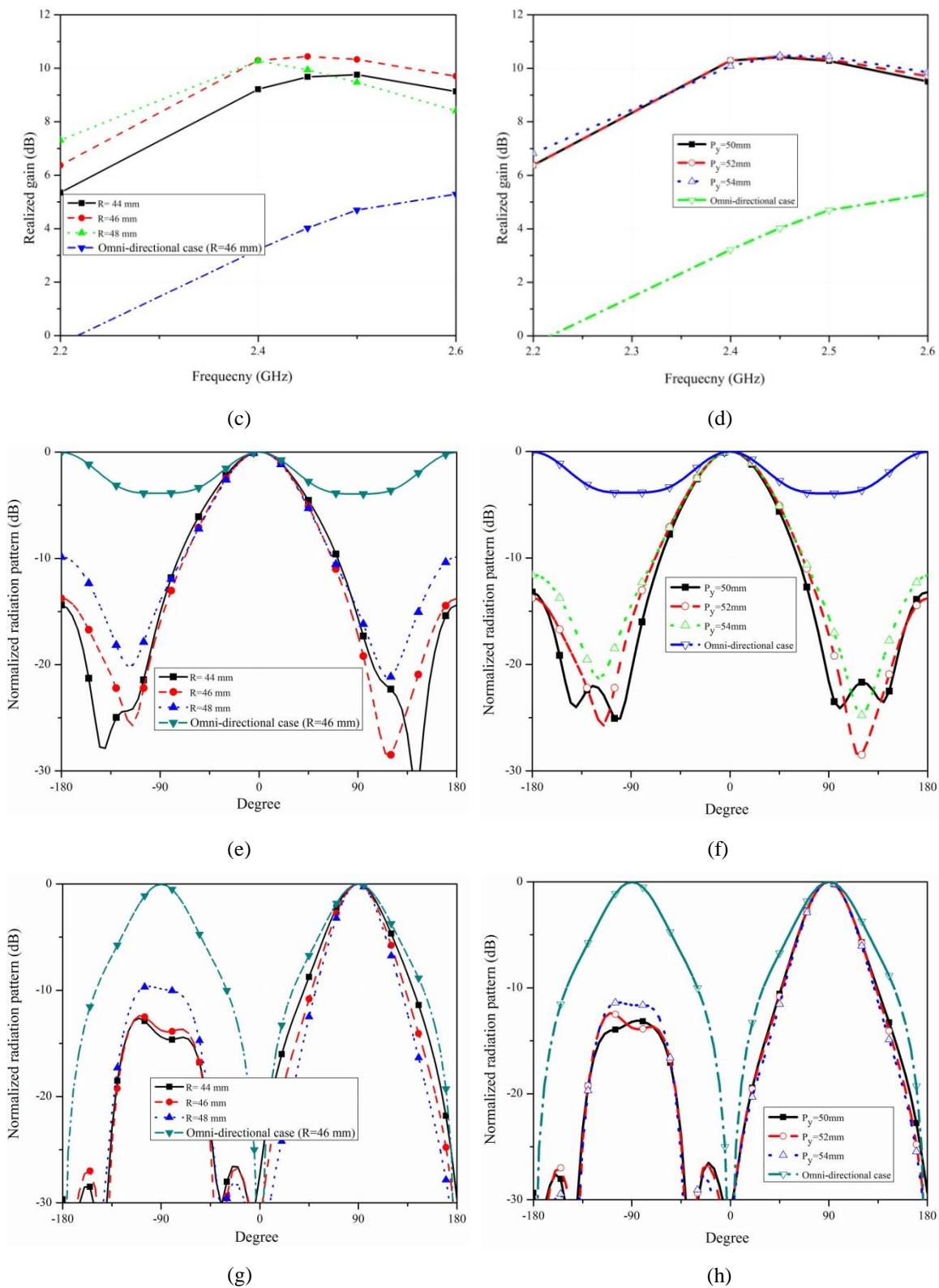


Fig. 5-10 Parametric study of antenna shown in Fig. 4-7 performed for various R values. (a and b) Reflection coefficient for various R and P_y . (c and d) Gain for various R and P_y . (e and f) Normalized H-plane radiation-pattern for various R and P_y . (g and h) Normalized E-plane radiation-pattern for various R

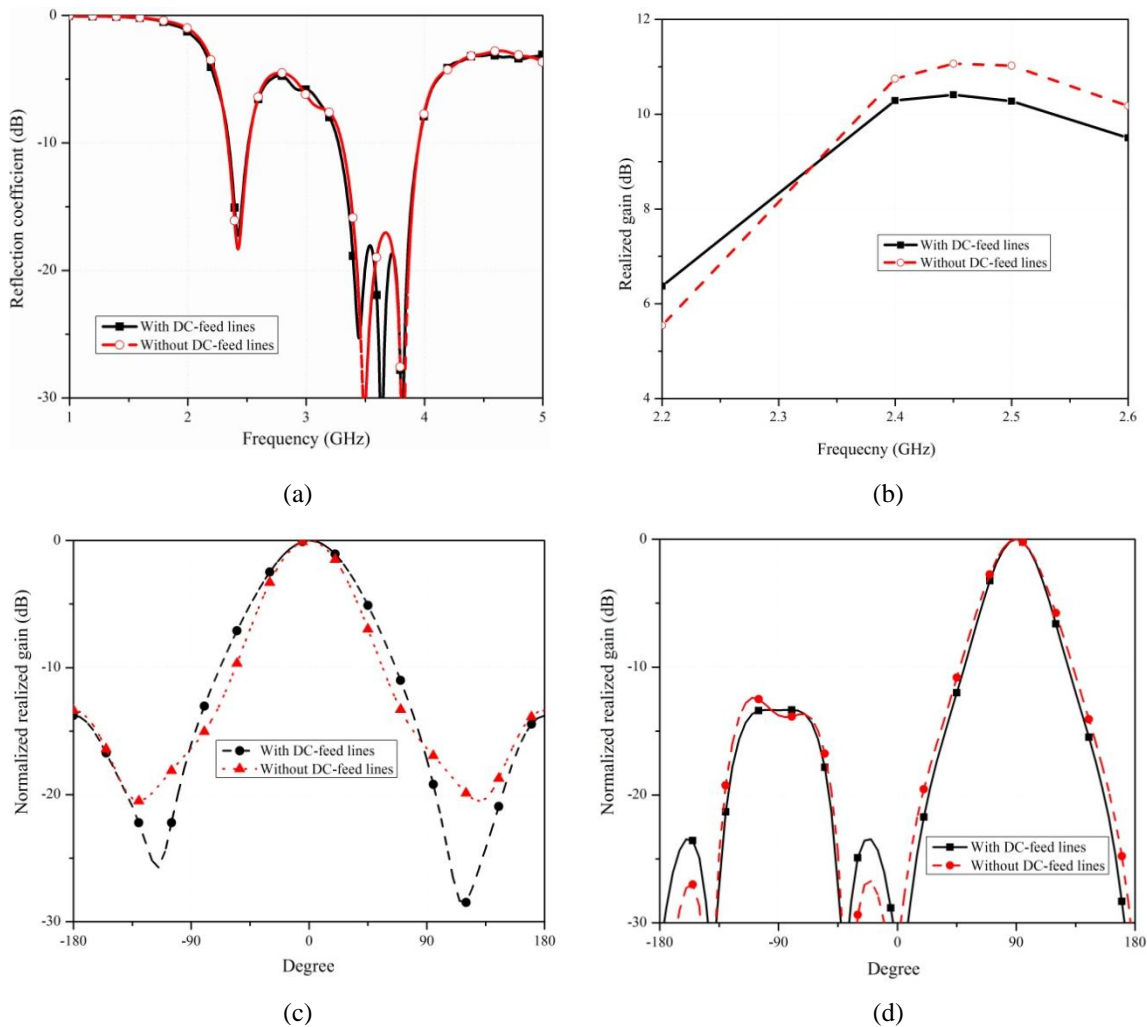


Fig. 5-11 Comparison of antenna radiation characteristics for the cases with and without parallel DC-feeding lines. (a) Reflection coefficient. (b) Gain. (c) H-plane radiation-pattern. (d) E-plane radiation-pattern.

5.4.3 DC-Feeding lines effect

As it is demonstrated in Fig. 5-10, the parallel DC-feed lines along the cylinder sides deteriorated the antenna performances when antenna radiation-pattern is reconfigured from directive case to omni-directional one. In this part, the effect of these feed lines on the directive radiation-pattern is also investigated. Fig. 5-11 shows the antenna parameters compared to the cylindrical FSS without these parallel feeds. As it can be noticed, these feeds do not have any effect on the reflection coefficient and the E-plane radiation-pattern. However, those do affect the H-plane pattern and antenna gain. The calculated realized gain of the antenna without DC-feed lines is 11.1dB. Therefore, these feed lines cause about 0.6dB reduction in gain and broadening the half power H-plane beam-width. In addition, these curves show that they do not noticeably change the side-

lobe level in the principal planes. The antenna half-power beam-width and side-lobe level in the E- and H-planes in this case are (38° , -13.3dB) and (57° , -13.4dB), respectively.

5.4.4 Measurement results and discussion

Fig. 5-12 shows a photo of the fabricated switched-beam reconfigurable antenna prototype based on the dimensions provided in Tab. 5-1. A simple dipole antenna is used as an excitation element. This dipole is fabricated by soldering two pieces of a rolled thin copper sheet directly to an RF-SMA connector. High frequency PIN-diodes biased with DC-feed network are connected to the FSS grid using RF-Chock inductors. RF-chocks separate the biasing feed network from the FSS screen over the desired antenna bandwidth. Ridged foam is used as a stand to fix the dipole antenna in the middle of the cylinder.



Fig. 5-12 Photo of fabricated switched-beam reconfigurable antenna.

To examine the performances of the proposed design, firstly the return losses of antenna was measured. Then, some measurements were performed for the directive H-plane radiation-pattern of antenna at different frequencies to find the best radiation-pattern in terms of desired main beam, realized gain, side-lobe and back lobe levels. Finally, other patterns were measured to evaluate the radiation performances in the other plane as well as omni-directional case. Fig. 5-13 shows the measured results of the switched-beam compared to the ones measured for the applied dipole resonator. As it can be noticed, the wideband dipole is efficiently working above 2.6GHz; but when it is placed at the center of the cylindrical FSS, it operates effectively around 2.45GHz. The

measured return loss for this structure demonstrates better matching compared to the simulation. In addition, deactivating the diodes leads to a little shift in the return loss curve, which has been predicted by simulations. Its E- and H-plane radiation-patterns at the frequency 3.2GHz are compared to the ones related to the reconfigurable antenna. Some asymmetry is noticed in the E- and H-planes of the dipole antenna, which is mainly because of the RF-cable and the SMA connector used in the antenna implementation.

However, its H-plane pattern is uniformly radiating over all angles. The measured E- and H-plane radiation-patterns demonstrate the best performance at the frequency 2.45GHz, which confirms the integrity of the proposed concept. It is clear that the proposed configuration can provide a directional radiation-pattern with back-lobe level better than -17dB and -14dB for H- and E-plane patterns, respectively. Because of scattering from the aperture edge, this level is a little degrading at the other angles in the back plane. As it would be expected, the parallel DC-feed lines in the sides affect the H-plane pattern when all diodes are off.

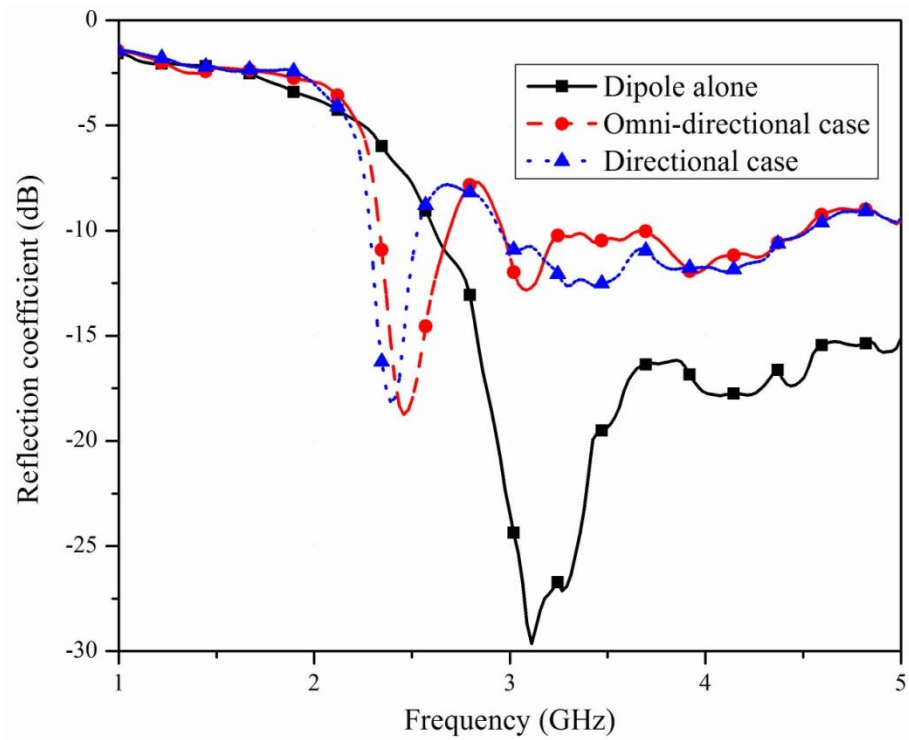
The gain of antenna was measured using the gain measurement comparison-method. It can be calculated from expression (5-3), in which P_{AUT} is the received power by the antenna under test. P_{STD} and G_{STD} are also the received power and gain of the standard horn antenna.

$$G_{AUT} = G_{STD} + P_{AUT} - P_{STD} \quad (\text{All units are in dB}) \quad (5-3)$$

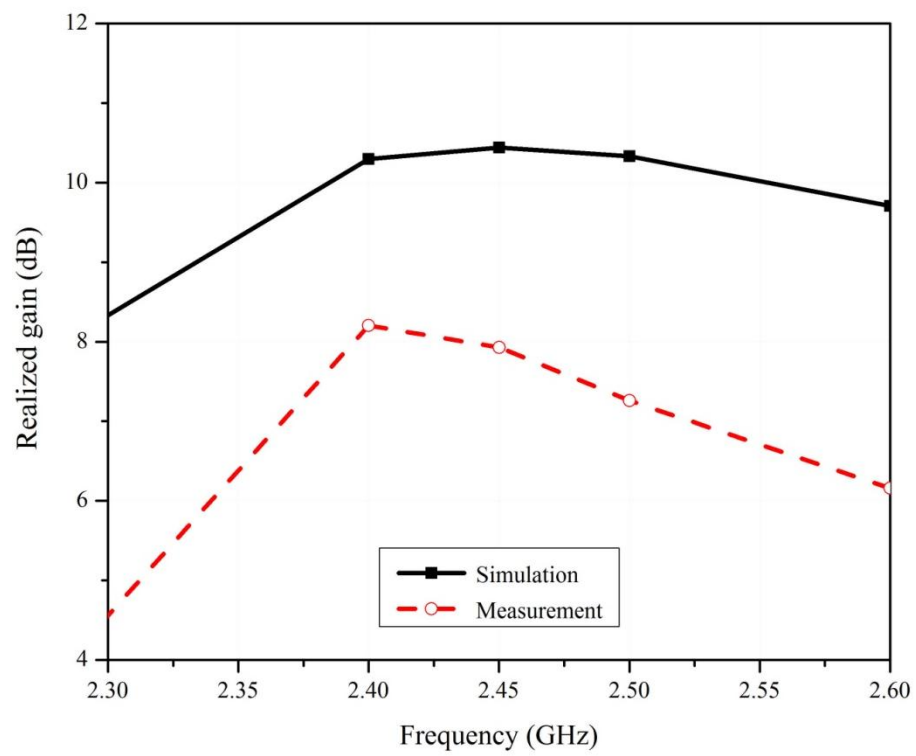
Fig. 5-13b shows the measured gains for the antenna at different frequencies. From this figure, it can be noticed that the antenna is able to offer a directive radiation-pattern with more than 8dB gain close to the desired operating frequency. The difference between simulation and measurement is believed because of the design and measurement inaccuracy. The achieved characteristics for this antenna are compared to the simulation results of the relevant semi-cylindrical solid reflector antenna in Tab. 5-2.

Tab. 5-2 Radiation characteristics of switched-beam antenna.

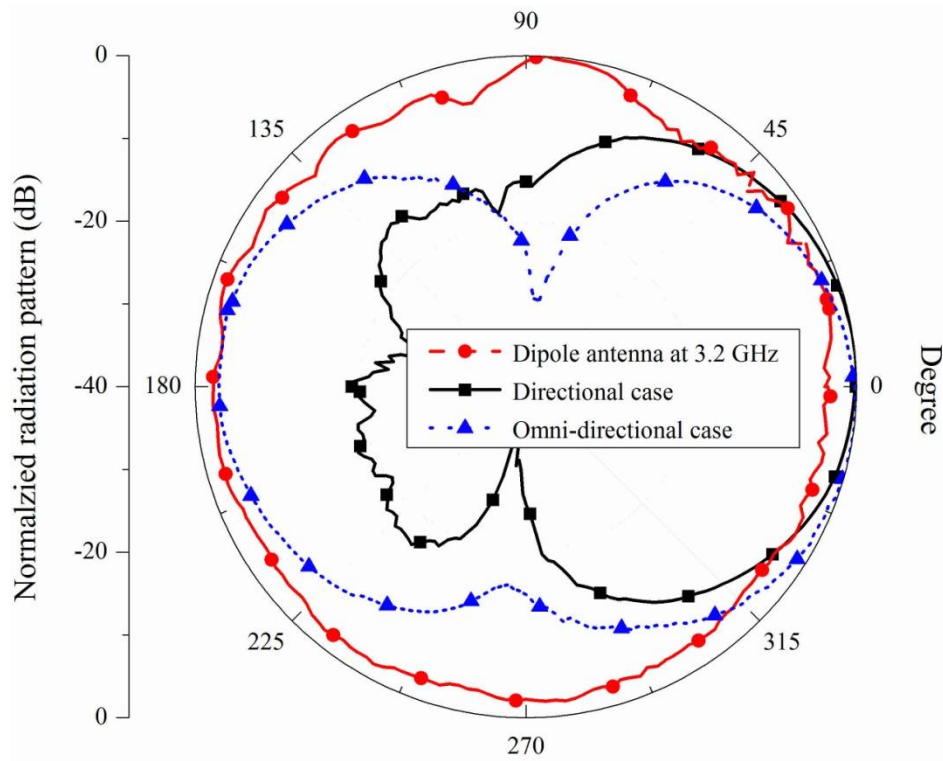
	Switched-beam antenna				Semi-cylindrical solid reflector	
	Simulation		Measurement		Simulation	
BW (MHz)	Omni	Dir.	Omni	Dir.	Directional beam	
	230	175	375	250	1250	
BL (dB)	-13.64		-17		-25.5	
HPBW (Deg.)	H	E	H	E	H	E
	68	43	75	45	70	46
Gain (dB)	10.2		7.5		10	



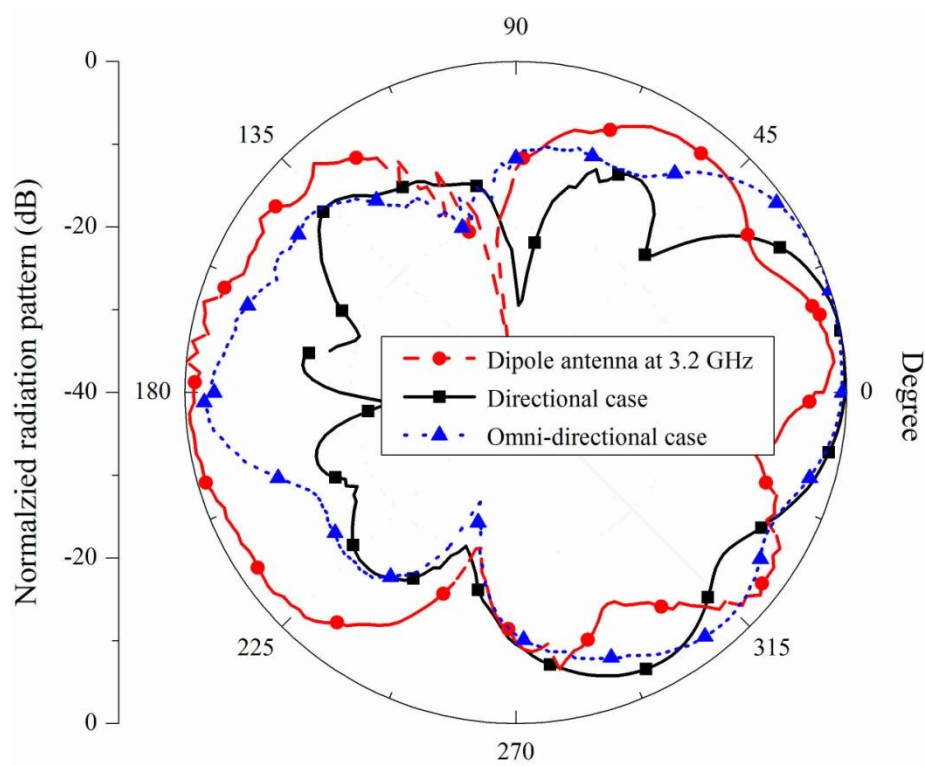
(a)



(b)



(c)



(d)

Fig. 5-13 Measured and simulated results for switched-beam reconfigurable antenna (a) Reflection coefficient. (b) Realized gain. (c) H-plane radiation-pattern. (d) E-plane radiation-pattern.

5.5 Nimble radiation-pattern antenna

In Section-5. 4, the proposed reconfigurable antenna was not able to sweep its radiation-pattern in all azimuth angles. The applied reconfiguration mechanism and required DC-feeding lines limited the space coverage to two switched-beam pattern oriented in opposite directions. Moreover, due to the presence of these feed lines, the antenna pattern was also noticeably deviated in omni-directional case.

In this section, an innovated antenna is addressed, overcoming the above mentioned constraints of the switched-beam reconfigurable antenna. Using this new antenna, the feed network constraints are alleviated, and hence more functionality is offered by the radiator. Indeed, in this case, not only the antenna can sweep the beam over the whole azimuth plane as an agile structure, but also can reconfigure its radiation-pattern from a directional to omni-directional as well. Because of introducing this original performance, i. e., agility to sweep all azimuth angles and reconfiguration from directive pattern to omni-directive one, this antenna was named as “Nimble-Radiation-Pattern” [91].

Fig. 5-14 depicts the proposed nimble antenna and the relevant distributed cylindrical FSS screen. Similarly, this antenna is constructed by a simple dipole antenna surrounded by a reconfigurable cylindrical surface. The radiation principle of this antenna is based on the radiation mechanism described in Fig. 5-1. Accordingly, the same number of unit cells along the cylinder circumference is chosen. However, the reconfiguration method for this case is realized by changing the semi-cylindrical FSS screen from inductive to capacitive case. It means that, by deactivating the active elements in the half part of the cylinder, a reflector is created. At the same time, all switches in the other part are activated to let the waves pass through the surface. Therefore, by sequentially biasing/deactivating a cluster of five columns around the cylinder, the radiation-pattern of the antenna can easily sweep entire azimuth angles in 10 steps. In the following subsections the antenna structure is introduced and its radiation mechanism and achieved results are presented and discussed.

5.5.1 Unit cell configuration and reconfiguration mechanism

The basic reconfiguration mechanism of this antenna stems from changing an inductive surface to capacitive one by using a simple unit cell shown in Fig. 5-15. As it was explained in Chapter-4, by switching the state of high frequency switch integrated into this unit cell, a reconfigurable partially transparent/reflective screen can be achieved. The capacitive screen for the off case is modeled with a resonant LC circuit. On the other hand, an inductance represents the equivalent transmission line circuit of the surface for the on case. With regard to the calculated transmission coefficient response of the unit

cell in Fig. 5-16, two dual reconfigurable operating regions are achieved by this reconfiguration mechanism. In the first region, ranging from low frequencies to around 1.5GHz, a reconfigurable transparent/opaque surface is obtained. This region has been used to create an agile beam EBG antenna by cascading a few layers of this FSS screen [90]. Alternatively, followed by the first reconfigurable frequency regime, a duality is introduced by appearance of the resonant stop-band of capacitive screen.

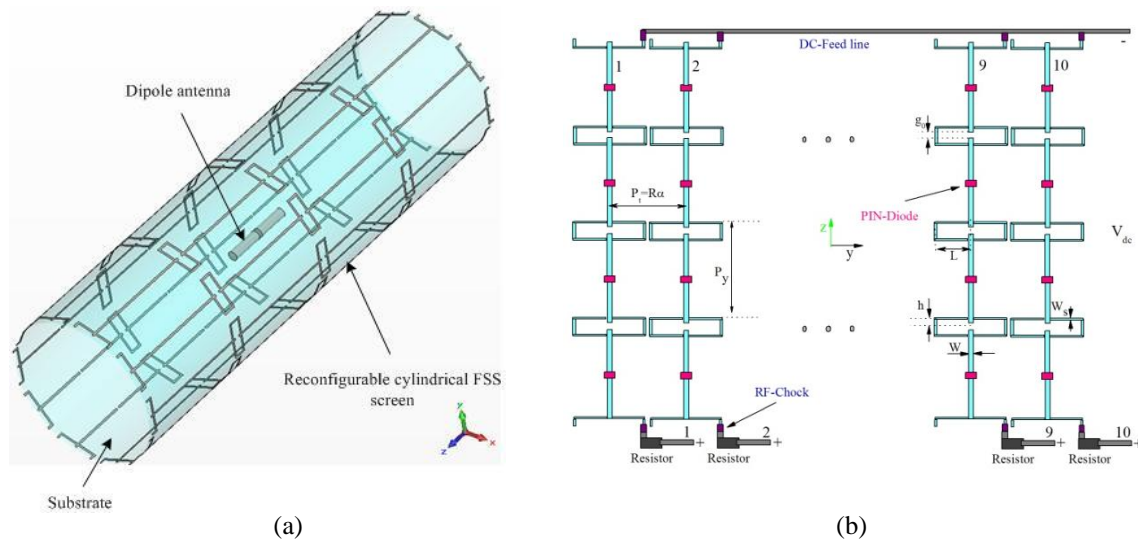


Fig. 5-14 Nimble radiation-pattern antenna. (a) Antenna configuration. (b) Distributed configuration of applied cylindrical FSS screen.

The primary simulation results for a cylindrical reflector created by the simple unit cell shown in this figure demonstrated its potential to create a versatile antenna, overcoming the demerits of designed switched-beam antenna [92]. Therefore, this unit cell is modified to increase the number of parameters in the unit cell controlling its transmission/reflection performance.

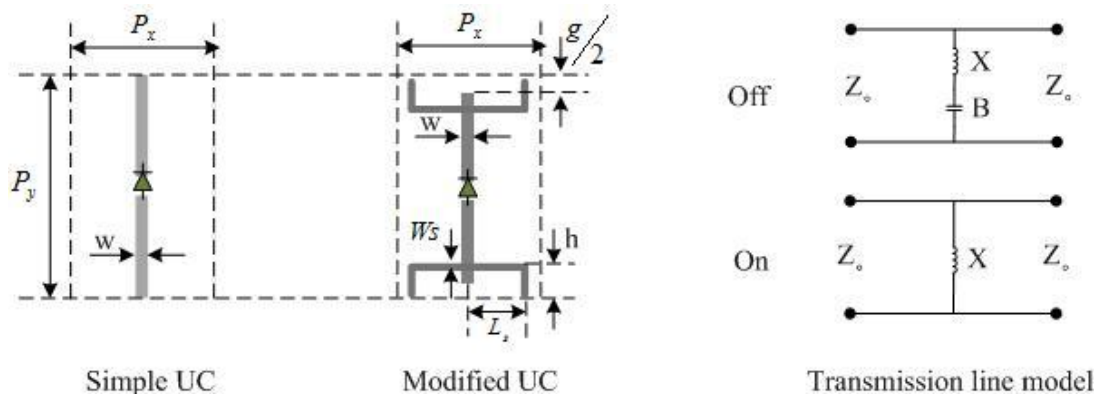


Fig. 5-15 Simple and modified unit cell configurations FSS screen used in nimble radiation-pattern antenna.

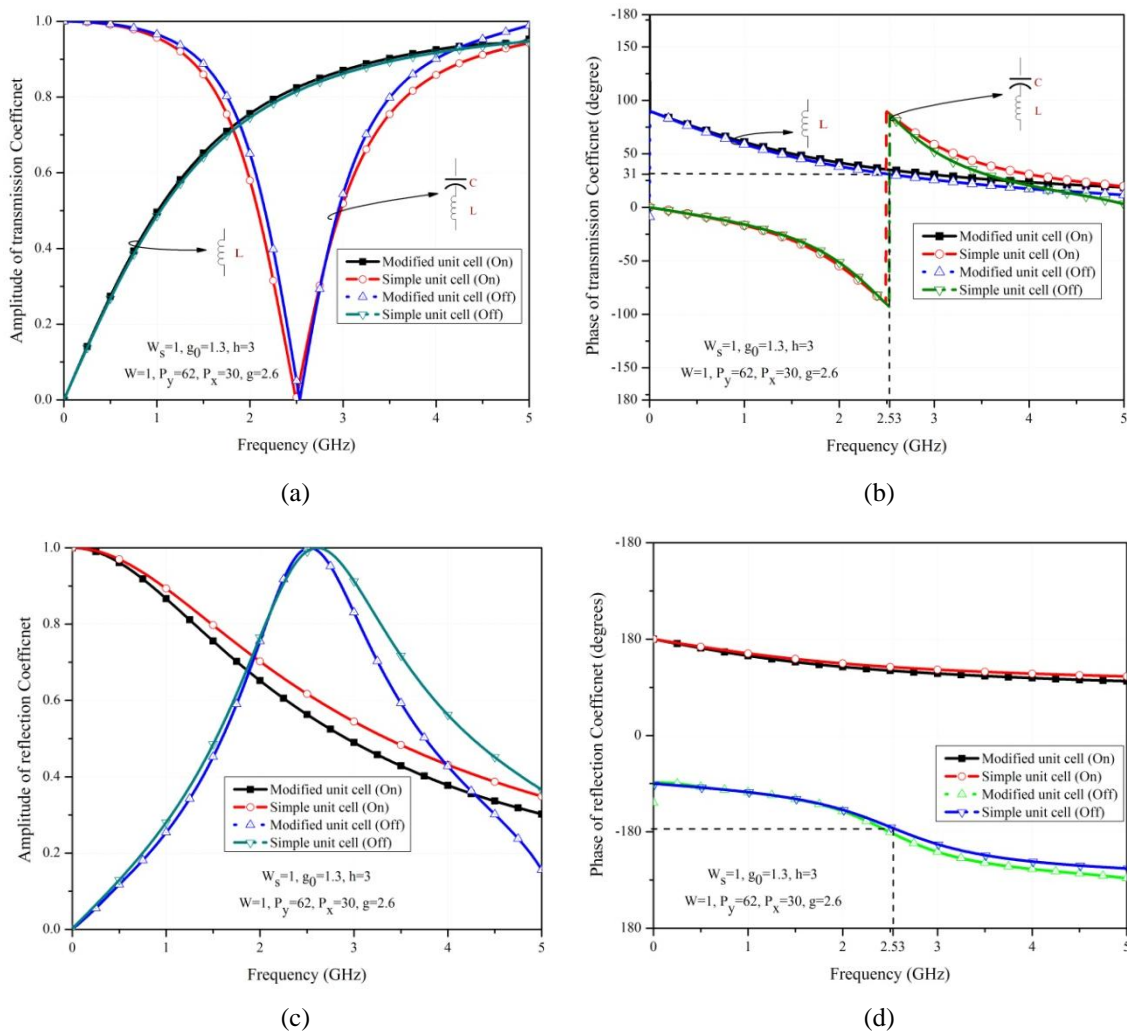


Fig. 5-16 Scattering parameters of simple and modified unit cells. (a) Amplitude of transmission coefficient. (b) Phase of transmission coefficient. (c) Amplitude of reflection coefficient. (d) Phase of reflection coefficient.

As shown in Fig. 5-17, by changing the stub dimensions added to the simple unit cell, its scattering parameters can be tuned without changing the unit cell dimensions. It will be demonstrated that this helps designer to control at somehow the antenna radiation performances.

From the amplitude and phase of the simulated reflection/transmission coefficients of the simple and modified unit cells shown in Fig. 5-16, it can be observed that the reflection phases of both unit cells in the off state are close to the desired $\varphi_G = -1.1\pi$, mimicking a perfect electric conductor response. The transmission phase of the transparent surface in the on state is about $\varphi_T = 0.3\pi$. Inserting these values in equation (5-2) gives a radius of $R = 0.3\lambda$ to achieve a directive radiation-pattern in front of the

cylinder. Therefore, the design guidelines described in Section 5. 2 holds true for this cylindrical FSS screen as well.

5. 5. 2 Antenna radiation performances and the effect of modified unit cell

Fig. 5-14 shows the proposed antenna geometry and distributed configuration of its cylindrical FSS screen. With regard to the calculated reflection phase for a unit cell of this FSS, $N_x = 10$ and $N_y = 4$ are chosen for a cylinder with a radius of about $R=0.3\lambda$. Then, a comprehensive parametric study was performed to optimize the antenna performance in terms of desired bandwidth, gain, and side/back lobe levels. The final antenna dimensions are summarized in Tab. 5-3.

In general, the cylinder radius R is the main parameter, which affects all antenna radiation characteristics. Therefore, the appropriate value for R is firstly determined and then other sizes are tuned. Stub dimensions also are used as extra parameters to control the radiation-pattern of the antenna. In this section, some parametric results performed for the crucial parameters are presented and discussed.

Fig. 5-17 and Fig. 5-18 show parametric studies carried out for R and L_s in terms of matching, gain and radiation-pattern. In Fig. 5-17 the results are compared with omni-directional case. These are obtained when the entire cylindrical FSS surface is transparent for the dipole radiator. From this figure, it is clear that the radius is the main parameter that controls all the antenna characteristics. As an interesting point in this antenna, the desired radiation-pattern is realized for a radius $R=39\text{mm}$, which is less than the one calculated for switched-beam antenna (46mm). Indeed, since the transmission phase of transparent part of cylinder is not zero as shown in Fig. 5-16b, this affects the phase of electric fields, and therefore a smaller value of radius is required to achieve a constructive radiation-pattern.

The return loss bandwidth predicted by the simulation is about 100MHz for directive case, while for omni-directional case, it seems that the structure does not have good matching bandwidth around the desired frequency. Because of the coupling effect of the cylindrical FSS, there is still some shift in the diagram for omni-directional radiation-pattern case. In addition, obtained results demonstrate that the proposed nimble configuration ameliorates the radiation-pattern degradation provided by DC-feed line of switched-beam antenna, and also when all diodes are on, it provides omni-directional pattern. Moreover, it is able to create an agile radiation beam covering all azimuth angles by selecting 5 columns of 10 at each time. This leads to sweep 360° azimuth area in 10 steps.

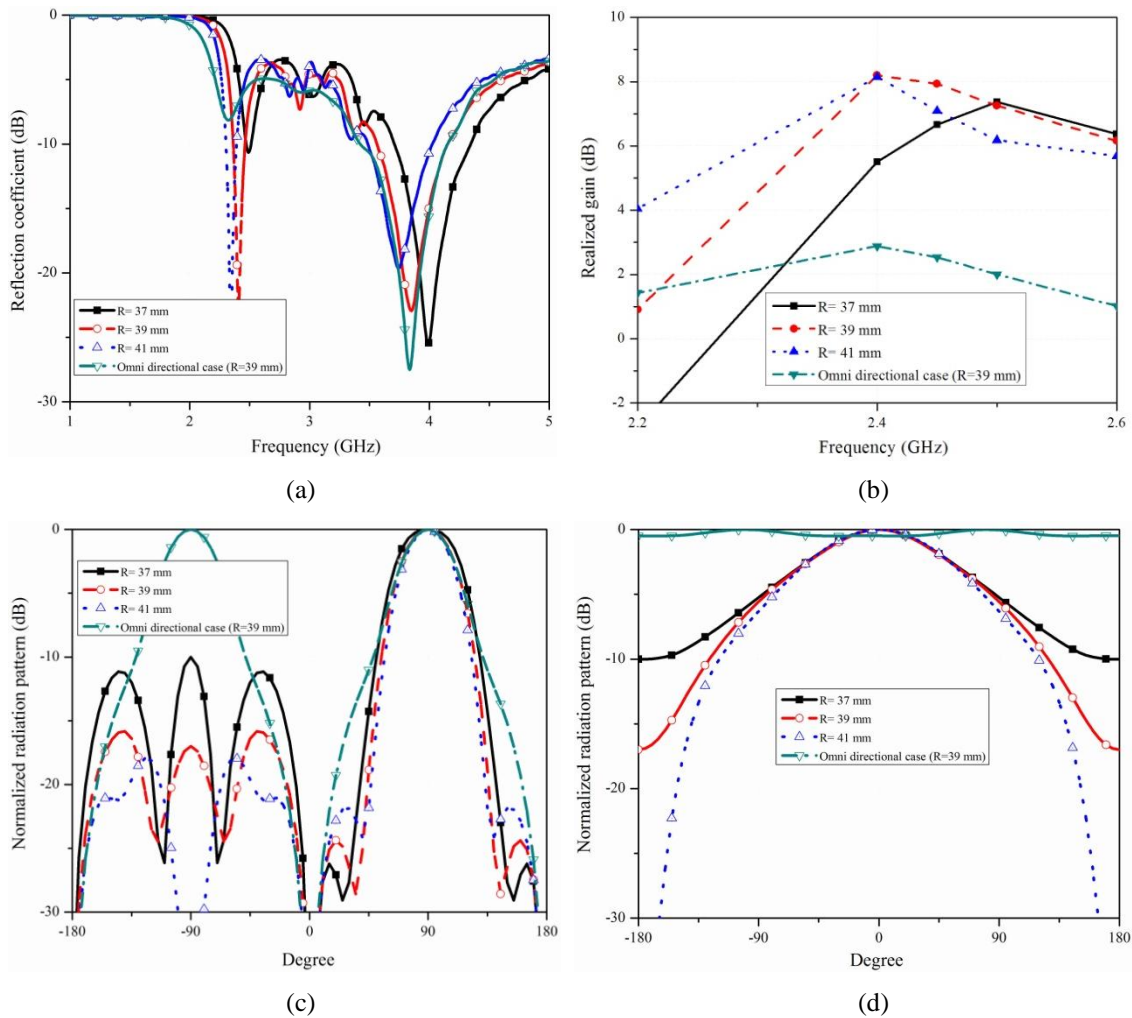


Fig. 5-17 Antenna radiation characteristics performed for various R values. (a) Reflection coefficient. (b) Realized gain. (c) E-plane radiation-pattern. (d) H-plane radiation-pattern.

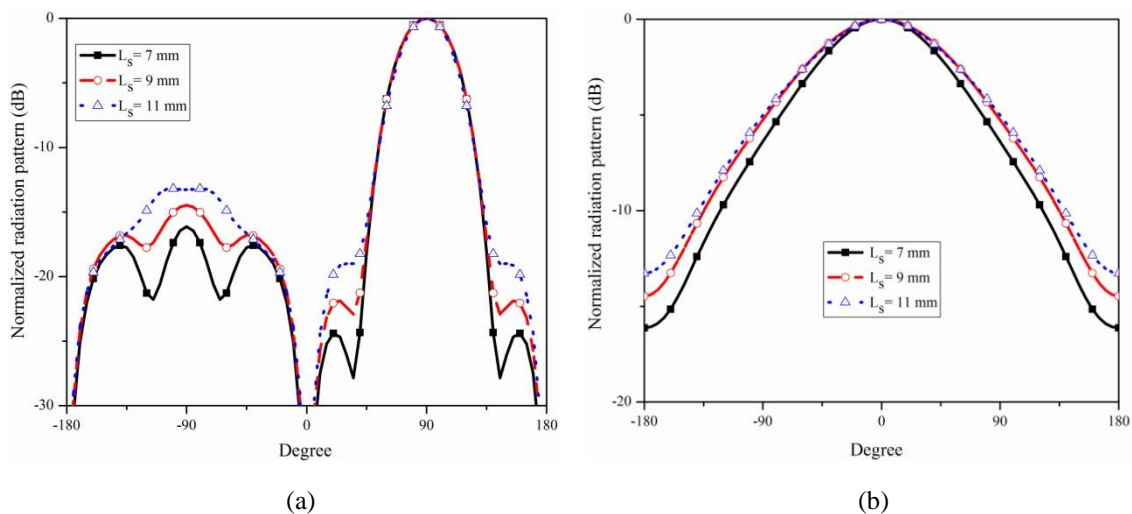


Fig. 5-18 Antenna radiation characteristics performed for various L_s values. (a) E-plane radiation-pattern. (b) H-plane radiation-pattern.

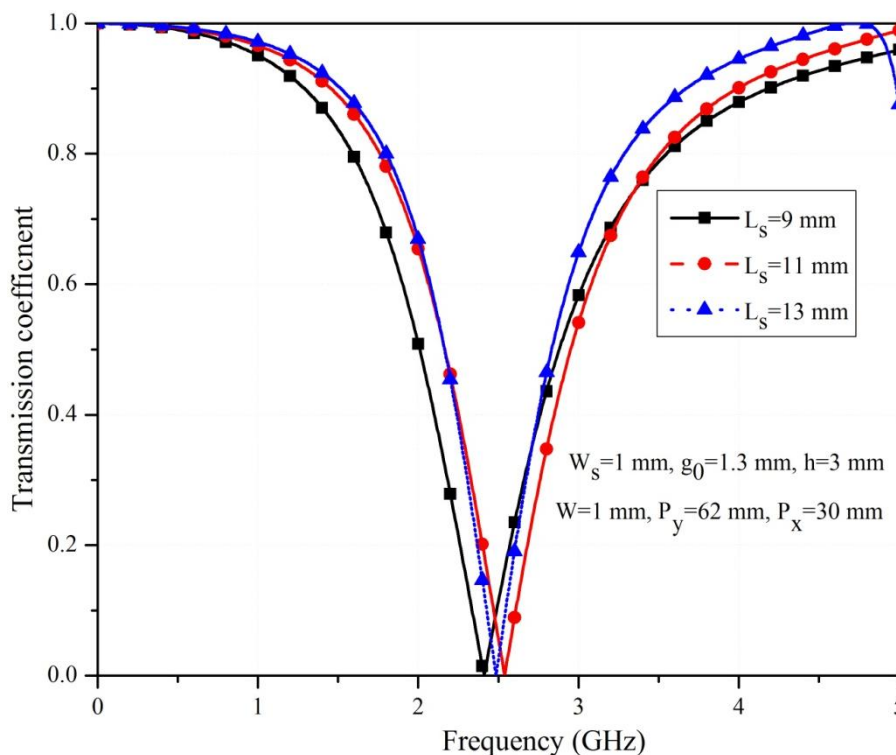


Fig. 5-19 Parametric study performed for different stub length showing its effect on the stop-band performance.

Tab. 5-3 Final dimensions of nimble radiation-pattern antenna. All dimensions are in mm.

Parameters	R	P_y	g_0	g	L_d	r_d	W	W_s	L_s	h
Value	39	66	2.6	1.3	37	2.5	2	1	9	3

Mainly because of smaller cylinder radius and the gap g , the gain of this antenna is smaller than the switched-beam antenna, and it is expected to be around 8dB. Total antenna radiation efficiency of about 94% is predicted for this antenna by simulation.

To demonstrate the effect of stub in controlling the back/side-lobe level in the E- and H-plane patterns, Fig. 5-18 depicts the influence of most crucial stub size. As it is clear, the stub length can also be used to tune the back lobe and in some extent the main radiation-pattern of the antenna. The final characteristics of antenna are compared to the measurement results in Tab. 5-4.

5.5.3 Measurement results and discussion

An antenna prototype was fabricated based on the final dimensions summarized in Tab. 5-3. Fig. 5-20 shows a photo of the fabricated nimble-beam reconfigurable antenna

prototype. A simple dipole antenna is used again as an excitation element. This dipole is fabricated by soldering two pieces of a rolled thin copper sheet directly to an RF-SMA connector. RF-chocks shown in the distributed configuration separate the biasing feed network from the FSS screen over the desired antenna bandwidth. To fix the dipole antenna in the middle of the cylinder and also as a stand for the flexible FSS screen, an appropriate frame is elaborated using ridged foam.

In this prototype, to mimic the blocking surface in directional beam operating state, five sequential DC-terminuses of FSS unit cells along the cylinder let to be deactivated, while the other five columns are activated. To sweep the antenna beam, it needs to just sequentially change the order of selected columns along the circumference of the cylinder as numbered in Fig. 4-14b. This provides 10 beam sweeping steps to cover all azimuth angles. On the other hand, to switch to the omni-directional radiation-pattern state, all ten columns of FSS screen are biased to make the screen transparent for the dipole antenna.

The same measurement process carried out for the switched-beam antenna is followed for nimble antenna as well to evaluate its performances. Therefore, the reflection coefficient is firstly measured by network analyzer and then the H-plane radiation-pattern is measured across the achieved matching bandwidth to find the best frequency, offering the most directive radiation-pattern with minimum side/back-lobe level. Because of antenna symmetry, 5 columns of FSS unit cells are randomly chosen as a blocking surface. Fig. 5-21 shows the measured return loss of the nimble-antenna for both operating states. As it can be noticed, the measured result is better than the simulated ones and antenna matches to 50Ω input impedance over a large frequency bandwidth in both directional and omni-directional cases.

The measurements for the directive H-plane radiation-patterns at different frequencies across the achieved bandwidth show that the best radiation-pattern in terms of directivity and side/back lobe level is obtained at the frequency of 2.35GHz for this antenna. As it is obvious in Fig. 5-22, the measurement results well confirm the predicted radiation-pattern at frequency 2.45GHz. This structure provides a back-lobe level better than -20 dB in the H-plane; while in some angles in the E-plane, it is not as good as the one in the H-plane. Moreover, the measured E-plane pattern for omni-directional case shows some undesired radiation in the Z direction. This is due to the fact that the stop-band of discontinuous strips shown in Fig. 5-16a is more close to the blocking regime of continuous strips at low frequencies, which results in reducing the transparency of continuous strips around the operating bandwidth. This causes to capture some RF energy inside the cylinder and hence leakage out from the Z and $-Z$ directions of the cylinder. Therefore, in order to obtain right performance, the stop-band of discontinuous wires should be far enough from the stop-band of the continuous ones.

As it is predicted by the E-plane measurement, because of power leakage in Z directions, some gain reduction would be expected in the radiation-pattern. This can be observed in the measured realized gain of the antenna in Fig. 5-23 performed by gain

comparison method. This is mainly due to the fact that the antenna does not effectively operate according to the expected EM behavior for each part of the FSS screen. This can be alleviated by optimizing the structure according to the achieved experimental results.

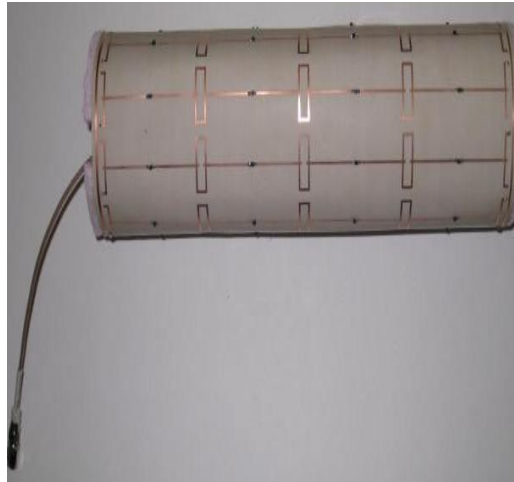


Fig. 5-20 Photo of fabricated nimble beam antenna.

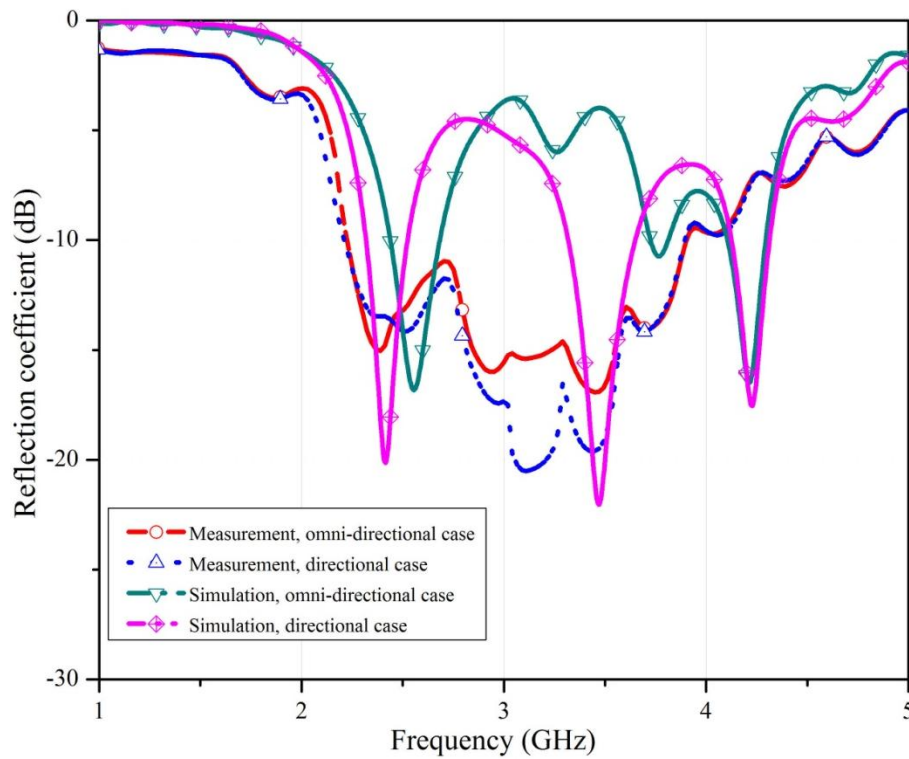
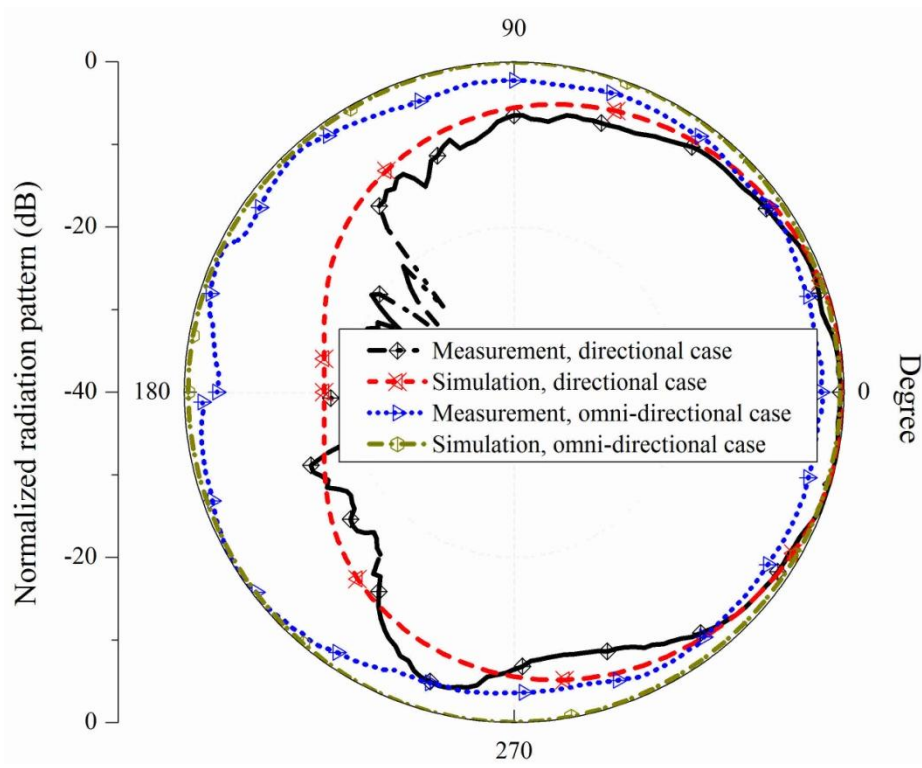
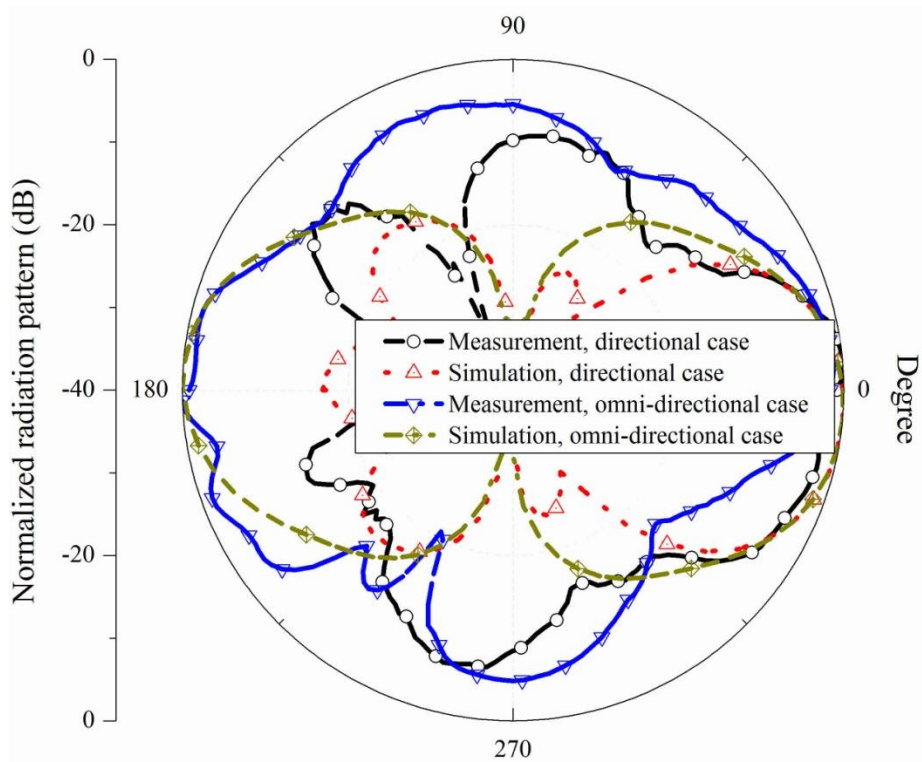


Fig. 5-21 Simulated and measured reflection coefficient for nimble beam antenna.



(a)



(b)

Fig. 5-22 Measured radiation-pattern for nimble beam antenna (a) H-plane radiation-pattern.
(b) E-plane radiation-pattern.

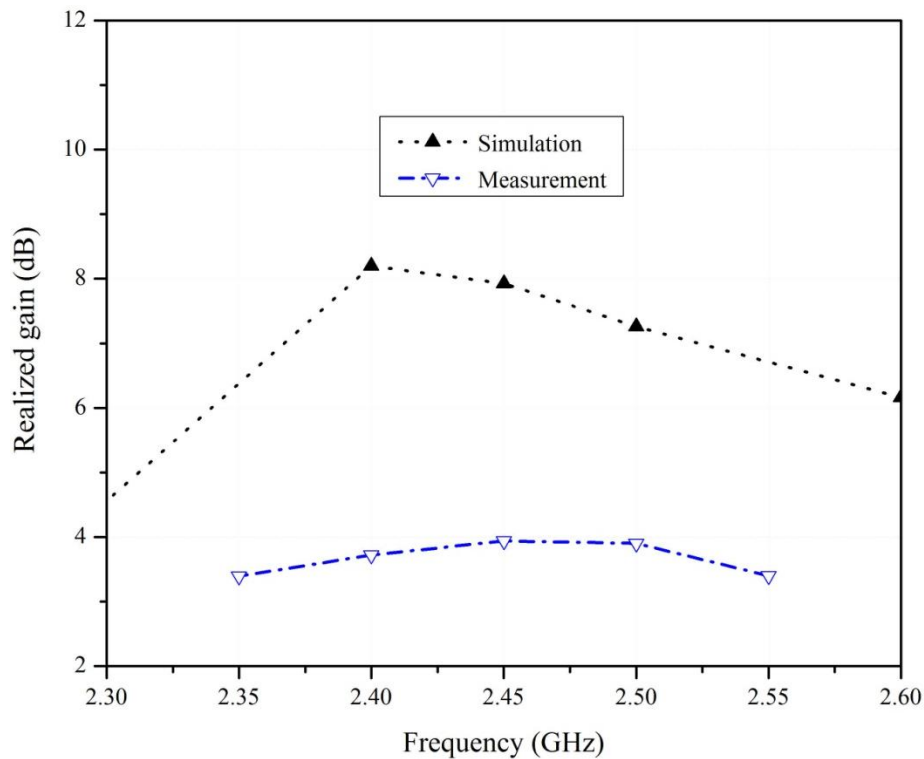


Fig. 5-23 Measured and simulated realized gain of nimble antenna.

Tab. 5-4 Radiation characteristics of Nimble antennas compared to semi-cylindrical reflector.

	Nimble antenna				Semi-cylindrical reflector antenna	
	Simulation		Measurement		Simulation	
BW (MHz)	Omni	Dir.	Omni	Dir.	Directional beam	
	-	102	Wide	Wide	1250	
BL (dB)	-15		-20		-25	
HPBW (Deg.)	H	E	H	E	H	E
	112	42	104°	40	70	46
Gain (dB)	8.2		3.94		10	

5.6 Conclusion

In this chapter, a new cylindrical radiation mechanism has been proposed to create a class of reconfigurable antennas, offering switching and scanning beam features with gain reconfiguration ability. The initial values of the antenna dimensions have been designed in two main steps. Firstly, the overall sizes of the antenna have been determined by principles of reflector antennas. Then, an appropriate FSS screen has been proposed to

mimic the related semi-cylindrical reflective/transparent screens for switched or scanning beam applications. The transmission/reflection phase and amplitude of the FSS surface in both transparent and reflection states have been considered to calculate the required radius for the cylindrical FSS sheet. Finally, CST Microwave studio is used to optimize the antenna. In summary, the design guideline steps can be itemized as followed:

1. The radius of the reflector is chosen in the range of 0.25λ - 0.4λ according to the phase relation achieved by the electric field interactions in front of the reflector, i. e. expression (5-2). It is shown that the required cylinder radius is larger for transparent capacitive surfaces than the inductive one.
2. Reflector length is selected to be greater than a wave length, fulfilling the desired side-lobe level in E-plane
3. Number of active elements along the length and circumference of the cylinder is calculated according to the unit cell periodicities by $N_y = L/P_y$ and $N_x = 2 \times \pi R/P_x$, respectively.
4. The dipole radius is chosen to create minimum 10% bandwidth at its resonant frequency.
5. The length of the dipole is chosen about 0.32λ at the desired operating frequency 2.45GHz.

According to the DC-feeding method of active elements two FSS screens were investigated. It has been proved that the effect of DC-feed lines must be considered in designing FSS sheets even when they are perpendicular to the incident electric fields. In addition, the effect of PIN-diode parasitic elements has been investigated, and it has been proved that they must be compensated to achieve the desired transparency/reflectivity level. It has also been shown that the adverse effects of DC-feed line and diode parasitic elements limit the operating range of the reconfigurable transparent/reflective FSS screens by shifting the stop-band of activated FSS screen toward the stop-band of deactivated one. Indeed, the required transparency level is deteriorated.

Finally, it has been shown that by appropriately choosing the reconfiguration mechanism and compensating the DC-feed line and parasitic elements effects, a multi-function antenna can be realized. Gain reconfiguration and sweeping beam over all azimuth angles are the interesting parameters that can be offered by the proposed cylindrical reconfigurable antenna mechanism. Moreover, the type of FSS pattern directly affects the antenna directivity by determining the required cylinder radius in the co-phase equation extracted from wave interaction passing through the transparent FSS screen in (4-4). In this respective, for the transparent capacitive FSS screen, the antenna has a larger gain than the case in which the transparent part is inductive FSS sheet.

Chapter 6

Agile frequency nimble antenna

6.1 Agile frequency nimble radiation-pattern antenna

In Chapter-5, a nimble radiation-pattern antenna was proposed, that was creating either agile sweeping beam or reconfigurable directional to omni-directional radiation-pattern features. However, because of adverse effect of PIN-diode parasitic elements, the transmission and reflection responses of both semi-cylindrical parts of FSS screen are deteriorated. This causes some degradation in the antenna radiation performances and also limits the designing range of frequency.

In this chapter, a new reconfigurable FSS screen is proposed to alleviate in some extent the above mentioned limitations of other proposed FSS screens. This reconfigurable FSS sheet is constructed by an array of hybrid elements [87]. Each element includes integrated discontinuous strips and elliptical ring. Indeed, by creating two stop-bands close to each other, the transparency level of the surface for the on state is considerably improved. In addition, the possibility of two dual responses at two different frequency bands is also analytically and experimentally investigated. Then, this surface is reformed to a cylindrical shape to implement another nimble radiation-pattern antenna [99]. As a bonus, it has also experimentally demonstrated that the new antenna is able to operate at two different frequency bands with almost the same functionalities. Moreover, the number of active elements has been reduced in this antenna by reducing the antenna size,

while keeping almost the same directivity. In the following sections, the design process and achieved results are presented and discussed.

6.1.1 Hybrid reconfigurable FSS screen design

Fig. 6-1 shows the geometry of the proposed reconfigurable dual-band FSS screen. It is constructed of periodic arrays of a hybrid resonant unit cell. This unit cell is created by combining two elements, including discontinuous strips and an elliptical ring. To reconfigure the transmission response of the surface, a high frequency PIN-diode is used across the discontinuity along the strip. By changing the state of the switch, dual transmission responses can be obtained over two narrow frequency regimes next to each other. This can be used as a partial reflector to design a reconfigurable cylindrical reflector antenna.

To describe the transmission response of this frequency selective screen, the treatments of its basic resonant elements to the incident vertically polarized electromagnetic waves (TE-incident) are investigated. Fig. 6-2 shows the amplitude and phase of transmission response of active short strips and a discontinuous elliptical ring. As it can be noticed from these curves, the isolated short discontinuous strips create a stop-band centered around frequency 2.2GHz. By activating the PIN-diode, the capacitive surface is changed to an inductive one and hence the resonant stop-band is disappeared. The reconfiguration mechanism and the characterization of this element were completely delineated in the previous chapter.

On the other hand, the isolated discontinuous elliptical ring creates a stop-band around 5.4GHz. This response is similar to a continuous elliptical ring with the same dimensions. Since the current distribution at the ends of ellipse major axis is zero, the discontinuities along the ellipse circumference do not change the unit cell response. These discontinuities provide the required space to combine two resonant elements. Therefore, by integrating these two elements, two stop-band regions can be realized around 2.2GHz and 4.5GHz.

The calculated amplitudes and phases of scattering parameters of this hybrid unit cell have been depicted in Fig. 6-3. These results show that the integration effectively reduces the resonant frequency of the isolated discontinuous elliptical ring without affecting the first stop-band position. Then, by switching the active element on, the first stop-band related to the discontinuous strips is disappeared, and therefore the surface is reconfigured to transparent state around the desired frequency 2.45GHz. In addition, one more frequency regime with dual responses is also obtained next to the first band. In the second band, one response is related to the blocking region of the on state and the other one is created by the transparency region between two stop-bands of the off state. It means that when the surface is transparent in the first band, it will be opaque at the same

time in the second band. Indeed, by this hybrid unit cell, a reconfigurable dual response across two different frequency bands can be realized for antennas or electromagnetic shielding applications [87].

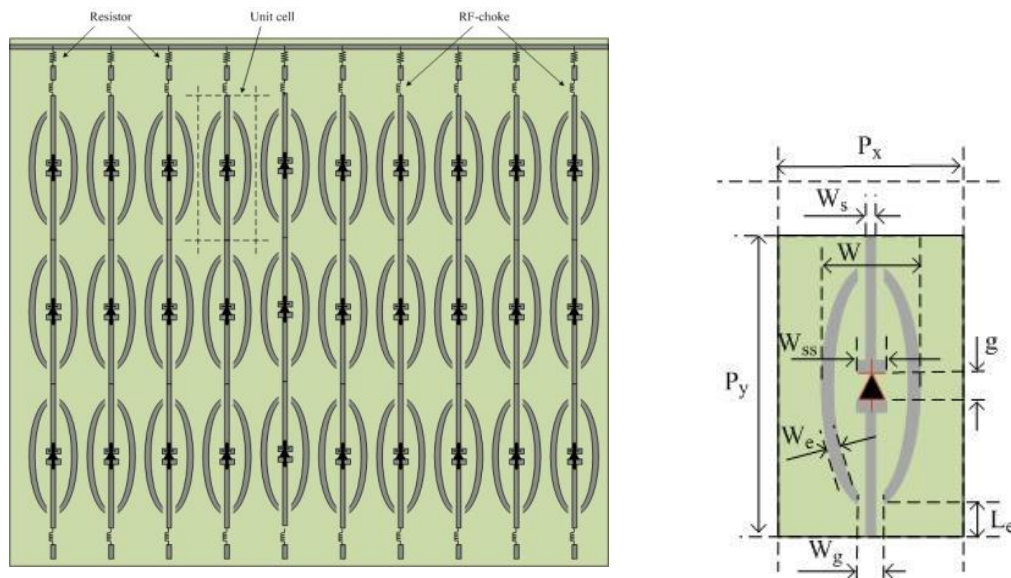


Fig. 6-1 Geometry of dual band reconfigurable FSS screen and transmission line model of its unit cell.

To examine the effect of unit cell parameters in response to the vertically polarized normal incident waves, Fig. 6-4 shows its transmission coefficients for different values of P_y , L_e , and W . These results indicate that the minor and major axes of elliptical ring significantly control the second resonant stop-band at high frequencies in both on and off states. The calculated curves also demonstrate that the periodicity P_y changes the lower and higher stop-band positions. Therefore, to manage the first stop-band performances, it needs to change the dimensions of the discontinuous strips in the FSS screen. In addition, by changing the ellipse sizes, the second reconfigurable regime can be shifted over a large frequency bandwidth. Those can be applied to easily adjust the second reconfigurable frequency band with good transitivity and reflectivity in on and off states. For instance, when the values of $P_y = 40\text{mm}$, $L_e = 10\text{mm}$, and $W = 15\text{mm}$ are selected, dual responses with good transmission and reflection levels are achieved at two bands centered around 2GHz and 3.3GHz. Therefore, this hybrid unit cell provides more design parameters in controlling the scattering parameters across two different reconfigurable operating regions.

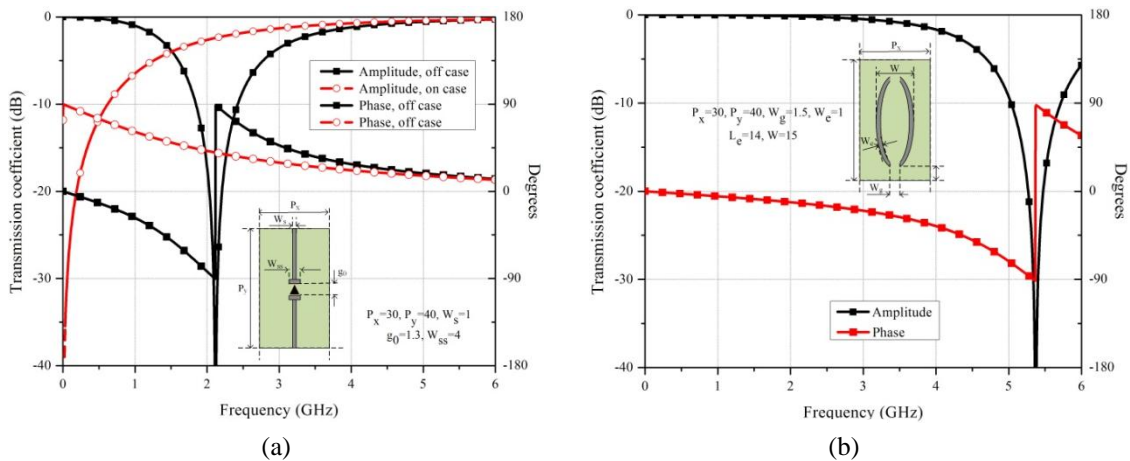


Fig. 6-2 Transmission coefficient response of two basic resonant elements. (a) Discontinuous strips. (b) Discontinuous elliptical rings.

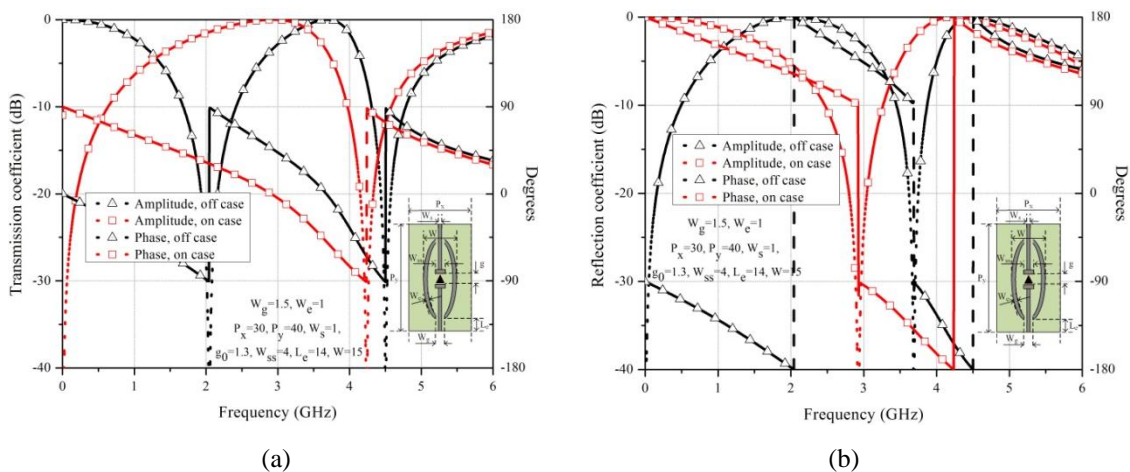
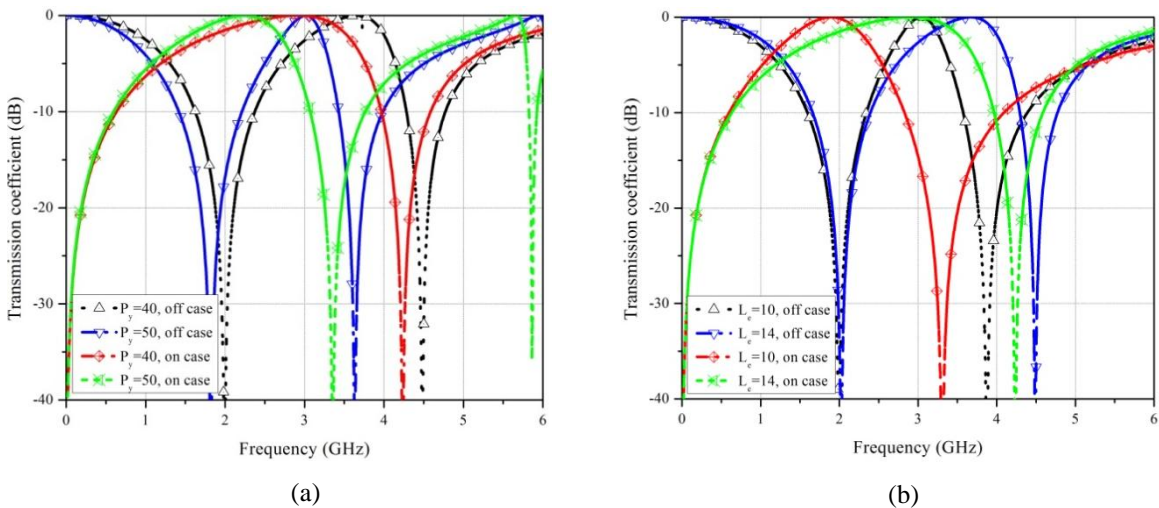


Fig. 6-3 Transmission and reflection coefficient response of hybrid dual band reconfigurable FSS screen (a) Transmission coefficient. (b) Reflection coefficient.



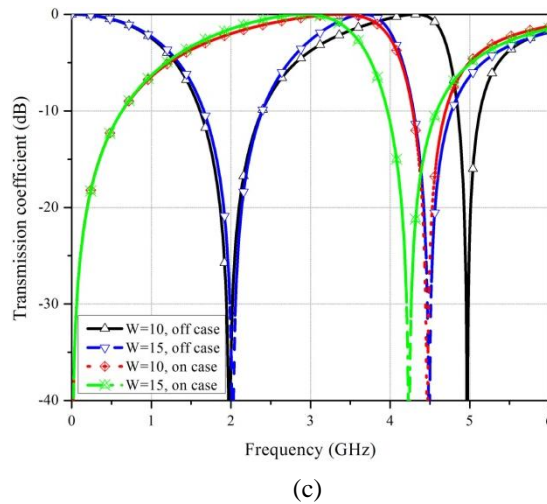


Fig. 6-4 Transmission coefficients of hybrid unit cell for different unit cell sizes. (a) For different values of P_y . (b) For different values of L_e . (c) For different values of W . (All values are in mm).

6.1.2 Antenna design

Fig. 6-5 shows the proposed agile frequency nimble radiation-pattern antenna. This antenna principally is based on the radiation mechanism described in Fig. 5-1. It is constructed of a dipole antenna at the center of a reconfigurable active frequency selective surface. Two pieces of perfect electric conductor are used at the top and bottom of the cylinder to improve the antenna directivity. The reconfigurable partially reflective/transparent surface represented in Fig. 6-1 has been used to create a dual-band nimble antenna. Since the design principle of this antenna is similar to the described nimble antenna in the previous chapter, therefore, both amplitude and phase of scattering parameters of this unit cell must be considered to assess the FSS performance in creating a directive beam.

With regard to the calculated phase responses in Fig. 6-3 for normal incident angle, the reflection phase of the blocking surface and transmission phase of the transparent surface at the desired operating frequency 2.45GHz are $\varphi_R = 160^\circ$ and $\varphi_T = 18^\circ$, respectively. These values are almost close to the desired $\varphi_R = 180^\circ$ and $\varphi_T = 0^\circ$ for ideal reflective and transparent FSS surfaces. In fact, this confirms that the radius calculated for a semi-cylindrical solid reflector antenna can be applied as initial radius value for this FSS reflector as well. However, it needs to be reminded that the calculated scattering parameters are carried out for normal incident to a planar FSS structure, while they are used in a cylindrical form and in a near field of a dipole antenna. Therefore, in the real situation of conformal FSS screen, the phase and amplitude of coefficient parameters might be noticeably changed. Indeed, this dictates a certain number of unit cells on the

cylinder to achieve the desired directive beam. Therefore, the unit cell dimensions need to be tuned in the antenna as well to compensate the curvature effect. Considering the periodicity of the unit cell in the x direction and the calculated radius, the number of unit cells along the cylinder for this antenna is $N_x = 10$. To reduce the number of active elements and antenna size compared to the nimble structure designed in Chapter-5, $N_y = 3$ of unit cells along the cylinder length is considered. In addition, by using this arrangement, all unit cells in the vertical direction provide a close reflection/transmission responses. This leads to a constructive radiation-pattern in front of the reflector. For instance, simulation results show that choosing $N_y = 4$ does not provide a uniform directive radiation-pattern with a low back lobe level.

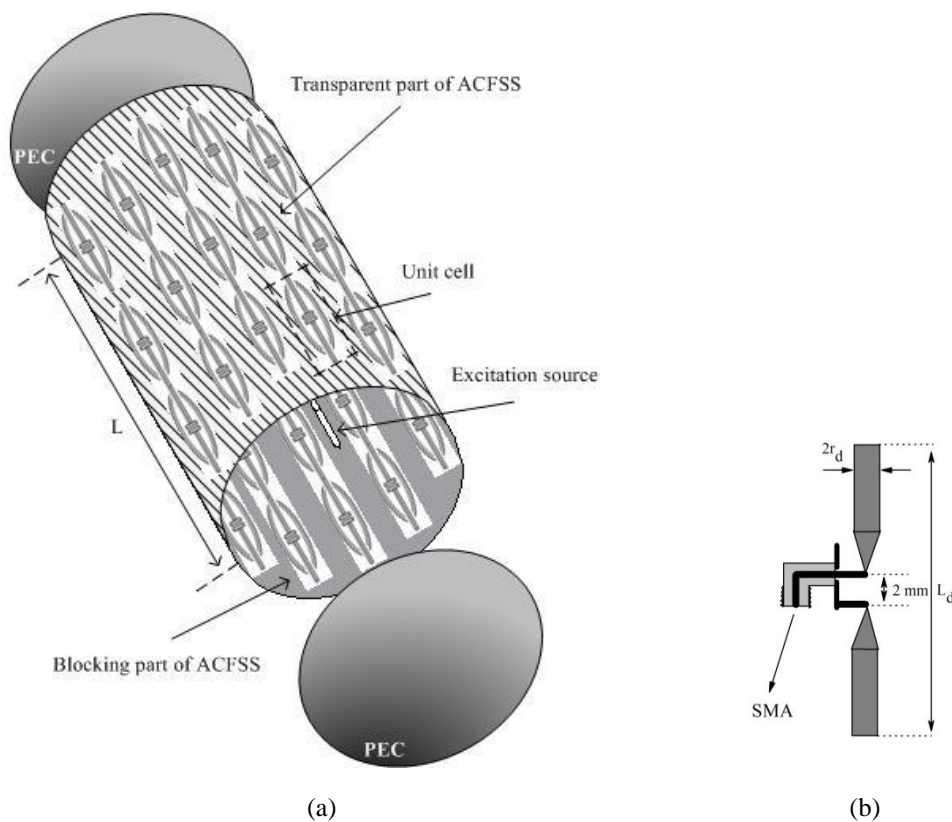


Fig. 6-5 Agile frequency nimble radiation-pattern antenna. (a) Antenna geometry. (b) Excitation source.

Therefore, by having the total numbers of required unit cells on the cylindrical FSS and its initial radius, comprehensive parametric studies were performed by CST on the most crucial sizes to optimize the antenna in terms of desired radiation. To carry out these studies, the radius of the cylinder is firstly adjusted to achieve a good matching bandwidth around 2.45GHz with a directive radiation-pattern. As it was demonstrated in Fig. 6-4, W , P_y , and L_e substantially control the response of FSS screen in creating one or

two reconfigurable frequency regions. Therefore, these are other most important parameters that must be precisely adjusted for directive radiation-pattern with low back-lobe level in both E- and H-plane patterns. By elaborating these parameters, a nimble antenna either for one operating band or two agile frequency bands can be obtained. In the following section, the effects of these parameters are parametrically represented for a nimble radiation-pattern antenna operating across the first reconfigurable band.

6.1.3 Simulation parametric study results

To demonstrate the impact of each dimension on the antenna radiation characteristics, here for brevity, some of the most substantial simulation results carried out for typical sizes of cylinder radius and elliptical ring axis are presented in Fig. 6-6 to Fig. 6-8. Tab. 6-1 shows the antenna dimensions used in this parametric study. In summary, this antenna provides a matching bandwidth of 480MHz ranging from 2.06GHz to 2.54GHz. It has a 3dB gain and a bandwidth of more than 600MHz from 2.09GHz to 2.7GHz. The realized gain at 2.45GHz is 9dB, and the half power beam-width and side/back-lobe levels in the E- and H-planes are (-19dB, 60°) and (-21dB, 73°), respectively.

As an interesting point, the FSS cylinder length of this structure is about 0.75 times of the one used in nimble antenna presented in Chapter-5, while this antenna provides better performances in terms of matching bandwidth, radiation-pattern, and gain. Moreover, the number of active elements has also been reduced in this case.

To describe the effect of antenna dimensions on the input impedance matching, Fig. 6-7 is considered. It depicts that all parameters including R , W , and L_e are significantly affecting the antenna matching. Nonetheless, the unit-cell dimensions on the cylindrical reflector, especially the minor radius of the ellipse, mostly determines the matching and antenna bandwidth around 2.45GHz. This is because of the effective interaction between the dipole and cylindrical partially reflector by increasing the effective illuminated area in each unit cell of the FSS screen.

Similar performances are noticed in the radiation-pattern represented in Fig. 6-7 and Fig. 6-8. It is clear that by fixing the radius of the cylinder in an acceptable range value, side-lobe level of the antenna, mainly in the H-plane, is slightly deviated with a small variation of R . In addition, as shown in Fig. 6-8a, this amount of variation can introduce maximum 0.8dB change in the peak realized gain. However, the unit cell sizes strongly control both the antenna radiation-patterns and peak value of the gain. This, indeed, is because of changes in the transmission/reflection properties of each part of the curved FSS screen. In other words, by changing the major and minor axes of the elliptical ring in the unit cells, the magnitude and phase of induced currents on each part of the conformal FSS screen are varied. This prescribes shape of the directive E- and H-plane radiation-patterns, and therefore, its side/back lobe levels, radiation beam-width, and maximum

peak gain. As another important issue deduced from these curves, the antenna radiation characteristics are strongly sensitive to all these parameters. It means that the final antenna sizes must be carefully chosen to obtain almost the same performances in practice. Moreover, because of having different parameters in controlling the antenna characteristics, more than one design can be obtained. In this way, a compromise between bandwidth, gain and side/back lobe level needs to be considered for final design selection.

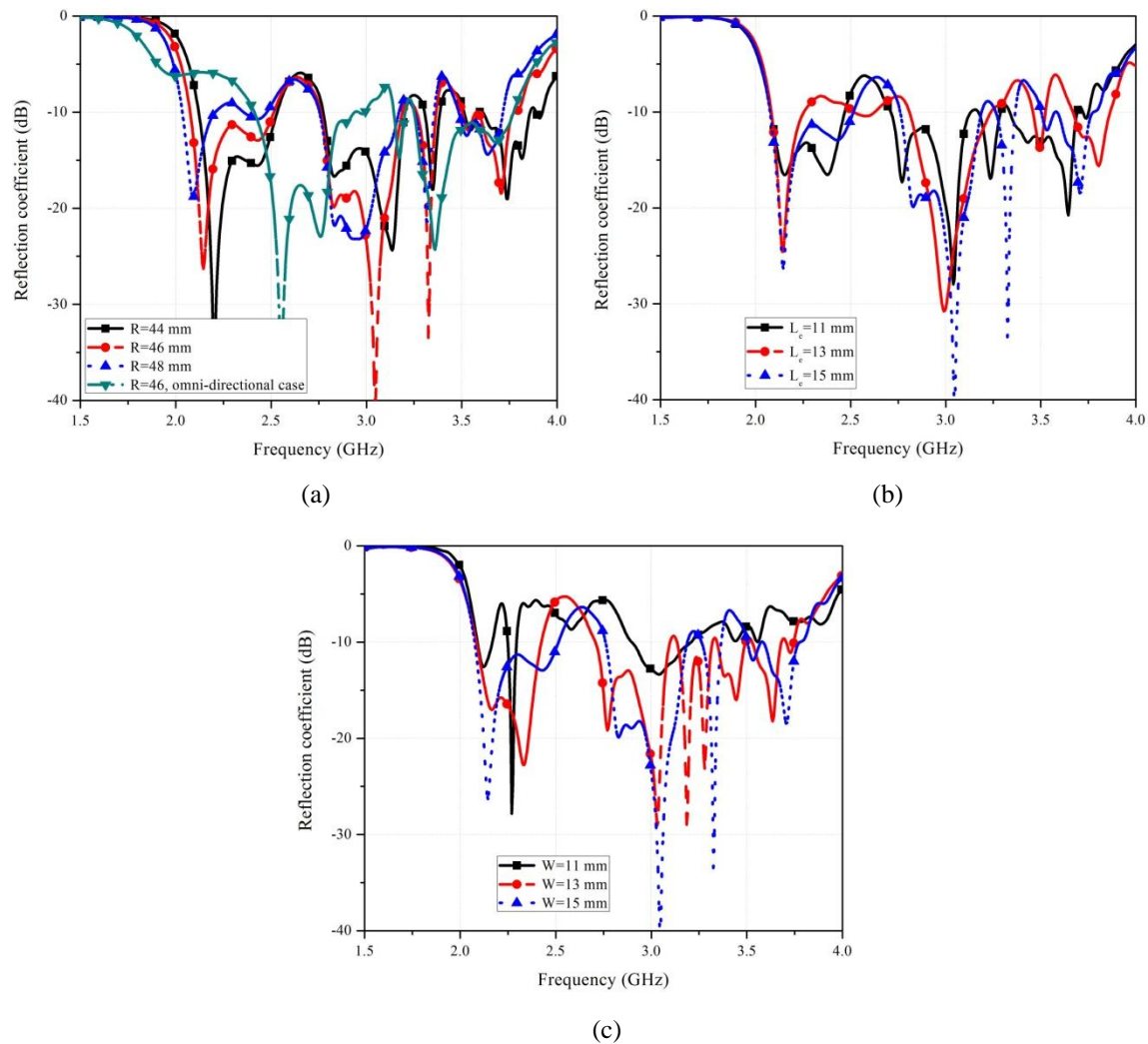


Fig. 6-6 Parametric studies on reflection coefficients carried out for the most crucial dimensions. (a) For different values of R . (b) For different values of L_e . (c) For different values of W .

Tab. 6-1 Final dimensions of the agile nimble beam antenna. All dimensions are in mm.

Parameters	R	P_y	g	W_s	W_{SS}	W_c	L_d	r_d	W	W_g	L_e
Values-Simulated	46	50	1.3	1	1	4	37	4	13	1.5	13

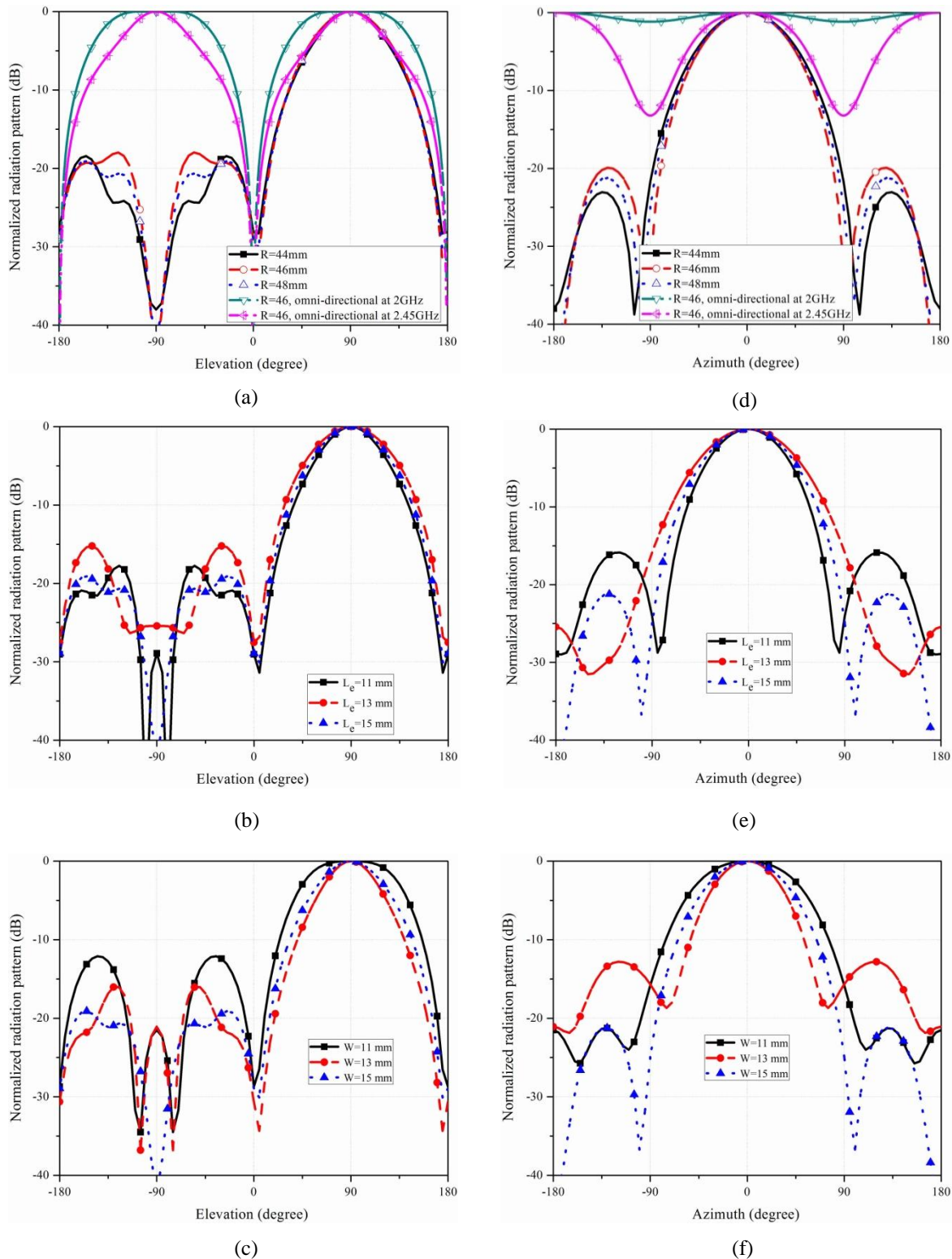


Fig. 6-7 Parametric studies on radiation-patterns carried out for the most crucial dimensions at 2.45GHz.

(a) E-plane for different values of R . (b) E-plane for different values of L_e . (c) E-plane for different values of W . (d) H-plane for different values of R . (e) H-plane for different values of L_e . (f) H-plane for different values of W .

To evaluate the ability in providing a reconfigurable directional to omni-directional pattern, all active elements on the FSS screen are turned on to make it transparent. Obviously, this considerably changes the antenna matching response almost at all frequencies. The radiation-pattern simulations show that for frequency of less than 2.3GHz, an omni-directional beam can be observed with an acceptable variation of power level in the range of -3dB. The best results is realized around 2GHz with about 0.5dB ripple in the H-plane pattern. At the desired operating range, the antenna provides a bi-directional beam, as shown in Fig. 6-7a and d. The simulated omni-directional gain at ($\varphi = 0^\circ, \theta = 90^\circ$) is also provided in Fig. 6-8a for the sake of comparison.

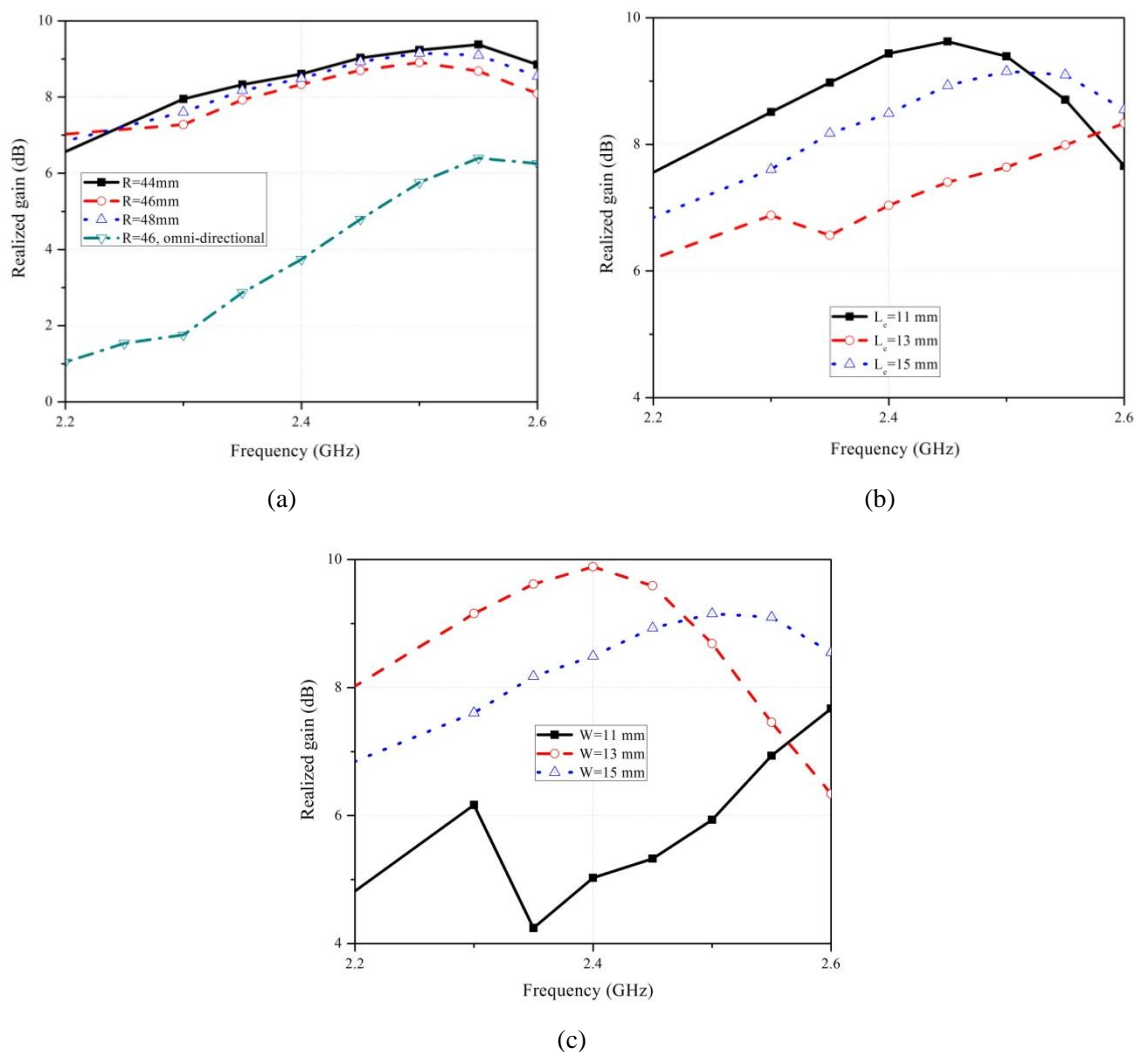


Fig. 6-8 Parametric studies on antenna gain carried out for the most crucial dimensions. (a) For different values of R . (b) For different values of L_e . (c) For different values of W .

6.2 Experimental results of agile frequency nimble antenna and discussion

In evaluating the FSS transmission/reflection coefficients, it is noticed that the unit cell dimensions substantially determines the screen response to the vertically polarized electric incident waves. This directly prescribes the performance of the reconfigurable cylindrical reflector antenna. Moreover, by reforming the planar FSS screen to a cylindrical shape and illuminating it by a dipole antenna in its near field, the reflection and transmission responses of the surface are expected to be changed. Therefore, to experimentally investigate this issue and successfully implement an agile nimble antenna, two reconfigurable FSS screens with different unit cell dimensions were fabricated and measured. Then, these FSS screens were used as a partially cylindrical reflector to implement the nimble antenna. The radiation characteristics of both antennas across a large frequency bandwidth were measured. Here, the final results of the antenna providing agile frequency nimble performances are presented. Tab. 6-2 summarizes dimensions of these two FSS sheets and the agile frequency nimble antenna.

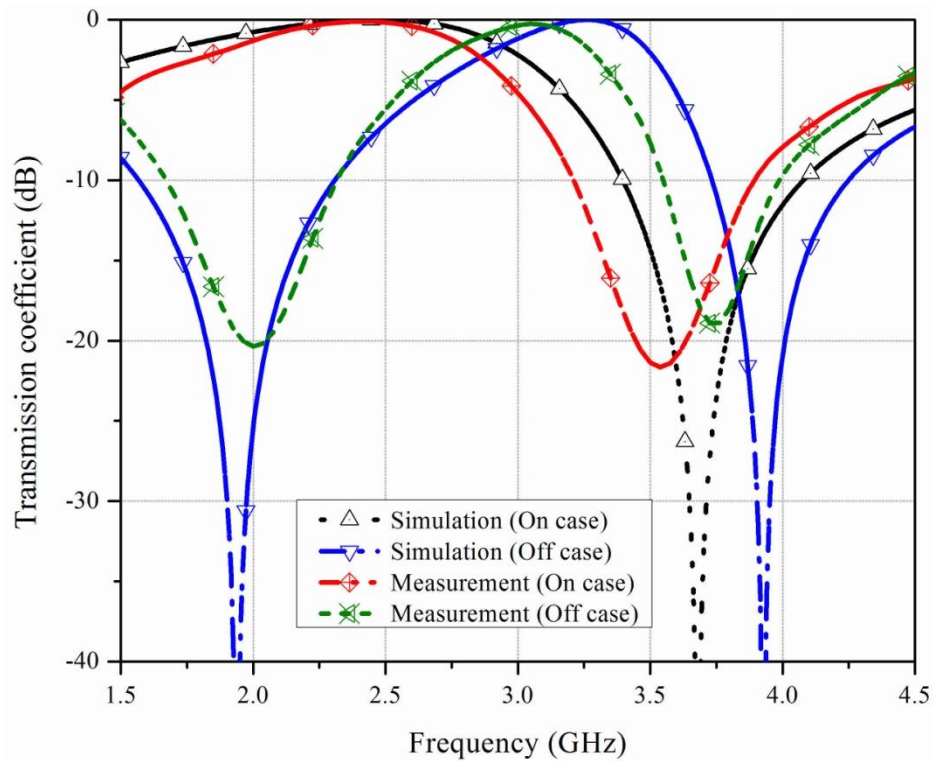
Tab. 6-2 Final dimensions of the fabricated FSS sheets and agile frequency nimble antenna.

Parameters	R	P_y	g	W_s	W_{ss}	W_c	L_d	r_d	W	W_g	L_e
FSS-A (mm)	-	40	1.3	1	1	4	-	-	15	15	14
Antenna-B (mm)	46	46	1.3	1	1	4	37	4	13	15	13

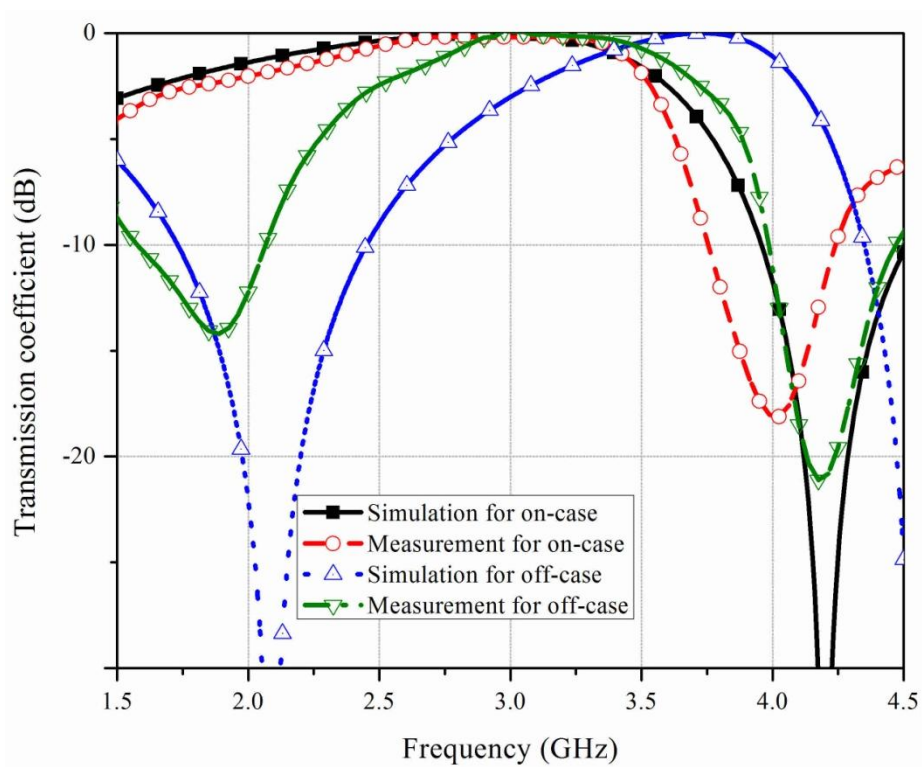
6.2.1 Transmission coefficient measurements

Transmission coefficients of FSS-A and B were measured using the set up shown in Fig. 4-20. The sheet sizes of 30cm \times 60cm and 15cm \times 30cm are used for FSS-A and B, respectively. The active elements of each column are biased by a resistor connected to the DC-voltage generator. The resistors and DC-feeding lines are isolated from the FSS screen by inductors at the operating bands.

The measurement results in Fig. 6-9 confirm that the unit cell dimensions must be precisely selected to achieve the desired reconfigurable dual responses over one or two distinct operating frequencies. In general, although the measured curves follow the simulation ones for both sheets, some deviations are noticed for both on and off states of Sheet-A and B. This is because of limited size of sheets and the measurement set up which is established in free space without eliminating multi-path reflections. Moreover, the horn antennas used in the measurement do not illuminate the entire FSS sheet with a uniform plane wave.



(a)



(b)

Fig. 6-9 Measured and simulated transmission coefficients. (a) FSS-A. (b) FSS-B.

Considering the result presented in Fig. 6-9a, the first measurement for FSS-A shows a dual response from 2.2GHz to 2.75GHz that can be reconfigured by changing the state of PIN-diodes in the sheet. Modifying the unit cell dimensions according to Tab. 6-1, it is confirmed that duality responses can be extended to two distinct frequency bands, almost ranging from 2GHz to 2.7GHz and 2.7GHz to 3.2GHz. This can be potentially used to design an agile frequency nimble radiation-pattern antenna as will be described in the following sections. More interesting, using this FSS screen, a nimble antenna can be designed for a large range of operating frequencies depending on the transmission/reflection coefficients of reconfigurable cylindrical screen. Therefore, the limitation in designing operating frequency range of the nimble antenna presented in Chapter-5 is overcome.

6. 2. 2 Antenna measurement results and discussion

Before inserting the dipole antenna in the center of the cylindrical FSS surface, as a reference, the radiation characteristics of the dipole antenna was measured. Then, two cylindrical reconfigurable reflector antennas were fabricated and their radiation parameters were measured. In the measurement process of these agile nimble antennas, firstly their reflection coefficients were measured. Then, their H-plane radiation-patterns were measured at different frequencies in the range from 2GHz to 3.2GHz to examine the ability of antennas in creating a directive radiation-pattern. The measurement results demonstrated that only the antenna with FSS-B is able to provide nimble performances in two different frequency bands. Fig. 6-10 depicts the fabricated antenna prototype based on the dimensions summarized in Tab. 6-2.

To establish the measurement for directional case, because of the symmetry in the antenna configuration, 5 columns of unit cells are randomly chosen along the cylinder to mimic the opaque part, while the others are biased to make the other side of cylinder transparent for the dipole antenna. On the other hand, for omni-directional case, all active elements are switched on or off to make the cylinder transparent across the first or second band, respectively.

The measured reflection coefficients of the agile nimble radiation-pattern antenna in directional and omni-directional cases are compared to the simulation in Fig. 6-11. In overall, some deviations between measurement and simulation results are noticed. This is due to the simplicity in the simulation in which only two pieces of metal rods have been used as dipole antenna; therefore, the effects of RF connector and cable have been neglected during the design process. The discrepancy between simulated and measured dipole reflection coefficient proves this explanation. Comparing the measured and simulated curves confirms that the dipole provides more than 1.5GHz matching

bandwidth when it is connected to the RF cable, while the predicted bandwidth by simulation is about 600MHz.

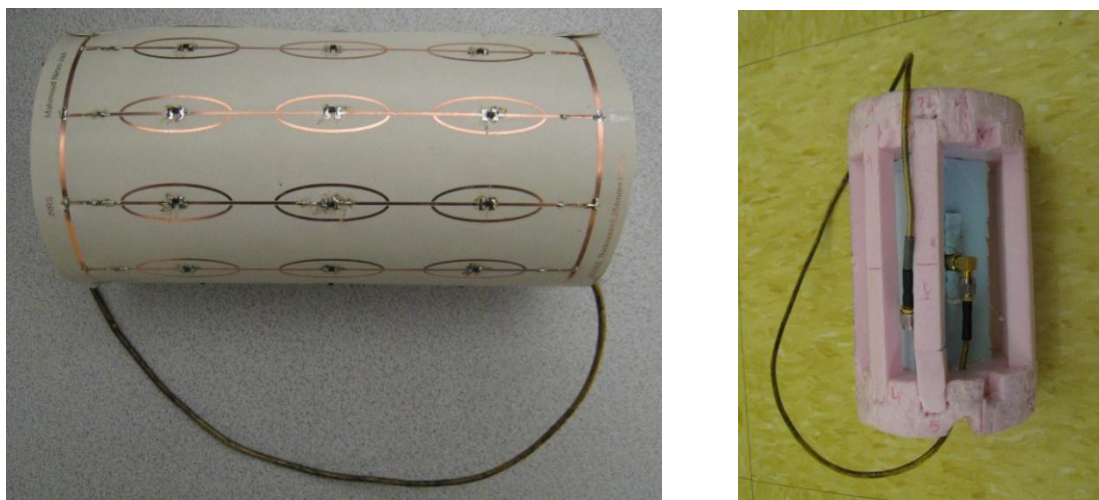


Fig. 6-10 Fabricated prototype of agile nimble radiation-pattern antenna.

To demonstrate the impact of FSS sheet on the dipole antenna, the measured reflection coefficient of the dipole is also used as a reference. The measured results for the agile nimble antenna show that the FSS sheet significantly influences the resonant length and matching of the dipole antenna placed at its center. In the directional case, the FSS sheet improves the antenna matching at the low frequencies and around 2.75GHz. However, when the antenna is reconfigured to the omni-directional case by activating all diodes on the FSS sheet, the reflection coefficient of the antenna naturally tends to follow the one of dipole, except some mismatching observed around 3GHz.

The antenna realized gain was measured at different frequencies for directional radiation-pattern in two opposite directions, i. e. $(\varphi = 0^\circ, \theta = 90^\circ)$ and $(\varphi = 180^\circ, \theta = 90^\circ)$. Fig. 6-12 demonstrates the measured results compared with the simulation ones. These curves clearly represent a dual-band directive radiation-pattern with about 7dB gain. This is in agreement with a dual-character in the reconfigurable transmission coefficient responses of the planar FSS-B sheet predicted across two frequency bands in Fig. 6-9. Moreover, since the transmission response of on state across the first band in Fig. 6-9 is larger than the second band, therefore, the antenna provides larger gain bandwidth for the first band as well. Nonetheless, there is some deviation between the measurement and simulation results, which is probably caused by the changes between simulated and fabricated antenna. The parametric studies, shown in Fig. 6-8, can also describe this discrepancy by assessing the sensitivity of the antenna gain to the cylinder radius. Alternatively, the measured antenna gain for omni-directional case is represented

for both operating regions. As it is expected, the results show that antenna closely follows the dipole resonator performance.

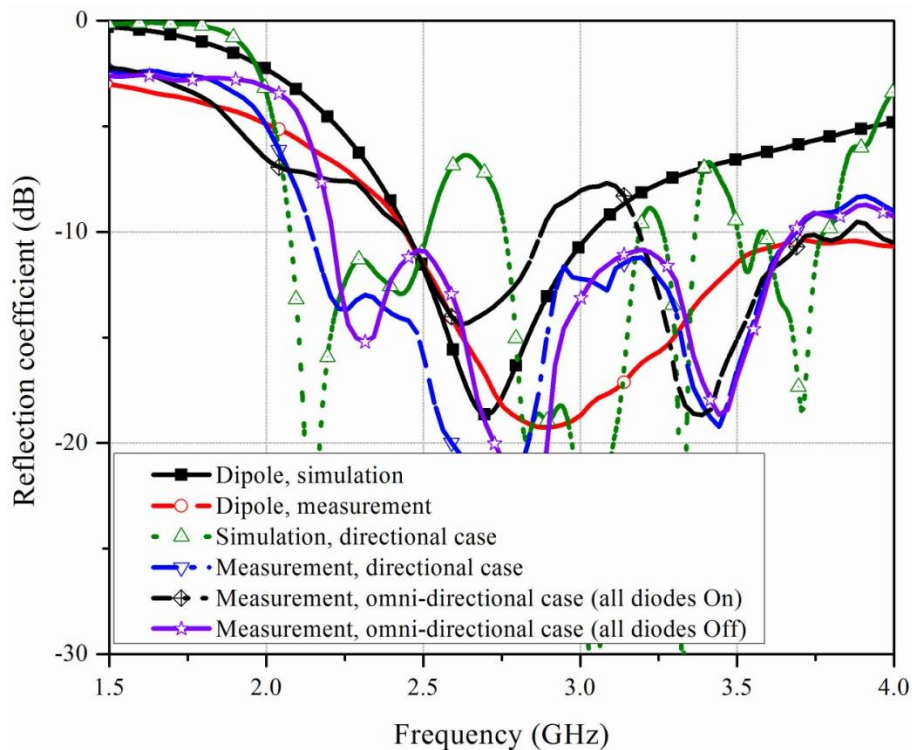


Fig. 6-11 Measured and simulated reflection coefficients of dipole and agile frequency nimble.

As an alternative proof of concept, antenna radiation-patterns were measured at different frequencies in the range of 2GHz to 3.2GHz. The results represented in Fig. 6-13 show that the antenna provides a minimum side/back lobe level of less than -20dB at frequency 2.35GHz. The half power beam-widths in the H- and E-plane patterns at 2.35GHz and 3.1GHz are about (59°, 66°) and (70°, 41°), respectively. Comparing these beam-widths with the simulations in Tab. 6-3 reveals a noticeable difference only for the H-plane pattern. Since the effect of active elements and other losses are considered in the simulation, this difference basically can be interpreted by the measured gain reduction. In addition, as it is expected from duality responses at the two operating bands, the antenna radiation-patterns are oriented at two opposite directions in the obtained bands. This technically confirms the frequency agility of this sweeping-beam antenna configuration.

To evaluate the reconfiguration functionality from directional to omni-directional case across the first and second operating bands, the antenna radiation-patterns are measured when all active elements on the FSS screen are switched on or off, respectively. For the sake of comparison, the measured gain of dipole antenna is provided in Fig. 6-12 to

assess the directivity performance of the antenna in different cases. According to this figure, when it is reconfigured to omni-directional case, the radiation-pattern directivity of the antenna is similar to the one measured for the dipole at both operating bands.

As more proof of concepts, the radiation-patterns for the omni-directional case are compared to the one of dipole antenna in Fig. 6-14. It is clear that when the radiation-pattern of antenna is reconfigured to the omni-directional case, it follows the one of dipole across the first desired frequency band. However, in the second reconfigurable band, the E-plane pattern is slightly deviated from the one of dipole antenna. Therefore, the proposed antenna successfully provides the nimble performance across the first obtained frequency band, while it provides fairly acceptable results in the second band. A summary of achieve results of this antenna has been compared to the antenna Nimble-Antenna presented in the previous chapter in Tab. 6-3, demonstrating the improvements obtained by the earlier proposed antenna.

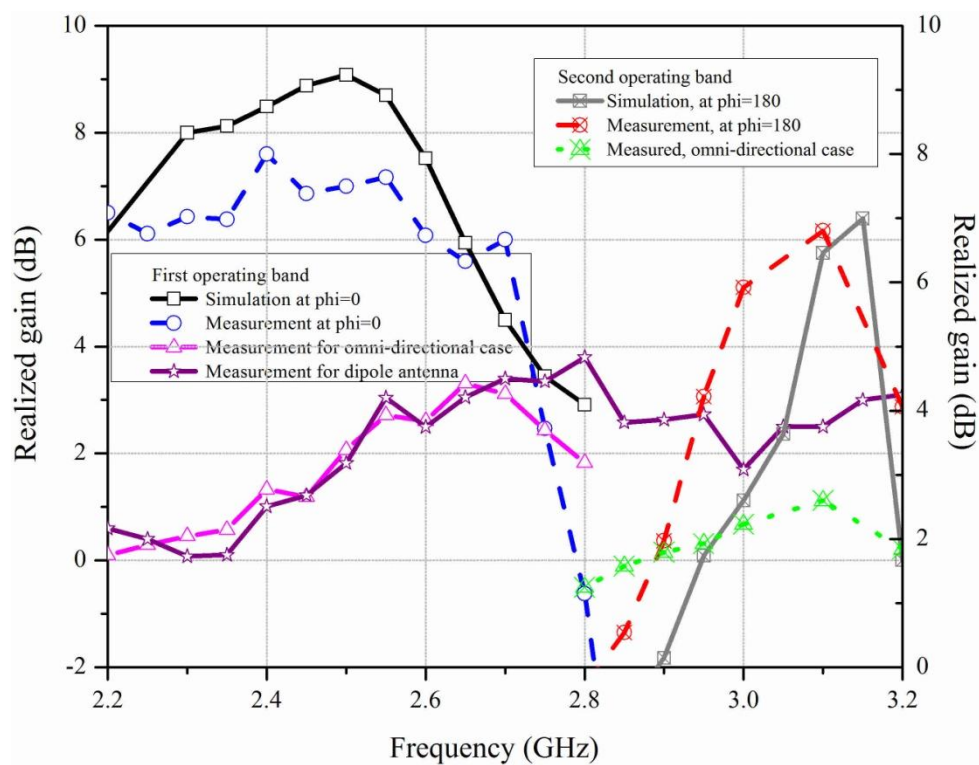
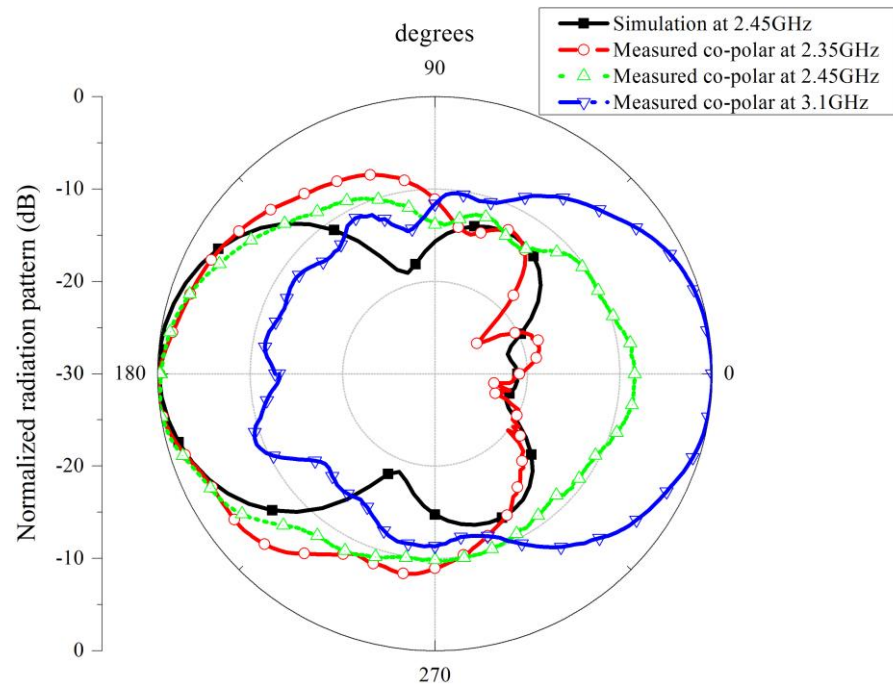
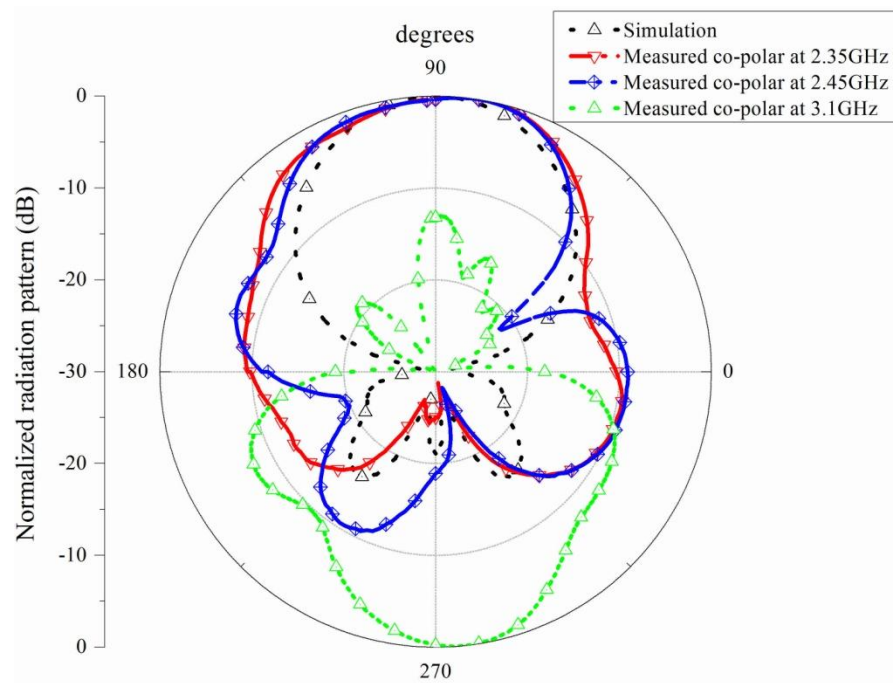


Fig. 6-12 Measured and simulated realized gain of agile frequency nimble antenna.



(a)



(b)

Fig. 6-13 Measured and simulated radiation-pattern of agile frequency nimble antenna in directional case.
(a) H-plane. (b) E-plane.

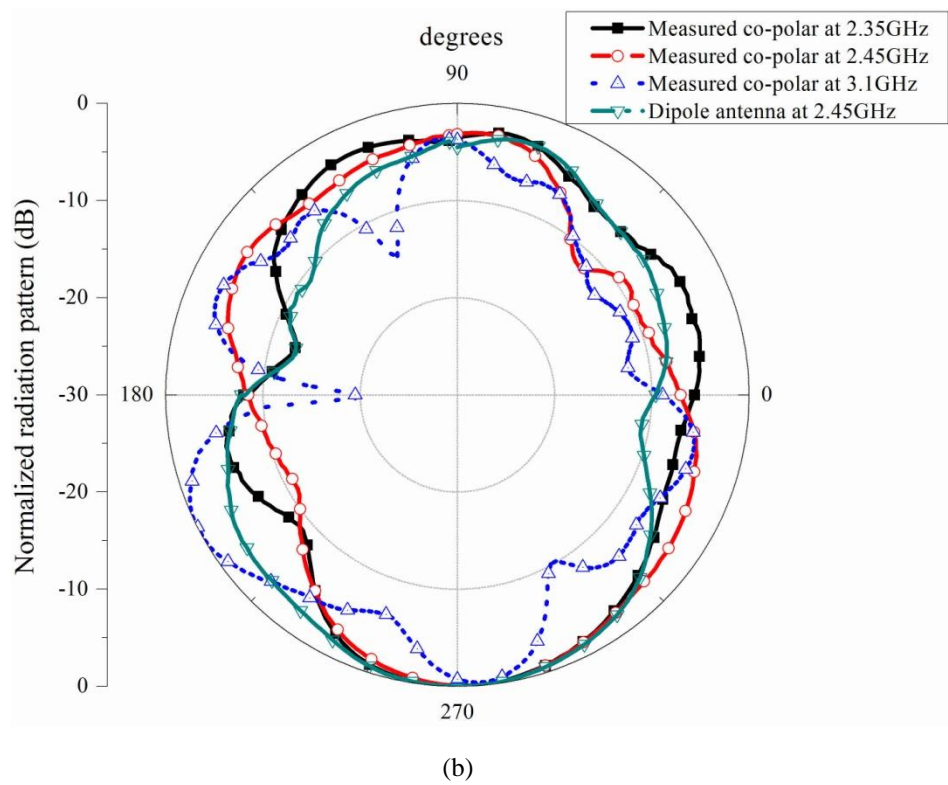
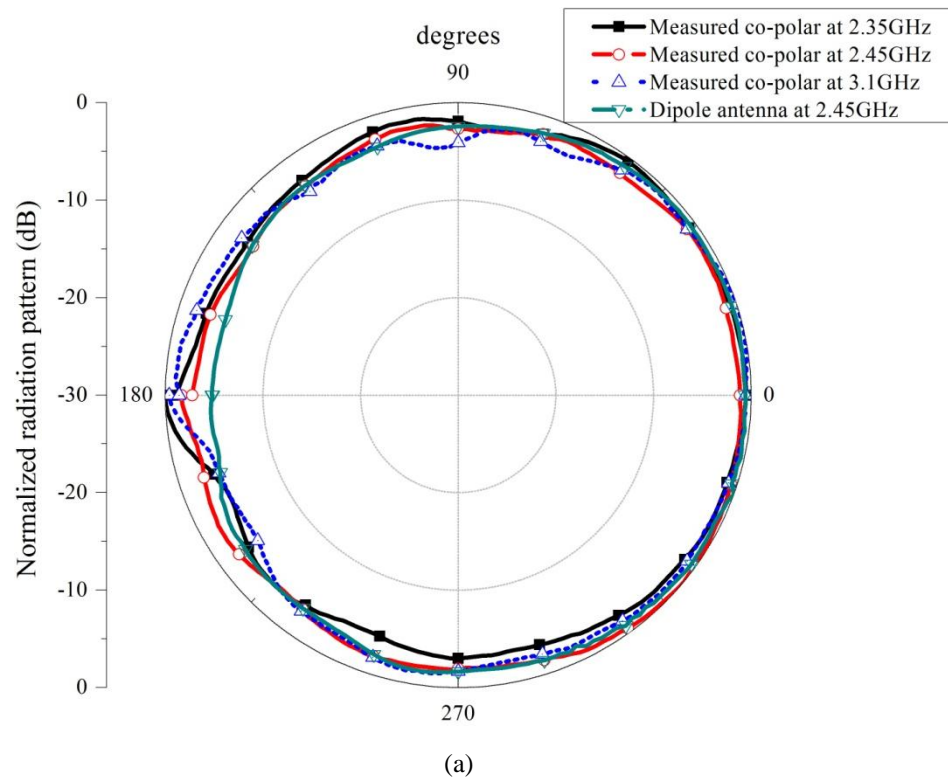


Fig. 6-14 Measured and simulated radiation-pattern of dipole and agile frequency nimble antenna in omni-directional case. (a) H-plane. (b) E-plane

Tab. 6-3 Antennas characteristics.

	Nimble antenna				Agile frequency nimble antenna					
	Simulation		Measurement		Simulation in the first band		Measured first band		Measured Second band	
Antenna aperture (A)	$2R_1 \times 4P_{y1}$		$2R_1 \times 4P_{y1}$		$2R \times 2P_{y2}$		$2R \times 2P_{y2}$		$2R \times 2P_{y2}$	
Bandwidth(MHz)	Omni.	Dir.	Omni.	Dir.	Omni.	Dir.	Omni.	Dir.	Omni.	Dir.
	-	102	Wide	Wide	600	468	475	Wide	Wide	Wide
HPBW(Deg.)	H	E	H	E	H	E	H	E	H	E
	112	42	104	40	71	61	59	66	70	41
Peak gain(dB)	8.2		3.94		9.1		7.6		6.8	
Back Lobe(dB)	-15		-20		-21		-20		-10	
Total efficiency	94		-		94.5		-		-	
$\eta = G\lambda^2/4\pi A$ (%)	38		14.5		76		54		45	

Note: The radius R and unit cell periodicities in two antennas are: $R_1 = 39mm$, $P_{y1} = 66mm$, $R_2 = 46mm$, and $P_{y2} = 46mm$.

6.3 Conclusions

In this chapter, a new hybrid unit cell has been proposed to create dual band reconfigurable FSS screen. This surface has been used to improve the performance of the nimble antenna presented in the previous chapter. The results have demonstrated the robustness of this antenna in providing the nimble functionality across a large frequency regime of more than 400MHz. It is able to sweep all azimuth angles in 10 steps and also reconfigure its radiation-pattern from directive to omni-directional case in this band. The antenna gain is more than 7dB across this bandwidth for the directional case, and it follows the dipole radiation for the omni-directional case.

As an extra bonus, this antenna can provide dual band responses over two operating bands. Indeed, it is able to create two oppositely oriented radiation-patterns in the two frequency bands at the same time. The final achievements of this have been summarized in Tab. 6-3.

To clarify the advantages if this antenna, it has also been compared to the nimble antenna proposed in the previous chapter. The size of this antenna has been reduced to 0.75 times of the nimble antenna proposed antenna in Chapter-5, while providing better directivity. The range of designing frequency of that antenna has been improved, and therefore antenna was able to efficiently operate at frequencies of less than 2.45GHz with nimble functionality. According to the obtained results in this chapter, it can be concluded that by precisely elaborating the FSS surface, different antenna radiation characteristics can be obtained. Moreover, by making FSS surface more complex and then conforming it to a certain surface, the original transmission/reflection response of

the sheet will be changed. Therefore, the final FSS surface dimensions must be adjusted in the conformal surface in interaction with the excitation source.

Chapter 7

Conclusion and future research works

7.1 Conclusion

In this thesis, the investigation results on the applications of frequency selective surfaces in reconfigurable antennas have been presented. As the main objective of the work, this type of periodic structure has been pulled together with certain reconfigurable mechanisms to propose a group of new versatile reflector antenna structures— those called “Nimble-Antenna”. This name is selected because of the functionalities they can provide. Indeed, these antennas are able to sweep all azimuth angles in prescribed steps, and they also can reconfigure their radiation-pattern from directional to omni-directional states. Moreover, by precisely designing the periodic structure, the functionality of frequency agility has been also introduced into the structure. To successfully accomplish this mission, a step-by-step design procedure has been performed in this work, which is concluded in the following paragraphs.

In the first step, the marvels of frequency selective surfaces in creating dual responses across different frequency bands have been explored and the possible reconfiguration mechanisms using high frequency switches are identified. It has been demonstrated that the type of feeding method of active elements dictates the reconfiguration mechanism of

the proposed reconfigurable frequency selective surfaces. Moreover, it is theoretically and experimentally shown that the DC-feeding lines of active elements significantly affect the transmission/reflection responses of the electromagnetic windows. It has also been investigated that non-ideal effects of active elements undesirably change their responses. Therefore, both DC-feeding line and parasitic elements of PIN-diodes must be considered in the design process to obtain the desired reconfiguration performances. It has been demonstrated that to precisely fit the measured transmission response of the reconfigurable sheet constructed by a periodic array of discontinuous strips, a correction factor is required. This is indeed required to incorporate the effect of the fringing field around the discontinuous gaps. These investigations correspond to the publications presented in [91, 93, 100].

Then, a cylindrical reconfigurable antenna topology has been proposed to meet the desired nimble-antenna functionalities. The obtained results have demonstrated that because of symmetrical illuminating mechanism used in this radiation topology, reforming the planar frequency selective surfaces to conformal cylindrical shape does not significantly change the transmission/reflection responses of the sheets. However, the undesired effect of non-ideal active elements significantly changes the radiation performances of the proposed nimble antenna by deviating the transmission/reflection responses of each semi-cylindrical parts of the reconfigurable electromagnetic window. It means that to obtain the desired radiation performances for the antenna, more care needs to be taken for this effect to enhance the relevant transparency/reflectivity levels of each semi-cylindrical part. These investigations correspond to the publications presented in [91, 92].

Finally, to improve the performances of the nimble antenna in which periodic array of discontinuous strips are used as its cylindrical reconfigurable partially reflector, a new agile frequency reconfigurable sheet is introduced. It is shown that the performances of frequency selective surfaces can be considerably enhanced for the current application by using hybrid resonant elements. This surface can either be designed for agile frequency operation or for only nimble applications. It has been shown that for the agile frequency operation, not being as good as the first operating region, the radiation pattern of the

antenna is fairly acceptable in omni-directional case across the second band. The results also demonstrated that, compared to the previous prototypes, using this hybrid unit cell, the antenna size is decreased, and its radiation performance is considerably improved. These investigations correspond to the publications presented in [99].

7.2 Future research works

In this thesis, some research work has been carried out on the single layer planar and conformal reconfigurable frequency selective surfaces for antenna applications. However, not fully covered in this limited work, some other interesting investigations in this area are still left for future research topics as articulated in the following paragraphs.

According to the multi-disciplinary research topics undertaken in this dissertation, three future avenues in different research topics can be foreseen. The first one deals with the alternative reconfiguration technologies that can be used for the proposed radiation topology in this thesis. As it is demonstrated, non-ideal switch effects and their biasing DC-feed lines significantly change the performances of the reconfigurable sheets. Finding other reconfiguration mechanism with emerging new technologies like MEMS, ferroelectric and plasma materials might be an interesting topic to tackle this problem and enhance the antenna performances and probably increasing its functionalities.

The second research avenue treats with the frequency selective surfaces. In this thesis, only a certain group of single layer screens are investigated just for TE-incident polarization. The possibility of applying other resonant elements, the effect of incident angles in improving their responses in conformal configuration, increasing the number of sheets in antenna configuration to improve its back radiation performances can also be some other future research topics. More importantly, the designed frequency selective surfaces are used in the near-field region of the dipole antenna. Calculating the radiation characteristics of the antenna with an appropriate full wave numerical method is another research topic that probably can explore some other attractive phenomena that are not considered in the current work.

Antenna radiation topology can be the third interesting future research topic. In this thesis, the antenna radiation-pattern is sweeping only the azimuth angles and it deals with vertical polarized waves. Changing the radiation mechanism to sweep the elevation angles, handling both vertical and horizontal polarizations and proposing a particular method to increase antenna gain by a minimum cylinder height can be recognized as other future research topics in the antenna avenue.

Chapter 8

Résumé

8.1 Introduction

8.1.1 Motivation

Les systèmes de communications avancés sans fil ont récemment reçu une attention croissante grâce à leurs habiletés à fournir différentes fonctionnalités dans une unité individuelle, introduisant plus de versatilité, robustesse, une production bon marché, et une économie significative. Par exemple, le nombre d'utilisateurs croissant de téléphones mobiles, sans considérer l'objectif principal de l'obtention d'une qualité de services vocaux, a aussi pour intérêt de bénéficier d'autres commodités incluant le multimédia, le GPS et l'internet [1, 2]. Chacun de ces services fonctionne sur une bande de fréquences différente, ou a besoin d'utiliser une diversité de polarisation/espace pour améliorer la qualité de transmission d'un système. Ces tendances montrent que de plus en plus de communications peuvent, de plus en plus, être effectuées sur une même plateforme.

En conséquence, un sujet particulier de recherche, appelé antenne reconfigurable (AR), a reçu récemment une attention croissante à explorer de nouvelles antennes avec différentes caractéristiques en termes de fonctionnement, de fréquence, de polarisation et de diagramme de rayonnement (AR) selon les exigences du système désiré [3]. Par conséquent, ce projet vise à concevoir, analyser, et fabriquer un nombre de

nouvelles antennes reconfigurables basées sur des structures périodiques pour des systèmes de communications sans fil tactiques.

8. 1. 2 Identification du problème

Les matériaux électromagnétiques à bande interdite (EBI) sont utilisés pour créer une réponse électromagnétique à bande interdites ou diriger les ondes en insérant un défaut dans la structure périodique. Ces propriétés ont trouvé des applications intéressantes dans le domaine des antennes pour supprimer les ondes de surface dans les configurations de réseaux planaires [4], pour augmenter le gain de l'antenne [5-10], et pour fournir des antennes efficaces à bas profile en créant des surfaces haute impédance (SHI) ou des conducteurs magnétiques artificiels (CMA) [4, 11].

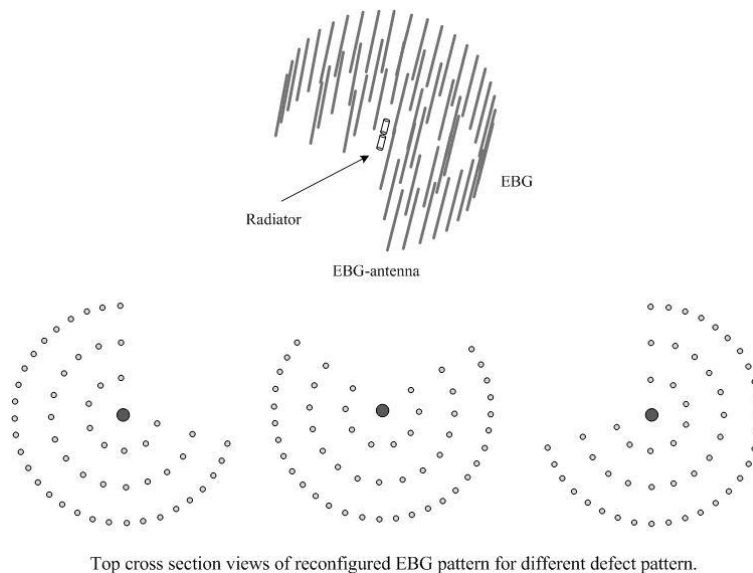


Fig. 8-1 Configuration d'antenne BIE cylindrique.

En changeant la forme du motif périodique et en utilisant un certain mécanisme de reconfiguration, les propriétés électromagnétiques des structures périodiques peuvent également être contrôlées. Ce concept a été utilisé dans le domaine des antennes pour contrôler leurs performances de rayonnement en termes de direction du diagramme de rayonnement ou de gain [12]. En particulier, dans [13], un réseau périodique de tiges métalliques disposés en forme cylindrique, comme indiqué dans la Fig. 8-1, a été utilisé pour créer un diagramme de rayonnement directif. D'autre part, le défaut angulaire inséré dans le motif périodique dirige les ondes électromagnétiques excitées par les sources en son centre. Par conséquent, un diagramme de rayonnement directif est créé par cette structure [14].

Il est bien connu qu'en insérant des discontinuités le long des tiges, la réponse bande interdite peut être éliminée à la fréquence de fonctionnement souhaitée. Ces discontinuités peuvent être réalisées en intégrant certaines diodes PIN haute fréquence dans la structure, offrant une reconfiguration au niveau de la réponse bande interdite pour le réseau périodique de tiges. Par conséquent, en utilisant ce mécanisme de reconfiguration, la direction angulaire du défaut dans le motif périodique est modifiée. Toutefois, cette structure doit être mise en œuvre en configuration multi-couches, ce qui la rendra complexe et difficile à fabriquer. Par ailleurs, un grand nombre d'éléments actifs est nécessaire, ce qui augmente le coût du système d'antenne.

Par conséquent, cette thèse vise à introduire une configuration d'antenne basée sur d'autres structures périodiques, i. e. surfaces sélectives en fréquence, afin de réduire le nombre d'éléments actifs utilisés et donc réduire la complexité de l'antenne. Par ailleurs, il est prévu de tirer avantages des structures hybrides périodiques et d'augmenter la fonctionnalité de l'antenne.

8. 1. 3 Solutions au problème et objectifs du projet

Dans ce travail, une gamme de surfaces sélective en fréquence (SSF) reconfigurables est proposée afin de créer un nombre d'antennes reconfigurables, et donc réduire les inconvénients de la structure reconfigurable, basée sur les BIE, mentionnée ci-dessus à la Fig. 8-1. En effet, la réponse de transmission/réflexion de chaque SSF planaire est soigneusement examinée et expliquée afin de minutieusement remodeler les SSF planaire à une forme cylindrique. La forme cylindrique est délibérément choisie pour atteindre les performances souhaitées du faisceau balayant tous les angles azimutaux. Puis, en contrôlant précisément les éléments actifs intégrés dans la SSF cylindrique, le champ rayonné d'une source RF au centre du cylindre est contrôlé pour obtenir la fonctionnalité désirée.

Comme objectifs spécifiques, les antennes conçus doivent fonctionner à 2.45GHz, pour être en mesure de balayer l'ensemble des angles azimutaux sur un minimum de 15% de bande passante en utilisant un diagramme de rayonnement directif avec un gain réalisable supérieur à 10dB. Cette fonctionnalité est exigée dans les systèmes d'antennes adaptatives ou intelligentes pour la diversité d'espace ou de diagramme de rayonnement. Nous sommes également intéressés à reconfigurer le diagramme de rayonnement afin d'obtenir le cas omnidirectionnel, couvrant instantanément tous les angles azimutaux. Cette fonctionnalité peut également être appliquée dans les systèmes intelligents exigeant un gain de diversité pour améliorer la performance du système en augmentant le rapport signal sur bruit. Le niveau des lobes arrière du diagramme de rayonnement dans le cas directif devrait être meilleur que 20dB. Dans le processus de conception, le

nombre d'éléments actifs doit être réduit au minimum pour diminuer le coût de l'antenne et également améliorer ses performances de rayonnement.

Pour atteindre les objectifs mentionnés ci-dessus, les performances de transmission d'une surface métallique active planaire sont d'abord examinées et puis une antenne à réflecteur reconfigurable planaire est fabriquée et ses performances sont mesurées. La reconfiguration possible du mécanisme, dictée par les lignes d'alimentation DC, est présentée et l'effet néfaste de l'imperfection des diodes PIN sur la performance de transmission de la surface est exploré. Ensuite, une topologie de rayonnement cylindrique est proposée pour atteindre les objectifs. En utilisant le mécanisme de la reconfiguration dictée par les lignes d'alimentation DC, deux prototypes d'antennes, ainsi que leurs avantages et inconvénients, sont présentés. Enfin, une nouvelle SSF bi-bande est présentée comme réflecteur cylindrique pour améliorer la fonctionnalité des précédents prototypes cylindriques.

8.2 Grille SSF active métallique planaire

La Fig. 8-2 montre une reconfiguration typique d'une grille construite avec des éléments réseau constitués de courts rubans se comportant comme des dipôles intégrant des éléments actifs. Dans cette surface, $w \ll p_x$, $p_x \ll \lambda$, et $g_0 \ll p_x$ sont considérés pour extraire les valeurs des éléments du modèle de la ligne de transmission correspondante.

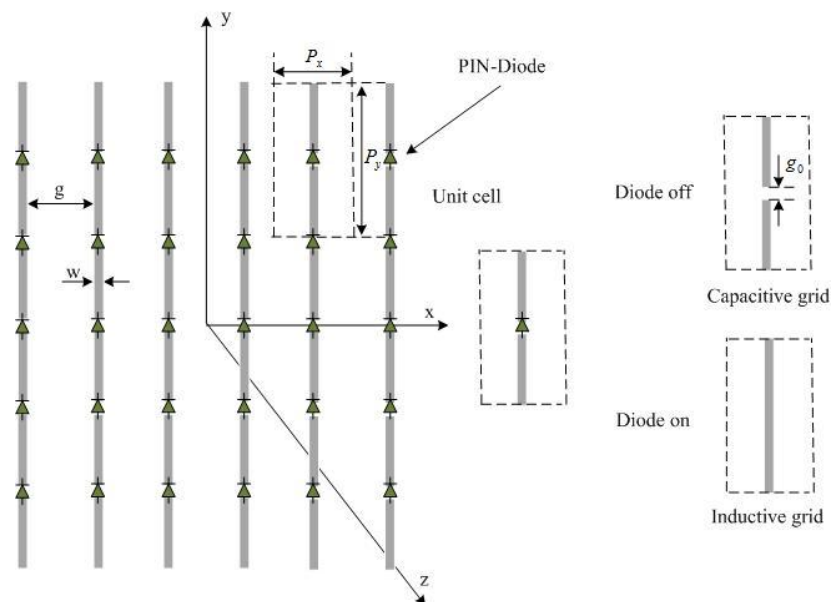


Fig. 8-2 Grille capacitive passive intégrée à des éléments actifs.

En outre, puisque l'épaisseur des rubans est très mince par rapport à la longueur d'onde, donc l'effet de l'épaisseur est négligé. Lorsque les diodes sont activées, une réponse passe-haut est créée pour une onde TE incidentes (polarisée parallèlement aux rubans). D'autre part, une bande interdite est obtenue dans la réponse de transmission en activant les diodes. Par conséquent, le niveau de transparence de la surface peut être contrôlé sur une gamme de fréquences en changeant l'impédance de surface.

8. 2. 1 Caractérisation d'une grille inductive

La Fig. 8-3 montre une grille inductive sans support diélectrique construite en utilisant un réseau parallèle de rubans, avec une périodicité P_x et une largeur w . La surface est éclairée par une onde plane polarisée parallèlement aux rubans. L'angle d'incidence mesuré, à partir de la normale au plan de la grille, est nommé θ . Selon la valeur de la réactance équivalente de la surface inductive, calculée par l'équation (3-7), cette expression peut être simplifiée pour les ondes incidentes normales par l'équation suivante:

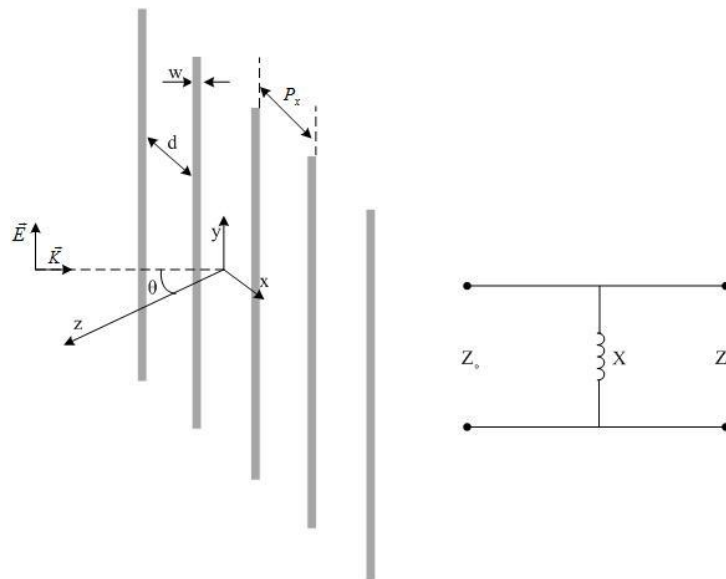


Fig. 8-3 Géométrie d'un écran SSF inductif et son model en ligne de transmission.

$$X_{TE} = F(p_x, w, \lambda) = \frac{p_x}{\lambda} \left[\text{Incossec} \left(\frac{\pi w}{2p_x} \right) + G(p_x, w, \lambda) \right], \quad w \ll p_x \quad (8-1)$$

Quand $p_x \ll \lambda$, le petit terme de correction G peut aussi être négligé et cette équation peut être réécrite comme :

$$X_{TE} = \frac{p_x}{\lambda} \ln\left(\frac{2p_x}{\pi w}\right), \quad w \ll p_x \ll \lambda \quad (8-2)$$

Utilisant cette expression, les performances de la réponse de transmission de la surface inductive, montrées à la Fig. 8-4, peuvent être facilement décrites en termes de dimensions de la grille réseau.

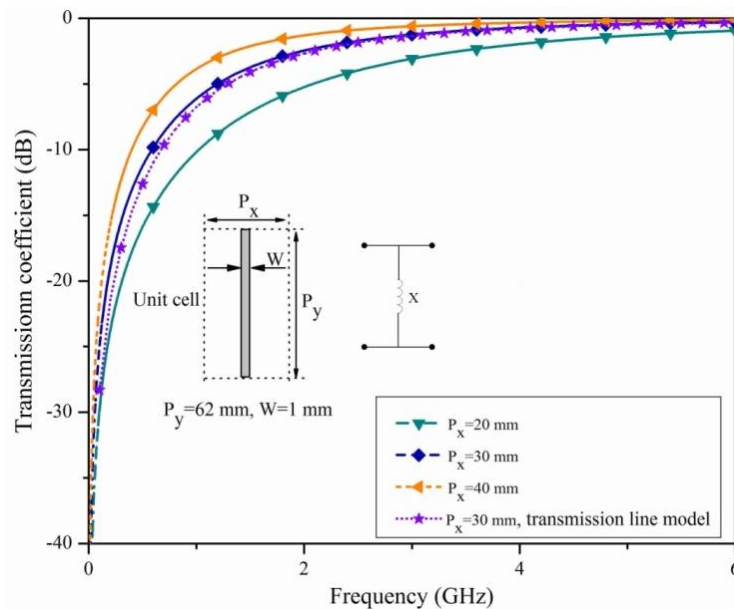


Fig. 8-4 Effet de la périodicité de la grille sur le coefficient de transmission.

8. 2. 2 Caractérisation de la grille capacitive

La désactivation des diodes PIN dans la Fig. 8-2 mène à une surface capacitive montrée à la Fig. 8-3. Cette surface résonante offre une réponse à bande interdite où sa fréquence de résonance est dictée par la longueur résonante des rubans discontinus inclus dans l'une des cellules de base de la SSF. La susceptance équivalente de la surface capacitive est obtenue à partir d'un circuit série LC équivalent en parallèle avec une ligne de transmission d'impédance caractéristique Z_0 . La longueur effective du dipôle résonant détermine la valeur de l'inductance. L'écart et le rapport P_y/P_x sont les principaux paramètres affectants la capacité du circuit [15]. Tant que les dimensions du réseau satisfont $w \ll p_x$, $p_x \ll \lambda$, et $g_0 \ll P_x$, le champ magnétique près de

la grille, en raison du courant circulant le long des rubans, est approximativement le même que celui autour d'une grille inductive uniforme correspondante et est exprimé en (4-3).

$$X_{TE} = \frac{P_y - g_0}{P_y} \frac{P_x}{\lambda} \ln\left(\frac{2P_x}{\pi w}\right) \approx \frac{P_x}{\lambda} \ln\left(\frac{2P_x}{\pi w}\right), \quad w \ll P_x \ll \lambda \quad (8-3)$$

D'autre part, concernant la distribution du champ électrique, il est noté, d'après des considérations de symétrie, qu'il n'y a aucune composante du champ électrique normale aux rubans entre chaque deux discontinuités. En d'autres termes, dans le cas quasi-statique, pour la dimension actuelle du réseau ($P_x \ll \lambda$ et $g_0 \ll P_x$), le flux électrique sur les éléments de la grille est concentré entre les discontinuités le long des rubans inductifs. Par conséquent, la largeur effective du ruban est un facteur crucial pour prévoir raisonnablement la fréquence de résonance.

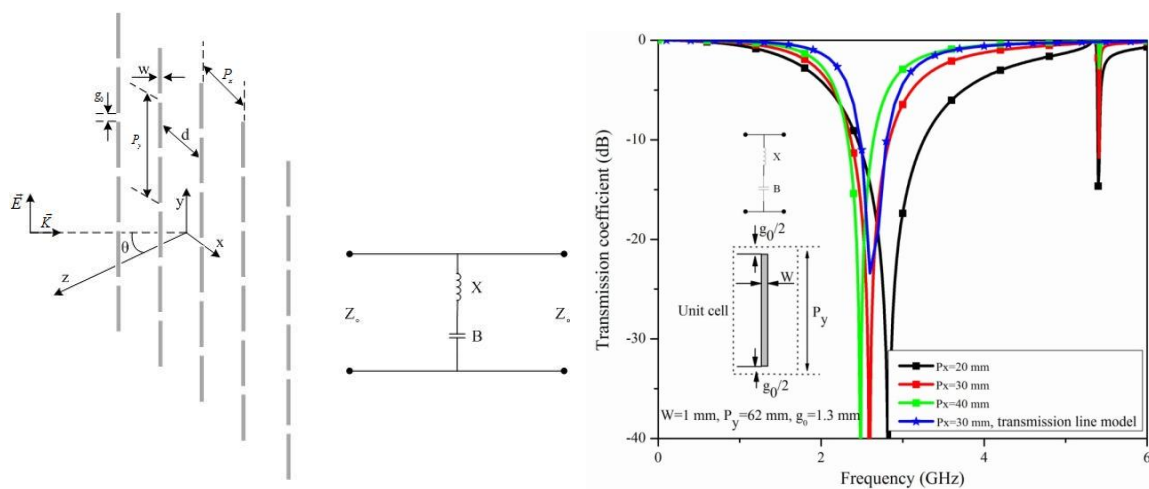


Fig. 8-5 Géométrie d'un écran capacitif SSF, son modèle en ligne de transmission, et sa réponse en coefficient de transmission.

Si l'effet du champ de fuite dans la discontinuité est incorporé dans la largeur effective des rubans comme $w_{eff} = A w$, la susceptance liée, selon l'équation (3-8), est calculée par:

$$B = 4F(p_y, g_0, \lambda) \frac{w_{eff}}{P_x} = \frac{4w_{eff} P_y}{P_x \lambda} \left[\text{Incos}ec\left(\frac{\pi g_0}{2p_y}\right) + G(p_y, g_0, \lambda) \right] \quad (8-3)$$

où, A est un facteur de correction incluant l'effet du champ de fuite et est proportionnel au rapport de périodicité. Concernant les dimensions du réseau de la grille, cette relation peut être simplifiée en :

$$B = \frac{4w_{eff} P_y}{p_x \lambda} \ln \frac{2p_y}{\pi g_0} = 4 \left(a \frac{P_y}{P_x} \right) \left(\frac{w}{P_x} \right) \frac{P_y}{\lambda} \ln \frac{2p_y}{\pi g_0} \quad (8-4)$$

Le rapport P_y/P_x est clairement un paramètre crucial qui affecte la valeur de la capacité. Un facteur de correction de $a=2.5$ est donc requis pour faire correspondre la fréquence de résonance calculée à celle des dimensions actuelles du réseau.

8. 2. 3 Intégration d'éléments actifs

Les diodes PIN haute fréquence sont généralement modélisées par des composants RLC dans leurs états passants et bloqués. Dans cette thèse, le modèle du circuit équivalent représenté à la Fig. 8-6 a été utilisé pour la diode PIN GMP4201 dans toutes les simulations [16]. Dans le cas d'un état passant, la diode représente principalement une faible résistance, qui a un effet négligeable sur la réponse souhaitée de la grille [17].

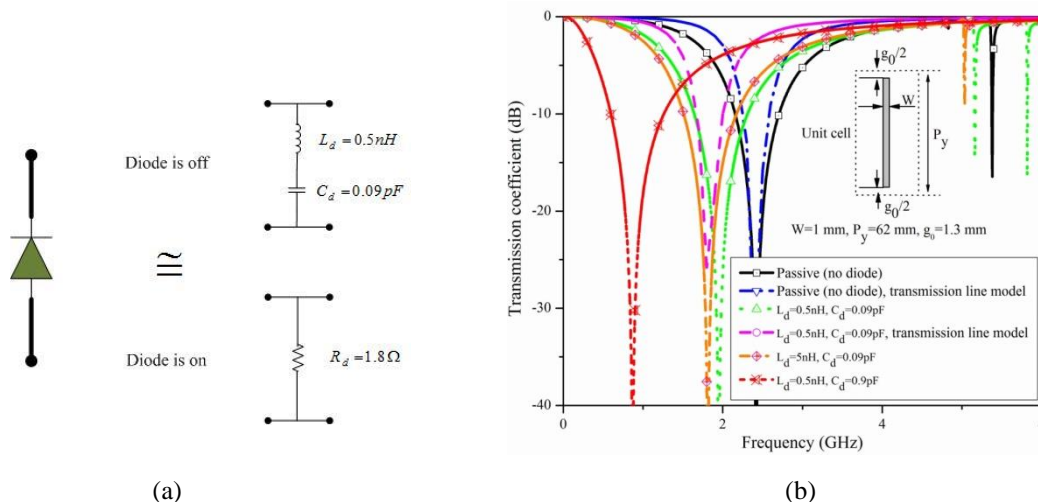


Fig. 8-6 Effet d'un élément actif sur la réponse de la grille (a) Modèle de la diode PIN. (b) coefficient de transmission Simulé pour différentes valeurs de capacités parasites.

Toutefois, lorsque la diode est désactivée, les éléments parasites LC modifient substantiellement la réponse de transmission de la grille en diminuant la fréquence centrale de la bande interdite comme indique dans la Fig. 8-6 pour différentes valeurs

de L_d et de C_d . La simulation montre que la capacité parasite a plus d'influence dans la réduction de la fréquence de la bande interdite que l'inductance. Dans cette figure, le coefficient de transmission simulé a aussi été comparé à celui calculé en utilisant le modèle équivalent de transmission, dans lequel, la capacité parasite est introduite en parallèle avec la capacité de discontinuité. Les bandes interdites calculées sont en accord avec celles simulées.

8. 2. 4 Mécanisme de reconfiguration et ligne d'alimentation de polarisation DC

La Fig. 8-7 montre deux types de mécanismes de reconfiguration et leurs performances de transmission pour cet élément résonant. Dans la première méthode, chaque colonne de rubans dipôles est verticalement alimentée, et le mécanisme de reconfiguration est obtenu en changeant l'état de la surface d'inductif à capacitif.

En agencant des éléments actifs avec une même polarité le long de chaque rangée et en les alimentant horizontalement, un nouveau mécanisme de reconfiguration peut être obtenu [18,19]. Dans ce mécanisme, la reconfiguration est réalisée en augmentant la fréquence de la bande interdite. Ceci fournit des réponses capacitives duales pour les états passants et bloqués des diodes. Cependant, le fait de charger avec les lignes d'alimentation continues change l'impédance équivalente de la surface par rapport à l'impédance calculée dans le cas du mécanisme d'alimentation vertical. Comme nous pouvons le constater à partir des courbes de coefficients de transmission simulées, en insérant les lignes d'alimentation, une réduction de la position dans la bande interdite est obtenue à la fois pour les états passants et bloqués. Essentiellement, en raison du changement de L et C total dans le modèle de circuit résonnant de la cellule de base proposée, l'effet de chargement de ces lignes dégrade la réponse EM de la cellule de base. Cela a tendance à baisser la position de la bande interdite.

En outre, l'effet du chargement, dans le cas discontinu, affecte plus la position de la bande interdite par rapport au cas continu. Ceci s'explique, dans ce cas, par l'importance du changement des valeurs de la capacité C et de l'inductance, provoquant une plus grande déviation. Par conséquent, nous pouvons en conclure que même si la structure permet d'obtenir la surface transparente et opaque souhaitée pour les ondes incidentes EM, les lignes d'alimentation DC influencent fortement la position de la bande interdite. Cela provoque une réduction de la transparence souhaitée de cet état. Par ailleurs, le réseau d'alimentation DC limite l'application de la surface à une structure de reconfiguration particulière. Dans la section suivante, cet effet sera étudié plus en détails pour les applications d'antennes cylindriques reconfigurables.

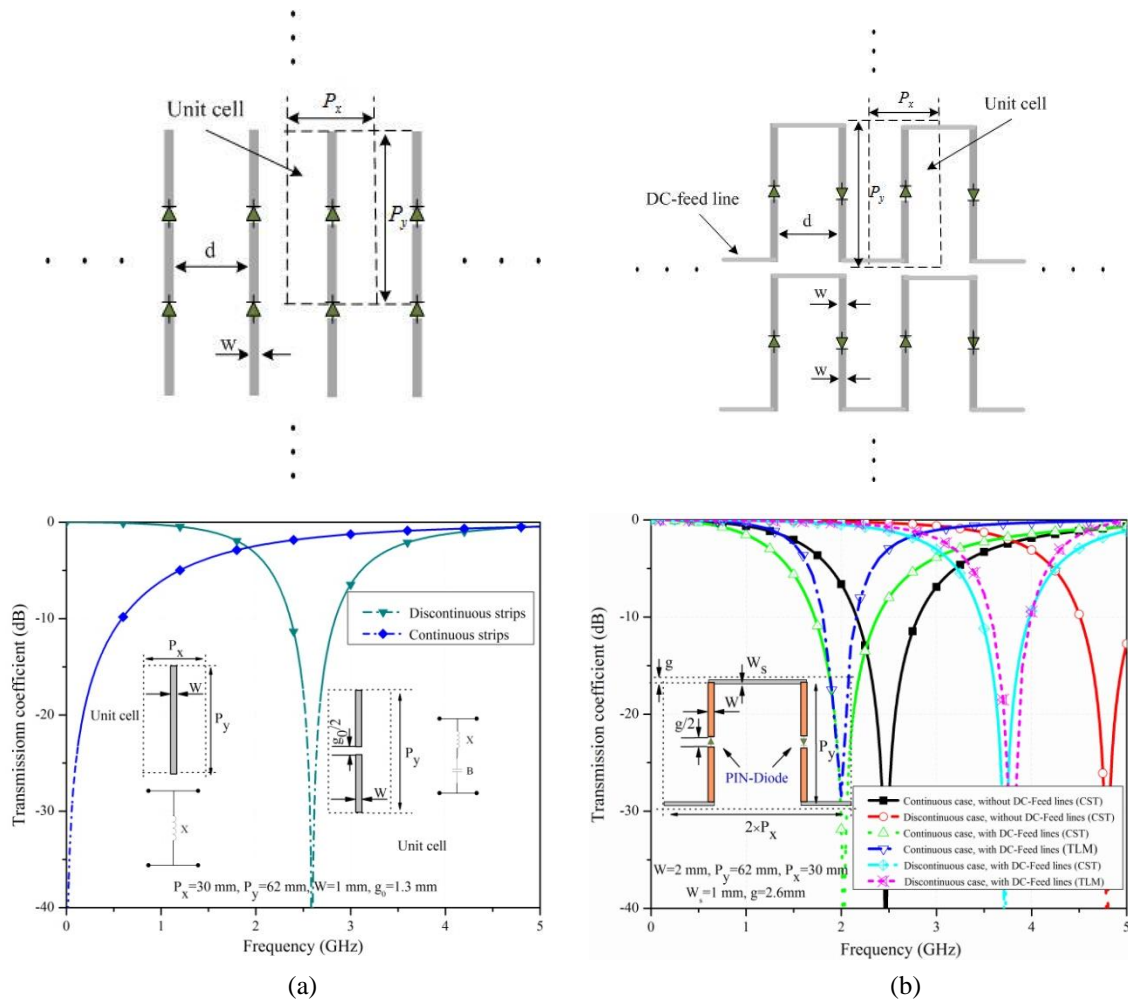


Fig. 8-7 Géométries de deux mécanismes de reconfiguration d'alimentations séries et leurs réponses en coefficient de transmission. (a) Alimentation verticale. (b) Alimentation horizontale.

8.3 Applications de surfaces agiles transparentes/opagues dans les antennes reconfigurables

Dans cette partie, une application du réseau planaire de rubans dipôles pour les antennes à diagramme de rayonnement reconfigurable est présentée. La Fig. 8-8 montre la géométrie de l'antenne dans laquelle le réflecteur métallique solide est remplacé par une surface partiellement réfléchissante reconfigurable. En modifiant l'état du réflecteur partiel d'opaque à transparent, le diagramme de rayonnement d'antenne est reconfiguré du cas uni-directionnel au cas omni-directionnel. Par cette méthode, un

filtrage spatial du signal transmis ou reçu est réalisé. La fréquence de fonctionnement de cette antenne est de 2.45GHz avec une polarisation verticale.

8.3.1 Résultats de simulations et de mesures

Un prototype d'antenne basé sur le second mécanisme de reconfiguration a été simulé et fabriqué [19]. La surface reconfigurable est composée de 8×4 lignes de la cellule de base idéale proposée dans la Fig. 8-7b, et est gravée sur un substrat RO3003 avec une constante diélectrique $\epsilon_r = 3$ et une épaisseur de 0.254 mm. Cette grille est placée à 20 mm d'un dipôle. Ce dernier est construit par deux tiges avec un rayon de 3 mm et de longueur 23 mm relié à un connecteur SMA. La diode PIN GMP4201 [16] haute fréquence a été utilisée comme élément de commutation dans les grilles proposées. Les éléments parasites inductifs et capacitifs ($L = 0.5$ nH et $C = 0.09$ pF) sont utilisés pour modéliser la diode dans la simulation. Cette surface est conçue pour fonctionner à la fréquence souhaitée dans laquelle la ligne d'alimentation DC et l'effet parasite sont compensés.

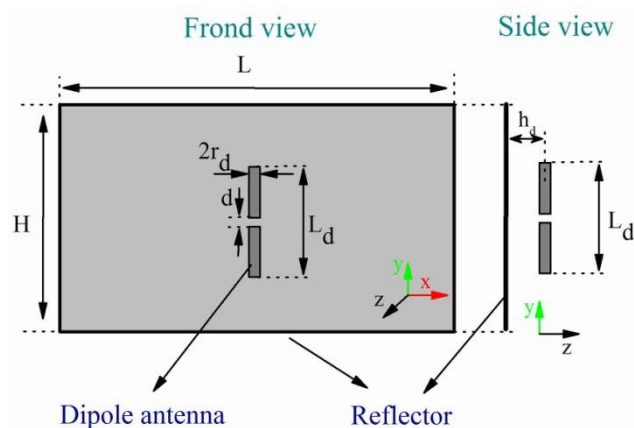


Fig. 8-8 Géométrie d'une antenne à réflecteur plan.

Pour évaluer précisément les performances de la grille proposée, son coefficient de transmission est mesuré. Les coefficients de transmission ont été mesurés pour quatre différents cas de Fig. 8-9, et ils montrent un bon accord avec ceux simulés.

Cette surface a été appliquée pour fabriquer l'antenne réflecteur reconfigurable plate de la Fig. 8 8. Le prototype fabriqué et les paramètres d'antenne ont été montrés à la Fig. 8 10a. Comme nous pouvons le remarquer, le coefficient de réflexion et les diagrammes de rayonnement mesurés à la Fig. 8 10 et Fig. 8-11 confirment ceux de simulations. Cela confirme le potentiel de la surface proposée pour créer une antenne à diagramme de

rayonnement reconfigurable dans laquelle la zone de couverture spatiale et également le gain de l'élément rayonnant placé à proximité de la surface sont commandés.

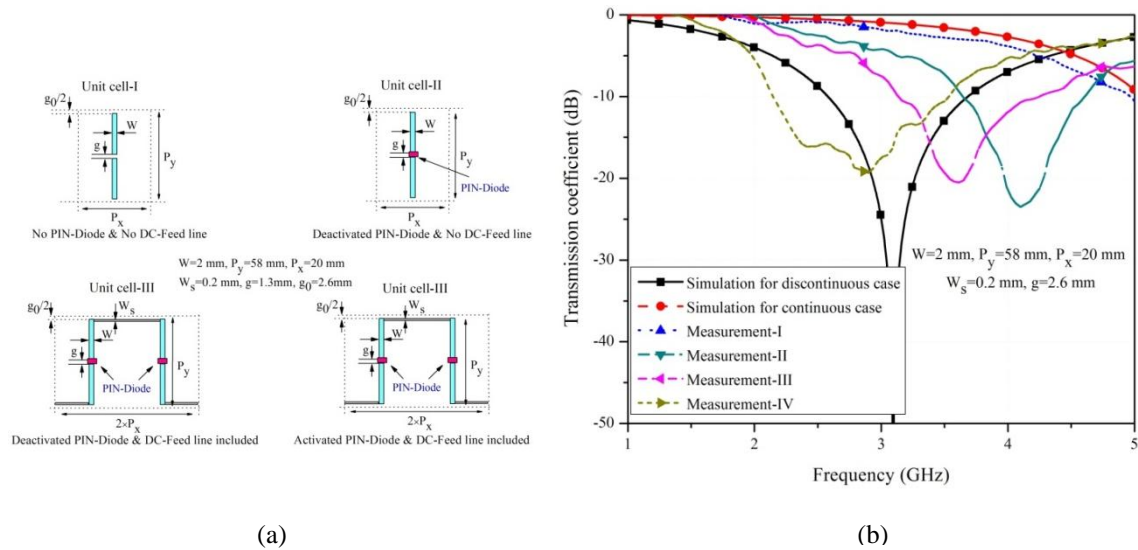


Fig. 8-9 Évaluation des performances d'une SSF basé sur la cellule de base proposée. (a) Quatre différents SSF construits en utilisant 24×4 éléments de ces cellules de base. (b) Coefficient de transmission mesuré comparé à la simulation.

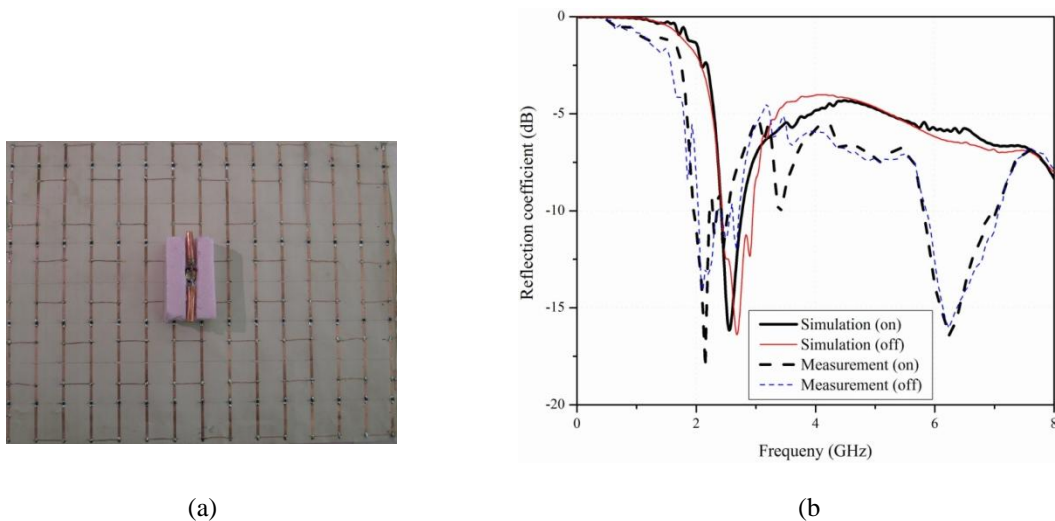


Fig. 8-10 Photo du prototype fabriqué (a), et des résultats du coefficient de réflexion (b).

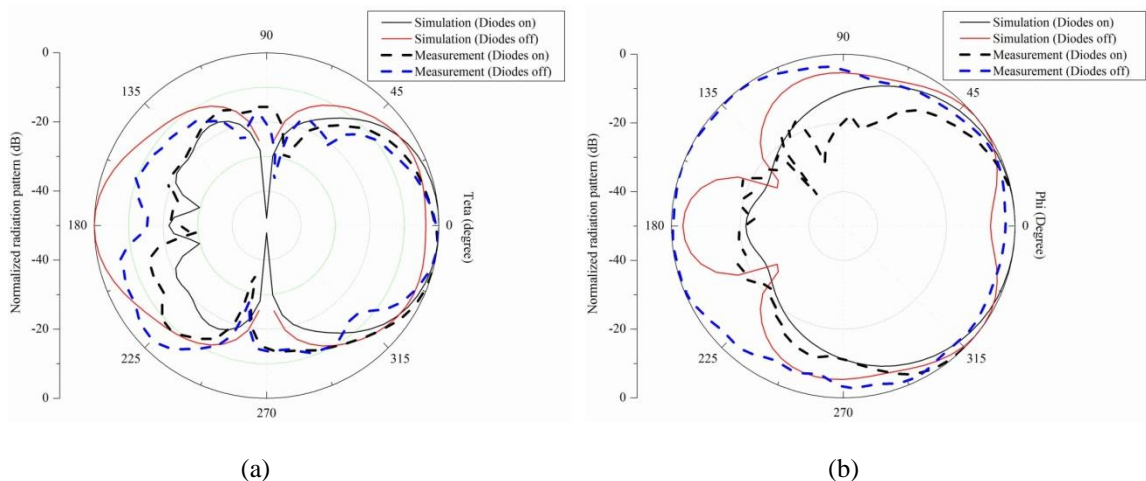


Fig. 8-11 Diagramme de rayonnement de l'antenne. (a) Diagramme E plan (b) Diagramme H plan.

8.4 SSF cylindrique et antennes agiles en diagramme de rayonnement

Cette partie vise à introduire une catégorie d'antennes reconfigurables avec plus de fonctionnalités en utilisant les SSF proposés à la Fig. 8-7 [18]. Les paramètres de rayonnement désirés de l'antenne sont brièvement résumés comme suit :

- Diagramme de rayonnement directionnel.
- Balayage de tous les angles azimutaux.
- Polarisation verticale.
- Diagramme de rayonnement reconfigurable de directionnel à omnidirectionnel.
- Un minimum de 10% bande passante tant pour l'impédance que pour le gain.
- Gain moyen autour de 8dB.
- Taille minimale de l'antenne et moins des éléments actifs.
- Fréquence de fonctionnement de 2.45GHz.
- Niveau des lobes secondaires/arrières inférieur à -20dB tant dans le pan E que dans le plan H.

Pour réaliser ces objectifs, une antenne à réflecteur cylindrique utilisant des surfaces reconfigurable sélective en fréquence, est proposée à la Fig. 8-12. Dans cette configuration, la surface réfléchissante/transparente partiellement commandée est éclairée par un simple dipôle rayonnant placé au centre du cylindre. Pour réaliser un faisceau directionnel, une partie de ce cylindre se comporte comme un réflecteur qui réfléchit les ondes émanant du dipôle, tandis que l'autre partie est transparente pour ces ondes. Par des interactions constructives entre ces ondes, un diagramme de rayonnement directif est

créé en face du réflecteur. Alternativement, lorsque toute la surface cylindre est transparente pour le dipôle rayonnant, le rayonnement de l'antenne globale devrait être seulement celui du dipôle. Par conséquent, le faisceau directif devient un diagramme omnidirectionnel à faible gain. Pour modifier la direction du rayonnement directif, la partie demi-cylindre opaque/transparente du réflecteur est déplacée autour du cylindre en activant/désactivant séquentiellement les cellules de base appropriées sur la SSF.

Selon l'approche de polarisation DC utilisée pour les éléments actifs, deux types de réseaux SSF constitués de rubans discontinus verticalement et horizontalement alimentés sont proposés comme une surface reconfigurable cylindrique utilisée dans l'antenne représentée à la Fig. 8-12. Ensuite, les avantages et les inconvénients de chaque antenne sont présentés et discutés. Pour effectuer ces tâches, l'encombrement du cylindre est d'abord déterminé en utilisant les principes d'antennes à réflecteur. Par la suite, les SSF planaires proposées sont transformées en une forme cylindrique pour construire une antenne reconfigurable basée sur le mécanisme de rayonnement mentionné précédemment. Les dimensions de l'antenne sont enfin optimisées par CST pour atteindre les objectifs de rayonnement souhaités pour chaque prototype d'antenne.

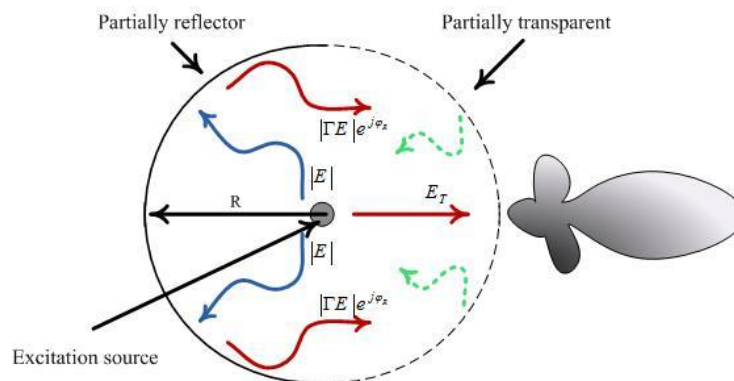


Fig. 8-12 Géométrie de l'antenne SSF active, reconfigurable, cylindrique proposée (ASSFARC).

8. 4. 1 Antenne reconfigurable à faisceau commuté utilisant une SSF cylindrique

La géométrie de l'antenne reconfigurable à faisceau commuté et la configuration distribuée de son réflecteur SSF cylindrique sont illustrés à la Fig. 8-13. Le mécanisme de reconfiguration est obtenu en modifiant la périodicité de la SSF capacitive. Comme il est évident à partir du schéma distribué de la SSF, à cause du mécanisme d'alimentation, cette antenne est seulement en mesure de fournir deux faisceaux commutables directifs orientés dans deux directions opposées. À chaque fois, une partie de l'antenne est

transparente pendant que l'autre partie se comporte comme une surface partiellement réfléchissante. Dans cette structure, les lignes d'alimentation DC parallèles, le long des axes des cylindres, sont isolées de la surface par des RF-Chocks. Il sera démontré que ces lignes d'alimentation de polarisation affectent considérablement le rayonnement dans le plan H et le gain de l'antenne.

8. 4. 1. 1 Résultats expérimentaux et discussion

La Fig. 5-12 montre une photo du prototype d'antenne à faisceau commuté reconfigurable fabriqué. Une simple antenne dipôle est utilisée comme élément d'excitation. Ce dipôle est fabriqué en soudant deux morceaux de feuille mince de cuivre laminé directement à un connecteur RF SMA. Les diodes PIN haute fréquence, polarisées avec un réseau d'alimentation DC, sont connectées à la grille SSF utilisant des inductances RF-Chock. Ces dernières séparent le réseau d'alimentation de polarisation de la FSS sur la bande passante souhaitée de l'antenne. De la mousse rigide est utilisée comme support pour positionner l'antenne dipôle au milieu du cylindre.

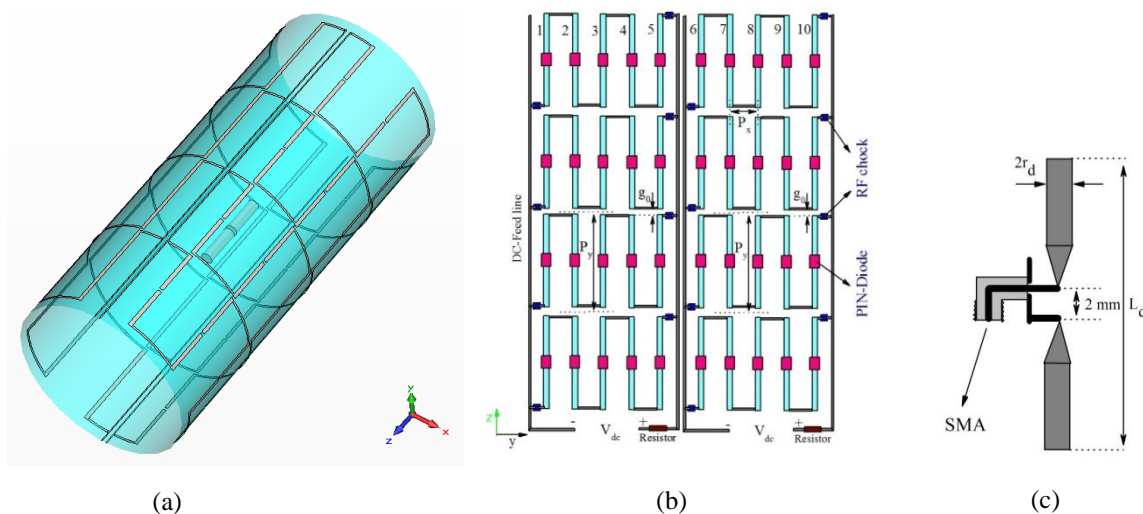


Fig. 8-13 Antenne reconfigurable à réflecteur cylindrique. (a) Vue en perspective de l'antenne (b) Schéma de la géométrie distribuée de la SSF $P_x = 28.8$, $P_y = 52$, $w = 1$. (c) Antenne dipôle utilisée dans l'antenne à réflecteur cylindrique à faisceau commuté $L_d = 40$, $R_d = 3$, (valeurs en mm).

Afin d'examiner les performances du concept proposé, premièrement, les pertes par désadaptation de l'antenne ont été mesurées. Ensuite, certaines mesures ont été effectuées pour des diagrammes de rayonnement directs dans le plan H de l'antenne à différentes fréquences. De cette façon, le meilleur diagramme de rayonnement en termes de faisceau principal désiré, de gain réalisé, de lobes secondaires et du niveau des

lobes arrière est identifié. Enfin, d'autres diagrammes ont été mesurés pour évaluer les performances de rayonnement dans l'autre plan ainsi que pour le cas omnidirectionnelle.



Fig. 8-14 Photo de l'antenne reconfigurable à faisceau commuté fabriquée.

La Fig. 5-13 montre les résultats expérimentaux du faisceau commuté comparés à ceux mesurés pour l'antenne dipôle. Comme on peut le constater, le dipôle large bande fonctionne efficacement au-dessus de 2.6GHz, alors que quand il est placé au centre de la SSF cylindrique, il fonctionne efficacement autour de 2.45GHz. La perte par désadaptation mesurée pour cette structure démontre une meilleure adaptation comparée aux résultats obtenus par simulation. En outre, la désactivation des diodes conduit à un léger déplacement de la courbe de perte par désadaptation, ce qui a été prédit par les simulations. Ses diagrammes de rayonnement dans le plan H et le plan E à la fréquence 3.2GHz sont comparés à ceux liés à l'antenne reconfigurable. Certaines asymétries sont remarquées dans le plan E et H de l'antenne dipôle ce qui est principalement dû au câble RF et au connecteur SMA utilisés dans la conception de l'antenne.

Cependant, son diagramme dans le plan H rayonne uniformément à tous les angles. Les diagrammes de rayonnement mesurés dans le plan E et dans le plan H démontrent des meilleures performances à la fréquence de 2.45GHz, ce qui confirme le concept proposé. Il est clair que la configuration proposée peut fournir un diagramme de rayonnement directif avec un meilleur niveau du lobe arrière que -17dB et -14dB, respectivement, pour les diagrammes des plans H et E. En raison de la diffraction sur les bords de l'ouverture, ce niveau est un peu dégradé à d'autres angles dans le plan arrière. Comme il fallait s'y attendre, les alimentations DC parallèles sur les côtés affectent le diagramme de rayonnement dans le plan H quand toutes les diodes sont boquées. La Fig. 5-13b montre les gains mesurés pour l'antenne à différentes fréquences. De cette figure, il peut être remarqué que l'antenne est en mesure de proposer un diagramme de rayonnement directif avec plus de 8dB de

gain proche de la fréquence de fonctionnement désirée. La différence entre les simulations et les mesures s'explique en raison des imprécisions de conception et de mesure. Les caractéristiques réalisées pour cette antenne ont été comparées aux résultats de simulation de l'antenne réflecteur solide semi-cylindrique appropriée, dans le Tab. 8-1.

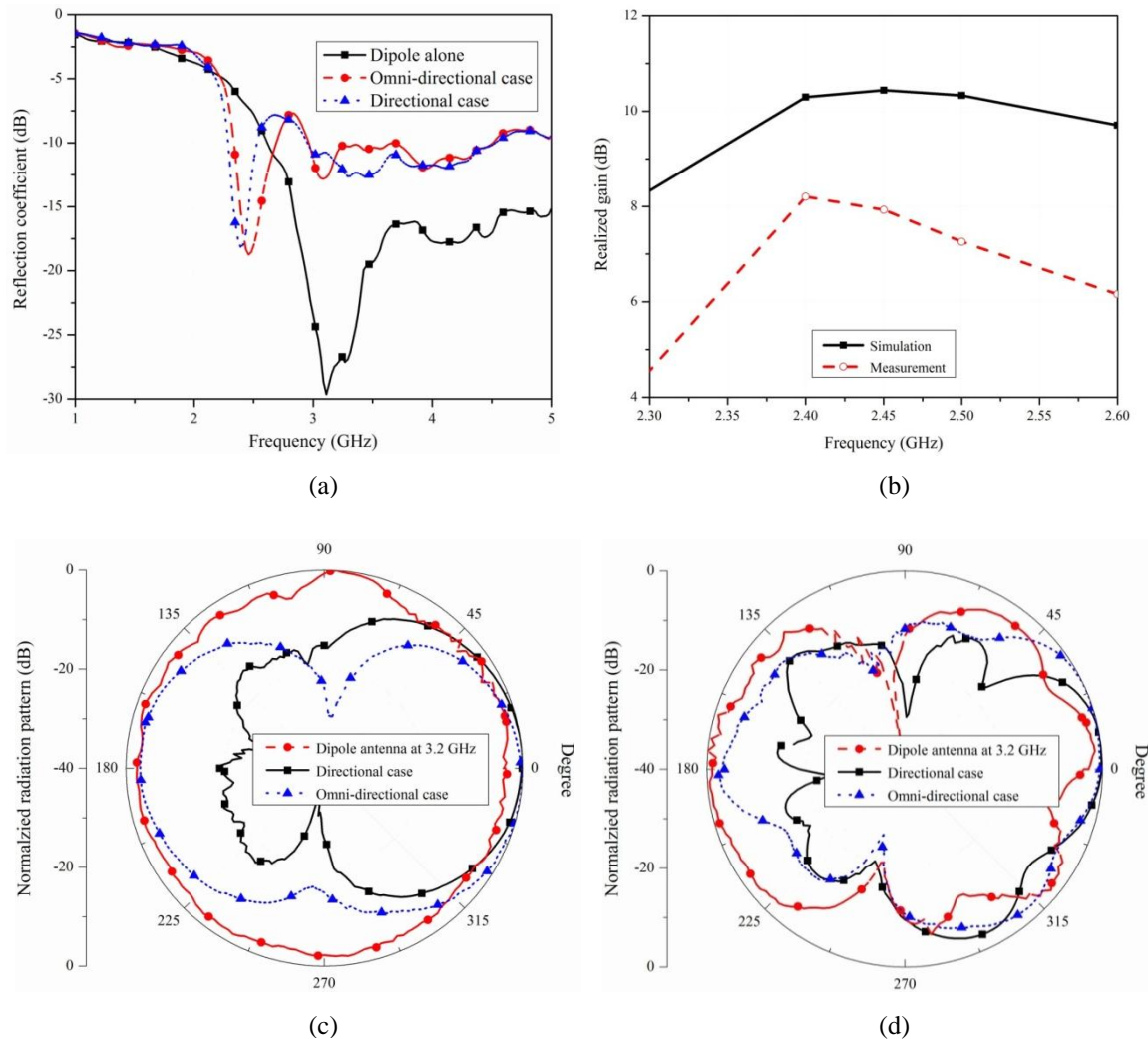


Fig. 8-15 Résultats mesurés et simulés pour l'antenne à faisceau reconfigurable commuté (a) Coefficient de réflexion (b) Gain réalisé. (c) Diagramme de rayonnement dans le plan H (d) Diagramme de rayonnement dans le plan E.

Tab. 8-1 Caractéristiques de rayonnement de l'antenne à faisceau commuté.

	Antenne à faisceau commuté				Réflecteur solide Semi-cylindrique	
	Simulation		Mesure		Simulation	
BW (MHz)	Omni 230	Dir. 175	Omni 375	Dir. 250	Faisceau directionnel 1250	
BL (dB)	-13.64		-17		-25.5	
HPBW (Deg.)	H 68	E 43	H 75	E 45	H 70	E 46
Gain (dB)	10.2		7.5		10	

8. 4. 2 Antenne agile en diagramme de rayonnement

Dans la partie précédente, le diagramme de rayonnement de l'antenne reconfigurable proposée n'a pas été en mesure de balayer tous les angles azimutaux. Le mécanisme de reconfiguration appliqué et les lignes d'alimentation DC requises limitaient la couverture de l'espace à deux faisceaux commutés orientés dans des directions opposées. Par ailleurs, en raison de la présence de ces lignes d'alimentation, le diagramme de l'antenne a également été sensiblement dévié dans le cas omnidirectionnel. Dans cette section, une nouvelle antenne est proposée, en surmontant les contraintes mentionnées ci-dessus de l'antenne reconfigurable à faisceau commuté. En utilisant cette nouvelle antenne, les contraintes du réseau d'alimentation sont atténuées, et donc plus de fonctionnalités sont offertes par l'élément rayonnant. En effet, dans ce cas, non seulement l'antenne peut balayer son faisceau sur la totalité du plan azimutal comme une structure agile, mais elle a aussi la possibilité de reconfigurer son diagramme de rayonnement de directionnel à omnidirectionnel. En raison de l'introduction de ces performances originales, i. e., l'agilité de balayer sur tous les angles azimutaux et la reconfiguration d'un diagramme de rayonnement de directif à omni-directionnel, cette antenne a été nommée "antenne à diagramme de rayonnement agile" [18].

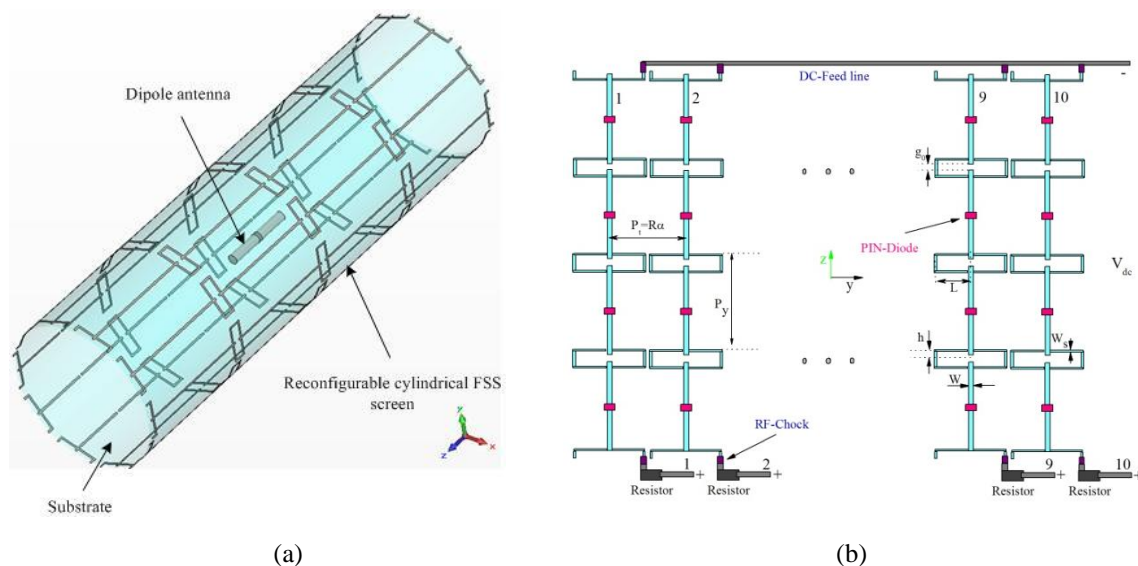


Fig. 8-16 Antenne agile en diagramme de rayonnement (a) Configuration de l'antenne (b) SSF cylindrique appliquée à une configuration distribuée.

La Fig. 5-14 représente l'antenne agile et sa SSF cylindrique distribuée appropriée. De la même manière, cette antenne est construite à partir d'une simple antenne dipôle entourée par une surface cylindrique reconfigurable. Le principe de rayonnement de cette antenne est basé sur le mécanisme de rayonnement décrit à la Fig. 8-12. En

conséquence, le même nombre de cellules de base le long de la circonférence du cylindre est choisi. Cependant, la méthode de reconfiguration pour ce cas est réalisée en changeant la SSF semi-cylindrique du cas inductif à capacitif. Cela signifie qu'en désactivant l'élément actif dans la moitié de la partie du cylindre, un réflecteur est créé. En même temps, tous les interrupteurs dans l'autre partie sont activés pour laisser les ondes passer à travers la surface. Par conséquent, en activant/désactivant séquentiellement un groupe de cinq colonnes autour du cylindre, le diagramme de rayonnement de l'antenne peut facilement balayer la totalité des angles azimutaux en 10 étapes.

8.4.2.1 Résultats expérimentaux et discussion

La Fig. 8-18 montre le prototype de l'antenne reconfigurable, à faisceau agile, fabriquée. Une simple antenne dipôle est utilisée à nouveau comme élément d'excitation. Ce dipôle est fabriqué en soudant deux morceaux de feuille minces de cuivre enroulés directement à un connecteur RF-SMA. Les RF-Chocks montrés dans la configuration distribuée séparent le réseau alimenté de polarisation de la SSF sur la bande passante souhaitée de l'antenne. Un cadre approprié est élaboré avec de la mousse rigide pour fixer l'antenne dipôle au milieu du cylindre et aussi comme support pour la souple SSF.

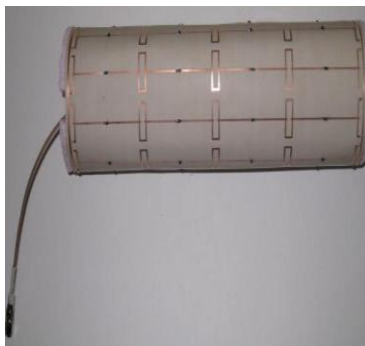


Fig. 8-18 Photo de l'antenne agile fabriquée.

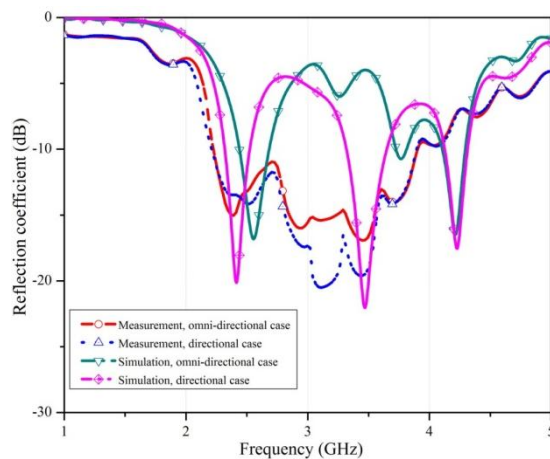


Fig. 8-19 Coefficient de réflexion simulé et mesuré pour antenne à faisceau agile.

La Fig. 8-19 montre la perte par désadaptation mesurée de l'antenne agile pour les deux états de fonctionnement. Comme on peut le constater, les résultats mesurés sont meilleurs que ceux simulés et l'antenne correspond à une impédance d'entrée de 50Ω sur une large bande de fréquence aussi bien dans le cas directif que dans le cas omnidirectionnel.

La Fig. 5-22 montre les diagrammes de rayonnements dans les plans H et E. Les mesures pour les diagrammes de rayonnement directifs dans le plan H à différentes fréquences de la bande passante couverte montrent que cette antenne a un meilleur diagramme de rayonnement en termes de directivité et de niveau des lobes secondaires/arrières à la fréquence 2.35GHz. Cette structure offre un niveau de lobe arrière meilleur que 20dB dans le plan H. Le niveau de lobe arrière à certains angles du plan n'est pas aussi bon que celui du plan H.

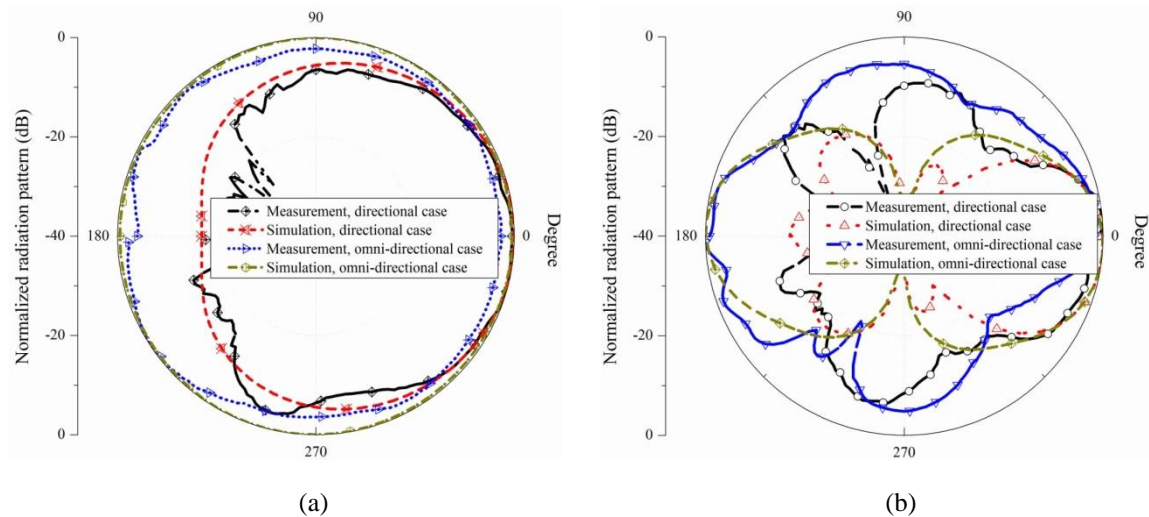


Fig. 8-20 Diagramme de rayonnement mesuré pour antenne à faisceau agile (a) Diagramme de rayonnement dans le plan H. (b) Diagramme de rayonnement dans le plan E.

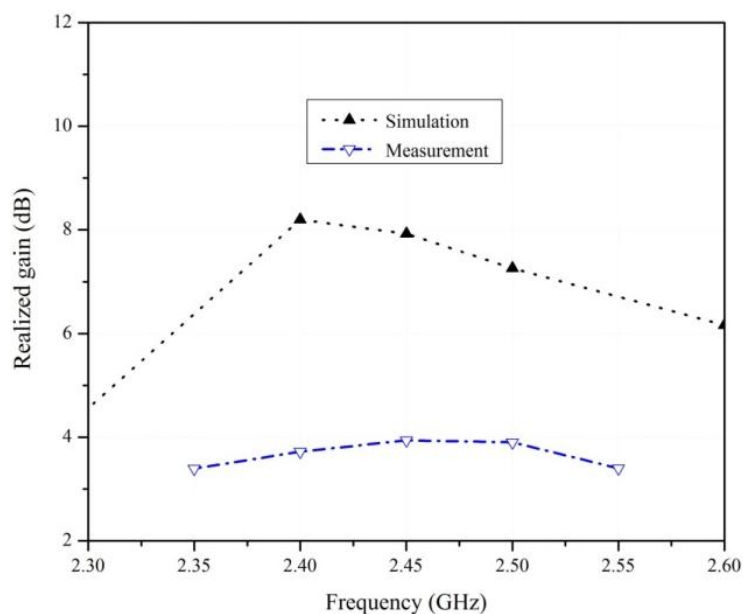


Fig. 8-21 Simulation et mesures du gain réalisé de l'antenne agile

Comme il a été prédit par les mesures dans le plan E, à cause des fuites de puissance dans la direction Z, une certaine réduction de gain est prévue dans le diagramme de rayonnement. Ceci peut être observé dans le gain réalisé mesuré de l'antenne à la Fig. 5-23, obtenu par la méthode de comparaison du gain. Ceci est principalement dû au fait que l'antenne ne fonctionne pas efficacement selon le comportement EM attendu pour chaque partie de la SSF. Ceci peut être atténué par l'optimisation de la structure selon les résultats expérimentaux obtenus. Les caractéristiques obtenues pour cette antenne ont été comparées, à la Tab. 8-2, aux résultats de simulation de l'antenne appropriée à réflecteur solide semi-cylindrique.

Tab. 8-2 Caractéristiques de rayonnement d'antennes agiles comparés au réflecteur semi-cylindrique.

	Antenne agile				Réflecteur antenne à Semi-cylindrique	
	Simulation		Mesure		Simulation	
BW (MHz)	Omni	Dir.	Omni	Dir.	Faisceau directionnel	
	-	102	Wide	Wide	1250	
BL (dB)	-15		-20		-25	
HPBW (Deg.)	H	E	H	E	H	E
	112	42	104°	40	70	46
Gain (dB)	8.2		3.94		10	

8. 4. 3 Antenne agile en diagramme de rayonnement et en fréquence

Dans la section précédente, une antenne agile en diagramme de rayonnement a été proposée. Cette antenne agile permettait d'obtenir soit le balayage de faisceau soit des caractéristiques de passage d'un diagramme de rayonnement directionnel à omnidirectionnel. Toutefois, en raison des effets néfastes des éléments parasites diode PIN, les réponses de transmission et de réflexion des deux parties semi-cylindrique de la SSF sont détériorées. Ceci a provoqué une certaine dégradation dans les performances de rayonnement de l'antenne et a aussi limité la bande passante réalisable.

Dans cette partie, une nouvelle SSF reconfigurable est proposée afin de s'affranchir, en quelque sorte, des limites, mentionnées ci-dessus, des autres SSF [18]. Cette SSF reconfigurable est construite par un réseau d'éléments hybrides. Chaque élément comprend des rubans discontinus et des anneaux elliptiques. En effet, en créant deux bandes interdites l'une près de l'autre, le niveau de transparence de la surface pour l'état passant a été considérablement amélioré. En outre, la possibilité de deux réponses duales à deux différentes bandes de fréquences a également été étudiée analytiquement et expérimentalement [20]. Ensuite, cette surface a été reformée en une forme cylindrique

pour concevoir une autre antenne agile en diagramme de rayonnement. En prime, il a aussi été démontré expérimentalement que la nouvelle antenne est capable de fonctionner sur deux différentes bandes de fréquences avec les mêmes fonctionnalités. Par ailleurs, le nombre d'éléments actifs de cette antenne a été réduit en réduisant la taille de l'antenne, tout en gardant quasiment la même directivité. Dans les sections suivantes, le processus de conception et les résultats obtenus sont présentés et discutés.

8.4.3.1 Conception d'une SSF hybride reconfigurable

La Fig. 6-1 montre la géométrie de la SSF reconfigurable double bande proposée. Elle est constituée par des réseaux périodiques d'une cellule de base hybride résonante. Cette cellule de base est créée en combinant deux éléments comprenant les rubans discontinus et un anneau elliptique. Pour reconfigurer la réponse en transmission de la surface, une diode PIN haute fréquence est utilisée à l'endroit de la discontinuité le long du ruban. En changeant l'état de l'interrupteur, des réponses duales en transmission peuvent être obtenues sur deux régimes de fréquence étroits et juxtaposés l'un à l'autre. Ceci peut être utilisé comme un réflecteur partiel pour concevoir une antenne reconfigurable à réflecteur cylindrique.

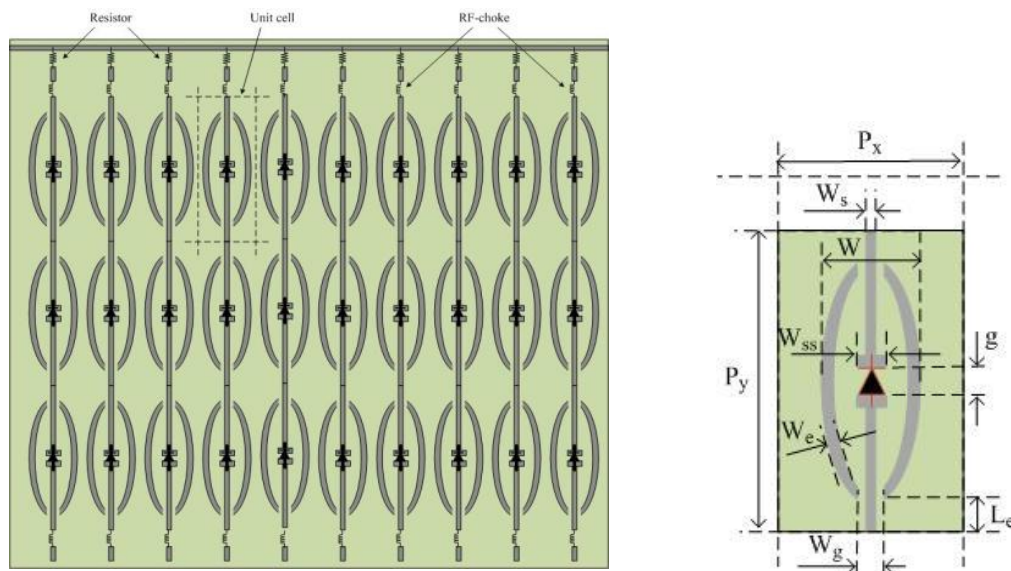


Fig. 8-22 Géométrie d'une SSF double bande reconfigurable et modèle de ligne de transmission de sa cellule de base.

L'amplitude et la phase calculées des paramètres de diffraction de cette cellule de base hybride ont été représentées à la Fig. 8-23. En configurant l'élément actif en mode passant, la première bande interdite reliée aux rubans discontinus disparaît, et donc la

surface est reconfigurée à l'état transparent autour de la fréquence désirée 2.45GHz. En outre, un régime de fréquence supplémentaire avec des réponses duales est obtenu à côté de la première bande. Dans la seconde bande, une réponse est liée à la région de blocage de l'état passant et l'autre est créée par la région transparente entre les deux bandes interdites de l'état bloqué. Cela signifie que lorsque la surface est transparente dans la première bande, elle sera opaque en même temps dans la seconde bande. En effet, par cette cellule de base hybride, une réponse duale reconfigurable sur deux différentes bandes de fréquences peut être réalisées pour les antennes ou les applications de blindage électromagnétique [20].

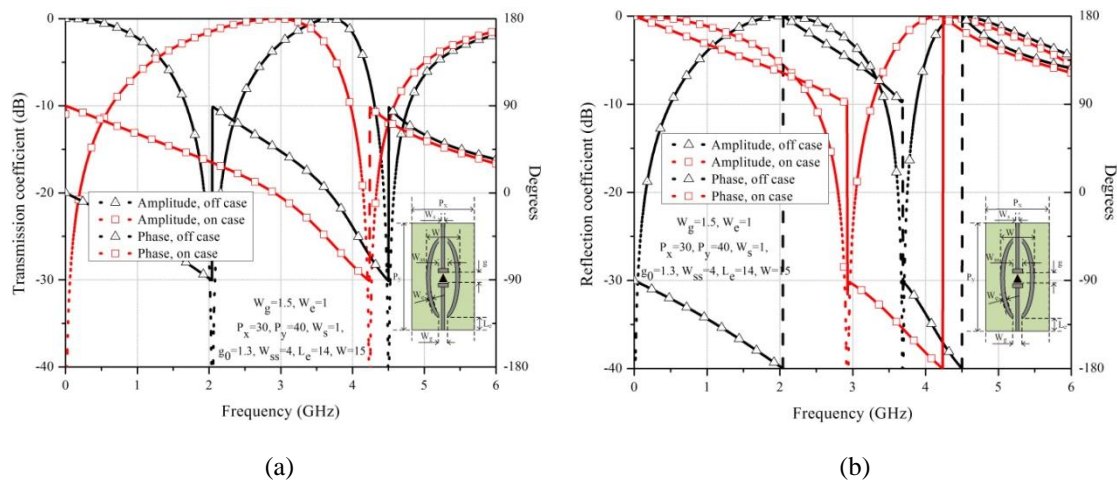


Fig. 8-23 Réponse des coefficients de transmission et réflexion d'une SSF double bande hybride reconfigurable. (a) Coefficient de transmission. (b) Coefficient de réflexion.

8.4.3.2 Conception de l'antenne et résultats expérimentaux

La Fig. 8-24 montre l'antenne agile en diagramme de rayonnement qui fonctionne sur deux bandes de fréquences. Cette antenne est essentiellement basée sur le mécanisme de rayonnement décrit à la Fig. 8-12. Elle est constituée d'une antenne dipôle placée au centre d'une surface active, reconfigurable, sélective en fréquences.

En évaluant les coefficients de transmission/réflexion de la SSF, nous avons remarqué que les dimensions de la cellule de base déterminent substantiellement la surface en réponse aux ondes électriques incidentes polarisées verticalement. Ceci détermine directement les performances de l'antenne reconfigurable à réflecteur cylindrique. Par ailleurs, en changeant la forme de la SSF planeaire en une forme cylindrique et en l'éclairant par une antenne dipôle dans son champ proche, les réponses de la surface en réflexion et en transmission devraient être modifiées. Par

conséquent, pour étudier expérimentalement cette question et mettre en œuvre avec succès une antenne agile, deux SSF reconfigurables avec différentes dimensions de cellules de base ont été fabriquées et leurs coefficients de transmission ont été mesurés. Ensuite, ces SSF ont été utilisées comme réflecteur partiel cylindrique pour fabriquer une antenne agile. Les caractéristiques de rayonnement de deux antennes sur une grande bande de fréquence ont été mesurées.

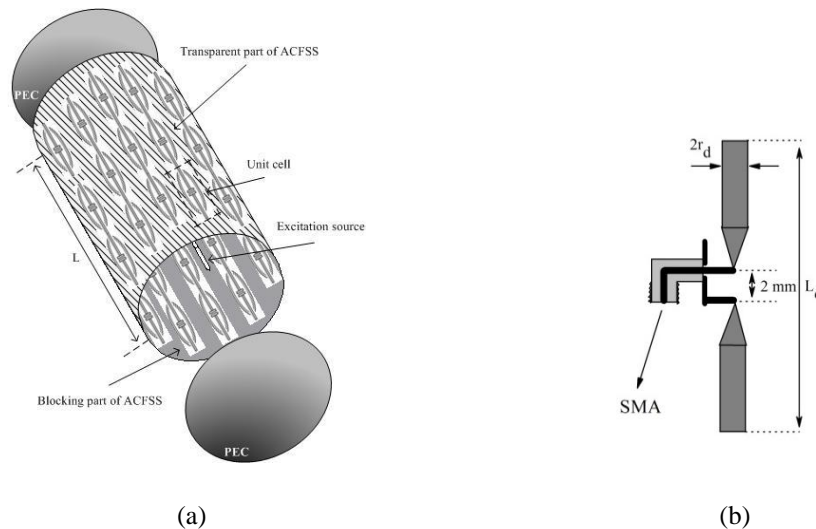


Fig. 8-24 Antenne agile en diagramme de rayonnement et en fréquence. (a) Géométrie de l'antenne (b) Source d'excitation.

8. 4. 3. 3 Mesure du coefficient de transmission

Des dimensions de surfaces de $30\text{cm} \times 60\text{cm}$ et $15\text{cm} \times 30\text{cm}$ ont été utilisées pour la SSF-A et B, respectivement. Les éléments actifs de chaque colonne ont été activés par une résistance connectée au générateur de tension continue. Les résistances et les lignes d'alimentation DC ont été isolées de la SSF par les inducteurs pour les déconnecter de la surface sur la bande de fonctionnement.

Les résultats de mesure dans la Fig. 8-25 confirment que les dimensions de la cellule de base doivent être précisément choisies pour obtenir des réponses duales reconfigurables souhaitées sur une ou deux fréquences de fonctionnement distinctes. En général, bien que les courbes de mesure suivent celles de simulation pour les deux surfaces, certains écarts sont observés à la fois pour les états passants et bloqués de la surface-A et B. Ceci s'explique par la taille limitée des surfaces et de la mesure mise en place qui a été effectuée en espace libre sans pour autant éliminer les réflexions multiples. Par

ailleurs, les antennes cornets utilisées dans les mesures n'éclairent pas toute la SSF avec une onde plane uniforme.

Considérant le résultat présenté à la Fig. 8-25a, la première mesure pour la SSF-A montre une réponse duale de 2.2GHz à 2.75GHz qui peut être reconfigurée en modifiant l'état des diodes PIN dans la surface. En modifiant les dimensions de la cellule de base, nous avons confirmé que des réponses duales peuvent être étendues à deux bandes de fréquences distinctes, allant presque de 2GHz à 2.7GHz et de 2.7GHz à 3.2GHz. Ceci peut être potentiellement utilisé pour concevoir une antenne agile en fréquence et en diagramme de rayonnement comme cela sera décrit dans les sections suivantes. Plus intéressant, en utilisant cette SSF, une antenne agile peut être conçue pour une large gamme de fréquences de fonctionnement selon les coefficients de transmission/réflexion de la surface cylindrique reconfigurables. Par conséquent, la limitation de la conception de la gamme de fréquences de fonctionnement de l'antenne agile présentée dans la partie précédente est surmontée.

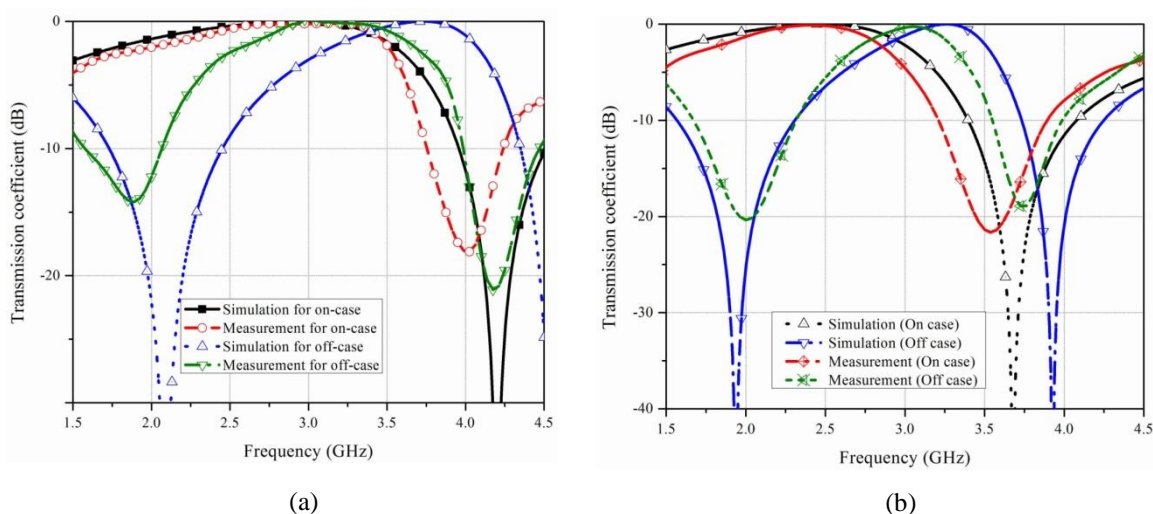


Fig. 8-25 Coefficients de transmission simulés et mesurés. (a) SSF-A. (b) SSF-B.

8. 4. 3. 4 Résultats expérimentaux de l'antenne et discussions

Avant d'insérer l'antenne dipôle au centre de la SSF cylindrique, comme une référence, les caractéristiques de rayonnement de l'antenne dipôle ont été mesurées. Puis, deux antennes à réflecteur reconfigurable cylindriques ont été fabriquées. Dans le processus de mesure de ces antennes agiles, premièrement, leurs coefficients de réflexion ont été mesurés. Ensuite, leurs diagrammes de rayonnement ont été mesurés dans le plan H à différentes fréquences comprises entre 2GHz à 3.2GHz afin d'examiner la capacité des

antennes à créer un diagramme de rayonnement directif. Les résultats de mesure ont démontré que seule l'antenne avec la FSS-B est en mesure de fournir des performances agiles dans deux différentes bandes de fréquences. Fig. 8-26 représente le prototype d'antenne fabriqué.

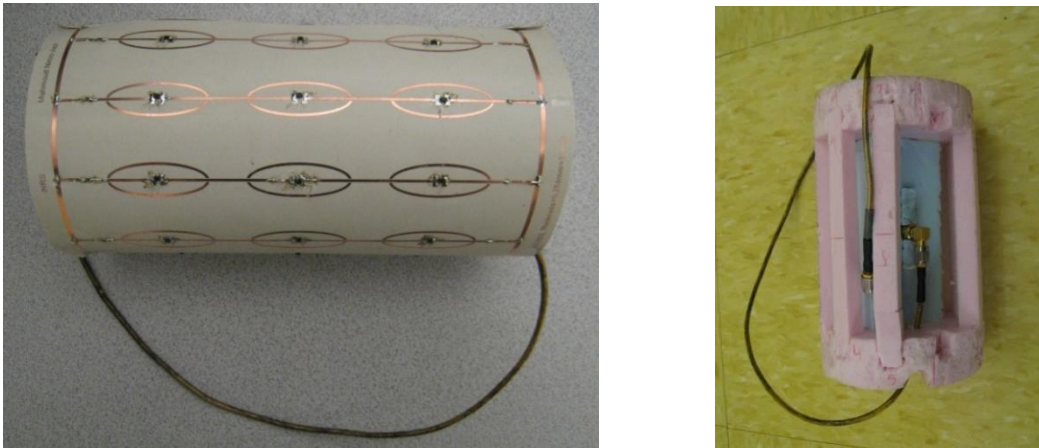


Fig. 8-26 Prototype fabriqué de l'antenne agile en diagramme de rayonnement.

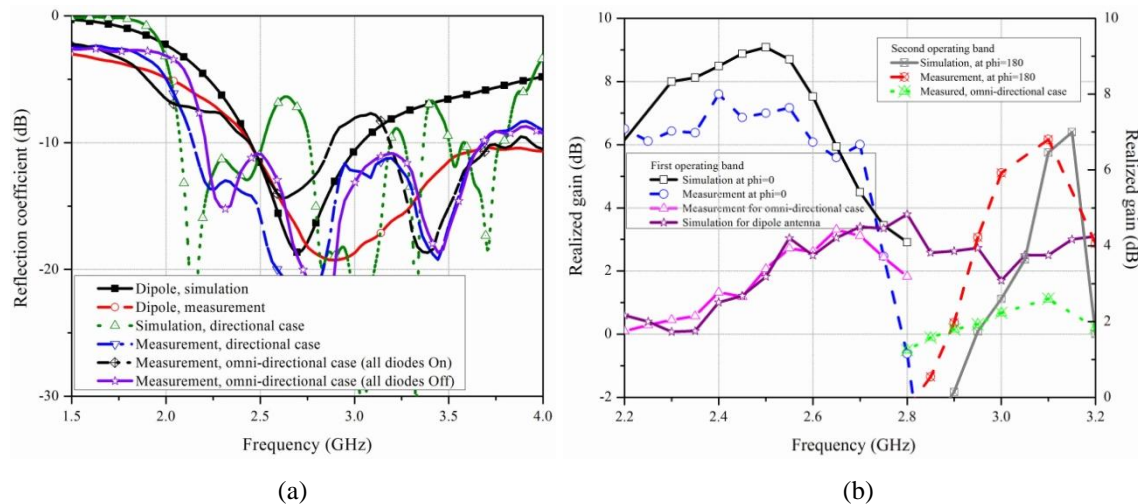


Fig. 8-27 Coefficients de réflexion simulé et mesuré et gain du dipôle et de l'antenne agile en fréquence.
(a) Coefficient de réflexion. (b) Gain.

Les coefficients de réflexion mesurés de l'antenne agile en diagramme de rayonnement dans les cas directif et omnidirectionnel ont été comparés aux simulations à la Fig. 8-27. Dans l'ensemble, certains écarts entre les résultats de simulation et expérimentaux sont remarquables. Ceci est dû à la simplicité dans la simulation qui utilise seulement deux morceaux de tiges métalliques comme antenne dipôle. Par conséquent, les effets des connecteurs RF et ceux du câble ont été négligés au cours du processus de

conception. De cette façon, afin de démontrer l'impact de la SSF sur l'antenne dipôle, le coefficient de réflexion mesuré du dipôle a également été représenté comme référence. La comparaison des courbes mesurées et simulées confirme que le dipôle offre une bande passante en adaptation supérieure à 1.5GHz quand il est connecté au câble RF, tandis que la bande passante prédite par la simulation est d'environ 600MHz.

Les résultats expérimentaux pour l'antenne agile montrent également que la SSF influence significativement la résonance et l'adaptation de l'antenne dipôle placée en son centre. Dans le cas du diagramme de rayonnement directif, la SSF améliore l'adaptation de l'antenne aux basses fréquences et autour de 2.75GHz. Toutefois, lorsque l'antenne est reconfigurée pour fonctionner en omnidirectionnel en activant toutes les diodes de la SSF, le coefficient de réflexion de l'antenne a naturellement tendance à suivre celui du dipôle, excepté les quelques désadaptations observées autour de 3GHz. Le gain réalisé de l'antenne a été mesuré à différentes fréquences pour le diagramme de rayonnement directif dans deux directions opposées, i. e. . ($\varphi = 0^\circ, \theta = 90^\circ$) et ($\varphi = 180^\circ, \theta = 90^\circ$). La Fig. 8-28 illustre les résultats expérimentaux comparés à ceux des simulations. Ces courbes représentent clairement un diagramme de rayonnement directif bi-bande avec environ 7dB de gain. Ceci est en accord avec le double comportement des réponses des coefficients de transmission reconfigurables de la SSF-B planeaire, prédit sur les deux bandes de fréquences à la Fig. 8-29.

En tant que preuve du concept, les diagrammes de rayonnement de l'antenne ont été mesurés à différentes fréquences comprises de 2GHz à 3.2GHz. Les résultats représentés à la Fig. 8-28 montrent que le niveau des lobes arrières/secondaires de l'antenne est inférieur à -20dB à la fréquence de 2.35GHz. Les largeurs des faisceaux à mi-puissance, dans les diagrammes de rayonnement du plan H et E, à 2.35GHz et 3.1GHz sont environ de (59°, 66°) et (70°, 41°), respectivement. La comparaison de ces largeurs de faisceaux avec les simulations de la Tab. 8-3 révèle une différence notable seulement pour le diagramme du plan H. Puisque les effets des éléments actifs et autres pertes ont été considérés dans la simulation, cette différence peut être interprétée essentiellement par la réduction du gain mesuré. En outre, comme il était prévu à partir des réponses duales aux deux bandes de fonctionnement, les diagrammes de rayonnement de l'antenne sont orientés dans deux directions opposées pour les bandes de fréquences obtenues. Cela confirme techniquement l'agilité en fréquence de cette configuration d'antenne à balayage de faisceau.

Afin d'évaluer la fonctionnalité de reconfiguration du cas directif au cas omnidirectionnel, les diagrammes de rayonnement de l'antenne ont également été mesurés lorsque tous les éléments actifs de la SSF sont activés ou désactivés pour la première et seconde bande de fonctionnement, respectivement. Par souci de comparaison, le gain mesuré de l'antenne dipôle est montré à la Fig. A 28 pour évaluer les performances de directivité de l'antenne dans différents cas. Selon cette figure, quand l'antenne est reconfigurée pour le cas omnidirectionnel, la directivité du diagramme de

rayonnement de l'antenne est similaire à celle mesurée pour le dipôle. La réduction du gain à des fréquences plus élevées peut être expliquée en raison de la faible transparence de la SSF, conduisant à capturer une partie de la puissance rayonnée à l'intérieur du cylindre.

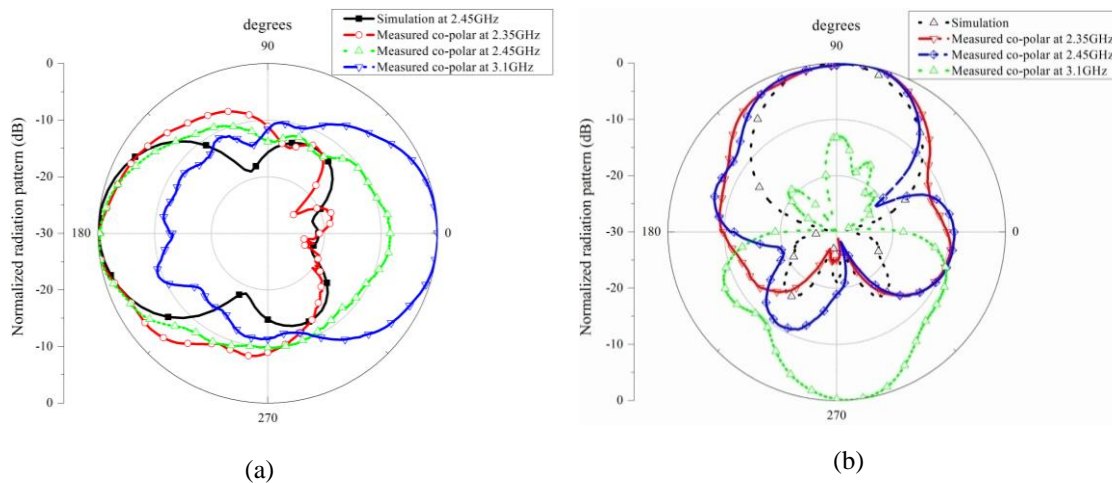


Fig. 8-28 Diagramme de rayonnement simulé et mesuré du cas d'une antenne agile en fréquence dans le cas directif. (a) Plan H. (b) Plan E.

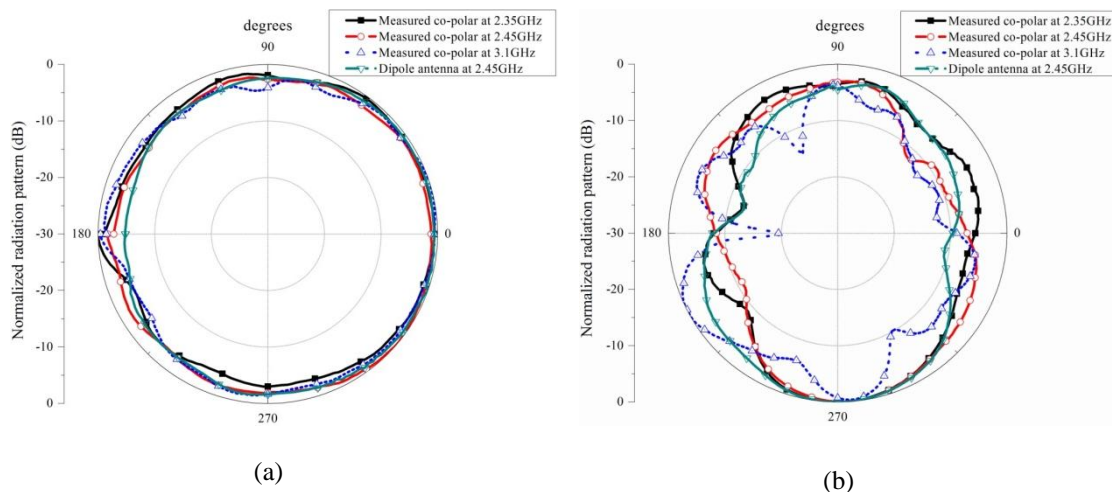


Fig. 8-29 Diagramme de rayonnement simulé et mesuré du cas d'une antenne agile en fréquence dans le cas omnidirectionnel. (a) Plan H. (b) Plan E.

Comme preuve supplémentaire de ce concept, les diagrammes de rayonnement du cas omnidirectionnel ont été comparés à ceux de l'antenne dipôle à la Fig. 8-29. Il est clair que lorsque l'antenne est reconfigurée pour le cas omnidirectionnel, son diagramme de rayonnement suit celui du dipôle sur la première bande de fréquence désirée. Toutefois, le diagramme de rayonnement du plan E est nettement dévié de celui du dipôle. Par

conséquent, l'antenne proposée peut offrir les performances assez agiles dans la seconde bande de fréquence obtenue.

Tab. 8-3 Caractéristiques des antennes.

	Antenne agile				Antenne agile fréquence					
	Simulation		Mesure		Simulation dans la bande		Première bande mesurée		Seconde bande mesurée	
Antenna aperture (A)	$2R_1 \times 4P_{y1}$		$2R_1 \times 4P_{y1}$		$2R \times 2P_{y2}$		$2R \times 2P_{y2}$		$2R \times 2P_{y2}$	
Bandwidth(MHz)	Omni.	Dir.	Omni.	Dir.	Omni.	Dir.	Omni.	Dir.	Omni.	Dir.
	-	102	Wide	Wide	600	468	475	Wide	Wide	Wide
HPBW(Deg.)	H	E	H	E	H	E	H	E	H	E
	112	42	104	40	71	61	59	66	70	41
Peak gain(dB)	8.2		3.94		9.1		7.6		6.8	
Back Lobe(dB)	-15		-20		-21		-20		-10	
Total efficiency	94		-		94.5		-		-	
$\eta = G\lambda^2 / 4\pi A$	38		14.5		73		51		47	

Note: Le rayon R et les périodicités de la cellule unitaire pour les deux antennes sont: $R_1 = 39mm$, $P_{y1} = 66mm$, $R_2 = 46mm$, and $P_{y2} = 46mm$.

8.5 Conclusion

Dans cette thèse, les résultats de l'étude sur les applications des surfaces sélectives en fréquence pour les antennes reconfigurables ont été présentés. Comme objectif principal de ce travail, ce type de SSF a été combiné avec certains mécanismes reconfigurables afin de proposer une nouvelle classe de structures d'antennes à réflecteurs polyvalentes—appelées “antenne agile”. Ce nom a été choisi en raison des fonctionnalités que ces antennes peuvent avoir. En effet, ces antennes sont capables de balayer tous les angles azimutaux dans des étapes déterminées, et elles peuvent également reconfigurer leurs diagrammes de rayonnement de l'état directionnel à un état omnidirectionnel. Par ailleurs, en concevant précisément une SSF, la fonctionnalité d'agilité en fréquence a également été introduite dans la structure. Pour réussir à accomplir cette mission, une procédure de conception étape par étape a été effectuée dans ce travail.

8.6 Axes des futures recherches

Dans cette thèse, plusieurs travaux de recherche ont été effectués sur les surfaces sélectives reconfigurables en fréquence à couche unique planaire et conforme pour des applications d'antenne. Cependant, ce travail ne couvre pas tout le domaine, d'autres

extensions dans ce domaine peuvent être effectuées telles qu'énoncés dans les paragraphes suivants.

Selon les thèmes des recherches multi-disciplinaires entrepris dans cette thèse, trois voies d'avenir dans les différents domaines de recherche peuvent être envisagées. La première peut être les technologies de reconfiguration alternatives qui peuvent être utilisées pour la topologie de rayonnement proposée dans cette thèse. Comme il a été démontré, les effets des commutateurs non idéaux et leur ligne d'alimentation DC de polarisation affectent les performances des surfaces reconfigurables. Trouver un autre mécanisme de reconfiguration avec de nouvelles technologies émergentes comme les MEMS, les matériaux plasma et ferroélectriques pourraient être un sujet intéressant pour surpasser ce problème et améliorer les performances de l'antenne et probablement augmenter ses fonctionnalités.

La seconde voie de recherche concerne les surfaces sélectives en fréquence. Dans cette thèse, seulement un certain groupe de surfaces à couche unique a été étudié juste pour une onde incidente à polarisation TE. La possibilité d'appliquer d'autres éléments résonants, l'effet des angles d'incidence dans l'amélioration de leurs réponses dans une configuration conforme, et augmenter le nombre de surfaces dans la configuration de l'antenne pour améliorer ses performances de rayonnement arrière peut également être un autre sujet de recherche. Plus important encore, les surfaces sélectives en fréquence conçues sont utilisées dans la région de champ proche de l'antenne dipôle. Calculer les caractéristiques de rayonnement de l'antenne utilisant les équations de Maxwell, qui sont résolues avec une méthode numérique appropriée est un autre sujet de recherche qui peut probablement explorer un autre phénomène attractif qui n'a pas été considéré dans les travaux actuels.

La topologie de rayonnement de l'antenne peut être le troisième sujet intéressant pour les recherches à venir. Dans cette thèse, le diagramme de rayonnement de l'antenne balaye uniquement les angles d'azimutaux et nous ne traitons que les ondes polarisées verticalement. La modification du mécanisme de rayonnement pour balayer les angles d'élévation, l'obtention aussi bien de la polarisation horizontale que verticale peut constituer un nouveau thème de recherche.

References

1. J. C. Liberti and T. S. Rappaport, *Smart Antennas for Wireless Communications: IS-95 and Third Generation CDMA Applications*, Prentice Hall, 1999.
2. C. A. Balanis and P. I. Ioannides, *Introduction to Smart Antennas*, Morgan & Claypool publications series, 2007.
3. A. J. Fenn, *Adaptive Antennas and Phased Arrays for Radar and Communication Systems*, Artech House, 2008.
4. J. T. Bernhard, *Reconfigurable Antennas*, Morgan & Claypool publications series, 2007.
5. N. Engheta and R. W. Ziolkowski, *Metamaterials: Physics and Engineering Explorations*, John Wiley & Sons, 2006.
6. F. Yang and Y. Rahmat-Samii, *Electromagnetic Band Gap Structures in Antenna Engineering*, Cambridge University Press, 2009.
7. A. Pirhadi, M. Hakkak, F. Keshmiri and R. Karimzadeh-Bae, "Design of Compact Dual Band High Directive Electromagnetic Bandgap (EBG) Resonator Antenna Using Artificial Magnetic Conductor," *IEEE Trans. on Ant. and Propag.*, Vol. 55, (No. 6, Part-2), p. p. 1682 –1690, 2007.
8. L. Leger, T. Monediere and B. Jecko, "Enhancement of Gain and Radiation Bandwidth for a Planar 1-D EBG Antenna," *Mic. and Wireless Components Lett.*, Vol. 15 (9), p. p. 573-575, 2005.
9. L. Zenguo. "Quasi- Periodic Structure Application in Fabry-Perot Resonator Printed Antenna," in *Asia-Pacific Mic. Conf.*, 16-20 Dec., 2008.
10. Y. J. Lee, J. Yeo, R. Mitra and W. S. Park, "Design of a High Directivity Electromagnetic Band Gap (EBG) Resonator Antenna Using a Frequency Selective

- Surface (FSS) Superstrate,” *Mic. and Opt. Tech. Lett.*, Vol. 43, p. p. 462-467, Dec. 2004.
11. A. R. Weily, L. Horvath, K. P. Esselle, B. C. Sanders and T. S. Bird, “A Planar Resonator Antenna Based on a Woodpile EBG Material,” *IEEE Trans. on Ant. and Propag.*, Vol. 53 (No. 1), p. p. 216-223, 2005.
 12. G. K. Palikaras, A. P. Feresidis and J. C. Vardaxoglou, “Cylindrical Electromagnetic Bandgap Structures for Directive Base Station Antennas,” *IEEE on Ant. and Wireless Propag. Lett.*, Vol. 3 (No. 1), p. p. 87-89, 2004.
 13. A. P. Feresidis, G. Goussetis, W. Shenhong and J. C. Vardaxoglou, “Artificial Magnetic Conductor Surfaces and Their Application to Low-Profile High-Gain Planar Antennas,” *IEEE Trans. on Ant. and Propag.*, Vol. 53 (No. 1), p. p. 209-215, 2005.
 14. D. Sievenpiper, J. Schaffner, R. Loo, G. Tangonan, et al., “A Tunable Impedance Surface Performing as a Reconfigurable Beam Steering Reflector,” *IEEE Trans. on Ant. and Propag.*, Vol. 50 (No. 3), p. p. 384-390, 2002.
 15. G. Poilasne, P. Pouliguen, K. Mahdjoubi, L. Desclos and C. Terret, “Active Metallic Photonic Band-Gap Materials (MPBG): Experimental Results on Beam Shaper,” *IEEE Trasn. on Ant. and Propag.*, Vol. 48 (No. 1), p. p. 117-119, 2000.
 16. H. Boutayeb, T. A. Denidni, K. Mahdjoubi, A. C. Tarot, et al., “Analysis and Design of a Cylindrical EBG-Based Directive Antenna,” *IEEE Trans. on Ant. and Propag.*, Vol. 54 (No. 1), p. p. 211-219, 2006.
 17. B. A. Munk, *Frequency Selective Surfaces Theory and Design* John Wiley & Sons, 2000.
 18. B. A. Munk, *Finite Antenna Arrays and FSS*, John Wiley & Sons, 2003.
 19. T. K. Wu, *Frequency Selective Surface and Grid Array*, John Wiley & Sons, 1995.
 20. J. Huang and J. A. Encinar, *Reflectarray Antennas*, John Wiley & Sons, 2008.
 21. A. Ourir, S. N. Burokur and A. d. Lustrac, “Electronically Reconfigurable Metamaterial for Compact Directive Cavity Antennas,” *Elec. Lett.*, Vol. 43 (No. 13), p. p. 698-700, 2007.
 22. A. Ourir, S. N. Burokur and A. D. Lustrac, “Phase-Varying Metamaterial for Compact Steerable Directive Antenna,” *Elec. Lett.*, Vol. 43 (No. 9), p. p. 493-494, 2007.
 23. A. R. Weily, T. S. Bird and Y. J. Guo., “A Reconfigurable High-Gain Partially Reflecting Surface Antenna,” *IEEE Trans. on Ant. and Propag.*, Vol. 56 (No. 11), p. p. 3382-3390, 2008.

24. F. Costa, A. Monorchio, S. Talarico and F. M. Valeri, "An Active High-Impedance Surface for Low-Profile Tunable and Steerable Antennas," *IEEE on Ant. and Wireless Propag. Lett.*, Vol. 7, p. p. 676-680, 2008.
25. P. Deo, A. Mehta, D. Mirshekar-Syahkal and H. Nakano, "An HIS-Based Spiral Antenna for Pattern Reconfigurable Applications," *IEEE on Ant. and Wireless Propag. Lett.*, Vol. 8, p. p. 196-199, 2009.
26. C. Chih-Chieh and A. Abbaspour-Tamijani, "Study of 2-bit Antenna-Filter-Antenna Elements for Reconfigurable Millimeter-Wave Lens Arrays," *IEEE Trans. on Mic. The. and Tech.*, Vol. 54 (No. 12), p. p. 4498-4506, 2006.
27. M. Riel and J. J. Laurin, "Design of an Electronically Beam Scanning Reflectarray Using Aperture-Coupled Elements," *IEEE Trans. on Ant. and Propag.*, Vol. 55 (No. 5), p. p. 1260-1266, 2007.
28. J. T. Aberle, O. Sung-Hoon, D. T. Auckland and S. D. Rogers, "Reconfigurable Antennas for Wireless Devices," *IEEE on Ant. and Propag. Mag.*, Vol. 45 (No. 6), p. p. 148-154, 2003.
29. C. B. J. Dietrich, W. L. Stutzman, K. Byung-Ki and K. Dietze, "Smart Antennas in Wireless Communications: Base-Station Diversity and Handset Beamforming," *IEEE on Ant. and Propag. Mag.*, Vol. 42 (No. 5), p. p. 142-151, 2000.
30. J. T. Bernhard. "Reconfigurable Multifunction Antennas: Next Steps for the Future," in *Int. Sym. on Mic., Ant., Propag. and EMC Tech. for Wireless Comm.*, 2007.
31. E. Erfani, J. Nourinia, C. Ghobad, M. Niropo-Jazi and T. A. Denidni, "Design and Implementation of an Integrated /Reconfigurable-Slot Antenna for Cognitive Radio Applications," *IEEE on Ant. and Wireless Propag. Lett.*, Vol. 11, p. 77-80, March 2012.
32. K. Boyon, P. Bo, S. Nikolaou, K. Young-Sik, et al., "A Novel Single-Feed Circular Microstrip Antenna With Reconfigurable Polarization Capability," *IEEE Trans. on Ant. and Propag.*, Vol. 56 (No. 3), p. p. 630-638, 2008.
33. F. Ferrero, C. Luxey, R. Staraj, G. Jacquemod, et al., "A Novel Quad-Polarization Agile Patch Antenna," *IEEE Trans. on Ant. and Propag.*, Vol. 57 (No. 5), p. p. 1563-1567, 2009.
34. M. K. Fries, M. Grani and R. Vahldieck, "A Reconfigurable Slot Antenna with Switchable Polarization," *Mic. and Wireless Components Lett.*, Vol. 13 (No. 11), p. p. 490-492, 2003.
35. S. Lim and H. Ling, "Design of Electrically Small, Pattern Reconfigurable Yagi Antenna," *Elec. Lett.*, Vol. 43 (No. 24), p. p. 1326-1327, 2007.

36. W. Sung-Jung and M. Tzyh-Ghuang, "A Wideband Slotted Bow-Tie Antenna With Reconfigurable CPW-to-Slotline Transition for Pattern Diversity," *IEEE Trans. on Ant. and Propag.*, Vol. 56 (No. 2), p. p. 327-334, 2008.
37. L. N. Pringle, P. H. Harms, S. P. Blalock, G. N. Kiesel, et al., "A Reconfigurable Aperture Antenna Based on Switched Links Between Electrically Small Metallic Patches," *IEEE Trans. on Ant. and Propag.*, Vol. 52 (No. 6), p. p. 1434-1445, 2004.
38. A. G. Besoli and F. D. Flaviis, "A Multifunctional Reconfigurable Pixeled Antenna Using MEMS Technology on Printed Circuit Board," *IEEE Trans. on Ant. and Propag.*, Vol. 59 (No. 12), p. p. 4413-4424, 2011.
39. G. H. Huff and J. T. Bernhard, "Integration of Packaged RF MEMS Switches with Radiation Pattern Reconfigurable Square Spiral Microstrip Antennas," *IEEE Trans. on Ant. and Propag.*, Vol. 54 (No. 2), p. p. 464-469, 2006.
40. W. Kim, M. F. Iskander and W. D. Palmer, "An Integrated Phased Array Antenna Design Using Ferroelectric Materials and the Continuous Transverse Stub Technology," *IEEE Trans. on Ant. and Propag.*, Vol. 54 (No. 11), p. p. 3095-3105, 2006.
41. R. R. Romanofsky, "Advances in Scanning Reflectarray Antennas Based on Ferroelectric Thin-Film Phase Shifters for Deep-Space Communications," *IEEE Proceedings*, Vol. 95 (No. 10), p. p. 1968-1975, 2007.
42. J. Taeksoo, H. Yoon, J. K. Abraham and V. K. Varadan, "Ku-Band Antenna Array Feed Distribution Network with Ferroelectric Phase Shifters on Silicon," *IEEE Trans. on Mic. The. and Tech.*, Vol. 54 (No. 3), p. p. 1131-1138, 2006.
43. S. L. Preston, D. V. Thiel, J. W. Lu, S. G. O'Keefe and T. S. Bird, "Electronic Beam Steering Using Switched Parasitic Patch Elements," *Elec. Lett.*, Vol. 33 (No. 1), p. p. 7-8, 1997.
44. R. Schlub, D. V. Thiel, J. W. Lu and S. W. O'Keefe, "Dual-Band Six-Element Switched Parasitic Array for Smart Antenna Cellular Communications Systems," *Elec. Lett.*, Vol. 36 (No. 16), p. p. 1342-1343, 2000.
45. B. Schaer, K. Rambabu, J. Bornemann and R. Vahldieck, "Design of Reactive Parasitic Elements in Electronic Beam Steering Arrays," *IEEE Trans. on Ant. and Propag.*, Vol. 53 (No. 6), p. p. 1998-2003, 2005.
46. R. Jakoby, P. Scheele, S. Muller and C. Weil. "Nonlinear Dielectrics for Tunable Microwave Components," in *15th Int. Conf. on Mic., Radar and Wireless Comm.*, 2004.
47. Y. Poplavko, V. Kazmirenko, Y. Prokopenko, J. Moongi and B. Sunggi. "Dielectric Based Frequency Agile Microwave Devices," in *15th Int. Conf. on Mic., Radar and Wireless Comm.*, 2004.

48. J. B. Mills, C. J. Stevens and D. J. Edwards. "Composite Materials for Planar Frequency Agile Microwave Devices," in *16th IEEE High Freq. Postgraduate Student Colloquium*, 2001.
49. G. M. Rebeiz and J. B. Muldavin, "RF MEMS Switches and Switch Circuits," *IEEE Mic. Mag.*, Vol. 2 (No. 4), p. p. 59-71, 2001.
50. N. Kingsley, G. E. Ponchak and J. Papapolymerou, "Reconfigurable RF MEMS Phased Array Antenna Integrated Within a Liquid Crystal Polymer (LCP) System-on-Package," *IEEE Trans. on Ant. and Propag.*, Vol. 56 (No. 1), p. p. 108-118, 2008.
51. R. Kumar and D. Bora, "A Reconfigurable Plasma Antenna," *Jour. of App. Phy.*, Vol. 107 (No. 5), p. p. 53303-53312, 2010.
52. G. V. Eleftheriades and K. G. Balmain, *Negative-Refractive Metamaterials: Fundamental Principles and Applications*, John Wiley and Sons, 2005.
53. Y. V. Rassokhina and V. G. Krizhanovski, "Periodic Structure on the Slot Resonators in Microstrip Transmission Line," *IEEE Trans. on Mic. The. and Tech.*, Vol. 57 (No. 7), p. p. 1694-1699, 2009.
54. J. Garcia-Garcia, J. Bonache and F. Martin, "Application of Electromagnetic Bandgaps to the Design of Ultra-Wide Bandpass Filters With Good Out-of-Band Performance," *IEEE Trans. on Mic. The. and Tech.*, Vol. 54 (No. 12), p. p. 4136-4140, 2006.
55. R. Abhari and G. V. Eleftheriades, "Metallo-Dielectric Electromagnetic Bandgap Structures for Suppression and Isolation of the Parallel-Plate Noise in High-Speed Circuits," *IEEE Trans. on Mic. The. and Tech.*, Vol. 51 (No. 6), p. p. 1629-1639, 2003.
56. P. d. Maagt, R. Gonzalo, Y. C. Vardaxoglou and J. M. Baracco, "Electromagnetic Bandgap Antennas and Components for Microwave and (Sub) Millimeter Wave Applications," *IEEE Trans on Ant. and Propag.*, Vol. 51 (No. 10), p. p. 2667-2677, 2003.
57. L. Moustafa and B. Jecko, "Design of a Wideband Highly Directive EBG Antenna Using Double-Layer Frequency Selective Surfaces and Multifeed Technique for Application in the Ku-Band," *IEEE on Ant. and Wir. Propag. Let.*, Vol. 9, p. p. 342-346, 2010.
58. R. Mittra, C. H. Chan and T. Cwik, "Techniques for Analyzing Frequency Selective Surfaces-A Review," *IEEE Proceedings*, Vol. 76 (No. 12), p. p. 1593-1615, 1988.
59. C. K. Lee and R. J. Langley, "Equivalent-Circuit Models for Frequency-Selective Surfaces at Oblique Angles of Incidence," *IEE Proc. on Mic., Ant. and Propag.*, Vol. 132 (No. 6), p. p. 395-399, 1985.

60. R. J. Langley and E. A. Parker, "Equivalent Circuit Model for Arrays of Square Loops," *Elec. Lett.*, Vol. 18 (No. 7), p. p. 294-296, 1982.
61. John L. Volakis, *Antenna Engineering Handbook*, McGraw-Hill, (Chapter 56: Frequency Selective Surfaces), 2007.
62. P. Callaghan and E. A. Parker, "Element Dependency in Dielectric Tuning of Frequency Selective Surfaces," *Elec. Lett.*, Vol. 28 (No. 1), p. p. 42-44, 1992.
63. S. M. A. Hamdy and E. A. Parker, "Influence of Lattice Geometry on Transmission of Electromagnetic Waves Through Arrays of Crossed Dipoles," *IEE Proc. on Mic., Optics and Ant.*, Vol. 129 (No. 1), p. p. 7, 1982.
64. C. Antonopoulos, R. Cahill, E. A. Parker and I. M. Sturland, "Multilayer Frequency-Selective Surfaces for Millimetre and Submillimetre Wave Applications," *IEE Proc. on Mic., Ant. and Propag.*, Vol. 144 (No. 6), p. p. 415-420, 1997.
65. P. W. B. Au, E. A. Parker and R. J. Langley, "Wideband Filters Employing Multilayer Gratings," *IEE Proc. Mic. Ant. and Propag.*, Vol. 140 (No. 4), p. p. 292-296, 1993.
66. P. Callaghan and E. A. Parker, "Tuning Interactions of Cascaded-Frequency Selective-Slot Arrays," *IEE Proc. on Mic., Ant. and Propag.*, Vol. 141 (No. 4), p. p. 290-294, 1994.
67. P. Callaghan, E. A. Parker and R. J. Langley, "Influence of Supporting Dielectric Layers on The Transmission Properties of Frequency Selective Surfaces," *IEE Proc. on Mic. Ant. and Propag.*, Vol. 138 (No. 5), p. p. 448-454, 1991.
68. R. Luebbers and B. Munk, "Some Effects of Dielectric Loading on Periodic Slot Arrays," *IEEE Trans. on Ant. Propag.*, Vol. 26 (No. 4), p. p. 536-542, 1978.
69. D. A. Palma and W. C. Wong. "Broadband Frequency Selective Surface," in *Military Comm. Conf. - Communications-Computers*, 1986.
70. E. Pelton and B. Munk, "Scattering From Periodic Arrays of Crossed Dipoles," *IEEE Trans. on Ant. and Propag.*, Vol. 27 (No. 3), p. p. 323-330, 1979.
71. C. Cheng-Nan, K. Chang-Hsin and L. Ming-Shing, "Bandpass Shielding Enclosure Design Using Multipole-Slot Arrays for Modern Portable Digital Devices," *IEEE Trans. on Elect. Comp.*, Vol. 50 (No. 4), p. p. 895-904, 2008.
72. O. Luukkonen, F. Costa, C. R. Simovski, A. Monorchio and S. A. Tretyakov, "A Thin Electromagnetic Absorber for Wide Incidence Angles and Both Polarizations," *IEEE Trans. on Ant. and Propag.*, Vol. 57 (No. 10), p. p. 3119-3125, 2009.

73. F. Sakran, Y. Neve-Oz, A. Ron, M. Golosovsky, et al., "Absorbing Frequency-Selective-Surface for the mm-Wave Range," *IEEE Trans. on Ant. and Propag.*, Vol. 56 (No. 8), p. p. 2649-2655, 2008.
74. G. H. H. Sung, K. W. Sowerby, M. J. Neve and A. G. Williamson, "A Frequency-Selective Wall for Interference Reduction in Wireless Indoor Environments," *IEEE Ant. and Propag. Mag.*, Vol. 48 (No. 5), p. p. 29-37, 2006.
75. B. A. Munk, P. Munk and J. Pryor, "On Designing Jaumann and Circuit Analog Absorbers (CA Absorbers) for Oblique Angle of Incidence," *IEEE Trans. on Ant. and Propag.*, Vol. 55 (No. 1), p. p. 186-193, 2007.
76. K. Karkkainen and M. Stuchly, "Frequency Selective Surface as a Polarisation Transformer," *IEE Proc. on Mic. Ant. and Propag.*, Vol. 149 (No. 56), p. p. 248-252, 2002.
77. A. Mortazwi, T. Itoh and J. Harvey, *Active Antennas and Quasi-Optical Arrays* Wiley-IEEE Press, 1998.
78. J. A. Arnaud and F. A. Pelow, "Resonant-Grid Quasi-Optical Diplexers," *The Bell System Technical Journal*, Vol. 54 (No. 2), p. p. 263-283, 1976.
79. N. Marcuvitz, *Waveguide Handbook*, Dover, 1965.
80. G. G. Macfarlane, "Surface Impedance of An Infinite Parallel-Wire Grid at Oblique Angles of Incidence," *Jour. of Institution of Radiolocation- Part IIIA*, Vol. 93 (No. 10), p. p. 1523-1527, 1946.
81. I. Anderson, "On The Theory of Self-Resonant Grids," *The Bell System Technical Journal*, Vol. 54 (No. 10), p. p. 1725-1731, 1975.
82. A. C. d. C. Lima, P. Grammatikakis and E. A. Parker. "Arrays of Stub Loaded Inductive Strips," in *18th Int. Conf. on Ant. and Propag.*, 1993.
83. R. J. Langley and E. A. Parker, "Double-Square Frequency-Selective Surfaces and Their Equivalent Circuit," *Elec. Lett.*, Vol. 19 (No. 17), p. p. 675-677, 1983.
84. W. Z. Liang, K. Hashimoto, N. Shinohara and H. Matsumoto, "Frequency-Selective Surface for Microwave Power Transmission," *IEEE Trans. on Mic. The. and Tech.*, Vol. 47 (No. 10), p. p. 2039-2042, 1999.
85. T. K. Chang, R. J. Langley and E. Parker, "An Active Square Loop Frequency Selective Surface," *IEEE Lett. on Mic. and Guided Wave*, Vol. 3 (No. 10), p. p. 387-388, 1993.
86. B. Sanz-Izquierdo, E. A. Parker, J. B. Robertson and J. C. Batchelor, "Tuning Technique for Active FSS Arrays," *Elec. Lett.*, Vol. 45 (No. 22), p. p. 1107-1109, 2009.

87. M. Niroo-Jazi and T. A. Denidni. "Reconfigurable Dual-Band Frequency Selective Surfaces Using a New Hybrid Element," in *IEEE Int. Sym. on Ant. and Propag.*, 2011.
88. A. Edalati and T. A. Denidni, "High-Gain Reconfigurable Sectoral Antenna Using an Active Cylindrical FSS Structure," *IEEE Trans. on Ant. and Propag.*, Vol. 59 (No. 7), p. p. 2464-2472, 2011.
89. A. M. Habib, M. N. Jazi, A. Djaiz, M. Nedil, et al. "On IP3 Performance Investigation in Reconfigurable Active EBG Antenna," in *IEEE Int. Sym. on Ant. and Propag.*, 2010.
90. M. A. Habib, M. N. Jazi, A. Djaiz, M. Nedil and T. A. Denidni. "Switched-Beam Antenna Based on EBG Periodic Structures," in *IEEE Int. Sym. on Mic. The. and Tech.*, 2009.
91. M. N. Jazi and T. A. Denidni, "Frequency Selective Surfaces and Their Applications for Nimble-Radiation Pattern Antennas," *IEEE Trans. on Ant. and Propag.*, Vol. 58 (No. 7), p. p. 2227-2237, 2010.
92. M. N. Jazi, M. A. Habib and T. A. Denidni. "Electronically Switching Radiation Pattern Antenna Using an Active Cylindrical Frequency Selective Surface," in *Int. Sym. on Ant. and Propag.*, 2009.
93. M. N. Jazi, M. A. Habib and T. A. Denidni. "Reconfigurable Radiation Pattern Antenna Based on Active Frequency Selective Surfaces," in *IEEE Int. Sym. on Ant. and Propag.*, 2009.
94. R. J. Langley and A. J. Drinkwater, "Improved Empirical Model for the Jerusalem Cross," *IEE Proc. on Mic., Optics and Ant.*, Vol. 129 (No. 1), p. p. 1-6, 1982.
95. GMP4200 PIN-Diode Series, [Online]. Available: <http://www.microsemi.com/datasheets/gmp4200%20series.pdf>.
96. A. Edalati and T. A. Denidni, "Reconfigurable Beamwidth Antenna Based on Active Partially Reflective Surfaces," *IEEE on Ant. and Wireless Propag. Lett.*, Vol. 8, p. p. 1087-1090, 2009.
97. J. D. Kraus, *Antennas*, McGraw-Hill, 1988.
98. B. Philips, E. A. Parker and R. J. Langley, "Finite Curved Frequency Selective Surfaces," *Elec. Lett.*, Vol. 29 (No. 10), p. p. 882-883, 1993.
99. M. Niroo-Jazi and T. A. Denidni, "Electronically Sweeping-Beam Antenna Using a New Cylindrical Frequency Selective Surface," *Submitted to the IEEE Trans. on Ant. and Propag.*, Vol., p., 2012.

100. M. N. Jazi and T. A. Denidni, "Agile Radiation-Pattern Antenna Based on Active Cylindrical Frequency Selective Surfaces," *IEEE on Antennas and Wireless Propag. Lett.*, Vol. 9, p. p. 387-388, 2010.